

# Mechanical behavior of Ti-5553 alloy

## Modeling of representative cells



A thesis submitted to the University of Liège  
for the degree of "Docteur en Sciences de l'Ingénieur"  
By Anne-Françoise Gerday  
March 2009



# Contact Information

Author's coordinates:

Mrs. Anne-Françoise GERDAY

University of Liège

ArGEnCo Department, MS<sup>2</sup>F division, building B52/3

1 Chemin des Chevreuils

4000 Liege 1

Belgium

OFFICE PHONE: +32(0)4 366 93 27

FAX: +32(0)4 366 91 92

EMAIL: *afgerday@ulg.ac.be*

WEBSITE: *http://www.argenco.ulg.ac.be*

Supervisor's coordinates:

Dr. Anne Marie HABRAKEN

Research Director (FNRS, Belgium)

University of Liège

ArGEnCo Department, MS<sup>2</sup>F division, building B52/3

1 Chemin des Chevreuils

4000 Liege 1

Belgium

OFFICE PHONE: +32(0)4 366 94 30

SECRETARY PHONE: +32(0)4 366 92 60

FAX: +32(0)4 366 91 92

EMAIL: *Anne.Habraken@ulg.ac.be*

WEBSITE: *http://www.argenco.ulg.ac.be*





# Jury Members

Prof. J. LECOMTE-BECKERS, president of the jury  
LTAS Department, University of Liège, Belgium  
*Jacqueline.Lecomte@ulg.ac.be*

Dr. A.M. HABRAKEN, supervisor of the thesis  
ArGEnCo Department, University of Liège, Belgium  
*Anne.Habraken@ulg.ac.be*

Prof. S. CESCOTTO  
ArGEnCo Department, University of Liège, Belgium  
*Serge.Cescotto@ulg.ac.be*

Prof. T. PARDOEN  
Unity of Applied Mechanics, University of Louvain-la-Neuve, Belgium  
*Thomas.Pardoen@uclouvain.be*

Prof. L. DELANNAY  
Unity of Applied Mechanics, University of Louvain-la-Neuve, Belgium  
*Laurent.Delannay@uclouvain.be*

Dr. A. LENAIN  
Techspace Aero, Belgium  
*alenain@techspace-aero.be*

Prof. X. FEAUGAS  
Laboratoire d' Etude des Matériaux en Milieux Agressifs (L.E.M.M.A),  
La Rochelle University, France  
*xavier.feugas@univ-lr.fr*



# Summary

This work focuses on a new  $\beta$  metastable titanium alloy, Ti-5553, for aeronautical applications. The goals of this study are the characterization of the two phases ( $\alpha$  and  $\beta$ ) of this titanium alloy and the numerical modeling of representative cells of this material, which will be used to determine the appropriate microstructure.

This thesis is divided into several parts. First, the numerical tools necessary to characterize this alloy and to model representative cells using the periodic homogenization theory will be presented. Secondly, the body-centered cubic  $\beta$  phase will be identified. Then, the third part will concentrate on the characterization of the hexagonal close-packed  $\alpha$  phase. Finally, the last part of this thesis will focus on choosing and modeling representative cells containing the phases identified in the previous parts.

The experimental tensile tests performed at different strain rates have demonstrated the necessity of using an elastic-viscous-plastic constitutive law. Guided by macroscopic (tensile and simple shear) experiments, a microscopic plasticity-based constitutive law was chosen to characterize this alloy instead of a macroscopic Norton-Hoff's constitutive one.

It will be shown that the  $\beta$  phase can be fully maintained in macroscopic samples at room temperature, making the characterization of the material behavior of this phase possible from macroscopic experiments. The optimized set of parameters was validated on nanoindentation tests performed in different  $\beta$  grain orientations. In addition, a sensitivity analysis of several parameters from nanoindentation tests was performed and shows the importance of accurately defining some parameters, such as the exact shape of the indenter, and the negligible influence of other parameters, such as Poisson's ratio. From this study of experimental and numerical nanoindentation tests, it also appears that the orientation of the  $\beta$  grain indented hardly affects the nanoindentation results.

The characterization of the  $\alpha$  phase was performed using nanoindentation experimental tests available for different grain orientations. This choice was influenced by the impossibility of maintaining only an  $\alpha$  phase in a macroscopic Ti-5553 sample at room temperature and by the failure to represent the phase accurately from macroscopic ( $\alpha + \beta$ ) samples. The material characterization of this phase is complex and difficulties occur when the behavior of this phase has to be characterized for different orientations by only one set of parameters.

Finally, experimental microstructures were chosen and their simplified corresponding representative cells were meshed. Numerical simulations of these representative cells were performed and the influence of several parameters will be studied, such as the effect of the appearance of the  $\alpha$  phase in the  $\beta$  matrix and the effect of the shape of the  $\alpha$  phase on the behavior of the cell.



# Acknowledgements

*First and foremost, I would like to express my sincere gratitude towards my adviser, Dr. Anne Marie Habraken, for her continuous guidance, encouragement and intellectual stimulation.*

*Secondly, I want to thank the Walloon Region for its financial support which has allowed me to achieve this research work.*

*I cannot forget the other members of this project for their critical and constructive remarks throughout this research work. A special thanks to Nicolas Clément who had the patience to answer all my questions. He was given the responsibility of performing the experimental part of this research work, which I needed for my work.*

*The greatest thanks are reserved for my colleagues for their friendly help, for their competent advice or simply for their kind presence. Particularly, I want to thank Frédéric Pascon who has tolerated my mess in our office and spent hours helping and Barbara Rossi for her advice in the manuscript correction. A special thanks also to Paulo Flores, Christophe Henrard, Renée Schwartz, Cédric Lequesne, Léo Studer, Laurent Duchêne and Mohamed Ben Bettaieb.*

*I would also like to acknowledge all the members of the Laboratory of Mechanics of Materials and Structure of the University of Liège for their help and their expertise in the sample cutting and to in carrying out the tests.*

*Thank you very much to the members of the jury who have read the present thesis and for their presence at my public defense.*

*Finally, I want to thank Ellen Harry for the manuscript correction and all the other people that have kindly contributed to the achievement of this work.*



# Contents

<b>I</b>	<b>Introduction</b>	<b>1</b>
<b>1</b>	<b>General introduction</b>	<b>3</b>
1.1	Titanium . . . . .	3
1.2	Context of the study . . . . .	5
<b>2</b>	<b>Titanium and its alloys</b>	<b>7</b>
2.1	Basic properties of titanium . . . . .	7
2.2	Pure titanium . . . . .	8
2.3	Titanium alloys . . . . .	9
2.3.1	Ti-LCB alloy . . . . .	10
2.3.2	Ti-5553 alloy . . . . .	11
2.3.3	Objectives for the selected microstructure . . . . .	13
<b>3</b>	<b>Objectives and outline of the study</b>	<b>17</b>
3.1	Objectives . . . . .	17
3.2	Outline of the thesis . . . . .	18
<b>II</b>	<b>Numerical Tools</b>	<b>19</b>
<b>4</b>	<b>Microscopic constitutive law</b>	<b>23</b>
4.1	Elastic-plastic constitutive formulation for single crystals . . . . .	23
4.1.1	General principle . . . . .	23
4.1.2	Kinematics of crystalline deformation . . . . .	25
4.1.3	Constitutive laws . . . . .	26
4.1.4	Hardening of rate-dependent crystalline materials . . . . .	27
4.1.5	Integration scheme . . . . .	29
4.1.6	Incremental formulation . . . . .	30
4.2	Introduction to the hexagonal phase . . . . .	33
4.3	Conclusions . . . . .	34
<b>5</b>	<b>Macroscopic constitutive law: Norton-Hoff's elastic-viscous-plastic law</b>	<b>35</b>
<b>6</b>	<b>Periodic homogenization: theory and implementation in the FE code</b>	<b>37</b>
6.1	Introduction . . . . .	37
6.2	Homogenization theory: definition and interests . . . . .	37
6.3	Stages of the homogenization procedure . . . . .	38

6.3.1	Definition of the scales and the RVE . . . . .	38
6.3.2	Localization step . . . . .	39
6.3.3	Homogenization step . . . . .	41
6.4	Periodic homogenization in small elastic strains . . . . .	42
6.4.1	Why periodic homogenization? . . . . .	42
6.4.2	The unit cell . . . . .	42
6.4.3	Periodicity of the microscopic fields . . . . .	42
6.4.4	Cellular problems of localization . . . . .	43
6.5	Numerical implementation . . . . .	44
6.5.1	Boundary conditions . . . . .	44
6.5.2	Implementation technique . . . . .	45
6.5.3	Validation of periodic homogenization's implementation . . . . .	52
6.6	Conclusions . . . . .	52

### **III Identification of the $\beta$ phase of Ti-5553** **55**

#### **7 Modeling tensile tests on 100% $\beta$ Ti-5553** **59**

7.1	Introduction . . . . .	59
7.2	Experimental tensile tests . . . . .	59
7.3	Modeling with Norton-Hoff's macroscopic constitutive law . . . . .	60
7.3.1	Introduction . . . . .	60
7.3.2	Description of the procedure to identify the parameters . . . . .	60
7.3.3	Identification of Norton-Hoff's parameters for the $\beta$ phase of Ti-5553 . . . . .	62
7.3.4	Conclusions . . . . .	64
7.4	Modeling with a crystal plasticity-based constitutive law . . . . .	66
7.4.1	Slip systems . . . . .	66
7.4.2	Constitutive law . . . . .	66
7.4.3	Identification of the $\beta$ phase with the first hardening law . . . . .	67
7.4.4	Identification of the $\beta$ phase with the second hardening law . . . . .	71
7.4.5	Modifications to optimize the $\beta$ phase . . . . .	78
7.4.6	Tensile test modeling accounting for the evolution of $h_s$ . . . . .	80
7.5	Conclusions . . . . .	82

#### **8 Experimental simple shear tests on Ti-5553 and numerical validation** **83**

8.1	Introduction . . . . .	83
8.2	Experimental tests . . . . .	83
8.2.1	Experimental device . . . . .	83
8.2.2	Experimental difficulties . . . . .	83
8.2.3	Results . . . . .	85
8.3	Numerical tests . . . . .	88
8.3.1	Simulations with Norton-Hoff's constitutive law . . . . .	88
8.3.2	Crystal plasticity-based constitutive law for $\beta$ Ti-5553 . . . . .	92
8.4	Comparison between the $\beta$ and ( $\alpha + \beta$ ) materials . . . . .	95
8.4.1	Reminder of the two microstructures . . . . .	95
8.4.2	Stress versus strain results . . . . .	95
8.4.3	Load versus displacement curves . . . . .	98



8.5	Conclusions . . . . .	98
<b>9</b>	<b>Nanoindentation in the <math>\beta</math> phase</b>	<b>101</b>
9.1	Introduction . . . . .	101
9.2	Nanoindentation experimental tests . . . . .	104
9.2.1	Principle . . . . .	104
9.2.2	Experimental tests . . . . .	106
9.3	Numerical models . . . . .	107
9.3.1	Constitutive laws . . . . .	107
9.3.2	Finite element meshes . . . . .	107
9.3.3	Material and parameters . . . . .	109
9.4	Sensitivity analysis . . . . .	112
9.4.1	Mesh refinement . . . . .	112
9.4.2	Geometry of the indenter tip . . . . .	114
9.4.3	Positioning of the indenter tip . . . . .	116
9.4.4	Elastic parameters . . . . .	117
9.4.5	Tangent modulus and yield strength . . . . .	119
9.4.6	Friction coefficient . . . . .	119
9.4.7	Pile-up or sink-in patterns . . . . .	121
9.4.8	Grain orientation . . . . .	128
9.5	Conclusions . . . . .	131
<b>IV</b>	<b>Identification of the <math>\alpha</math> phase of Ti-5553</b>	<b>133</b>
<b>10</b>	<b>Identification of the <math>\alpha</math> phase using nanoindentation</b>	<b>135</b>
10.1	Introduction . . . . .	135
10.2	Experimental data . . . . .	136
10.3	Choice of the experimental nanoindentation curves . . . . .	136
10.4	Effect of intermediate unloading during nanoindentation experiment . . . . .	139
10.5	Identification of the elastic parameters . . . . .	140
10.5.1	The elastic matrix of hexagonal materials . . . . .	140
10.5.2	Literature review . . . . .	142
10.5.3	Experimental point of view . . . . .	142
10.5.4	Numerical point of view . . . . .	146
10.5.5	Conclusions . . . . .	151
10.6	Identification of the plastic parameters . . . . .	151
10.6.1	Literature review . . . . .	151
10.6.2	First identification procedure of the plastic parameters . . . . .	153
10.6.3	Simulations to identify the plastic parameters . . . . .	154
10.6.4	Second identification procedure of the plastic parameters . . . . .	155
10.7	Conclusions . . . . .	162

<b>V</b>	<b>Representative cells of Ti-5553</b>	<b>165</b>
<b>11</b>	<b>Representative cells</b>	<b>167</b>
11.1	Introduction . . . . .	167
11.2	Choice of the microstructures to define representative cells . . . . .	168
11.2.1	First microstructure . . . . .	168
11.2.2	Second microstructure . . . . .	170
11.2.3	Comparison between the two meshes . . . . .	171
11.3	Numerical simulations of representative cells: presentation of the tests . . . . .	172
11.4	Results and comparison . . . . .	173
11.4.1	Influence of the presence of the $\alpha$ phase in the representative cell . . . . .	174
11.4.2	Influence of the shape of the $\alpha$ phase . . . . .	177
11.4.3	Influence of the loading phase . . . . .	178
11.4.4	Influence of $\alpha$ orientation in the cell . . . . .	184
11.5	Conclusions . . . . .	187
<b>VI</b>	<b>Conclusions and perspectives</b>	<b>191</b>
<b>VII</b>	<b>Appendix</b>	<b>197</b>
<b>A</b>	<b>Ti-5553 as-received: thermal treatment</b>	<b>199</b>
<b>B</b>	<b>Crystalline structure and crystal defects</b>	<b>201</b>
B.1	Introduction . . . . .	201
B.2	Lattice positions, directions and planes . . . . .	204
B.3	Metal structures . . . . .	205
B.3.1	Body-centered cubic (BCC) structure . . . . .	206
B.3.2	Face-centered cubic (FCC) structure . . . . .	206
B.3.3	Hexagonal close packed (HCP) structure . . . . .	207
B.3.4	Similarities and differences between FCC and HCP structures . . . . .	207
B.4	Crystal defects . . . . .	207
<b>C</b>	<b>Periodic homogenization - Validation of the implementation</b>	<b>213</b>
C.1	Introduction . . . . .	213
C.2	Elastic homogeneous case . . . . .	214
C.2.1	Updated coordinates . . . . .	214
C.2.2	Microscopic velocity gradient . . . . .	215
C.2.3	Macroscopic and microscopic stresses . . . . .	215
C.3	Elastic-plastic homogeneous case . . . . .	216
C.3.1	Updated coordinates . . . . .	216
C.3.2	Evolution of the microscopic velocity gradient . . . . .	217
C.3.3	Macroscopic and microscopic stresses . . . . .	217
C.4	Elastic heterogeneous case . . . . .	217
C.4.1	Stress in each element . . . . .	217
C.4.2	Periodic velocity . . . . .	219
C.4.3	Periodic displacement . . . . .	219

C.5	Elastic-plastic heterogeneous case . . . . .	221
C.5.1	Elastic heterogeneities . . . . .	221
C.5.2	Plastic heterogeneities . . . . .	223
C.6	Non-symmetrical loading matrix $\mathbf{L}$ . . . . .	224
C.6.1	Updated coordinates . . . . .	224
C.6.2	Periodic velocity and microscopic velocity gradient $l$ . . . . .	225
C.6.3	Stresses . . . . .	225
<b>D</b>	<b>Periodic homogenization in Lagamine</b> . . . . .	<b>227</b>
D.1	Practical use in Lagamine . . . . .	227
D.2	Periodic homogenization: Imposed macroscopic stress . . . . .	228
D.2.1	In the data files . . . . .	228
D.2.2	In the code . . . . .	229
<b>E</b>	<b>Finite element "BWD3D" and mechanical contact</b> . . . . .	<b>231</b>
E.1	3D finite element BWD3D . . . . .	231
E.2	Modeling of the mechanical contact . . . . .	232
E.2.1	General aspects . . . . .	232
E.2.2	Unilateral contact . . . . .	233
E.2.3	Coulomb's model . . . . .	234
E.2.4	Penalty technique . . . . .	235
<b>F</b>	<b>Modifications in the FE code to allow for <math>h_s</math>'s evolution</b> . . . . .	<b>237</b>
F.1	Modifications in the preprocessor . . . . .	237
F.2	Modifications in the constitutive law subroutine . . . . .	237
<b>G</b>	<b>Orientations of the <math>\beta</math> grains in numerical simulations of shear tests</b> . . . . .	<b>239</b>
<b>H</b>	<b>Definition of the positions in nanoindentation simulations</b> . . . . .	<b>241</b>
<b>I</b>	<b>Influence of the friction coefficient: complementary information</b> . . . . .	<b>243</b>
<b>J</b>	<b>Effect of the verticality defect</b> . . . . .	<b>245</b>
J.1	Tip 1 . . . . .	245
J.2	Tip 2 . . . . .	245
J.3	Tip 3 . . . . .	245
<b>K</b>	<b>Influence of the indenter's position on pile-up patterns</b> . . . . .	<b>247</b>
K.1	Introduction . . . . .	247
K.2	Finite element simulations . . . . .	248
K.3	Conclusions . . . . .	250
<b>L</b>	<b>Mechanical properties from nanoindentation curves</b> . . . . .	<b>251</b>
<b>M</b>	<b>Indentation on FCC materials</b> . . . . .	<b>255</b>
M.1	Introduction . . . . .	255
M.2	Material, parameters and numerical aspects . . . . .	255
M.3	Numerical results . . . . .	257

<b>N</b>	<b>Identification of the <math>\alpha</math> phase</b>	<b>259</b>
N.1	Introduction . . . . .	259
N.2	Basal - prismatic - pyramidal $\langle a \rangle$ slip systems . . . . .	259
N.3	Basal - prismatic - pyramidal $\langle c+a \rangle$ slip systems . . . . .	261
N.4	Basal - pyramidal $\langle a \rangle$ - pyramidal $\langle c+a \rangle$ slip systems . . . . .	261
<b>O</b>	<b>Identification of the plastic parameters of the <math>\alpha</math> phase</b>	<b>267</b>
<b>P</b>	<b>Slip systems and CRSS for the <math>\alpha</math> phase</b>	<b>269</b>

## Part I

# Introduction



# Chapter 1

## General introduction

### 1.1 Titanium

It is widely known that titanium is an attractive material and is used extensively in various applications thanks to its high strength, low density and excellent corrosion resistance [LW07]. Titanium is often used in aircraft (for its high strength combined with low density) [TAAG<sup>+</sup>07], [ABB<sup>+</sup>07], in aero-engines (for its high strength, low density and creep resistance up to about 550 °C) [WWJ<sup>+</sup>08], in biomedical devices (for its corrosion resistance, high strength, low Young's modulus, and biocompatibility) [RQ06], [LCD04], and in chemical processing components (for its corrosion resistance).

Nevertheless, the widespread use of titanium is limited by its high cost. To compete with other structural materials, the potential applications must take advantage of the benefits of titanium. This optimal use requires a more complete understanding of titanium alloys as compared to less expensive materials, involving a compromise between cost, processing methods, and structural performance.

The interest in titanium's properties started after the Second World War [LW07] and alloy development in the USA has rapidly progressed since 1950. A major breakthrough occurred with the appearance of the Ti-6Al-4V alloy in the USA in 1954, which rapidly became the most important ( $\alpha+\beta$ ) alloy, combining excellent properties and good processability. Nowadays, this alloy is still the best-known and most frequently used titanium alloy.

The development of the worldwide titanium industry can be divided into two phases. The first phase was dominated by technical progress that started in the 1950s and that lasted until the mid-1980s. The second and ongoing phase is characterized by the evolution toward a commercial industry where technology is important but cost has become a dominant preoccupation.

As mentioned above, titanium is used in numerous domains. Titanium alloys are traditionally used, for example, in airframes and aero-engines because the structural efficiency of titanium alloys is of great importance in these applications. In modern aero-engines, the weight loss achieved from the use of titanium is about 25% [LW07]. Chemical and power industries also use titanium mainly as corrosion resistant material, as in offshore structures. Recently, building applications such as exterior walls and roofing material have emerged as a new market for titanium. As an example of this, the Fukuoka Dome, in Japan, built in 1993 (Figure (1.1))

features a retractable roof covered with sheets of titanium. The use of this material is also growing in the area of consumer products like cameras, jewelry and various kind of sporting goods (e.g., golf club heads, tennis rackets, bicycle frames, and spikes in sprinter's running shoes). Some applications of titanium are shown in Figure (1.1).



**Figure 1.1:** Examples of titanium applications: Fukuoka Dome<sup>1</sup>, watches<sup>2</sup>, golf club heads<sup>3</sup>, and bicycle frames<sup>4</sup>.

Titanium is also well rooted in the biomedical field in which it is used as implant material. The main advantages of  $\beta$  alloys in this application, compared to Ti-6Al-4V, are its higher fatigue resistance, lower elastic Young's modulus, and improved biocompatibility.

The last area to mention here is the application of titanium in the automotive industry. Applications in this sector are extremely challenging because of cost sensitivity. In this context, the cost includes both the raw material and the fabrication. Indeed, titanium could be successfully incorporated into family automobiles if significant cost reduction is achieved. For example, today's price for titanium sponge alone is already close to the maximum price that the automobile industry is willing to pay for fabricated titanium parts [LW07]. On the other hand, today's environmental policy mandates higher fuel economy and thus generates the need for weight saving material even if it is more expensive, as is the case for titanium.

Other applications can also be cited; for more details, the interested reader can refer to [LW07].

Stimulated partly by the shortage of titanium that appeared in late 2004 or early 2005 but also by the ongoing desire for lower cost titanium, a recent resurgence of research and development

<sup>1</sup>Figure from [http://www.takenaka.co.jp/takenaka\\_e/t-file\\_e/b\\_first/fukuoka\\_dome/index.html](http://www.takenaka.co.jp/takenaka_e/t-file_e/b_first/fukuoka_dome/index.html), 10/07/2008.

<sup>2</sup>Figure from <http://www.princetonwatches.com><http://www.princetonwatches.com>, 10/07/2008.

<sup>3</sup>Figure from <http://www.golfworks.com>, 10/07/2008.

<sup>4</sup>Figure from <http://www.sibexsports.com>, 10/07/2008.



on new titanium production methods has emerged. Currently, researchers are more willing to develop new, lower cost processes for titanium parts [LW07].

## 1.2 Context of the study

Presently, aeronautical manufacturers are in a rush to improve the performance of structural parts. The purposes of these improvements are (i) the decrease in the weight of the components in order to improve their efficiency, (ii) the reduction of fuel consumption, and (iii) the reduction of polluting emissions. To reduce the mass of the parts, it is necessary to use new materials of lower density for the same level of performance, to develop new alloys with improved mechanical properties or to optimize their design.

This work was conducted according to the objectives of the *Titaero* project. Its main goal was to develop the performance of one titanium alloy to lighten aeronautical structural parts. The project partners belong to the *IMAP* Department of the *UCL*<sup>1</sup> and the *MMS* Department of the *ULg*<sup>2</sup>. The Wallonia Region [Reg] has provided the financial support for this project which is also performed in collaboration with *Cenaero* [Cen] and *Techspace Aero* [Tec], member of the *Safran* group [Saf].

In this context, the flanges linking the synchronizing rings together (Figure (1.2)) have been studied. Currently, these flanges are made using the well-known Ti-6Al-4V alloy. In view of decreasing the weight of the components, another titanium alloy has been studied in this work.

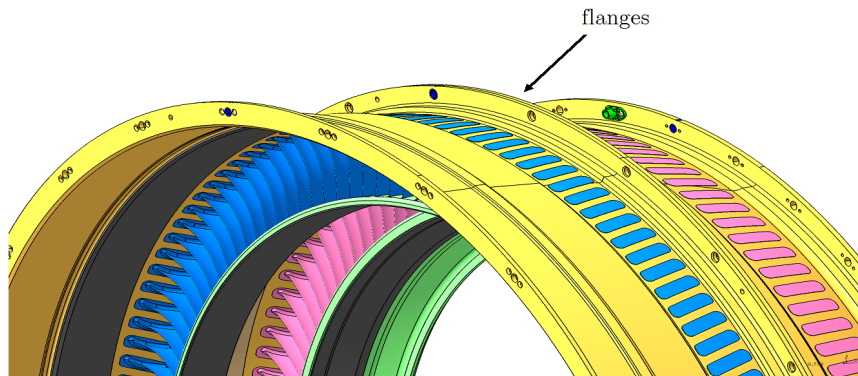


**Figure 1.2:** Flanges linking the synchronizing rings together.

The main goal of the project is to characterize and optimize a microstructure obtained from an existing titanium alloy. This alloy should have superior static behavior compared to Ti-6Al-4V in order to save weight.

With this goal in mind, choosing Ti-5553 titanium alloy seemed to be well-suited to replace Ti-6Al-4V. Unlike the latter, Ti-5553 has a large range of microstructures, which leads to

<sup>1</sup>IMAP: Materials and Process Engineering at the University of Louvain-la-Neuve in Belgium [IMA].

<sup>2</sup>MMS: Metallurgy and Materials Science, in the Aerospace and Mechanical Engineering Department of the University of Liège in Belgium [MMS].

different mechanical properties as shown in Figure (1.3). The higher yield stress of the  $(\alpha + \beta)$  alloy should lead to lighter pieces and superior fatigue behavior. Indeed, this material is less loaded in terms of yield stress than Ti-6Al-4V. Consequently, a greater number of cycles should be possible before rupture.

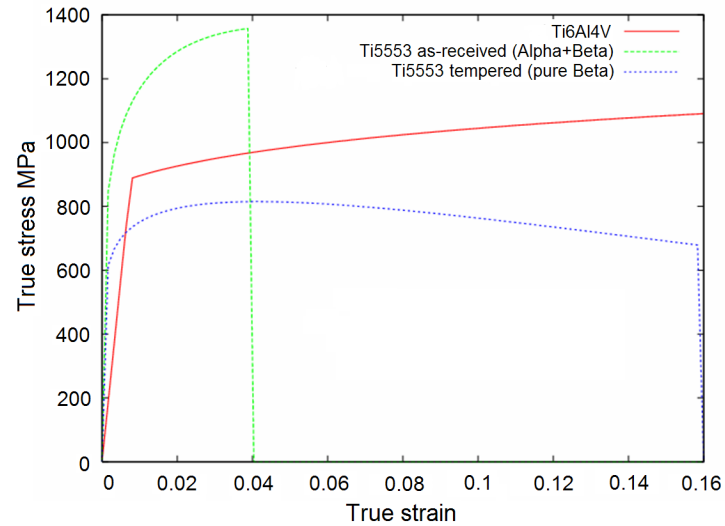


**Figure 1.3:** Stress versus strain curves for Ti-6Al-4V and for Ti-5553 alloys.

In this work, the subject under investigation is the static behavior of Ti-5553. More specifically, the main objective was to optimize the thermal treatments encountered by the alloy and the microstructures of the material. A numerical model of the behavior of the microstructures generated should help to better understand its performance and, thus, facilitate its use in structural components.

## Chapter 2

# Titanium and its alloys: Theory and microstructure

### 2.1 Basic properties of titanium

Some important characteristics<sup>1</sup> of titanium and its alloys are listed in Table (2.1). They have been compared to other metallic structural materials based on Fe, Ni, and Al.

	<b>Ti</b>	<b>Fe</b>	<b>Ni</b>	<b>Al</b>
Melting Temperature (°C)	1670	1538	1455	660
Allotropic Transformation (°C)	$\beta \xrightarrow{882} \alpha$	$\gamma \xrightarrow{912} \alpha$	/	/
Crystal structure	BCC $\rightarrow$ HCP	FCC $\rightarrow$ BCC	FCC	FCC
Room Temperature Young's modulus E (GPa)	115	215	200	72
Yield Stress (MPa)	1000	1000	1000	500
Density (g/cm <sup>3</sup> )	4.5	7.9	8.9	2.7
Comparative Corrosion Resistance	Very High	Low	Medium	High
Comparative Reactivity with Oxygen	Very High	Low	Low	High
Comparative Price of Metal	Very High	Low	High	Medium

**Table 2.1:** Characteristics of titanium and titanium alloys and comparison with other metals based on Fe, Ni, and Al [LW07].

As can be seen above, titanium has the highest strength-to-density ratio, but unfortunately it is expensive. This high price has several origins. The first is the high reactivity of titanium with oxygen, which requires the use of an inert atmosphere or a vacuum during production and the melting process. Also, the energy required for production and the high initial cost of the raw material can explain the price of titanium devices.

However, the high reactivity with oxygen gives rise to one advantage. Indeed, a stable and adherent oxide surface layer is quickly developed when exposed to the air, which increases the

---

<sup>1</sup>More details about the crystalline structure of metals and crystal defects are given in Appendix (B).

corrosion resistance of titanium.

The main competitor of titanium in lightweight structural applications is aluminum. However, this material has a lower melting temperature that gives titanium an advantage above application temperatures of about 150°C [LW07].

## 2.2 Pure titanium

Pure titanium can present several crystallographic structures depending on temperature range. This type of transformation is called allotropic transformation. The temperature that separates the allotropic varieties is called the transus temperature,  $T_\beta$ , which is 882°C for pure titanium. Above this temperature, the  $\beta$  phase is stable and, below this temperature, the  $\alpha$  phase is stable (Figure (2.1)). At temperatures higher than 1670°C, titanium is in a liquid state.

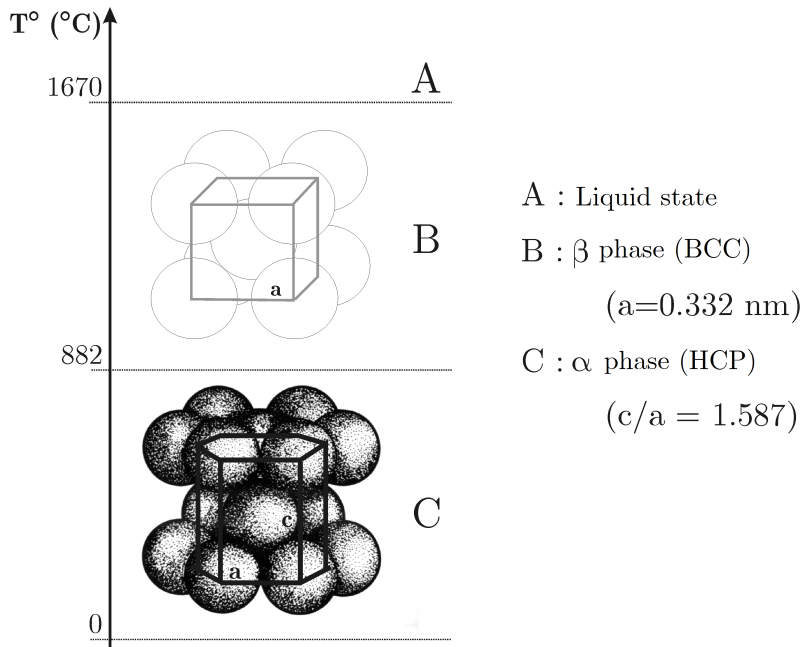


**Figure 2.1:** Crystallography of pure titanium at different temperatures. Figure from [Pri00].

- The  $\alpha$  phase, stable at room temperature, is *hexagonal close packed (HCP)*. For this phase, the most densely packed types of lattice planes are the basal  $\{0002\}$  plane, the three  $\{10\bar{1}0\}$  prismatic planes and the six  $\{10\bar{1}1\}$  first-order pyramidal planes. The  $\mathbf{a}_1$ ,  $\mathbf{a}_2$  and  $\mathbf{a}_3$  axes are the most compact directions  $\langle 11\bar{2}0 \rangle$  (Figure (2.2)). The ratio between the height of the crystal and the edge of the base,  $c/a$  (Figure (2.1)), is less than  $1.633^2$ . This value corresponds to the theoretical ideal compactness ratio of the hexagonal system. Consequently, due to this  $c/a$  ratio in titanium alloys, the basal plane

<sup>2</sup>Lattice parameters of the  $\alpha$  phase:  $a = 0.295$  nm;  $c = 0.468$  nm and then,  $c/a = 1.587$ .

is not the atomic plane of high density compared to the faces of the prism and the pyramidal planes (Figure (2.2)). This implies a great number of slip systems or twinning, which partly explains the relatively high ductility<sup>3</sup> of titanium. This phase has a high elastic limit and a high level of hardness.

- The  $\beta$  phase is the most stable phase at high temperatures in titanium. It is a *body centered cubic (BCC)* phase. The most densely packed planes of this phase are the six  $\{110\}$  planes and the most compact directions are the four  $\langle 111 \rangle$  directions (Figure (2.2)). Generally, due to the great number of available slip systems in BCC materials, twinning is not common<sup>4</sup>.

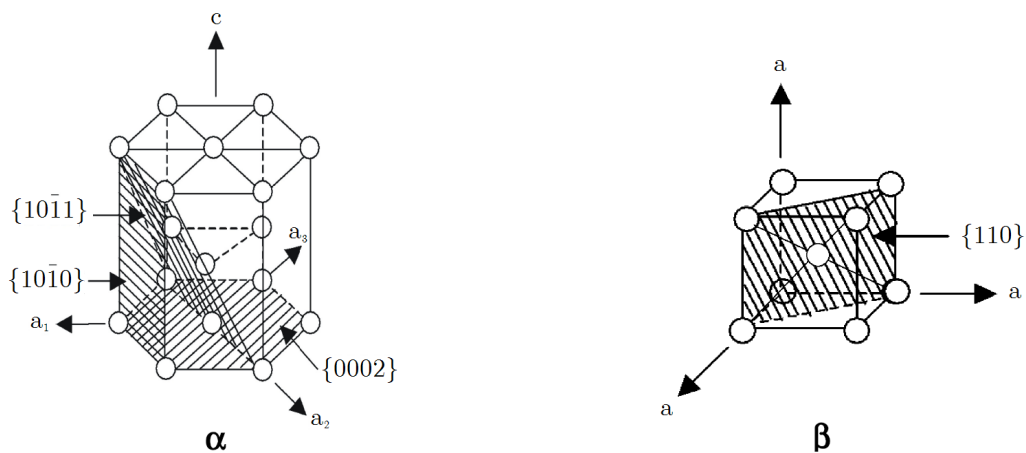


Figure 2.2: Unit cells of  $\alpha$  and  $\beta$  phases of titanium [Len07].

## 2.3 Titanium alloys

In aerospace applications, alloys with a significant specific stiffness and high strength are required to replace structural steel in order to reduce the total weight, and thus, the fuel consumption per flight [WSD07]. Moreover, to increase the lifetime of the part, the alloys should present high fracture toughness associated with good fatigue and corrosion properties.

Near  $\beta$  titanium alloys are especially attractive in the aerospace industry because they have excellent workability and a low  $\beta$  transus temperature. These alloys are currently used, for examples, as landing gear components [FZNH07], flap tracks [WSD07], helicopter rotor systems parts [BTW<sup>+</sup>07], and in structures.

In the beginning of this project, the choice of Ti-LCB (*Low Cost Beta*), a low cost titanium alloy, seemed to be well-adapted to *Titaero* project. However, despite its interesting proper-

<sup>3</sup>Ductility is defined here as the ultimate strain.

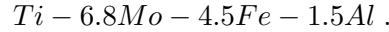
<sup>4</sup>The twinning systems generally found in titanium alloys are  $\{112\}\langle 111 \rangle$  for the plane and the direction of twinning, respectively.

ties, this alloy is exclusively available in small diameter billet, which is not well adapted to aeronautical applications. It was thus logical to study an existing alloy created for aeronautical applications, so the Timetal Ti-5553 alloy was chosen.

To begin the discussion of these two alloys, the properties of the well-known  $\beta$ -metastable Ti-LCB alloy will be presented. Ti-5553 is also a  $\beta$ -metastable alloy; thus, some parallels with Ti-LCB will be highlighted. Secondly, general information about Ti-5553 will be presented. More detailed information about this alloy and its behavior will be given in the following chapters.

### 2.3.1 Ti-LCB alloy

The Ti-LCB alloy was developed by *Timet* and was used in the automotive industry for the suspension springs of the Volkswagen Lupo [Len07]. The chemical composition<sup>5</sup> of the titanium alloy Ti-LCB is:



It is a  $\beta$ -metastable alloy, which means that 100% of the  $\beta$  phase can be maintained at room temperature [Pri00]. The  $T_\beta$  temperature of this alloy is 810°C. This  $T_\beta$  is lower than the transus temperature of pure titanium because of the addition of alloying elements. Some elements (like Al, C, N, and O) stabilize the  $\alpha$  phase and then raise  $T_\beta$  while others (like Fe, Mo, V, Cr) stabilize the  $\beta$  phase, decreasing  $T_\beta$ . Some mechanical physical properties of Ti-LCB are presented in Table (2.2). The Young's moduli provided were obtained from nanoindentation tests in selected grains<sup>6</sup>. In the case of ( $\alpha + \beta$ ) material or 100%  $\beta$  material, the measured Young's moduli are equal to 83 and 87.5 GPa, respectively.

Parameter	Value
$E_\beta$	$\sim 120$ GPa
$E_\alpha$	$\sim 140$ GPa
$\nu$	$\sim 0.2 - 0.25$
$T_\beta$	810°C

**Table 2.2:** Parameters of Ti-LCB (indicative values): Young's modulus  $E$  of the  $\beta$  and the  $\alpha$  phases, Poisson's ratio  $\nu$  and  $T_\beta$ .

As depicted in Figure (2.3), depending on the ageing temperature after quenching, several phases are present in Ti-LCB. More details about these phases can be found in [Pri00] and in [Len07].

Quenching makes it possible to obtain the metastable  $\beta$  phase at room temperature. For the  $\omega$  phase, two types exist, coherent with the  $\beta$  phase:

<sup>5</sup>The numbers represent the percentage (in weight) of the different elements present along with titanium in this alloy.

<sup>6</sup>Tests performed at the IMA Department of the University of Louvain-la-Neuve [IMA].

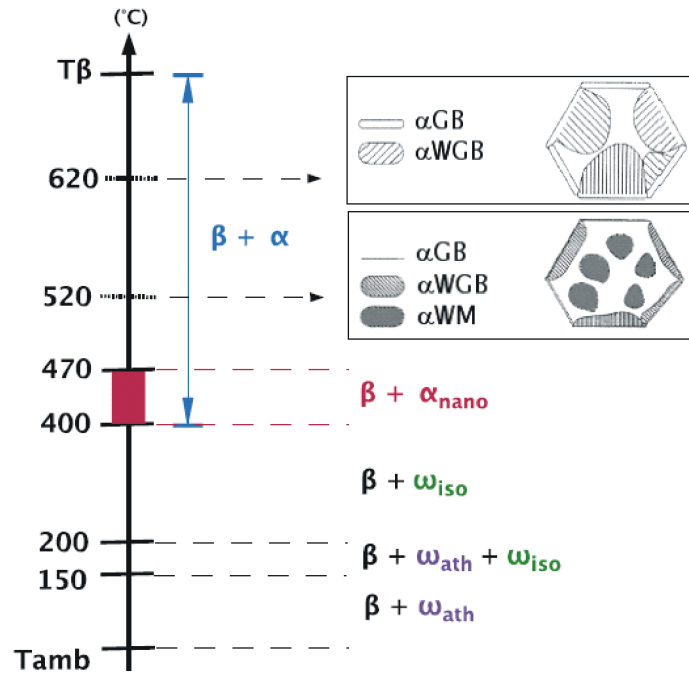


**Figure 2.3:** Phases of Ti-LCB as a function of the ageing temperature after quenching (at room temperature) [Dep04].

- The  $\omega_{ath}$  phase (athermal) is hexagonal and appears when the  $\beta$  phase breaks up into thin particles (2 to 4 nm) during rapid cooling. This phase does not need thermal activation and is reversible. The coherence of this phase with the  $\beta$  one generally leads to a more brittle  $\beta$  matrix.
- The  $\omega_{iso}$  phase (isothermal), also hexagonal, appears during ageing at temperatures close to the initiation temperature of the  $\omega$  phase. Thermal activation is needed for its growth. This phase creates a metastable structure halfway between the metastable  $\beta$  phase after quenching and the stable  $\alpha$  phase appearing after the thermal treatment. After appropriate thermal treatments, the presence of this phase can generate a precipitation of the  $\alpha$  phase in a very thin and homogeneous distribution, which is very useful from a mechanical point of view.

### 2.3.2 Ti-5553 alloy

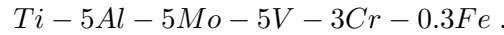
Nowadays, very little information is available for this relatively new alloy. Ti-5553 is a high strength, near- $\beta$  titanium alloy (Figure (2.4)) designed for improved processability with excellent mechanical properties [CBB<sup>+</sup>07]. It is a variation of the Russian alloy VT22 (Ti-5Al-5V-5Mo-1Cr-1Fe) [LW07] and is an alternative to Ti-10-2-3 [JJDD07]. However, compared to this alloy, Ti-5553 has higher strength and friendlier processing [JJDD07]. Indeed, Ti-5553 provides a more robust forging process and air cooling after solution treatment. This results in better control of the residual stresses, which has a positive effect on the distortion of large

complex parts after machining [BTW<sup>+</sup>07]. The hot working behavior and microstructure evolution of large section components manufactured from Ti-5553 are more predictable, controllable and reproductive than those of Ti-10-2-3.

The weaker  $\beta$ -stabilized Ti-5553 has a higher  $\alpha/\beta$  transformation temperature  $T_\beta$ , between 845°C and 860°C [LW07], [FNPM07], [VKF07] and exhibits greater hot working strength than Ti-10-2-3. Thus, industrial forging of this alloy requires higher forces and/or increased billet temperatures, raising the total process cost.

Ti-5553 alloy was developed for large parts subjected to high loading during forging. It should present sufficient mechanical properties in order to be used in aeronautical applications such as aircraft landing gears or axes. This alloy is also used for assembly in structures requiring high mechanical resistance [Zen].

Ti-5553 is also a  $\beta$ -metastable alloy. Thus, a partial comparison with Ti-LCB will be possible. Ti-5553 chemical composition is:



Regarding the quantities of the so-called alloying elements Al equivalent and Mo equivalent<sup>7</sup>, the position of Ti-5553 compared to other titanium alloys is given in Figure (2.4). A similar table with more alloys can be found in [NFB05].

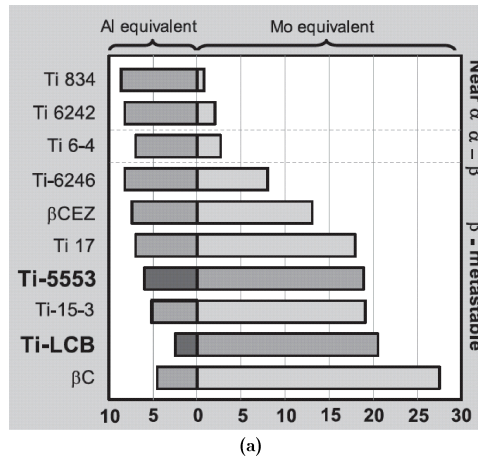


**Figure 2.4:** Ti-5553 compared to other usual titanium alloys. Classification based on their  $[Mo]_{eq}$  and  $[Al]_{eq}$  contents.

Four other properties are given in Table (2.3). It is worth noting that  $T_\beta$  for Ti-5553 is higher than that of Ti-LCB (Table (2.2)).

<sup>7</sup> $[Al]_{eq} = [Al] + [Sn]/3 + [Zr]/6 + 10([O2] + [N2] + [H2])$  ,  $[Mo]_{eq} = [Mo] + 2[V]/3 + [Nb]/3 + 3([Fe] + [Cr])$  from [CLJ07].



Parameter	Value
$E_\beta$	$\sim 70 - 90$ GPa
$E_\alpha$	$\sim 115 - 125$ GPa
$\nu$	$\sim 0.297 - 0.33$
$T_\beta$	845 - 860°C

**Table 2.3:** Parameters of Ti-5553 (indicative values): Young’s modulus of  $\beta$  and  $\alpha$  phases, Poisson’s ratio and  $T_\beta$  temperature of the transformation  $\alpha \leftrightarrow \beta$ .

### 2.3.3 Objectives for the selected microstructure

On the basis of the different phase characteristics analyzed for Ti-LCB ([Dep04], [LDJ04] and [Pri00]), the optimal Ti-5553 alloy microstructure should contain a metastable  $\beta$  phase and secondary thin  $\alpha$  phase dispersed homogeneously. To obtain this microstructure, it seems important primarily to have a precipitate  $\omega$  phase that will permit  $\alpha$  grains to undergo nucleation in a thin and homogeneous manner.

To summarize, the objectives needed to obtain the microstructure required of this alloy are:

- a thin and homogeneous distribution of the  $\alpha$  phase,
- no  $\omega$  phase,
- no thick, continuous  $\alpha$  precipitates along the grain boundaries,
- a small grain size.

These objectives are further explained below.

#### Thin and homogeneous distribution of the $\alpha$ phase

In the  $\beta$  matrix,  $\alpha$  precipitates are not coherent and must thus be bypassed by dislocations. These precipitates slow down the dislocations, leading to a hardened material. This phenomenon is more efficient for smaller precipitates, as demonstrated by Orowan (Figure (2.5)).

Homogeneity is also necessary to avoid localization of the deformation in areas not hardened by the precipitates, which could lead to premature rupture.

This is why the  $\alpha$  nucleation should be thin and homogeneous. Nevertheless, in order to avoid  $\alpha$ -phase grain-boundary precipitates that could lead to cracks, the  $\omega$  phase has to nucleate first. Unlike the  $\alpha$  phase, this phase nucleates everywhere and not only at the grain boundaries. Thus, the  $\alpha$  phase should nucleate from these distributed  $\omega$  nucleations. This technique results in the optimization of the microstructure by providing a well distributed  $\alpha$  phase inside the  $\beta$  grains.

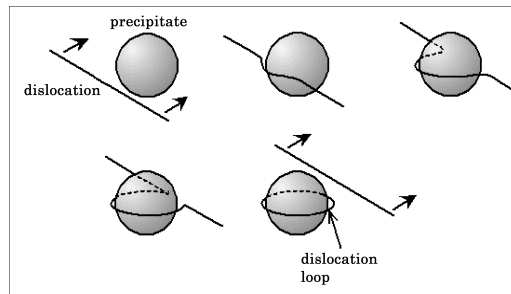


**Figure 2.5:** Orowan mechanism: the dislocations cannot go through the precipitate (because the deformation propagated by the dislocation is not compatible with the crystal structure of the precipitate). The dislocation bypasses the precipitate and leaves a dislocation loop around the precipitate [Oro].

### Avoiding the $\omega$ phase

The  $\omega$  phase is hexagonal and compatible with the  $\beta$  phase. This former phase, which can be sheared by the dislocations, is an effective obstacle due to the elastic stress field that surrounds the particles. Consequently, this phase considerably increases yield stress but significantly reduces ductility.

The first dislocations shear the  $\omega$  precipitates, thereby causing their disappearance and leaving behind an easy slip plane for the next dislocations to move. Consequently, the deformation is confined to an area where there are no  $\omega$  precipitates (Figure (2.6)).

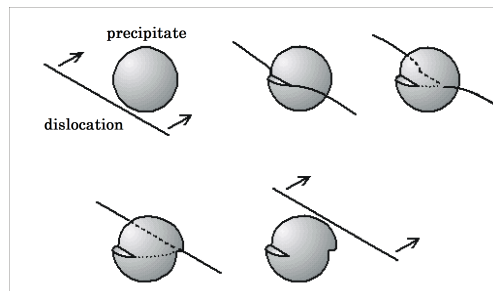


**Figure 2.6:** Shearing of the precipitate: the deformation propagated by the dislocation is compatible with the crystalline structure of the precipitate. Thus, the dislocation deforms the precipitate [Oro].

Nevertheless, as mentioned above, it is important for the  $\omega$  phase to nucleate, allowing a homogeneous  $\alpha$  phase to develop. As a consequence of this, the  $\omega$  phase must be avoided only in the final microstructure.

### Avoiding thick, continuous $\alpha$ precipitates along the grain boundaries

Continuous  $\alpha$  precipitates at the grain boundaries must be avoided because they facilitate the propagation of cracks. Still, it has been demonstrated that this precipitation is not readily avoided (thermodynamic arguments [Ger06]).

**Small grain size**

Dislocations interact with grain boundaries. This leads to hardened material depending on the grain size  $d$ , as mentioned in Hall-Petch's law:

$$\sigma_y = \sigma_0 + \frac{k_y}{\sqrt{d}}$$

where  $\sigma_y$  is the yield stress of the material,  $\sigma_0$  is the resistance of the lattice to dislocation motion and  $k_y$  is the strengthening coefficient, a constant unique to each material. Thus, the yield stress  $\sigma_y$  grows as  $d^{-1/2}$ . The smaller the grains are, the greater the density of boundaries is and the more difficult for the dislocations to move.

To achieve all these objectives, it is necessary to adapt the thermal treatments accordingly. Those treatments were studied during the experimental part by another partner (N. Clement, from UCL) of this project.



## Chapter 3

# Objectives and outline of the study

### 3.1 Objectives

The main objective of this contribution is a quantitative understanding of the mechanical behavior of Ti-5553. For that purpose, several numerical models will be developed to investigate various microstructures in order to grasp their respective interest and to better understand their mechanical behavior. Micromechanical cells representative of the microstructure will be modelled using the concepts of crystalline plasticity and periodic homogenization theories. This should help to understand the effects of the microstructural parameters on the material's behavior.

The first step of this investigation consists in studying the  $\beta$  phase of Ti-5553. This was facilitated by the possibility of obtaining macroscopic  $\beta$  samples. The material parameters of the constitutive law chosen will be optimized on the basis of macroscopic<sup>1</sup> or microscopic<sup>2</sup> experimental tests.

During the second step, the  $\alpha$  phase of Ti-5553 will also be characterized using experimental tests, although no sample with 100%  $\alpha$  phase was available. The material identification will be based on several types of tests, namely macroscopic<sup>3</sup> and microscopic<sup>4</sup> tests.

In the last step, the aforementioned results will be used to model representative cells containing  $\alpha$  and  $\beta$  phases. A sensitivity analysis will be performed on the influence of the geometry and the orientation of the  $\alpha$  phase in the  $\beta$  matrix. This will be used to provide the definition of the ideal microstructure. The knowledge of P. Jacques's team will help determining the thermal treatments to be applied to obtain the microstructure needed.

All the numerical simulations were performed in 3D and the efficiency of the different models will be assessed against the experimental tests, namely macroscopic (tensile and shear tests) and microscopic ones (nanoindentation tests).

---

<sup>1</sup>Uniaxial tensile and simple shear tests on macroscopic  $\beta$  samples.

<sup>2</sup>Nanoindentation tests on  $\beta$  grain.

<sup>3</sup>Uniaxial tensile and simple shear tests on macroscopic ( $\alpha + \beta$ ) samples.

<sup>4</sup>Nanoindentation tests on  $\alpha$  grain.

## 3.2 Outline of the thesis

This work is divided into six different parts. The first part has served to introduce the context and objectives of the work in the preceding chapters.

In the second part, the different numerical tools used in the present research are presented. The constitutive laws used in the later parts to model the material behavior of both phases of Ti-5553 alloy are briefly described. The first is a microscopic crystal plasticity-based constitutive law. The second is a macroscopic Norton-Hoff constitutive law. The concept of periodic homogenization is also explained since this technique is used to model representative cells of Ti-5553.

Characterizing the material behavior of the  $\beta$  phase of Ti-5553 alloy is the main goal of the third part. Various experimental macroscopic and microscopic tests are modelled using finite elements in order to choose the constitutive law best able to represent the mechanical behavior of this phase. The numerical models are also used to optimize the material parameters of the constitutive law chosen.

The fourth part concerns the material characterization of the hexagonal  $\alpha$  phase. The identification procedure, also based on experimental tests and on numerical models, is described. The choice of the experimental tests used for characterization is explained and the results obtained are then discussed in detail.

The last part is dedicated to assembling the results obtained in the previous parts in order to model representative cells of the material, containing both  $\alpha$  and  $\beta$  phases. Several parameters, such as the geometry of the  $\alpha$  phase in the  $\beta$  matrix, are studied in order to predict the optimal microstructure for industrial applications.

Finally, the author will provide conclusions and perspectives relevant to the present matter.

## Part II

# Numerical Tools





# Introduction to Numerical Tools

In Part (I), the main objectives of this thesis were outlined. To achieve these, the Lagamine finite element (FE) code will be used. Some numerical tools had to be implemented in the code in order to characterize both phases of the Ti-5553 alloy and to model representative cells of this material. Consequently, Part II aims to present these numerical tools, which will be used in the later parts of the thesis.

First, two constitutive laws will be presented. The first one is an elastic-viscous-plastic microscopic plasticity-based constitutive law, written by Y. Huang and modified by J.W. Kysar [Hua91] for the *Abaqus* FE code and implemented in *Lagamine* for this research. This constitutive law will be described in Chapter (4).

The second constitutive law, already available in *Lagamine*, is a macroscopic elastic-viscous-plastic Norton-Hoff constitutive law. This law will be briefly referred to in Chapter (5).

Once the constitutive laws have been presented, the periodic homogenization concept will be introduced. A few theoretical comments will be given on this technique, which has been implemented in the FE code. This tool will be used in Part (V) to model representative cells of Ti-5553.



## Chapter 4

# Crystalline elastic-viscous-plastic plasticity-based constitutive law

One of the objectives of this work is the use of micromechanical models to represent the microstructure by using a crystalline plasticity theory in order to quantify the effect of microstructural parameters on material behavior.

To reach this goal, a single crystal plasticity subroutine was chosen and incorporated in the *Lagamine* finite element code. This user-material subroutine was written for the finite element code *Abaqus* [Aba03] by Y. Huang (1991) [Hua91] and later modified by J.W. Kysar (1997) [Kys01]. Its finite element formulation will be shortly described in this chapter.

In the finite element code *Abaqus*, the stresses, strains and state variables are solved incrementally by *Abaqus*. At each time step, the input parameters of the constitutive law are the material's state at the start of the time step (stress, state variables), with the strain increments and the time increment. This subroutine performs two functions: it updates the stresses and the state variables to their values at the end of the time step, and it provides the Jacobian matrix for the material's constitutive model as required for an iterative Newton-Raphson solution in a finite element code.

Plastic deformation of metals can occur via the motion of crystalline line defects (called dislocations) by diffusion, by twinning, and by boundary sliding. Here, inelastic deformation of a single crystal is supposed to arise only from a crystalline slip, which is assumed to obey Schmid's law [Hua91].

Various self and latent hardening relations between resolved shear stress and shear strain in slip systems are implemented in the subroutine. They will be described below.

### 4.1 Elastic-plastic constitutive formulation for single crystals

#### 4.1.1 General principle

As mentioned above, this subroutine was written for the finite element code *Abaqus*. The general principle and the modifications necessary for using it within *Lagamine* are summarized in Figure (4.1).

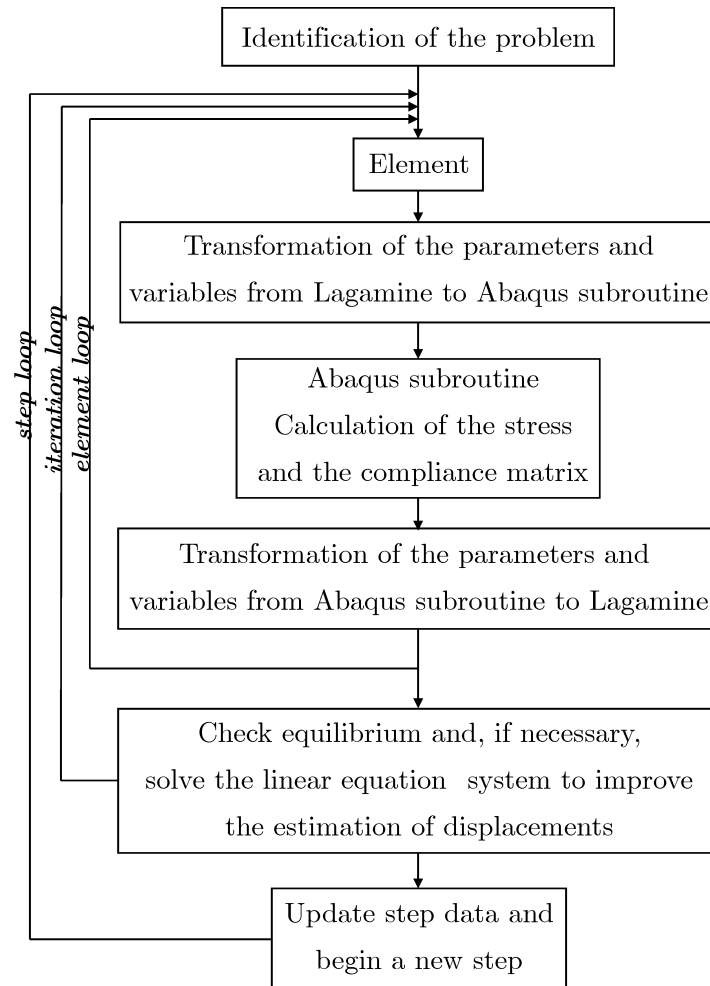


**Figure 4.1:** Microscopic constitutive law subroutine. General principle of implementation in the *Lagamine* FE code.

### 4.1.2 Kinematics of crystalline deformation

To describe crystalline deformation, a deformation gradient tensor  $\mathbf{F}$  between the current configuration ( $\mathbf{X}$ ) and the deformed configuration ( $\mathbf{x}$ ) is defined as

$$\mathbf{F} \equiv \frac{\partial \mathbf{x}}{\partial \mathbf{X}} . \quad (4.1)$$

The formulation relies on the multiplicative decomposition of the total deformation gradient,  $\mathbf{F}$ :

$$\mathbf{F} = \mathbf{F}^* \mathbf{F}^p , \quad (4.2)$$

where  $\mathbf{F}^*$  accounts for the elastic stretching and rotation of the lattice, and  $\mathbf{F}^p$  denotes the slip of the crystallographic planes of the material to an intermediate reference configuration. In this configuration, lattice orientation and spacing are the same as in the original reference configuration. This decomposition is illustrated in Figure (4.2).

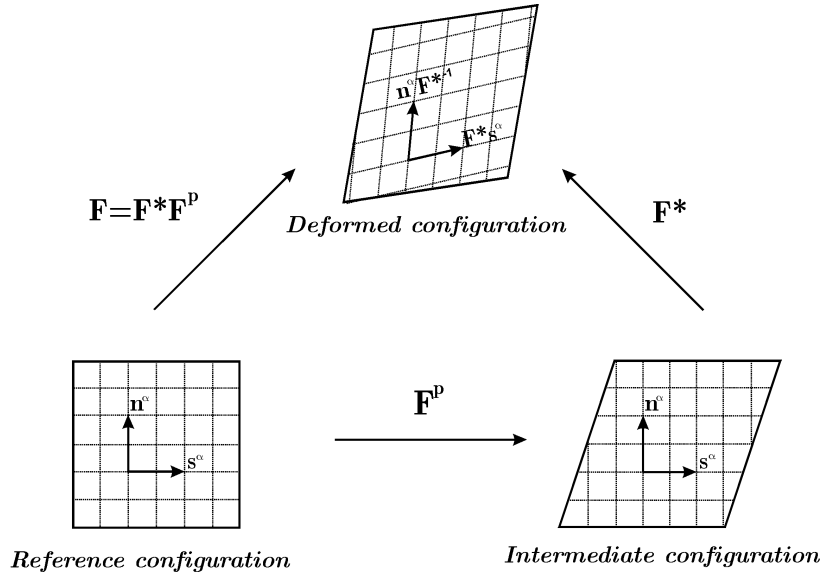


**Figure 4.2:** Multiplicative decomposition of the total strain gradient tensor,  $\mathbf{F} = \mathbf{F}^* \mathbf{F}^p$ . The rotation and stretching of the lattice are taken into account through the elastic deformation gradient  $\mathbf{F}^*$ . Figure inspired from [BMO00].

The rate of change of  $\mathbf{F}^p$  can be linked to the slipping rate or the shear strain rate of different slip systems [ACO08]. If  $\dot{\gamma}^{(\alpha)}$  is the shear strain rate and if the lattice has  $\alpha$  slip systems, one can write the following relation:

$$\dot{\mathbf{F}}^p (\mathbf{F}^p)^{-1} = \sum_{\alpha} \dot{\gamma}^{(\alpha)} \mathbf{s}^{(\alpha)} \mathbf{n}^{(\alpha)} , \quad (4.3)$$

where unit vectors  $\mathbf{s}^{(\alpha)}$  and  $\mathbf{n}^{(\alpha)}$  represent the slip direction of the  $\alpha$  slip system and the normal to the slip plane respectively, in the reference configuration. In the current configuration<sup>1</sup>, these vectors are

$$\begin{cases} \mathbf{s}^{*(\alpha)} = \mathbf{F}^* \cdot \mathbf{s}^{(\alpha)} \\ \mathbf{n}^{*(\alpha)} = \mathbf{n}^{(\alpha)} \cdot \mathbf{F}^{*-1} \end{cases} . \quad (4.4)$$

They are used to define the symmetric tensor  $\boldsymbol{\mu}^{(\alpha)}$  and the antisymmetric one  $\boldsymbol{\omega}^{(\alpha)}$ :

$$\begin{cases} \boldsymbol{\mu}^{(\alpha)} = \frac{1}{2} (\mathbf{s}^{*(\alpha)} \otimes \mathbf{n}^{*(\alpha)} + \mathbf{n}^{*(\alpha)} \otimes \mathbf{s}^{*(\alpha)}) \\ \boldsymbol{\omega}^{(\alpha)} = \frac{1}{2} (\mathbf{s}^{*(\alpha)} \otimes \mathbf{n}^{*(\alpha)} - \mathbf{n}^{*(\alpha)} \otimes \mathbf{s}^{*(\alpha)}) \end{cases} . \quad (4.5)$$

In the current state, the velocity gradient  $\mathbf{L}$  is given by

$$\mathbf{L} \equiv \dot{\mathbf{F}}\mathbf{F}^{-1} = \mathbf{D} + \boldsymbol{\Omega} , \quad (4.6)$$

where  $\mathbf{D}$  is the symmetric stretching tensor and  $\boldsymbol{\Omega}$  is the antisymmetric spin tensor. Tensors  $\mathbf{D}$  and  $\boldsymbol{\Omega}$  are additively broken down into elastic (superscript  $*$ ) and plastic (superscript  $p$ ) parts as

$$\begin{cases} \mathbf{D} = \mathbf{D}^* + \mathbf{D}^p \\ \boldsymbol{\Omega} = \boldsymbol{\Omega}^* + \boldsymbol{\Omega}^p \end{cases} \quad (4.7)$$

satisfying

$$\mathbf{D}^* + \boldsymbol{\Omega}^* = \dot{\mathbf{F}}^*(\mathbf{F}^*)^{-1} \quad \mathbf{D}^p + \boldsymbol{\Omega}^p = \sum_{\alpha} \dot{\gamma}^{(\alpha)} \mathbf{s}^{*(\alpha)} \mathbf{n}^{*(\alpha)} . \quad (4.8)$$

From Eqn.(4.8) and Eqn.(4.5), the following formulae are obtained:

$$\mathbf{D}^p = \sum_{\alpha} \boldsymbol{\mu}^{\alpha} \dot{\gamma}^{\alpha} \quad \boldsymbol{\Omega}^p = \sum_{\alpha} \boldsymbol{\omega}^{\alpha} \dot{\gamma}^{\alpha} . \quad (4.9)$$

### 4.1.3 Constitutive laws

Assuming that the crystal elasticity is not modified by the crystallographic plane slipping, according to Hill and Rice [HR72]:

$$\overset{\circ}{\boldsymbol{\tau}}^* = \mathbf{C} : \mathbf{D}^* , \quad (4.10)$$

where  $\mathbf{C}$  is the elastic tensor and  $\overset{\circ}{\boldsymbol{\tau}}^*$  is Jaumann's rate of Kirchhoff's stress  $\boldsymbol{\tau} \equiv \det(\mathbf{F})\boldsymbol{\sigma}$ , for which  $\boldsymbol{\sigma}$  is Cauchy's stress for axes rotating with the crystalline structure ( $xy$  axes). Thus,

<sup>1</sup>superscript  $*$  indicates that the vectors are implemented in the deformed configuration following lattice stretching and rotation

$$\overset{\circ}{\boldsymbol{\tau}}^* = \dot{\boldsymbol{\tau}} - \boldsymbol{\Omega}^* \cdot \boldsymbol{\tau} + \boldsymbol{\tau} \cdot \boldsymbol{\Omega}^* . \quad (4.11)$$

For axes that rotate with the material, Jaumann's objective rate of  $\boldsymbol{\tau}$  is given by

$$\overset{\circ}{\boldsymbol{\tau}} = \dot{\boldsymbol{\tau}} - \boldsymbol{\Omega} \cdot \boldsymbol{\tau} + \boldsymbol{\tau} \cdot \boldsymbol{\Omega} . \quad (4.12)$$

Removing Eqn.(4.11) from Eqn.(4.12) and using Eqn.(4.5) and (4.8) give

$$\overset{\circ}{\boldsymbol{\tau}} = \mathbf{C} : \mathbf{D} - \sum_{\alpha} \left\{ \mathbf{C} : \boldsymbol{\mu}^{(\alpha)} + \boldsymbol{\omega}^{(\alpha)} \cdot \boldsymbol{\tau} - \boldsymbol{\tau} \cdot \boldsymbol{\omega}^{(\alpha)} \right\} \dot{\gamma}^{(\alpha)} . \quad (4.13)$$

The resolved shear stress on slip system  $\alpha$ , written  $\tau^{(\alpha)}$ , is defined so that  $\tau^{(\alpha)}\dot{\gamma}^{\alpha}$  is equal to the work (per volume unit in the reference configuration) of internal loading due to slipping of system  $\alpha$ . Thus, from Eqn.(4.9),

$$\boldsymbol{\tau} : \mathbf{D}^p = \sum_{\alpha} \tau^{(\alpha)} \dot{\gamma}^{(\alpha)} . \quad (4.14)$$

Therefore, by identification,

$$\tau^{(\alpha)} = \boldsymbol{\mu}^{(\alpha)} : \boldsymbol{\tau} . \quad (4.15)$$

#### 4.1.4 Hardening of rate-dependent crystalline materials

To complete the constitutive formulation (Eqn.(4.13)), the slipping rate  $\dot{\gamma}^{(\alpha)}$  of the  $\alpha^{th}$  slip system must be defined. Based on Schmid's law<sup>2</sup>,  $\dot{\gamma}^{(\alpha)}$  is determined by the corresponding resolved shear stress  $\tau^{(\alpha)}$  as proposed by Hutchinson [Hut76]:

$$\dot{\gamma}^{(\alpha)} = \dot{a}^{(\alpha)} \left| \frac{\tau^{(\alpha)}}{g^{(\alpha)}} \right|^n \text{sgn}(\tau^{(\alpha)}) , \quad (4.16)$$

where the constant  $\dot{a}^{(\alpha)}$  is the reference strain rate on slip system  $\alpha$ ,  $n$  is the rate sensitivity exponent, and  $g^{(\alpha)}$  is a variable called critical resolved shear stress (CRSS) which describes the current strength of that system. Every system begins to slip for non zero values of  $\tau^{(\alpha)}$ , but a sufficiently high value of  $n$  ensures that the slipping of a system becomes significant only for systems in which  $\tau^{(\alpha)} \simeq g^{(\alpha)}$ . At the limit  $n \rightarrow \infty$ , the system's behavior tends to a rate-independent material.

Strain hardening is characterized by the evolution of the CRSS  $g^{(\alpha)}$  through the incremental relation

---

<sup>2</sup>Schmid's law is assumed to govern the onset of plastic deformation, so that dislocation glide becomes active at a critical value of shear stress:  $\tau^{(\alpha)} = g^{(\alpha)}$ .

$$\dot{g}^{(\alpha)} = \sum_{\beta} h_{\alpha\beta}(\gamma) |\dot{\gamma}^{(\beta)}| , \quad (4.17)$$

where the initial value for each slip system is  $g^{(\alpha)}(0) = \tau_0$ ,  $h_{\alpha\beta}$  is the slip hardening moduli, and the sum's range includes all activated slip systems. Here,  $h_{\alpha\alpha}$  (no sum) and  $h_{\alpha\beta}$  ( $\alpha \neq \beta$ ) are called self and latent hardening moduli respectively.

Actually, two phenomenological hardening models are programmed, involving different forms for the hardening matrix  $h_{\alpha\beta}$ . They are used to integrate Eqn.(4.17) to provide instantaneous values of  $g^{(\alpha)}$  in the active slip systems. The strain-rate dependent formulation in Eqn.(4.16) is computed to obtain instantaneous values of the shear strain  $\dot{\gamma}^{(\alpha)}$  in all active systems.

The first phenomenological hardening model was defined by Peirce, Asaro and Needleman [Hua91] and the second is Bassani and Wu's model [BW91], [WBL91]. These hardening models will now be briefly described.

### Peirce, Asaro and Needleman's model (PAN model)

In this phenomenological model, a simple form is used for the self hardening moduli:

$$\begin{cases} h_{\alpha\alpha} = h(\gamma) = h_0 \operatorname{sech}^2 \left| \frac{h_0 \gamma}{\tau_s - \tau_0} \right| \\ h_{\alpha\beta} = qh(\gamma) \quad (\alpha \neq \beta) \end{cases} , \quad (4.18)$$

where  $h_0$  is the initial hardening modulus,  $\tau_0$  (the value of the critical resolved shear stress at the onset of plastic deformation) is the initial value of  $g^{(\alpha)}$ ,  $\tau_s$  is the shear stress level that marks hardening saturation, and  $\gamma$  is Taylor's cumulative shear strain on all slip systems:

$$\gamma = \sum_{(\alpha)} \int_0^t |\dot{\gamma}^{(\alpha)}| dt . \quad (4.19)$$

In Eqn.(4.18),  $q$  is a constant<sup>3</sup>.

### Bassani and Wu's model

The second hardening model was defined by Bassani and Wu [BW91], [WBL91]. Its expression depends on the shear strains of all slip systems [Hua91]:

$$\begin{cases} h_{\alpha\alpha} = \left\{ (h_0 - h_s) \operatorname{sech}^2 \left| \frac{(h_0 - h_s) \gamma^{(\alpha)}}{\tau_s - \tau_0} \right| + h_s \right\} G(\gamma^{(\beta)}; \beta \neq \alpha) \\ h_{\alpha\beta} = qh_{\alpha\alpha} \quad (\alpha \neq \beta) \end{cases} \quad (4.20)$$

<sup>3</sup>A  $q$  value between 1.0 and 1.8 is recommended ( $q = 1$  corresponds to isotropic hardening) [Kys01].



with

$$G(\gamma^{(\beta)}; \beta \neq \alpha) = 1 + \sum_{\beta \neq \alpha} f_{\alpha\beta} \tanh\left(\frac{\gamma^{(\beta)}}{\gamma_0}\right),$$

where  $h_0$  defines the hardening slope immediately following the initial yield point. The initial yield stress,  $\tau_0$ , is equal to the initial value of  $g^{(\alpha)}$  and  $\tau_s$  is the saturation stress level at which large plastic flow arises. The parameter  $h_s$  defines the hardening slope during easy glide (Figure (4.3)).  $\gamma^{(\alpha)}$  is the total shear strain in slip system  $\alpha$ , while "sech" is the hyperbolic secant function.  $\gamma^{(\beta)}$  is the total shear strain in slip system  $\beta$ ,  $\gamma_0$  is the amount of slip after which the interaction between slip systems reaches the peak strength, and each component  $f_{\alpha\beta}$  represents an interaction matrix that depends on the nature of the junctions formed between slip systems  $\alpha$  and  $\beta$ . The  $G$  function deals implicitly with cross-hardening that occurs between slip systems during the second stage of hardening [SSH07].

The parameter  $q$  defines the factor applied to the off-diagonal terms. In this model,  $q = 0$  (diagonal hardening) is recommended [Kys01].

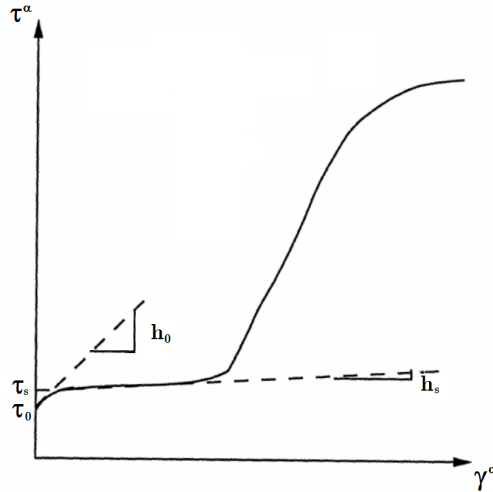


**Figure 4.3:** Schematic diagram for Bassani and Wu's form of hardening. Figure from [Bal95].

#### 4.1.5 Integration scheme

For each slip system  $\alpha$ , the increment  $\Delta\gamma^{(\alpha)}$  of shear strain within the increment  $\Delta t$  is determined, using linear interpolation within  $\Delta t$ :

$$\Delta\gamma^{(\alpha)} = \left[ (1 - \theta)\dot{\gamma}_t^{(\alpha)} + \theta\dot{\gamma}_{t+\Delta t}^{(\alpha)} \right] \Delta t \quad (4.21)$$

with the parameter  $\theta$  ranging from 0 to 1. A choice of  $\theta$  between 0.5 and 1 is recommended [Hua91].

The slipping rate (Eqn.(4.16)) is a function of the resolved shear stress  $\tau^{(\alpha)}$  and the current strength  $g^{(\alpha)}$ . Taylor's expansion of the slipping rate in a time step is therefore

$$\dot{\gamma}_{t+\Delta t}^{(\alpha)} = \dot{\gamma}_t^{(\alpha)} + \left( \frac{\partial \dot{\gamma}^{(\alpha)}}{\partial \tau^{(\alpha)}} \right) \Delta \tau^{(\alpha)} + \left( \frac{\partial \dot{\gamma}^{(\alpha)}}{\partial g^{(\alpha)}} \right) \Delta g^{(\alpha)} , \quad (4.22)$$

where  $\Delta \tau^{(\alpha)}$  and  $\Delta g^{(\alpha)}$  are the increments of resolved shear stress and current strength respectively in slip system  $\alpha$  within the time step  $\Delta t$ . Using Eqn.(4.21) and (4.22),  $\Delta \gamma^{(\alpha)}$  becomes

$$\Delta \gamma^{(\alpha)} = \Delta t \left[ \dot{\gamma}_t^{(\alpha)} + \theta \left( \frac{\partial \dot{\gamma}^{(\alpha)}}{\partial \tau^{(\alpha)}} \right) \Delta \tau^{(\alpha)} + \theta \left( \frac{\partial \dot{\gamma}^{(\alpha)}}{\partial g^{(\alpha)}} \right) \Delta g^{(\alpha)} \right] . \quad (4.23)$$

#### 4.1.6 Incremental formulation

The different steps involved in updating variables are presented in Figure (4.4). Subscript  $A$  is linked to variable values at the beginning of the step and subscript  $B$  is used for updated variables (at the end of the step).

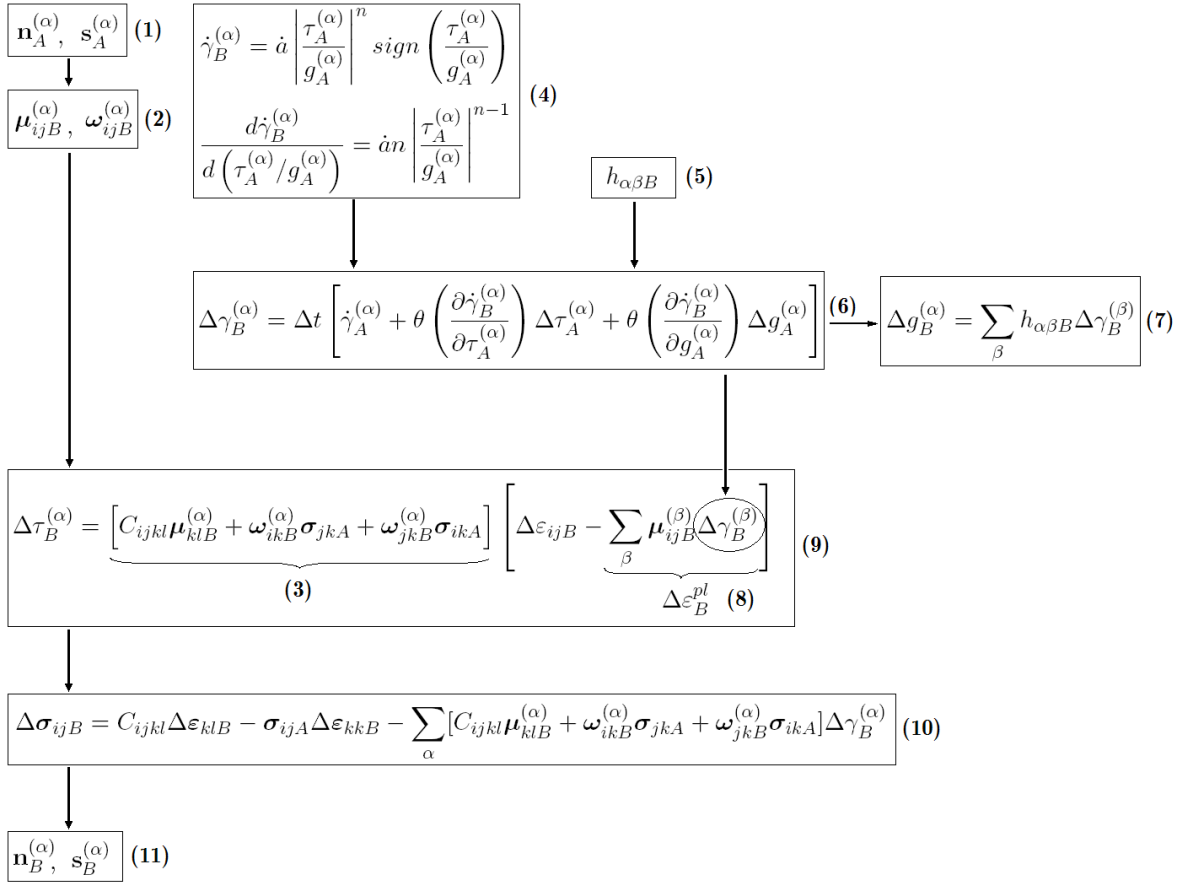


Figure 4.4: Integration scheme of the plastic law.

At the first stage, (1), the normal to the slip plane and the slip direction of each  $\alpha$  slip system are updated, thanks to the data provided by the preceding step. Then, from these values, the deformation tensor ( $\boldsymbol{\mu}_{ij}$ ) and the spin tensor ( $\boldsymbol{\omega}_{ij}$ ) are calculated from Eqn.(4.5) (stage (2)).

The increments of resolved shear stress  $\Delta\tau_B^{(\alpha)}$  (stage (9)) are obtained from Eqn.(4.13), (4.9), and by (4.15):

$$\Delta\tau_B^{(\alpha)} = C_{ijkl}\boldsymbol{\mu}_{kl}^{(\alpha)}\Delta\varepsilon_{ij} - \sum_{\beta} \{C_{ijkl}\boldsymbol{\mu}_{kl}^{(\alpha)} + \boldsymbol{\omega}_{ik}^{(\alpha)}\boldsymbol{\sigma}_{jk} + \boldsymbol{\omega}_{jk}^{(\alpha)}\boldsymbol{\sigma}_{ik}\}\boldsymbol{\mu}_{ij}^{(\beta)}\Delta\gamma_B^{(\beta)} .$$

This equation can be written as

$$\Delta\tau_B^{(\alpha)} = \left[ C_{ijkl}\boldsymbol{\mu}_{klB}^{(\alpha)} + \boldsymbol{\omega}_{ikB}^{(\alpha)}\boldsymbol{\sigma}_{jkA} + \boldsymbol{\omega}_{jkB}^{(\alpha)}\boldsymbol{\sigma}_{ikA} \right] \left[ \Delta\varepsilon_{ijB} - \sum_{\beta} \boldsymbol{\mu}_{ijB}^{(\beta)}\Delta\gamma_B^{(\beta)} \right] . \quad (4.24)$$

To compute this stress increment, stages (3) to (8) are needed in advance. In practice,  $\Delta\gamma_B^{(\beta)}$  (stage (6)) is computed from an iterative procedure. Replacing  $\Delta\tau^{(\alpha)}$  and  $\Delta g^{(\alpha)}$  by their expressions from Eqn.(4.24) and (4.17), the equation

$$\Delta\gamma_B^{(\alpha)} = \Delta t \left[ \dot{\gamma}_A^{(\alpha)} + \theta \left( \frac{\partial\dot{\gamma}_B^{(\alpha)}}{\partial\tau_A^{(\alpha)}} \right) \Delta\tau_A^{(\alpha)} + \theta \left( \frac{\partial\dot{\gamma}_B^{(\alpha)}}{\partial g_A^{(\alpha)}} \right) \Delta g_A^{(\alpha)} \right]$$

is written as

$$\begin{aligned} \sum_{\beta} \left\{ \delta_{\alpha\beta} + \theta\Delta t \frac{\partial\dot{\gamma}_B^{(\alpha)}}{\partial\tau_A^{(\alpha)}} \left[ C_{ijkl}\boldsymbol{\mu}_{klB}^{(\alpha)} + \boldsymbol{\omega}_{ikB}^{(\alpha)}\boldsymbol{\sigma}_{jkA} + \boldsymbol{\omega}_{jkB}^{(\alpha)}\boldsymbol{\sigma}_{ikA} \right] \boldsymbol{\mu}_{ijB}^{(\beta)} - \theta\Delta t \frac{\partial\dot{\gamma}_B^{(\alpha)}}{\partial g_A^{(\alpha)}} h_{\alpha\beta B} \text{sgn}(\dot{\gamma}_B^{(\beta)}) \right\} \Delta\gamma_B^{(\beta)} \\ = \dot{\gamma}_A^{(\alpha)}\Delta t + \theta\Delta t \frac{\partial\dot{\gamma}_B^{(\alpha)}}{\partial\tau_A^{(\alpha)}} \left[ C_{ijkl}\boldsymbol{\mu}_{klB}^{(\alpha)} + \boldsymbol{\omega}_{ikB}^{(\alpha)}\boldsymbol{\sigma}_{jkA} + \boldsymbol{\omega}_{jkB}^{(\alpha)}\boldsymbol{\sigma}_{ikA} \right] \Delta\varepsilon_{ijB} \quad (4.25) \\ \Leftrightarrow K.\Delta\gamma_B^{(\beta)} = R . \end{aligned}$$

In Eqn.(4.25),  $\frac{\partial\dot{\gamma}_B^{(\alpha)}}{\partial\tau_A^{(\alpha)}}$  and  $\frac{\partial\dot{\gamma}_B^{(\alpha)}}{\partial g_A^{(\alpha)}}$  are deduced from  $\frac{d\dot{\gamma}_B^{(\alpha)}}{d(\tau_A^{(\alpha)}/g_A^{(\alpha)})}$ , computed in stage (4):

$$\begin{cases} \frac{\partial\dot{\gamma}_B^{(\alpha)}}{\partial\tau_A^{(\alpha)}} = \frac{d\dot{\gamma}_B^{(\alpha)}}{d(\tau_A^{(\alpha)}/g_A^{(\alpha)})} \cdot \frac{1}{g_A^{(\alpha)}} \\ \frac{\partial\dot{\gamma}_B^{(\alpha)}}{\partial g_A^{(\alpha)}} = \frac{\tau_A^{(\alpha)}}{g_A^{(\alpha)}} \cdot \frac{d\dot{\gamma}_B^{(\alpha)}}{d(\tau_A^{(\alpha)}/g_A^{(\alpha)})} \cdot \frac{1}{g_A^{(\alpha)}} . \end{cases} \quad (4.26)$$

The hardening matrix computed from Eqn.(4.18) or (4.20) (stage (5)) is also used to compute Eqn.(4.25).

Thus, in Eqn.(4.25),  $K$  can be determined using previous steps and  $R$  is obtained using the right-hand side of this equation. Finally, by linear resolution,  $\Delta\gamma_B^{(\beta)}$  is obtained (stage (6)).

The increment of critical resolved shear stress  $\Delta g_B^{(\alpha)}$  (stage (7)) can be determined from values obtained at stages (5) and (6), using

$$\Delta g_B^{(\alpha)} = \sum_{\beta} h_{\alpha\beta B} \Delta\gamma_B^{(\beta)} .$$

The plastic strain increment is also solved (stage (8)) by

$$\Delta\varepsilon_B^{pl} = \sum_{\beta} \mu_{ijB}^{(\beta)} \Delta\gamma_B^{(\beta)} .$$

The increment of elastic strain is obtained by removing the increment of plastic strain from the total strain increment. Then, the increment of the strain rate associated with the stretching lattice (i.e.  $L\Delta t$  where  $L$  is the strain rate) is calculated.

From these stages,  $\Delta\tau^{(\alpha)}$  is finally determined using Eqn.(4.24) (stage (9)).

The corotational stress increment is then calculated (stage (10)). It is obtained from Eqn.(4.13) and with  $\overset{\circ}{\sigma}^* = \mathbf{C} : \mathbf{D}^* - \sigma(\mathbf{I} : \mathbf{D}^*)$  from Hill and Rice [HR72]:

$$\Delta\sigma_{ijB} = C_{ijkl}\Delta\varepsilon_{klB} - \sigma_{ijA}\Delta\varepsilon_{kkB} - \sum_{\alpha} [C_{ijkl}\mu_{klB}^{(\alpha)} + \omega_{ikB}^{(\alpha)}\sigma_{jkA} + \omega_{jkB}^{(\alpha)}\sigma_{ikA}]\Delta\gamma_B^{(\alpha)} . \quad (4.27)$$

Consequently, the value of  $\sigma_B$  can be determined. This stress increment is used to determine the Jacobian matrix of the material  $\partial\sigma_{ij}/\partial\varepsilon_{kl}$ , used in turn to determine Newton-Raphson's iterative solution.

Finally, the increments of the normal to the slip system and slip direction (stage (11)) are computed. By differentiating Eqn.(4.4), one finds

$$\dot{\mathbf{s}}^{*(\alpha)} = (\mathbf{D}^* + \mathbf{\Omega}^*)\mathbf{s}^{*(\alpha)} \quad (4.28)$$

$$\dot{\mathbf{n}}^{*(\alpha)} = -\mathbf{n}^{*(\alpha)}(\mathbf{D}^* + \mathbf{\Omega}^*) . \quad (4.29)$$

The corresponding increments in terms of the strain increments  $\Delta\varepsilon_{ij}$  and increments of shear strain  $\Delta\gamma^{(\alpha)}$  in slip systems are given by [Hua91]

$$\Delta s_{iB}^{*(\alpha)} = \left\{ \Delta\varepsilon_{ijB} + \Omega_{ij}\Delta t - \sum_{\beta} [\mu_{ijB}^{(\beta)} + \omega_{ijB}^{(\beta)}] \Delta\gamma_B^{(\beta)} \right\} s_j^{*(\alpha)} \quad (4.30)$$

$$\Delta n_{iB}^{*(\alpha)} = -n_{jB}^{*(\alpha)} \left\{ \Delta\varepsilon_{jiB} + \Omega_{ji}\Delta t - \sum_{\beta} [\mu_{jiB}^{(\beta)} + \omega_{jiB}^{(\beta)}] \Delta\gamma_B^{(\beta)} \right\} \quad (4.31)$$

## 4.2 Introduction to the hexagonal phase

Initially, the crystalline plasticity subroutine was implemented for cubic materials, but it may also be used for hexagonal materials with a few changes. These changes have been performed in order to allow the characterization of the hexagonal  $\alpha$  phase of Ti-5553 with this constitutive law.

In a cubic phase, the three components of the slip direction and the three components of the normal to slip planes must be supplied by (orthogonal) axes linked to the crystal to define a slip system (Figure (4.5)).

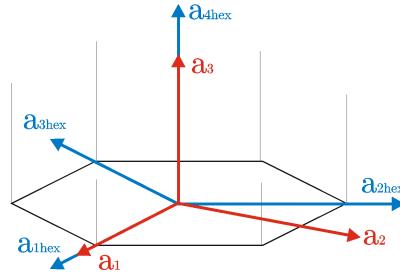


**Figure 4.5:** Axes in the hexagonal system ( $a_{i\text{hex}}$ ) and in the corresponding orthogonal one ( $a_i$ ).

For a hexagonal material, slip systems are generally defined by four components (Figure (4.5)). These four dependent components can be expressed in the orthogonal axes. The rotational matrices from one reference system to the other are given hereafter, with  $s(i)$  and  $n(i)$ , as the components of  $\mathbf{s}$  and  $\mathbf{n}$  in the orthogonal reference system, and  $s_{\text{hex}}(i)$  and  $n_{\text{hex}}(i)$  the same components in the hexagonal reference system.

For the slip directions ( $\mathbf{s}$ )

$$\begin{pmatrix} s(1) \\ s(2) \\ s(3) \end{pmatrix} = \begin{pmatrix} 1 & 0 & 0 & 0 \\ \frac{1}{\sqrt{3}} & \frac{2}{\sqrt{3}} & 0 & 0 \\ 0 & 0 & 0 & \frac{1}{c/a} \end{pmatrix} \begin{pmatrix} s_{\text{hex}}(1) \\ s_{\text{hex}}(2) \\ s_{\text{hex}}(3) \\ s_{\text{hex}}(4) \end{pmatrix}.$$

For the normal to slip planes ( $\mathbf{n}$ )

$$\begin{pmatrix} n(1) \\ n(2) \\ n(3) \end{pmatrix} = \begin{pmatrix} 1 & -\frac{1}{2} & -\frac{1}{2} & 0 \\ 0 & \frac{\sqrt{3}}{2} & -\frac{\sqrt{3}}{2} & 0 \\ 0 & 0 & 0 & \frac{1}{c/a} \end{pmatrix} \begin{pmatrix} n_{\text{hex}}(1) \\ n_{\text{hex}}(2) \\ n_{\text{hex}}(3) \\ n_{\text{hex}}(4) \end{pmatrix}.$$

The subroutine implemented in the *Lagamine* finite element code was successfully validated. Results can be found in [Ger06].

### 4.3 Conclusions

This well-known microscopic constitutive law (the crystalline elastic-viscous-plastic plasticity-based constitutive law written by Y. Huang) was chosen, examined and implemented in the *Lagamine* FE code. Its implementation was then successfully validated and the extension to hexagonal materials was performed.

## Chapter 5

# Macroscopic constitutive law: Norton-Hoff's elastic-viscous-plastic law

Norton-Hoff's constitutive law links flow stress,  $\sigma$ , to the strain,  $\varepsilon$ , the strain rate,  $\dot{\varepsilon}$ , and the temperature,  $T$  [JDDJ08]:

$$\sigma = K(\sqrt{3})^{m+1} \varepsilon^m \dot{\varepsilon}^n \exp\left(\frac{Q}{RT}\right) , \quad (5.1)$$

where  $m$  is the strain rate sensitivity,  $n$  the work hardening exponent,  $Q$  the activation energy,  $R$  the universal gas constant and  $K$  a material constant.

For a constant temperature and with  $K^* = K\sqrt{3}\exp\left(\frac{Q}{RT}\right)$ , Eqn.(5.1) can be rewritten:

$$\sigma = K^*(\sqrt{3}\dot{\varepsilon})^m \varepsilon^n . \quad (5.2)$$

This Norton-Hoff's constitutive model is not appropriate for materials that show flow softening. However, as shown in the introduction in Figure (1.3), softening can appear in the titanium alloy chosen here. To extend this law to be able to include softening modeling, a modification was performed [Pas03] in the *Lagamine* FE code, by including a new parameter. It can be written as

$$\sigma = \varepsilon^{p_4} \exp(-p_1\varepsilon) p_2 \sqrt{3} (\sqrt{3}\dot{\varepsilon})^{p_3} , \quad (5.3)$$

where  $p_1$  is the strain hardening parameter and  $p_2$ , the scaling factor. The parameter  $p_3$  is the strain sensitivity parameter and  $p_4$  is the hardening parameter.  $p_3$  and  $p_4$  correspond to  $m$  and  $n$  respectively in Eqn.(5.2).

The above law was formulated for uniaxial tension. In three dimensions, in the viscous-plastic domain, the time integration of stress tensor  $\sigma_{ij}$  is based on a plasticity flow rule associated to a Von Mises' yield surface with isotropic hardening [PH07]:

$$\hat{\varepsilon}_{ij} = \frac{3\bar{\varepsilon}}{2\bar{\sigma}} \hat{\sigma}_{ij} \quad (5.4)$$

where  $\bar{\sigma}$  and  $\bar{\varepsilon}$  are the Von Mises' equivalent stress and equivalent strain rate respectively considering

$$\bar{\varepsilon} = \sqrt{\frac{2}{3} \dot{\varepsilon}_{ij} \dot{\varepsilon}_{ij}} \quad \bar{\sigma} = \sqrt{\frac{3}{2} \hat{\sigma}_{ij} \hat{\sigma}_{ij}}$$

and where  $\hat{\sigma}_{ij}$  is the deviatoric component of the stress tensor.

As mentioned above, the following modified formulation of Norton-Hoff's law was proposed [PH07]:

$$\bar{\sigma} = \bar{\varepsilon}^{p_4} \exp(-p_1 \bar{\varepsilon}) p_2 \sqrt{3} (\sqrt{3} \bar{\varepsilon})^{p_3} . \quad (5.5)$$

Hence, the relation between deviatoric stress,  $\hat{\sigma}_{ij}$ , and strain rate,  $\hat{\varepsilon}_{ij}$ , tensors can be derived from Eqn.(5.4) and (5.5):

$$\hat{\sigma}_{ij} = 2p_2 (\sqrt{3} \bar{\varepsilon})^{p_3 - 1} \bar{\varepsilon}^{p_4} \exp(-p_1 \bar{\varepsilon}) \hat{\varepsilon}_{ij} . \quad (5.6)$$

This macroscopic law was available in the code. It permits the user to define elastic-viscous-plastic behavior with hardening or softening.



## Chapter 6

# Periodic homogenization: theory and implementation in the FE code

### 6.1 Introduction

The aim of this chapter is to introduce the periodic homogenization theory. This method is studied and implemented within the goal of representative cells. Whole theses can be focused on this subject alone, so the discussion below will be limited to those points concerning the choices made in this study. Here, just the essential information about this technique and its use in modeling a unit cell of Ti-5553 are provided. To find more information about this topic, please consult the references cited in the text.

### 6.2 Homogenization theory: definition and interests

To predict the behavior of some structures on the *macroscopic* scale, it is sometimes essential to take into account the behavior of their constituents (or phases), called *microscopic* ones. At a sufficiently small scale, all materials are heterogeneous, included materials generally called homogeneous. In the case of a material composed of two phases (or constituents) with different materials and geometrical features, it is expected that the rupture of the material will depend highly on the characteristics of its phases and on their interaction. However, taking into account all the microscopic mechanisms present in a macroscopic material is not realistic. The first problem is the difficulty in accurately describing the microstructure. Indeed, the description of the exact heterogeneous structure can be extremely complicated. Moreover, for a macroscopic structure, the scale is so high that a statistical average of the microscopic properties is observed. Thus, the assumption of material continuity is justifiable. In this context, homogenization methods have been designed to derive the equivalent properties of the material from the knowledge of the constitutive law and spatial distribution of their components [KFG<sup>+</sup>03]. The homogeneous medium is one that has the same properties in each point.

The homogenization theory can be defined in this way: *The homogenization theory consists in replacing the real heterogeneous material by a fictitious homogeneous one that must have the same behavior as the real one, once submitted to loadings.* This technique makes the evaluation of the global behavior of the heterogeneous material possible, taking into account the mechanical phenomena appearing at the scale of heterogeneities.

The homogenization technique also seems essential from a numerical point of view. To model a macroscopic structure directly, it should be meshed at the heterogeneity scale, which is not possible considering the delay of such simulations. The homogeneous fictitious material will help analyze the structure's behavior.

In this bibliographic section, the assumption of small elastic strains is made.

## 6.3 Stages of the homogenization procedure

### 6.3.1 Definition of the scales and the RVE

The sample of the heterogeneous material, representative of the heterogeneities of the structure, is called a *Representative Volume Element* (RVE). The RVE is usually regarded as a volume  $V$  of heterogeneous material that is sufficiently large to be statistically representative of the composite material, i.e., to include a cross-sectional sampling of all microstructural heterogeneities that occur in the composite material. The RVE must be chosen "sufficiently wide" compared to the microstructural size for a validated approach; however, it must remain small enough to be considered a volume element of continuum mechanics [KFG<sup>+</sup>03]. In [DW96], another definition of the RVE is also proposed: "It is the smallest material volume element of the composite for which the usual spatially constant (overall modulus) macroscopic constitutive representation is a sufficiently accurate model to represent mean constitutive response". This approach does not consider statistical fluctuations of the correspondent properties over finite domains. The estimates for the RVE's size found by these authors turn out to be much smaller than those in the previous definitions [Kan03].

In short, the RVE is chosen so that all (macroscopic) points of the structure, considered to be homogeneous, should be represented by an RVE.

To define an RVE, two categories of material can be distinguished:

- *disordered materials* for which the heterogeneities are randomly distributed and, thus, for which a statistical representation is required,
- *periodic materials*, which present a repetitive microstructure. For these materials, an RVE, such as a unit cell, can be chosen. This unit cell makes the generation of the whole material possible by periodicity or by spatial translation.

In the RVE, the different materials (or phases), their spatial distribution and their mechanical behavior are described.

At this stage, it is important to distinguish between both scales mentioned earlier:

- the *macroscopic scale*, corresponding to the scale of the structure, the loadings and all quantities dependent only on the global (macroscopic) position, called  $\mathbf{X}$ . At this scale, the heterogeneities are not distinguished.
- the *microscopic scale*, (the RVE scale) in which the microstructure can be described. Location is defined by a vector  $\mathbf{x}$ , representing the local position. This scale is linked to the size of the heterogeneities.

These scales are illustrated in Figure (6.1). To study the physical phenomena on the RVE scale, a homothetic transformation of ratio  $1/\delta$  is applied to the structure, where  $\delta$  is a minor parameter of the problem. The volume of the RVE is noted  $|V|$  and  $\partial V$  denotes its boundary.

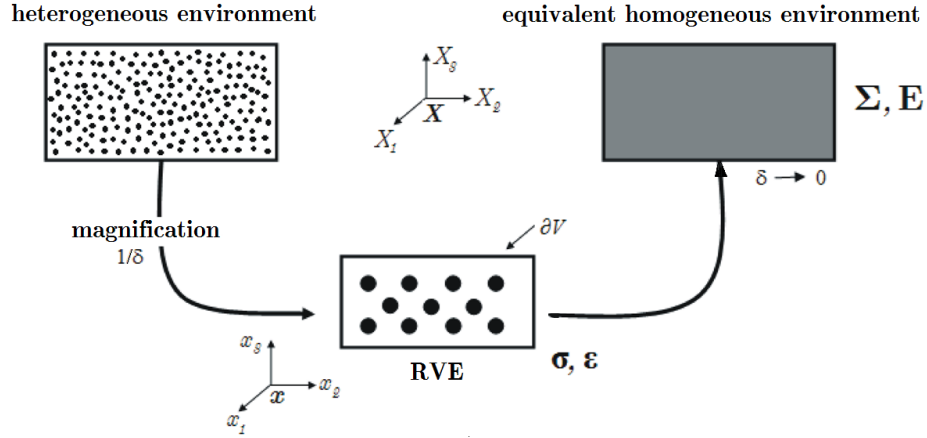


**Figure 6.1:** Homogenization principle. Heterogeneous and equivalent homogeneous environments. Definitions of the RVE and the microscopic and macroscopic scales. Figure inspired from [BB06].

Thus, if the local strain and stress in the RVE are noted  $\boldsymbol{\varepsilon}$  and  $\boldsymbol{\sigma}$ , the global macroscopic values in the homogenized medium,  $\mathbf{E}$  and  $\boldsymbol{\Sigma}$ , are defined as:

$$\begin{cases} \boldsymbol{\Sigma} = \lim_{\delta \rightarrow 0} \boldsymbol{\sigma} \\ \mathbf{E} = \lim_{\delta \rightarrow 0} \boldsymbol{\varepsilon} \end{cases} \quad (6.1)$$

### 6.3.2 Localization step

In this stage, the global variables  $\boldsymbol{\Sigma}$  and  $\mathbf{E}$  are linked to the corresponding local ones,  $\boldsymbol{\sigma}$  and  $\boldsymbol{\varepsilon}$ :

$$\begin{cases} \boldsymbol{\Sigma} = \frac{1}{|V|} \int_V \boldsymbol{\sigma} \, d\mathbf{x} \equiv \langle \boldsymbol{\sigma} \rangle_V \\ \mathbf{E} = \frac{1}{|V|} \int_V \boldsymbol{\varepsilon} \, d\mathbf{x} \equiv \langle \boldsymbol{\varepsilon} \rangle_V \end{cases}, \quad (6.2)$$

where the brackets  $\langle \cdot \rangle$  denote the average of a field on the unit cell.

Two means can be used to solve the localization problem in order to express the microscopic quantity derived from corresponding macroscopic ones. The loading imposed can be set as the average loading  $\mathbf{E}$  or the average loading  $\boldsymbol{\Sigma}$ . The systems obtained are as follows

1. Strain approach: imposed  $\mathbf{E}$

$$\begin{cases} \mathbf{div}\boldsymbol{\sigma} = \mathbf{0} & \text{in } V \\ \boldsymbol{\sigma} = \mathbf{d} : \boldsymbol{\varepsilon} & \text{in } V \\ \langle \boldsymbol{\varepsilon} \rangle = \mathbf{E} . \end{cases} \quad (6.3)$$

2. Stress approach: imposed  $\boldsymbol{\Sigma}$

$$\begin{cases} \mathbf{div}\boldsymbol{\sigma} = \mathbf{0} & \text{in } V \\ \boldsymbol{\sigma} = \mathbf{d} : \boldsymbol{\varepsilon} & \text{in } V \\ \langle \boldsymbol{\sigma} \rangle = \boldsymbol{\Sigma} . \end{cases} \quad (6.4)$$

Both problems present the same equilibrium equations for RVE (no body loads) and the same local constitutive laws, defined by a tensor  $\mathbf{d}$  chosen at the first step (definition of the RVE). The difference between both problems stems only from the imposed loading: the macroscopic strain in the first case and the macroscopic stress in the second case. To avoid problems of non-uniqueness of the solution (due to the average relations without true boundary conditions), boundary conditions on the border of the RVE,  $\partial V$ , have to be added to represent the phenomena endured by the heterogeneous material and their consequences as accurately as possible.

In this part, only the case of the macroscopic strain imposed is described, in the case of the small elastic strains. The case of large strains will be mentioned later. The main deformation theories are explained below [Mag03].

- *Voigt's approximation (uniform strain)*

This approximation consists in assuming that the strain is uniform in an RVE:

$$\boldsymbol{\varepsilon}(\mathbf{X}, \mathbf{x}) = \mathbf{E}(\mathbf{X}) \quad \forall \mathbf{x} \in V \quad \text{noted } \boldsymbol{\varepsilon} = \mathbf{E} \quad \text{in } V . \quad (6.5)$$

This approximation leads to simplifications of the problem but does not take into account the fluctuations of the microscopic state variables due to the local heterogeneities of the RVE, nor does it take into account the equilibrium relation ( $\mathbf{div}\boldsymbol{\sigma} = \mathbf{0}$  in  $V$ ). It has been shown that this approximation leads to an overestimation of the real properties.

- *Hill and Mandel's equivalent modulus method in deformation*

Here, the strain is free within the RVE, but, on the edges  $\partial V$ , the displacement  $\mathbf{u}$  is set to be homogeneous (Figure (6.2a)):

$$\mathbf{u}(\mathbf{X}, \mathbf{x}) = \mathbf{E}(\mathbf{X}) \cdot \mathbf{x} \quad \forall \mathbf{x} \in \partial V \quad \text{noted } \mathbf{u} = \mathbf{E} \cdot \mathbf{x} \quad \text{on } \partial V . \quad (6.6)$$

This approximation is closer to reality than the first one, but the assumption is valid only if the concentration of heterogeneities is minor. Moreover, in the case of periodic materials, results obtained using this method are dependent on the unit cell chosen. Consequently, as

for the previous approximation, this method is not adapted here.

- *Periodic homogenization in deformation*

This last method, more realistic than both previous ones, is applicable in the case of periodic microstructure materials. The local displacement field  $\mathbf{u}$  admits the following decomposition:

$$\mathbf{u} = \mathbf{E} \cdot \mathbf{x} + \mathbf{u}_{per} \quad (6.7)$$

where  $\mathbf{u}_{per}$  represents a periodic fluctuation of the local displacement field due to the presence of heterogeneities. This periodic displacement field  $\mathbf{u}_{per}$  (of period  $V$ ), is illustrated in Figure (6.2b). The local strain tensor then takes on the form

$$\boldsymbol{\varepsilon} = \mathbf{E} + \boldsymbol{\varepsilon}_{per} \quad , \quad (6.8)$$

where the fluctuation value  $\boldsymbol{\varepsilon}_{per}$  vanishes under volume averaging.

Moreover, this method supposes that the force vector  $\boldsymbol{\sigma} \cdot \mathbf{n}$  is anti-periodic on  $\partial V$  parts that correspond by periodicity:

$$\begin{cases} \mathbf{u}_{per}(\mathbf{X}, \mathbf{x}) = \mathbf{u}_{per}(\mathbf{X}, \mathbf{x} + V) & \forall \mathbf{x} \in \partial V \\ \boldsymbol{\sigma}(\mathbf{X}, \mathbf{x}) \cdot \mathbf{n}(\mathbf{X}, \mathbf{x}) = -\boldsymbol{\sigma}(\mathbf{X}, \mathbf{x} + V) \cdot \mathbf{n}(\mathbf{X}, \mathbf{x} + V) & \forall \mathbf{x} \in \partial V \\ \langle \boldsymbol{\varepsilon}(\mathbf{X}, \mathbf{x}) \rangle_{V(\mathbf{X})} = \mathbf{E}(\mathbf{X}) \end{cases} \quad (6.9)$$

Consequently,  $\mathbf{u}_{per}$  must be periodic over  $\partial V$ ,  $\boldsymbol{\sigma} \cdot \mathbf{n}$  must be anti-periodic over  $\partial V$  and  $\langle \boldsymbol{\varepsilon} \rangle_V = \mathbf{E}$ , where  $\mathbf{n}$  is the external normal on  $\partial V$  edges. The principal advantage of this theory is its accuracy in the case of a periodic medium [Mag03].

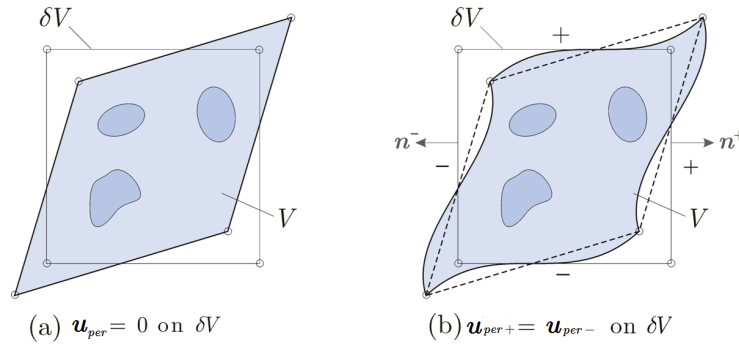


**Figure 6.2:** Illustration of the deformation of a cube-shaped microstructure  $V$  for the constraints on the boundary  $\partial V$ : (a) homogeneous displacement fluctuations  $\mathbf{u}_{per} = 0$  and (b) periodic fluctuations  $\mathbf{u}_{per+} = \mathbf{u}_{per-}$ , figure adapted from [MSL02].

### 6.3.3 Homogenization step

The last step is that of homogenization. This is used to obtain the behavior of the equivalent homogenized medium from an average operation on the RVE. The equivalent homogeneous

behavior is determined from the localized relations, the average relations and the microscopic constitutive laws attributed to each constituent of the RVE.

In concrete terms, this step consists in linking  $\mathbf{E}$  and  $\Sigma$ , using the above relations to obtain such homogenization law, where  $A$  and  $S$  characterize the homogenized behavior:

$$\begin{cases} \mathbf{E} = \langle \boldsymbol{\varepsilon} \rangle_V = S(\Sigma) : \Sigma \\ \Sigma = \langle \boldsymbol{\sigma} \rangle_V = A(\mathbf{E}) : \mathbf{E} \end{cases} \quad (6.10)$$

## 6.4 Periodic homogenization in small elastic strains

### 6.4.1 Why periodic homogenization?

Periodic homogenization is chosen here for two reasons:

- The choice of the unit cell is not unique [MMS99]. However, the equivalent behavior of the composite material computed from different unit cells generating the same microstructure should coincide (example shown in Figure (6.3)).
- Moreover, several studies [MMS99], [KFG<sup>+</sup>03] have shown that the periodic homogenization method was perfectly applicable to random media. In this case, the results lose some of their accuracy but give excellent estimates.

In short, the periodic homogenization theory is the most appropriate technique for a material with an ordered or disordered microstructure.

### 6.4.2 The unit cell

As mentioned above, the unit cell (RVE) defines the entirety of the periodic heterogeneous material. Thus, it has to represent the heterogeneity of the initial material sufficiently. Nevertheless, the choice of the cell is not unique. As mentioned in [MMS99], different unit cells having the same amount of heterogeneities lead to the same equivalent behavior. Consequently, the shape and symmetries of the unit cell should be chosen to simplify the periodic boundary conditions. This is illustrated in Figure (6.3) and explained by [MMS99]. In the hexagonal array, the simplest unit cell is the hexagon itself. However, the periodicity conditions on the hexagon may be difficult to handle and it may be easier to consider the rectangular unit cell also shown in this figure.

### 6.4.3 Periodicity of the microscopic fields

The material and geometrical periodicity of the medium influence the local strain and stress fields that also have period  $V$ . Thus, the local strain field is composed of the following:

- a homogeneous part represented by the average field,  $\langle \boldsymbol{\varepsilon} \rangle = \mathbf{E}$ , that corresponds to the strain field in a corresponding homogeneous unit cell,

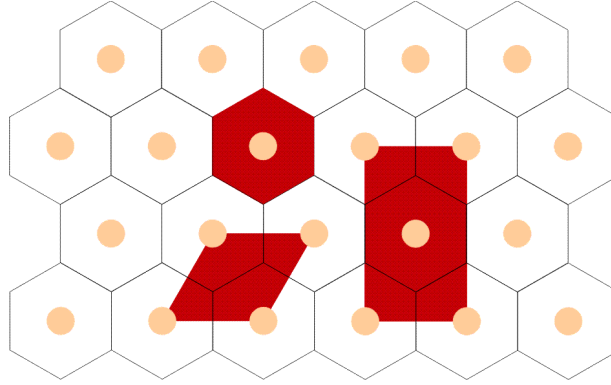


**Figure 6.3:** Hexagonal array. Different possible choices for the unit cell, adapted from [MMS99].

- a periodic fluctuated correction part,  $\boldsymbol{\varepsilon}_{per}$ , due to heterogeneities.

The displacement field can be written

$$\mathbf{u} = \langle \boldsymbol{\varepsilon} \rangle \cdot \mathbf{x} + \mathbf{u}_{per} \quad , \quad (6.11)$$

where  $\mathbf{u}_{per}$  is the displacement field from which the fluctuated  $\boldsymbol{\varepsilon}_{per}$  originates. The direct consequence of the periodicity of the periodic displacement  $\mathbf{u}_{per}$  is that the average value of  $\boldsymbol{\varepsilon}_{per}$  is defined as

$$\langle \boldsymbol{\varepsilon}_{per} \rangle_V = \mathbf{0} \quad \text{and} \quad \langle \boldsymbol{\varepsilon} \rangle = \mathbf{E} \quad . \quad (6.12)$$

This result was proved in [MMS99]. The microscopic stress field  $\boldsymbol{\sigma}$  is also periodic (of period  $V$ ) and respects the equilibrium equations in  $V$ :

$$\mathbf{div} \boldsymbol{\sigma} = \mathbf{0} \quad \text{in } V \quad . \quad (6.13)$$

The equilibrium condition between connected cells is expressed by  $\boldsymbol{\sigma} \cdot \mathbf{n}$  anti-periodic stress projection on boundaries  $\partial V$  that correspond by periodicity (see Eqn.(6.9)).

#### 6.4.4 Cellular problems of localization

The loading imposed on the structure (due to the displacement, for example) induces a stress field  $\boldsymbol{\Sigma}$  for each macroscopic point  $\mathbf{X}$ . Thus, these macroscopic quantities are considered to be external loadings for the unit cell. The localization problem to solve in the case of macroscopic strain imposed  $\mathbf{E}$  is therefore:

$$\left\{ \begin{array}{l} \mathbf{div} \boldsymbol{\sigma} = \mathbf{0} \quad \text{in } V \\ \boldsymbol{\sigma} = \mathbf{d} : \boldsymbol{\varepsilon}(\langle \boldsymbol{\varepsilon} \rangle_V \cdot \mathbf{x} + \mathbf{u}_{per}) \quad \text{in } V \\ \mathbf{u}_{per} \quad \text{periodic on } \partial V \\ \boldsymbol{\sigma} \cdot \mathbf{n} \quad \text{anti-periodic on } \partial V \\ \langle \boldsymbol{\varepsilon} \rangle_V = \mathbf{E} \quad . \end{array} \right. \quad (6.14)$$

Thanks to the addition of the periodic boundary conditions, these systems now have a unique solution.

## 6.5 Numerical implementation

Here, the implementation work is performed for large deformations. Consequently, the strain tensor  $\boldsymbol{\varepsilon}$  (or  $\mathbf{E}$ ) is replaced by the velocity gradient tensor  $\mathbf{l}$  (or  $\mathbf{L}$ ):

$$\mathbf{l} = \mathbf{L} + \text{grad}(\mathbf{v}_{per}) \quad \text{periodic on } V \quad , \quad (6.15)$$

where  $\mathbf{v}_{per}$  is the periodic velocity vector (of period  $V$ ).

### 6.5.1 Boundary conditions

The unit cell is meshed with finite elements and the average loading ( $\mathbf{L}$ ) is imposed on all elements of the mesh. Periodic boundary conditions must be imposed. This means that the corresponding nodes of the boundary of the unit cell must have the same periodic velocity. Thus, as illustrated in Figure (6.4),

$$\dot{\mathbf{u}}(\mathbf{x}) = \dot{\mathbf{u}}(\mathbf{x}') + \mathbf{L}(\mathbf{x} - \mathbf{x}') \quad ,$$

where  $\mathbf{x}$  and  $\mathbf{x}'$  denote opposite sides by pairs (for a rectangular pattern). As mentioned by [Fey99] for small strains, this equality directly results from applying<sup>1</sup>  $\dot{\mathbf{u}} = \mathbf{L}\mathbf{x} + \mathbf{v}_{per}$  to two similar points on opposite sides:

$$\left. \begin{array}{l} \dot{\mathbf{u}} = \mathbf{L}\mathbf{x} + \mathbf{v}_{per}(\mathbf{x}) \\ \dot{\mathbf{u}}' = \mathbf{L}\mathbf{x}' + \mathbf{v}_{per}(\mathbf{x}') \end{array} \right\} \Rightarrow \dot{\mathbf{u}} - \dot{\mathbf{u}}' = \mathbf{L}(\mathbf{x} - \mathbf{x}') + \mathbf{v}_{per}(\mathbf{x}) - \mathbf{v}_{per}(\mathbf{x}') \quad (6.16)$$

where  $\mathbf{v}_{per}(\mathbf{x}) - \mathbf{v}_{per}(\mathbf{x}') = \mathbf{0}$  by periodicity.

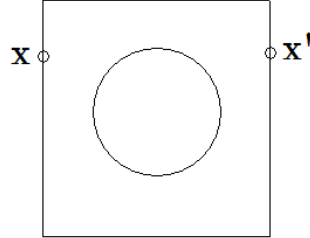


**Figure 6.4:** Periodicity conditions: notations.

An example of a 3D unit cell meshed with 8 elements is given in Figure (6.5). The periodic boundary conditions<sup>2</sup> for corresponding nodes are as follows:

- One node is fixed in order to avoid rigid-body displacements. In this case, it is one corner, node 1, for which no displacement is imposed. Due to the periodic relations, the other nodes must have the same periodic displacement (no periodic displacement). Consequently, for corner nodes 1, 3, 7, 9, 19, 21, 25 and 27,  $\mathbf{u}_{per} = \mathbf{0}$

<sup>1</sup>This corresponds to Eqn.(6.11) in the case of small strains.

<sup>2</sup>To take into account the periodicity conditions in the *Lagamine* finite element code, one solution is to condense the tangent matrix (using IDMAT in the data file). More details are given in Appendix (D).



- On the boundaries, corresponding nodes have the same periodic displacement:  
 $\mathbf{u}_{per}(2) = \mathbf{u}_{per}(8) = \mathbf{u}_{per}(20) = \mathbf{u}_{per}(26)$   
 $\mathbf{u}_{per}(4) = \mathbf{u}_{per}(6) = \mathbf{u}_{per}(22) = \mathbf{u}_{per}(24)$   
 $\mathbf{u}_{per}(10) = \mathbf{u}_{per}(12) = \mathbf{u}_{per}(18) = \mathbf{u}_{per}(16)$  .
- Similarly, on the faces:  
 $\mathbf{u}_{per}(5) = \mathbf{u}_{per}(23)$   
 $\mathbf{u}_{per}(11) = \mathbf{u}_{per}(17)$   
 $\mathbf{u}_{per}(13) = \mathbf{u}_{per}(15)$  .

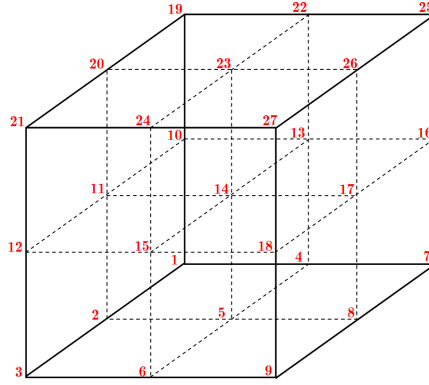


Figure 6.5: FE mesh of eight elements composed of eight nodes.

### 6.5.2 Implementation technique

The macroscopic nodes technique [DLM<sup>+</sup>06], [Bou97], [DL99] was chosen for implementation. With this technique, macroscopic fictive nodes are added and used to impose the macroscopic loading.

Periodic homogenization consists in finding the evolution of the velocity  $\mathbf{v}$ , the velocity gradient  $\mathbf{l}$ , the stress  $\boldsymbol{\sigma}$  and the macroscopic stress  $\boldsymbol{\Sigma}$  satisfying the conditions described below.

- The average relations between macroscopic and microscopic variables:

$$\mathbf{L} = \frac{1}{|V|} \int_V \mathbf{l} dV \quad ; \quad \boldsymbol{\Sigma} = \frac{1}{|V|} \int_V \boldsymbol{\sigma} dV \quad ;$$

- The periodicity of  $\mathbf{l}$  and  $\boldsymbol{\sigma}$ :

$$\begin{cases} \mathbf{l} & \text{is periodic with a period } V \\ \boldsymbol{\sigma} & \text{is periodic in } V \Rightarrow \boldsymbol{\sigma} \cdot \mathbf{n} \text{ anti-periodic on } \partial V \end{cases} ;$$

- The microscopic equilibrium equation:

$$\mathbf{div} \boldsymbol{\sigma} = \mathbf{0} \quad ;$$

- The relation between  $\mathbf{v}$  and  $\mathbf{l}$ :

$$\mathbf{l} = \frac{\partial \mathbf{v}}{\partial \mathbf{x}} ;$$

- The microscopic constitutive law.

Taking these equations into account, the virtual power theorem ensuring the equilibrium of the unit cell can be written,  $\forall \delta \mathbf{v}_{\text{per}}$  periodic with a period  $V$ ;  $\forall \delta \mathbf{L}$ :

$$\int_V \boldsymbol{\sigma} : \delta \mathbf{l} dV = |V| \boldsymbol{\Sigma} : \delta \mathbf{L} \quad (6.17)$$

where  $\delta \mathbf{l}_{ij} = \frac{\partial \delta v_i}{\partial x_j}$ , the virtual velocity gradient at time  $t$  of the microscopic particle.

This theorem (6.17) suggests considering  $\mathbf{L}$  as 9 supplementary degrees of freedom (DOF) joined to each element of the mesh, and considering  $|V| \boldsymbol{\Sigma}$  as the nodal forces associated to these DOF [BB06].

In this technique, the elementary displacement  $\mathbf{u}$  is replaced by the two components  $\Delta t \mathbf{v}_{\text{per}}$  (periodic displacement) and  $\Delta t \mathbf{L}$  (here,  $\mathbf{L}$  is the average (= macroscopic) velocity gradient):

$$\mathbf{u}' = \begin{pmatrix} \Delta t \mathbf{v}_{\text{per}} \\ \Delta t \mathbf{L} \end{pmatrix} . \quad (6.18)$$

The elementary differentiation matrix,  $[\mathbf{B}]$ , can be replaced by a  $[\mathbf{B}']$  matrix,

$$[\mathbf{B}'] = [[\mathbf{B}][\mathbf{I}]] \quad (6.19)$$

where  $[\mathbf{I}]_{9 \times 9}$  is an identity matrix. Thus,

$$[\Delta t \mathbf{l}] = [[\mathbf{B}][\mathbf{u}]] \Rightarrow [\Delta t \mathbf{l}] = [[\mathbf{B}'][\mathbf{u}']] . \quad (6.20)$$

Using Eqn.(6.18), (6.19) and (6.20), the discretization of the velocity gradient becomes:

$$\mathbf{l} = [\mathbf{B}]\mathbf{v}_{\text{per}} + \mathbf{L} . \quad (6.21)$$

The elementary residue vector that contains the out-of-equilibrium forces takes on the form, at equilibrium,

$$\mathbf{r} = \left\{ \begin{array}{c} \mathbf{0} \\ |V| \boldsymbol{\Sigma} \end{array} \right\} \quad (6.22)$$

and the iterative form of the virtual power theorem becomes

$$[\mathbf{K}] d\mathbf{u} = \mathbf{r} \quad (6.23)$$

where the incremental displacement  $\Delta \mathbf{u}$  of the form

$$\Delta \mathbf{u}' = \left\{ \begin{array}{c} \Delta t \mathbf{v}_{\text{per}} \\ \Delta t \mathbf{L} \end{array} \right\} . \quad (6.24)$$

### Algorithm

For each iteration, the resolution algorithm is given in Figure (6.6). The different steps of the resolution are described below.

At each iteration, the updated coordinates,  $\mathbf{x}^{t+\Delta t}$ , are computed from the macroscopic velocity gradient  $\mathbf{L}$ , from the coordinates of the last step  $\mathbf{x}^t$  and from the periodic velocity  $\mathbf{v}_{per}^t$  obtained in the previous iteration. The computation of the updated coordinates is performed using the equation from step (1). More details about that computation will be given below.

Then, from the updated coordinates, the microscopic velocity gradient is computed for each element using the equation from step (2). This microscopic velocity gradient is used as input data for the constitutive law. The stress tensor,  $\boldsymbol{\sigma}$ , and the corresponding local stiffness matrix,  $\mathbf{C}$ , are output data of the constitutive law (step (3)).

After that, the internal forces and the elementary tangent matrix are deduced from the preceding results (step (4)).

These values are used to fill the global tangent matrix and the out-of-equilibrium force vector (steps (5) and (6)).

Once these steps have been performed for each element of the mesh, the system is solved (step (7)). From this solution, the increment of periodic displacement and the macroscopic stress tensor are obtained.

At the end of an iteration, equilibrium is checked and displacement changes are imposed for the next iteration if the results are not as accurate as aimed for. If not, another step will begin.

### Modification of the element subroutine for periodic homogenization

#### a) Computation of the evolution of $\mathbf{x}^{t+\Delta t}$

The first problem in step (1) is to determine the updated coordinates. In fact, in the element subroutine, the usual displacement of the coordinates is replaced by a periodic one. Consequently, modifications must be made to define the coordinates, taking the periodic and the macroscopic (which come from the macroscopic velocity gradient matrix  $\mathbf{L}$ ) parts of the displacement into account. From [BB06], it appears that the total coordinates can be computed from

$$\mathbf{l}^{t+\Delta t} = \mathbf{L} + \frac{\partial \mathbf{v}_{per}}{\partial \mathbf{x}^{t+\Delta t}} \quad , \quad (6.25)$$

where  $\mathbf{l}^{t+\Delta t}$  is the microscopic velocity gradient matrix at the end of the time step, and  $\mathbf{v}_{per}$  the periodic velocity constant during the time step. First, to determine the evolution of  $\mathbf{x}^t$  during the time step, Eqn.(6.25) is spatially integrated over the updated configuration of the representative cell, where  $t$  is the time at the beginning of the step.

$$\dot{\mathbf{x}}^t = \mathbf{L}\mathbf{x}^t + \mathbf{v}_{per} \quad (6.26)$$

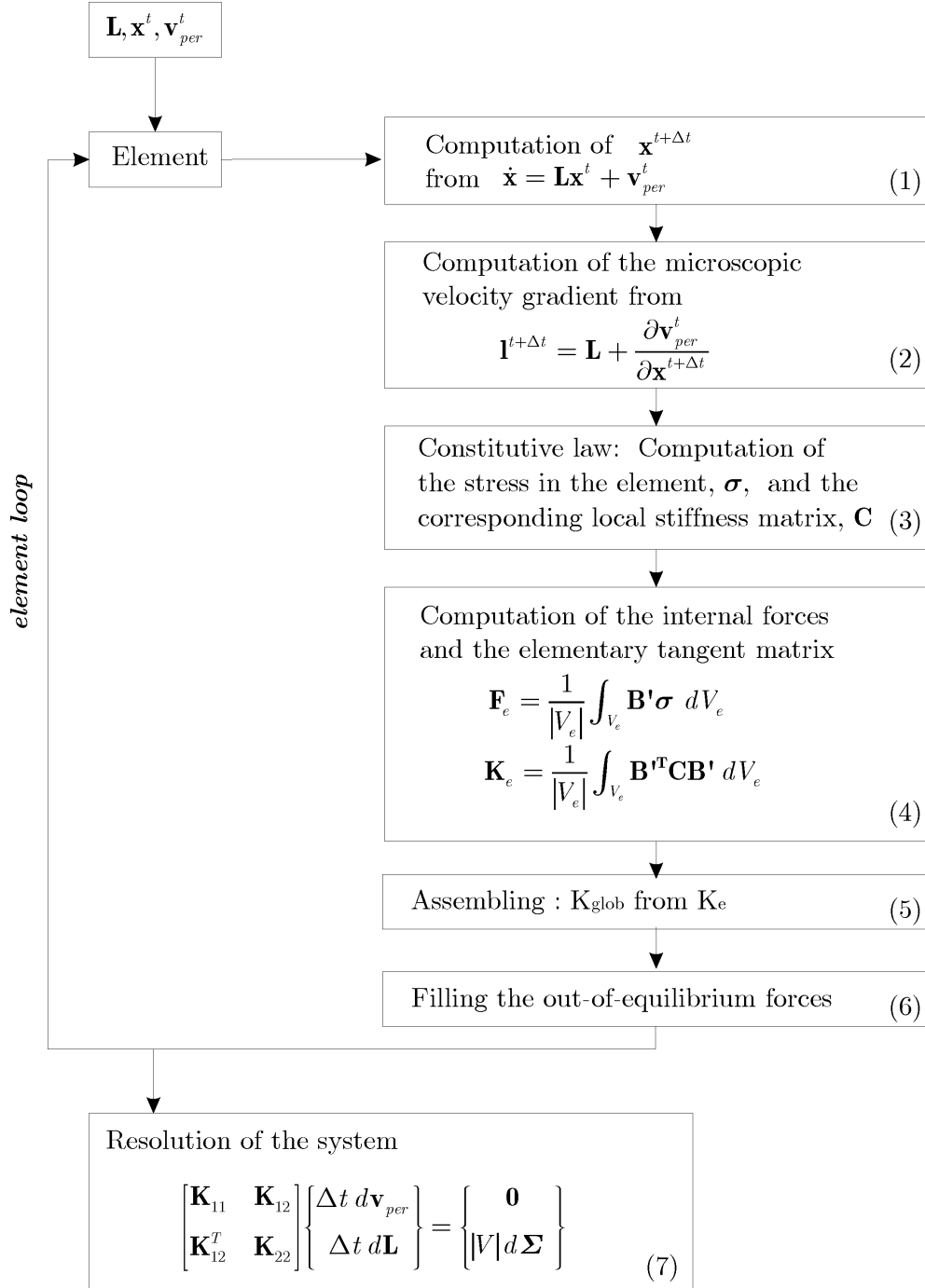


Figure 6.6: Resolution algorithm.

**Solution 1**

The first solution presented here [BB06] is found from the integration of the differential equation (Eqn.(6.26)):

$$\mathbf{x}^{t+\Delta t} = e^{\Delta t \mathbf{L}} \mathbf{x}^t + \boldsymbol{\lambda}^{-1} (e^{\Delta t \mathbf{L}} - \mathbf{I}) \mathbf{v}_{per} \quad (6.27)$$

where  $\boldsymbol{\lambda}$  contains the eigenvalues of  $\mathbf{L}$  and  $e^{\Delta t \mathbf{L}}$  the exponential component of  $\Delta t \mathbf{L}$ . The first term comes from the solution of the homogeneous component of the equation and the second one is a particular solution. The difficulty here concerns the  $\boldsymbol{\lambda}$  matrix. In fact, this matrix can be singular and the components of  $e^{\Delta t \mathbf{L}}$  can be complex if the eigenvalues or the eigenvectors of  $\Delta t \mathbf{L}$  are complex. This is possible because the matrix  $\mathbf{L}$  can be non-symmetric.

Eqn.(6.27) can be written differently. In fact, a matrix can generally be written as the product of 3 matrices where the first is the eigenvectors matrix, the second is a matrix that contains the eigenvalues on the diagonal and the third is equivalent to the first one, but transposed. Thus, if  $\mathbf{v}$  is the eigenvector matrix and  $\boldsymbol{\lambda}$  the eigenvalue matrix,  $\mathbf{L}$  can be written:

$$\mathbf{L} = \mathbf{v} \boldsymbol{\lambda} \mathbf{v}^T \quad (6.28)$$

where  $\mathbf{v}^T = \mathbf{v}^{-1}$  for orthogonal matrices. Consequently, Eqn.(6.27) can be written:

$$\mathbf{x}^{t+\Delta t} = \mathbf{v} e^{\Delta t \boldsymbol{\lambda} \mathbf{v}^T} \mathbf{x}^t + \boldsymbol{\lambda}^{-1} (\mathbf{v} e^{\Delta t \boldsymbol{\lambda} \mathbf{v}^T} \mathbf{x}^t - \mathbf{I}) \mathbf{v}_{per} \quad (6.29)$$

The problem with this solution is that  $\mathbf{L}$  can be non symmetric and in this case  $\mathbf{L} \neq \mathbf{v} \boldsymbol{\lambda} \mathbf{v}^T$  if  $\mathbf{v}$  and  $\boldsymbol{\lambda}$  are the eigenvector and eigenvalue matrices. In this case, the computation of the exponential component is not possible. Therefore, another solution must be found.

**Solution 2**

Another solution consists in approaching the exponential function from its limited development:

$$e^x = \sum \frac{x^n}{n!} = 1 + x + \frac{x^2}{2} + \frac{x^3}{6} + \dots \quad (6.30)$$

For a development limited to the second order (which [BB06] showed to be sufficient), the equation becomes:

$$\mathbf{x}^{t+\Delta t} = (\mathbf{I} + \Delta t \mathbf{L} + \frac{(\Delta t \mathbf{L})^2}{2}) \mathbf{x}^{t+\Delta t} + \boldsymbol{\lambda}^{-1} (\Delta t \mathbf{L} + \frac{(\Delta t \mathbf{L})^2}{2}) \mathbf{v}_{per}^{t+\Delta t} \quad (6.31)$$

This solution solves the problem of the computation of the exponential function but not the solution of this equation when the eigenvalue matrix has non real components.

**Solution 3**

This solution is less accurate but, fortunately, avoids the problems presented above. Here,

just a linear approximation is considered. It is worth noting that this is the usual case in finite element programs, justified by the sufficiently small size of the time step:

$$\dot{\mathbf{x}}^t = \frac{\mathbf{x}^{t+\Delta t} - \mathbf{x}^t}{\Delta t} . \quad (6.32)$$

So, the updated coordinates are given by

$$\mathbf{x}^{t+\Delta t} = \Delta t \{ \mathbf{L} \mathbf{x}^t + \mathbf{v}_{per} \} + \mathbf{x}^t . \quad (6.33)$$

These three solutions were implemented in the element subroutine.

The computation of  $\mathbf{x}^{t+\Delta t}$  is necessary in order to determine of the  $\mathbf{B}$  matrix used in the computation of the microscopic velocity gradient (step 2 in Figure (6.6)).

### b) Determination of $\mathbf{l}^{t+\Delta t}$

It is now possible to compute  $\mathbf{l}^{t+\Delta t}$  from this equation (step 2 in Figure (6.6)):

$$\mathbf{l}^{t+\Delta t} = \mathbf{L} + \frac{\partial \mathbf{v}_{per}}{\partial \mathbf{x}^{t+\Delta t}} = \mathbf{L} + \mathbf{B} \mathbf{v}_{per} . \quad (6.34)$$

The computation of  $\mathbf{B}$  is performed in the element subroutine using the preceding computation of  $\mathbf{x}^{t+\Delta t}$ . This step was necessary to compute the  $\mathbf{B}$  matrix. If anything was changed, the coordinates used for the differentiation operator would be "periodic" ones instead of the total ones, which is not correct for the computation of the  $\mathbf{B}$  matrix.

Consequently,  $\mathbf{l}^{t+\Delta t}$  can be computed using Eqn.(6.34). This microscopic velocity gradient is used as input for the constitutive law.

### c) Resolution

At the end of the constitutive law, the elementary stress tensor  $\boldsymbol{\sigma}$  and the corresponding local stiffness matrix  $\mathbf{C}$  are provided. The internal forces  $\mathbf{F}_e$  and the elementary tangent matrix  $\mathbf{K}_e$  are then computed using these matrices. These contributions are used to fill the components of the basic system to solve

$$[\mathbf{K}_{glob}] \{d\mathbf{u}\} = \{\mathbf{r}\} \quad (6.35)$$

where  $[\mathbf{K}_{glob}] = \sum_e [\mathbf{K}_e]$  and  $\{\mathbf{r}\}$  is the out-of-equilibrium force vector.

When the unit cell is in equilibrium, the system to solve is commonly written in this way:

$$\begin{bmatrix} K_{11} & K_{12} \\ K_{12}^T & K_{22} \end{bmatrix} \begin{Bmatrix} \Delta t d\mathbf{v}_{per} \\ \Delta t d\mathbf{L} \end{Bmatrix} = \begin{Bmatrix} \mathbf{0} \\ |V|d\boldsymbol{\Sigma} \end{Bmatrix} . \quad (6.36)$$

Consequently, once the system is solved, the  $\Delta t \mathbf{v}_{per}$  unknowns are obtained.

As mentioned above, to solve this system, the first step is to compute the internal forces  $\{\mathbf{F}_e\}$  of the element and the elementary tangent matrix  $[\mathbf{K}_e]$ . Usually,  $\mathbf{F}_e$  is computed using:

$$\{\mathbf{F}_e\} = \frac{1}{|V_e|} \int_{V_e} [\mathbf{B}]^T \{\boldsymbol{\sigma}\} dV_e \quad (6.37)$$

and  $\mathbf{K}_e$  is obtained from

$$[\mathbf{K}_e] = \frac{1}{|V_e|} \int_{V_e} [\mathbf{B}]^T [\mathbf{C}] [\mathbf{B}] dV_e \quad (6.38)$$

where  $\mathbf{C}$  is the local stiffness matrix and  $V_e$  is the elementary volume.

In the current periodic homogenization approach, the modification of  $[\mathbf{B}]$  used previously for the computation of the microscopic velocity gradient is also used for the computation of  $\mathbf{F}_e$  and  $\mathbf{K}_e$  in order to write the system to solve as the one given in Eqn.(6.36):

$$[\mathbf{B}] \rightarrow [\mathbf{B}'] = [[\mathbf{B}][\mathbf{I}]] \quad (6.39)$$

Thus, the vector of the internal forces can be written as

$$\{\mathbf{F}_e\} = \left\{ \frac{1}{|V_e|} \int_{V_e} [\mathbf{B}']^T \{\boldsymbol{\sigma}\} dV_e \right\} = \left\{ \begin{array}{c} \frac{1}{|V_e|} \int_{V_e} [\mathbf{B}]^T \{\boldsymbol{\sigma}\} dV_e \\ \frac{1}{|V_e|} \int_{V_e} \{\boldsymbol{\sigma}\} dV_e \end{array} \right\}, \quad (6.40)$$

and the elementary tangent matrix becomes

$$[\mathbf{K}_e] = \frac{1}{|V_e|} \int_{V_e} [\mathbf{B}']^T [\mathbf{C}] [\mathbf{B}'] dV_e. \quad (6.41)$$

By decomposition, the tangent matrix can be written with the form of Eqn.((6.36)), in which

- $[\mathbf{K}_{11}] = \frac{1}{|V_e|} \int_{V_e} [\mathbf{B}]^T [\mathbf{C}] [\mathbf{B}] dV_e$
- $[\mathbf{K}_{12}] = \frac{1}{|V_e|} \int_{V_e} [\mathbf{B}]^T [\mathbf{C}] dV_e$
- $[\mathbf{K}_{21}] = [\mathbf{K}_{12}]^T$
- $[\mathbf{K}_{22}] = \frac{1}{|V_e|} \int_{V_e} [\mathbf{C}] dV_e.$

The elementary tangent matrix and the internal force vector are then used to fill the global tangent matrix and the out-of-equilibrium force vector, taking into account the free or fixed degrees of freedom. Once these components have been filled with the contribution of each element of the mesh, the system of Eqn.(6.36) is solved to determine the unknown periodic displacements.

### 6.5.3 Validation of periodic homogenization's implementation

Different numerical simulations were performed to check the implementation of the periodic homogenization, some of which are presented in Appendix (C) using a 3D mesh composed of eight elements.

## 6.6 Conclusions

After a short literature review, choices were made and the periodic homogenization technique was implemented. Several approaches of the computation of  $\mathbf{x}^{t+\Delta t}$  were implemented. Choosing one of them will be influenced by the compromise between accuracy, convergence and mathematical possibilities.



## Conclusions on Numerical Tools

In this part, the numerical tools that will be used in the following parts to characterize the material behavior of the Ti-5553 alloy were presented.

Two new tools were implemented in the *Lagamine* FE code. The first one is an elastic-viscous-plastic microscopic plasticity-based constitutive law (Chapter 4). This constitutive law, written for another FE code, was implemented in the *Lagamine* FE code and modifications were carried out to be able to use hexagonal materials. The second tool implemented is the periodic homogenization technique (Chapter 6). This technique, available using the 3D eight-node brick elements BWD3D<sup>3</sup>, will be used in Part (V) for the numerical simulations of representative cells of Ti-5553.

Another constitutive law was also presented in this part (Chapter 5). It is a Norton-Hoff elastic-viscous-plastic constitutive law, available in the FE code and well-adapted to the global behavior observed for the Ti-5553 alloy.

---

<sup>3</sup>This element is briefly described in Appendix (E).



## Part III

# Identification of the $\beta$ phase of Ti-5553



# Introduction to the $\beta$ Phase's Identification

The main goal of this part, divided into several chapters, is to characterize the material behavior of the body-centered cubic  $\beta$  phase of Ti-5553.

Chapter (7) focuses on the characterization of the  $\beta$  phase of Ti-5553 from experimental tensile tests performed at different strain rates on the 100%  $\beta$  material. To model this phase, two constitutive laws will be used: macroscopic Norton-Hoff's type and microscopic plasticity-based constitutive laws. The results and the suitability of these laws to describe the experimental results and model the material behavior will be discussed.

In Chapter (8), the set of parameters obtained in Chapter (7) will be validated using experimental simple shear tests on the  $\beta$  material. For that purpose, numerical simulations will be compared against test results. The performance of the two constitutive laws will be discussed once again.

Finally, the last chapter of this section (Chapter (9)) is focused on nanoindentation tests performed on  $\beta$  grains of Ti-5553. In this chapter, a sensitivity analysis is carried out in order to study the effect of material parameters on the load versus displacement nanoindentation curves and on the patterns around the indent. The results will be compared with experimental ones and with results collected in the literature.



## Chapter 7

# Modeling tensile tests on 100% $\beta$ Ti-5553

### 7.1 Introduction

The goal of this chapter is to characterize the material behavior of the body-centered cubic  $\beta$  phase of Ti-5553 from experimental tensile tests performed at different strain rates on the 100%  $\beta$  material.

Once the experiments have been presented, the numerical modeling of these tests will be discussed. First, a macroscopic Norton-Hoff constitutive law will be used to model this phase. The accuracy of this law in reproducing experimental behavior will be discussed.

Secondly, an elastic-viscous-plastic microscopic plasticity-based constitutive law will be applied to simulate the same experiments. In this constitutive law, described in Chapter (4) of Part (II), two different hardening laws are available. They will be used in this chapter to improve the modeling of  $\beta$  phase behavior. The results obtained will be discussed and any necessary modifications will be explained.

Finally, the parameters of the constitutive and hardening laws able to model the  $\beta$  phase behavior of Ti-5553 will be provided. These parameters will be used in the next chapters.

### 7.2 Experimental tensile tests

Experimental tensile tests were performed at different strain rates<sup>1</sup> on 100%  $\beta$  Ti-5553<sup>2</sup>. The true stress versus true strain curves are presented in Figure (7.1)<sup>3</sup>.

---

<sup>1</sup>Theoretically, each experimental test is performed with a constant strain rate. In practice, it was not possible to perform experimental tests at a constant strain rate [Ger06]. In the next sections, the curves are mentioned with the assumed constant strain rate, but the identification of the material parameters was carried out using the real strain rate, which changes during the test.

<sup>2</sup>The 100%  $\beta$  material is obtained by a 30 minutes ageing at 875°C. The grain size of this material is around 200  $\mu\text{m}$ .

<sup>3</sup>It was shown in [Ger06] that, for the curve at a strain rate of  $10^{-2} \text{ s}^{-1}$ , the localization is diffusive in a great part of the curve. The end of the curves will not be used for the identification of the parameters.

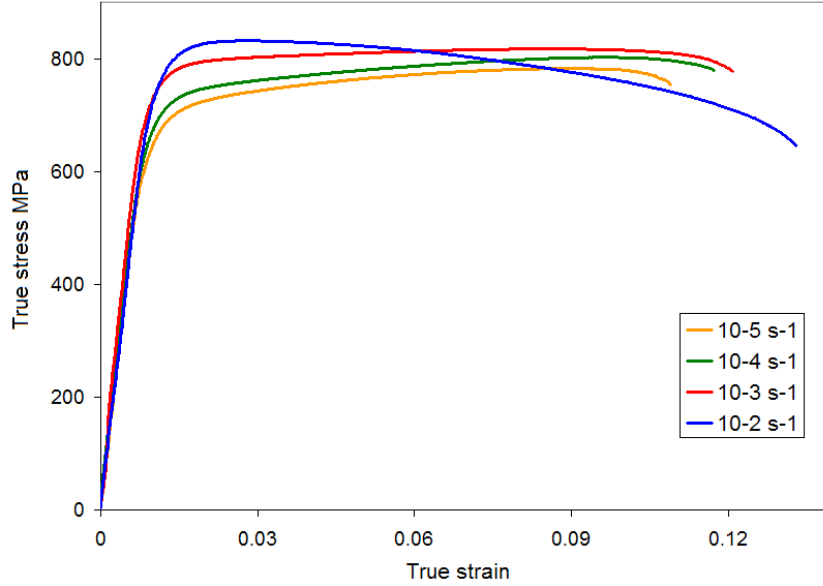


**Figure 7.1:** Experimental tensile tests performed on 100%  $\beta$  Ti-5553 at different strain rates:  $10^{-2}$ ,  $10^{-3}$ ,  $10^{-4}$  and  $10^{-5} \text{ s}^{-1}$  (UCL, July 2006).

## 7.3 Modeling with Norton-Hoff's macroscopic constitutive law

### 7.3.1 Introduction

As shown in Figure (7.1), the behavior of Ti-5553's  $\beta$  phase is influenced by the strain rate used to perform the test. The highest strain rate shows a softening behavior. Thus, to model this phase, a constitutive Norton-Hoff law was chosen<sup>4</sup>. It is an elastic-viscous-plastic constitutive law with four parameters:  $p_1$ ,  $p_2$ ,  $p_3$  and  $p_4$ . In the uniaxial case, it can be written [Pas03] and [Pas00] as

$$\bar{\sigma} = \bar{\varepsilon}^{p_4} \exp(-p_1 \bar{\varepsilon}) p_2 \sqrt{3} (\sqrt{3} \bar{\varepsilon})^{p_3} . \quad (7.1)$$

The stress  $\bar{\sigma}$  is the equivalent stress and the strain  $\bar{\varepsilon}$  is the equivalent total Von Mises' strain (it assumes isotropic behavior). In a tensile test, the equivalent plastic strain is equal to the longitudinal strain.

### 7.3.2 Description of the procedure to identify the parameters

In this paragraph, the procedure to identify Norton-Hoff's parameters from experimental curves and with the use of *Excel* as an optimizer is briefly described. The experimental data are the displacement, the load, and the corresponding time.

1. First, it is sometimes necessary to smooth the experimental displacement versus time curve.

<sup>4</sup>This constitutive law is briefly presented in Chapter (5) of Part (II).



2. The number of experimental points has to be adapted in order to acquire more data in "critical" regions where the changes are significant in a small range and less where there is no significant change in a large range. This step is necessary to adjust all the parts of the experimental curves correctly and it automatically defines the weight of the experiment for optimization. This simple approach corresponds to a direct use of an *Excell* optimization. Using *Optim*<sup>5</sup>, it is possible to weigh some parts of the curve independently.
3. The nominal strain,  $\varepsilon_{nom}$ , and the nominal stress,  $\sigma_{nom}$  are computed from

$$\varepsilon_{nom} = \frac{l - l_0}{l_0} \quad \text{and} \quad \sigma_{nom} = \frac{F}{A_0} , \quad (7.2)$$

where  $A_0$  is the initial section of the sample,  $l_0$  and  $l$  are the initial and the updated length of the sample respectively and  $F$  is the corresponding load. This nominal stress does not take into account area reduction during the tensile test.

4. The true strain,  $\varepsilon_{true}$ , and the true stress,  $\sigma_{true}$  [HR93], are computed from

$$\varepsilon_{true} = \ln \left( \frac{l}{l_0} \right) \quad \text{and} \quad \sigma_{true} = \frac{F}{A} = \sigma_{nom}(1 + \varepsilon_{nom}) , \quad (7.3)$$

where  $A$  is the updated area. The right-hand side of the equation for the true stress is deduced assuming that the volume of the sample is conserved ( $A_0 l_0 = A l$ ) [Lin96].

5. The true strain rate used in Norton-Hoff's law is obtained using the value of the true strain calculated just above, at time ( $t$ ) and ( $t-1$ ):

$$\dot{\varepsilon}_{true} = \frac{\varepsilon_t - \varepsilon_{t-1}}{t_t - t_{t-1}} . \quad (7.4)$$

6. The curve  $\dot{\varepsilon}(t)$  is smoothed. The strain rate of the sample is not always constant and may show a number of discontinuities. To smooth the curve, another program is sometimes used (*Matlab*, [Mat]).

7. Afterwards, the stress in the plastic part is evaluated by Norton-Hoff's model (Eqn.(7.1)) for a set of parameters,  $p_1$ ,  $p_2$ ,  $p_3$  and  $p_4$ , using Eqn.(7.3) and (7.4). As a reminder,

$$\bar{\sigma} = \bar{\varepsilon}^{p_4} \exp(-p_1 \bar{\varepsilon}) p_2 \sqrt{3} (\sqrt{3} \bar{\varepsilon})^{p_3} .$$

The parameters influence each other. Nevertheless, some of them have more influence in different parts of the curve. The parameter  $p_1$  influences the softening of the curve,  $p_2$  has an effect on the level of the curve,  $p_3$  can be linked to viscosity and  $p_4$  to hardening. It is also important to remember that several sets of parameters are sometimes possible to identify only one experimental curve.

---

<sup>5</sup> *Optim* is the identification tool that couples the *Lagamine* finite element code to an optimizer and experiments.

8. Eqn.(7.1) contains the elastic and plastic components of the strain. However, this law does not model the beginning of the curve. The elastic part is replaced by Hooke's law:

$$\sigma^{el} = E\varepsilon^{el}$$

where  $E$  is Young's modulus and  $\varepsilon^{el}$  is the elastic strain.

9. The total model is composed of Hooke's law for small strains and of Norton-Hoff's law for larger strains. The later is used when the elastic linear curve intercepts that of Norton-Hoff. An example of the elastic, plastic and total models is illustrated in Figure (7.2).

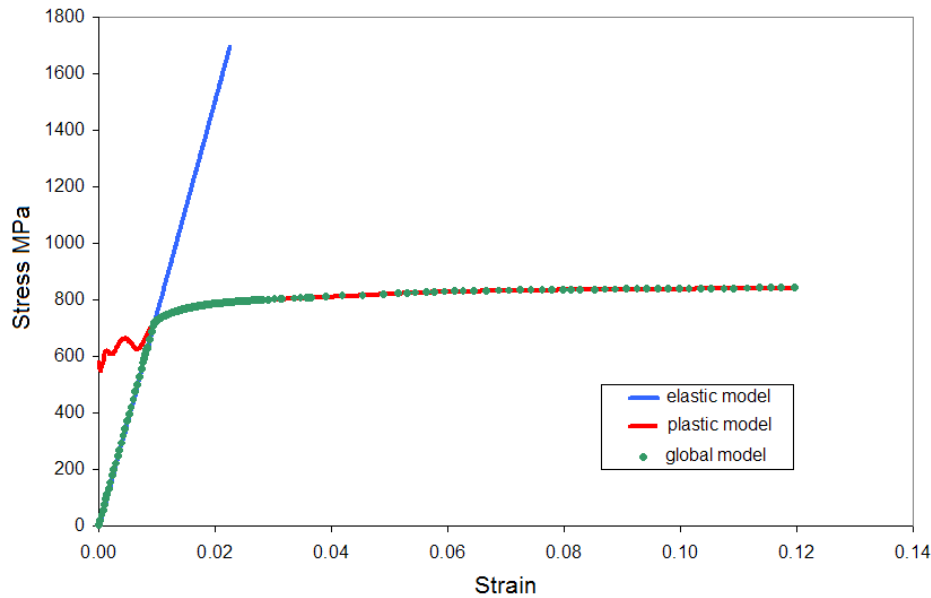


**Figure 7.2:** Example of true stress versus true strain for a tensile test using Norton-Hoff. Elastic, plastic and total models.

10. Finally, the last step is to optimize the parameters  $p_i$  (with  $i = 1$  to 4) in order to obtain a stress versus strain curve (computed just above) as close as possible to the experimental one. The optimization is done with a "macro" in *Excel* where the last square difference between the experimental and calculated data is minimized.

### 7.3.3 Identification of Norton-Hoff's parameters for the $\beta$ phase of Ti-5553

#### Identification with one set of parameters for all curves

The goal of this paragraph is to optimize the experimental tensile curves obtained for different strain rates (Figure (7.1)) with only one set of Norton-Hoff's parameters, using the procedure presented above. The optimized parameters are given in Table (7.1) and the corresponding

Norton-Hoff's parameters	Value
$p_1$	3.97517
$p_2$	1063.8608
$p_3$	0.011396
$p_4$	0.183951

**Table 7.1:** A set of Norton-Hoff's parameters optimized for 100%  $\beta$  Ti-5553 at different strain rates ( $\dot{\epsilon} \simeq 10^{-2}$  to  $10^{-5} \text{ s}^{-1}$ ).

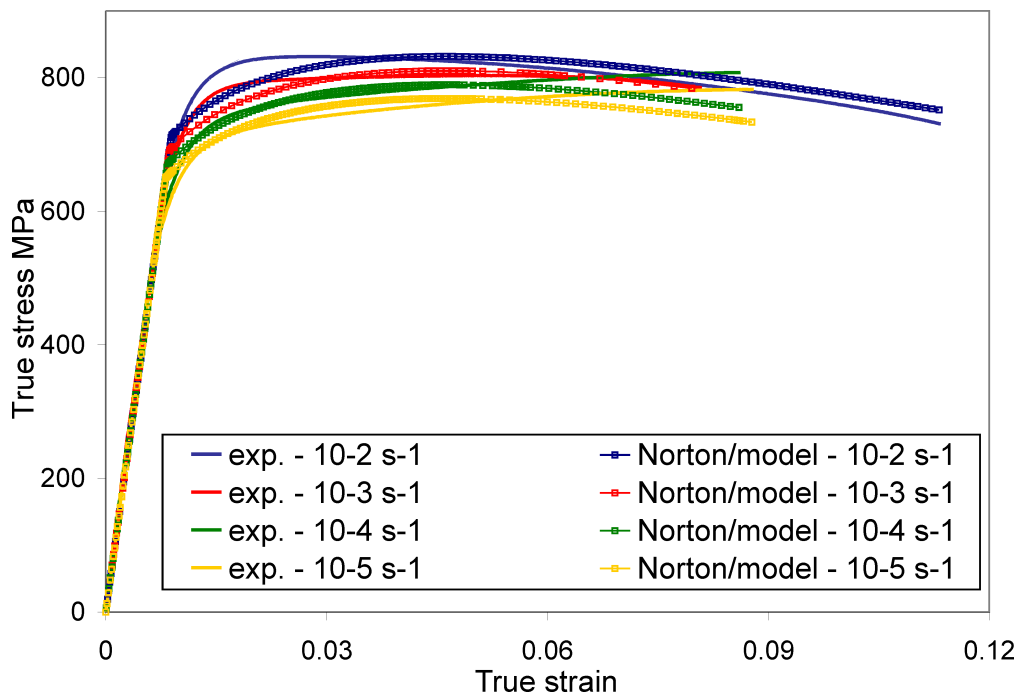


**Figure 7.3:** Comparison of the true stress versus true strain experimental tensile tests for different strain rates and the corresponding curves computed from Norton-Hoff and the parameters of Table (7.1).

optimized curves are shown in Figure (7.3).

As can be seen, the set of parameters obtained does not correctly reproduce the behavior of the material at each strain rate. With only one set of parameters, it is not possible to represent both softening and hardening, depending on the strain rate used for the test.

$\Rightarrow$  *Consequently, it is not possible to represent the behavior of 100 %  $\beta$  Ti-5553 at different strain rates (in the range of  $\dot{\epsilon} \simeq 10^{-2}$  to  $10^{-5} \text{ s}^{-1}$ ) with only one set of Norton-Hoff's parameters.*

### Identification with 2 sets of parameters for all curves

Due to the difficulties encountered while identifying the  $\beta$  phase with one set of Norton-Hoff's parameters, another solution had to be found.

Looking at the four experimental tensile curves in Figure (7.1), it is possible to separate two different types of behavior:

- *softening* for high strain rates ( $10^{-2}$  -  $10^{-3} \text{ s}^{-1}$ ),
- *hardening* for smaller strain rates ( $10^{-5}$  -  $10^{-4} \text{ s}^{-1}$ ).

Thus, the next step consists in identifying two sets of parameters (one for small strain rates and one for the larger ones) using parameter values as close as possible for the two sets.

The optimized parameters obtained have the same values for parameters  $p_2$  and  $p_3$  but different values for  $p_1$  and  $p_4$ . They are presented in Table (7.2).

Parameters	Strain rate $s^{-1}$	
	$10^{-2}$ - $10^{-3} \text{ s}^{-1}$	$10^{-4}$ - $10^{-5} \text{ s}^{-1}$
$p_1$	3.52725826	2.140885778
$p_2$	910.564995	910.5649949
$p_3$	0.01481757	0.014817573
$p_4$	0.13616601	0.14977472

**Table 7.2:** Sets of Norton-Hoff's parameters optimized for 100%  $\beta$  Ti-5553 and for two strain rate ranges.

The results obtained with the two sets of parameters in Table (7.2) are shown in Figures (7.4) and (7.5).

### 7.3.4 Conclusions

It is impossible to represent the behavior of the 100 %  $\beta$  Ti-5553 material correctly with only one set of Norton-Hoff's parameters for the range of strain rates studied ( $10^{-5}$  to  $10^{-2} \text{ s}^{-1}$ ).

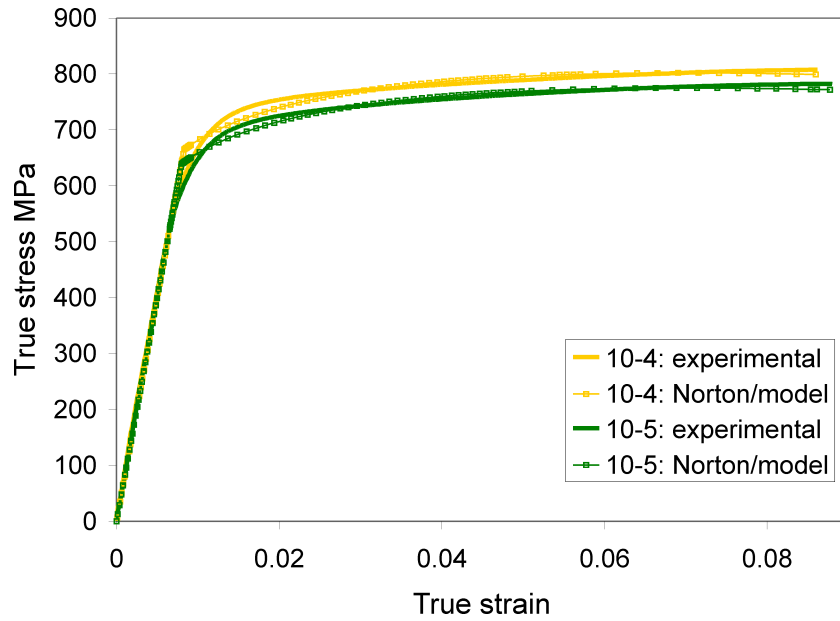


**Figure 7.4:** Comparison of true stress versus true strain curves obtained from experimental tensile tests for different strain rates ( $10^{-5}$  and  $10^{-4} \text{ s}^{-1}$ ) with the corresponding curves obtained with Norton-Hoff and the parameters from Table (7.2).

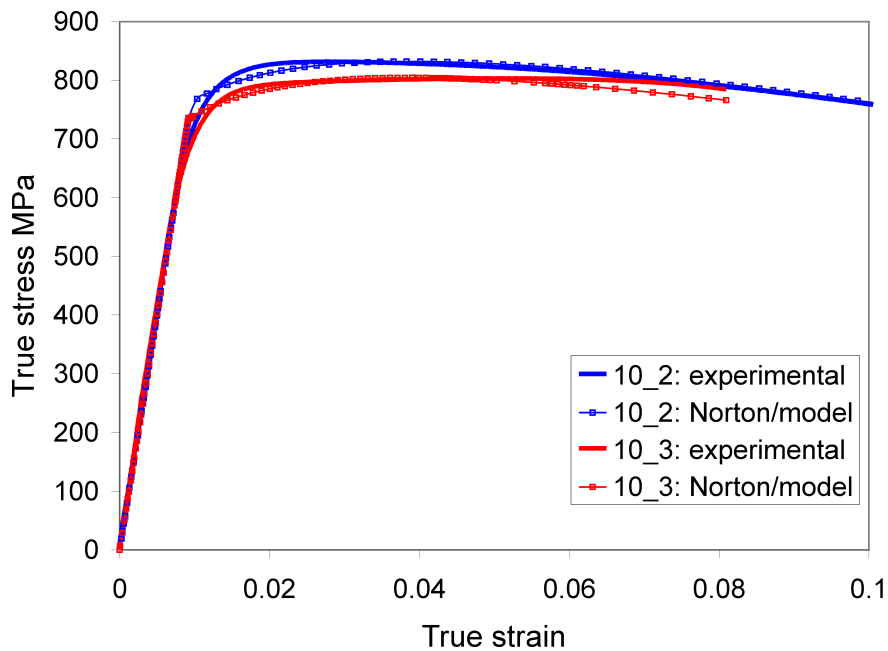


**Figure 7.5:** Comparison of true stress versus true strain curves obtained from experimental tensile tests for different strain rates ( $10^{-2}$  and  $10^{-3} \text{ s}^{-1}$ ) with the corresponding curves obtained with Norton-Hoff and the parameters from Table (7.2).

Nevertheless, it is possible to represent the behavior for all strain rates with this constitutive law if the modification of two parameters ( $p_1$  and  $p_4$ ) is allowed. For this phase of the Ti-5553 alloy, the optimized parameters are given in Table (7.2). When using an average value for the parameter  $p_4$  in order to have only one parameter ( $p_1$ ) that varies between both sets of curves, the results are not conclusive, as was the case for the Ti-LCB alloy [Ger06].

Therefore, in the next section, another constitutive law will be used to improve the modeling of the  $\beta$  phase.

## 7.4 Modeling with a crystal plasticity-based constitutive law

In this section, the identification of the  $\beta$  phase with the microscopic plasticity-based constitutive law presented in Chapter (4) of Part (II) is explained.

### 7.4.1 Slip systems

The  $\beta$  phase of Ti-5553 is body-centered cubic (BCC). This phase contains a set of 24 slip systems that can be activated during loading [Duc03]. These 24 slip systems ( $(\mathbf{s})\langle\mathbf{n}\rangle$ )<sup>6</sup> are composed of 12 (110) $\langle$ 111 $\rangle$  slip systems and 12 (112) $\langle$ 111 $\rangle$  slip systems. These slip systems are taken into account in the microscopic plasticity law.

### 7.4.2 Constitutive law

The constitutive law is repeated in Eqn.(7.5). The parameters  $n$  and  $\dot{a}$  have to be determined for each set of slip systems.

$$\dot{\gamma}^{(\alpha)} = \dot{a}^{(\alpha)} \left( \frac{\tau^{(\alpha)}}{g^{(\alpha)}} \right)^{n^{(\alpha)}} \quad (7.5)$$

$\dot{\gamma}^{(\alpha)}$  is the slipping rate,  $\dot{a}^{(\alpha)}$  is the reference strain rate on the slip system  $\alpha$ ,  $g^{(\alpha)}$  is a variable which describes the current strength of that system, and  $n$  is linked to the strain rate sensitivity. The strain hardening is characterized by the evolution of the strength  $g^{(\alpha)}$  through the relation

$$\dot{g}^{(\alpha)} = \sum_{\beta} h_{\alpha\beta} \dot{\gamma}^{(\beta)} \quad (7.6)$$

where  $h_{\alpha\beta}$  is the slip hardening moduli, and the sum's range includes all activated slip systems.

As shown in Figure (7.6) for tensile tests performed at a strain rate of  $\dot{\epsilon} \sim 10^{-4} \text{ s}^{-1}$ , the effect of these parameters ( $\dot{a}$  and  $n$ ) on the results is significant. Once the parameters vary, the curves are shifted up or down, but without modification of the slope of the curves. A greater value of  $\dot{a}$  leads to a downward shift of the level of the curves whereas an increase in  $n$  shifts the curves up.

---

<sup>6</sup> $\mathbf{s}$  represents the slip direction and  $\mathbf{n}$  is the corresponding normal to the slip plane.

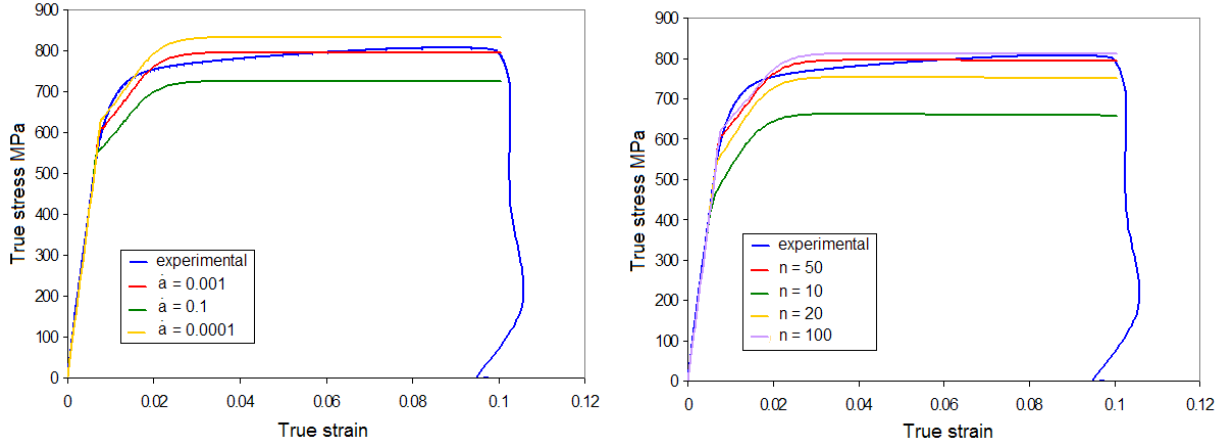


**Figure 7.6:** Influence of parameters  $\dot{a}$  (left) and  $n$  (right). The other parameters used here are  $h_0 = 15000$  ;  $\tau_0 = 300$  and  $\tau_s = 545$ .  $\dot{a}$  is taken to 0.001 when  $n$  changes and  $n$  is equal to 50 when  $\dot{a}$  varies. For both figures, the strain rate is approximately  $10^{-4} \text{ s}^{-1}$ .

### 7.4.3 Identification of the $\beta$ phase with the first hardening law

As previously mentioned (Chapter (4) of Part (II)), two hardening laws are available. The first one, given by Asaro and Pierce<sup>7</sup> [Hua91], can be written

$$\begin{cases} h_{\alpha\alpha} = h(\gamma) = h_0 \text{sech}^2 \left| \frac{h_0 \gamma}{\tau_s - \tau_0} \right| \\ h_{\alpha\beta} = qh(\gamma) \quad (\alpha \neq \beta) \end{cases} \quad (7.7)$$

where  $h_0$  is the initial hardening modulus,  $\tau_0$  is the initial value of  $g^{(\alpha)}$ ,  $\tau_s$  is the saturation value and  $q$  characterizes the latent hardening.

Thus, using this hardening law, 5 parameters must be identified for each set of slip systems:  $\dot{a}$ ,  $n$ ,  $h_0$ ,  $\tau_0$  and  $\tau_s$ . For the BCC  $\beta$  phase, as usual, the same parameters will be chosen for each set of slip systems.

The parameters of this hardening law will be optimized using *Optim*. The following approaches were tested to identify the  $\beta$  phase with this hardening law.

#### First optimization

First, the five parameters  $\dot{a}$ ,  $n$ ,  $h_0$ ,  $\tau_0$  and  $\tau_s$  were optimized using the four experimental tensile curves in Figure (7.1). Unfortunately, as is often the case, the optimization of several parameters on several curves is slow and inconclusive. Indeed, the results obtained with this technique were not satisfactory. The optimized parameters rapidly led to curves far from the experimental ones. Thus, another approach was used to identify the parameters.

<sup>7</sup>The identification of the  $\beta$  phase is first tested with Asaro and Pierce's hardening law because it requires fewer parameters than the second available hardening law, Bassani and Wu's.

### Second optimization

From the experimental tests in Figure (7.1), two types of behavior appear, depending on the strain rate used to perform the test: *hardening* or *softening*. Thus, like the work performed to optimize Norton-Hoff's parameters, this identification of the parameters was performed in several steps.

In the first step, the parameters are optimized for three of the four curves, corresponding to strain rates of  $10^{-3}$ ,  $10^{-4}$  and  $10^{-5} s^{-1}$ . The two curves at  $10^{-4}$  and  $10^{-5} s^{-1}$  present hardening behavior and the curve at  $10^{-3} s^{-1}$  shows intermediate behavior, more like a perfectly plastic one. The parameters optimized for these three curves are given in Table (7.3).

Optimized parameters	
$h_0 = 100$	$\dot{a} = 0.0359$
$\tau_0 = 300$	$n = 63.972$
$\tau_s = 342.5$	

**Table 7.3:** Optimized parameters of the microscopic plasticity law using Asaro and Pierce's hardening for tensile tests performed at  $10^{-3}$ ,  $10^{-4}$  and  $10^{-5} s^{-1}$ .

The second step consists in modeling the curve obtained with the last strain rate ( $10^{-2} s^{-1}$ ). The parameters optimized in the first step are maintained, except for  $h_0$ . This parameter is optimized for the last curve in order to obtain an appropriate modeling of this curve. The optimized values of the parameter  $h_0$  are given in Table (7.4).

Strain rate ( $s^{-1}$ )	$h_0$
$10^{-5}$ to $10^{-3} s^{-1}$	100
$10^{-2} s^{-1}$	15000

**Table 7.4:** Optimized parameter  $h_0$  for tensile tests performed at all strain rates.

The corresponding optimized curves, obtained using parameters from Table (7.3) and Table (7.4), are presented in Figure (7.7).

However, this optimization is not wholly satisfactory, principally in the elastic-plastic transition. Thus, a third method must be tried.

### Third optimization

Due to the inconclusive results previously obtained, another method was tested. First, the parameters ( $\dot{a}$ ,  $n$ ,  $h_0$  and  $\tau_s$  optimized and  $\tau_0$  fixed) were optimized using the curve at a strain rate of  $10^{-5} s^{-1}$ . Secondly, the curve at a strain rate of  $10^{-4} s^{-1}$  was modeled, using the initial parameter values optimized with the first curve and trying to modify the minimum number of parameters. The parameter  $\tau_s$  was allowed to vary and, if it was not sufficient,  $h_0$  was also modified. Afterwards, the other curves were similarly optimized. These results will



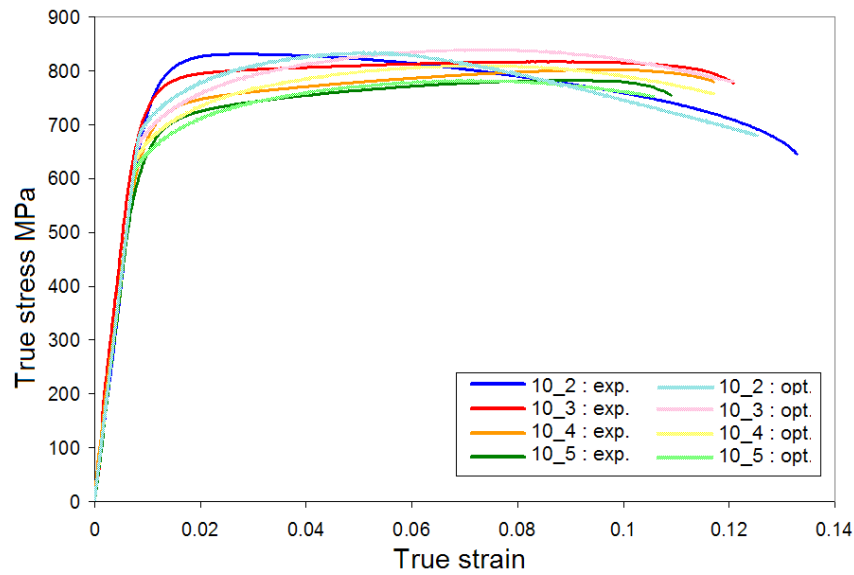


**Figure 7.7:** Experimental and numerical tensile tests for different strain rates on 100 %  $\beta$  Ti-5553. The parameters used are those given in Table (7.3) and in Table (7.4).

be shown below.

\*) *First curve:*  $\dot{\epsilon} = 10^{-5} \text{ s}^{-1}$

The parameters optimized (with  $\tau_0 = 300$ , fixed) for this curve and the corresponding results are shown in Figure (7.8).

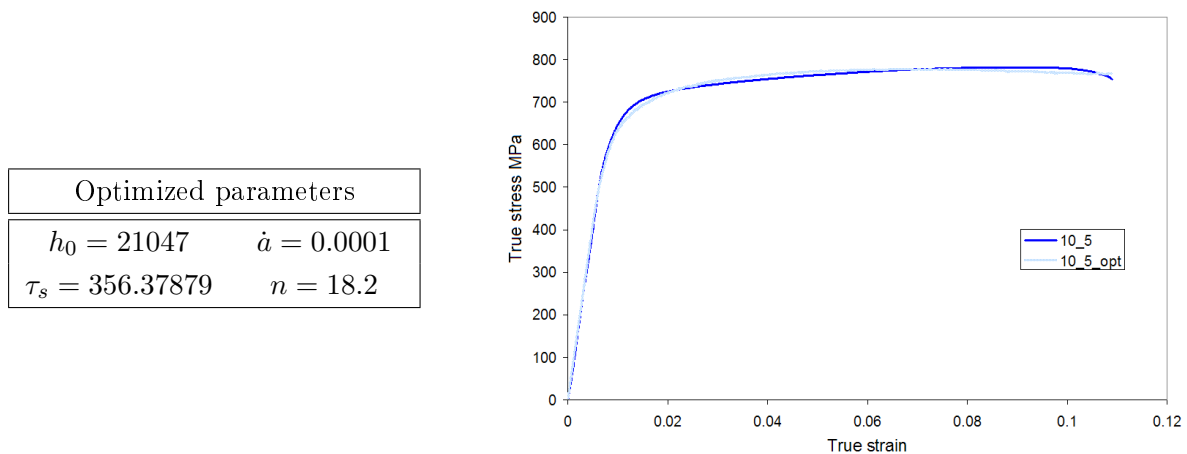


**Figure 7.8:** Optimized parameters for tensile tests performed at  $10^{-5} \text{ s}^{-1}$ . Experimental (10-5) and numerical (10-5-opt) tensile tests for a strain rate of  $10^{-5} \text{ s}^{-1}$  on 100%  $\beta$  material.

\*) *Second curve:*  $\dot{\epsilon} = 10^{-4} \text{ s}^{-1}$

For this curve, the parameters were the same as for the previous curve (table in Figure (7.8)) except for  $\tau_s$ , which is optimized to  $\tau_s = 323.44$  MPa. Results are shown in Figure (7.9).

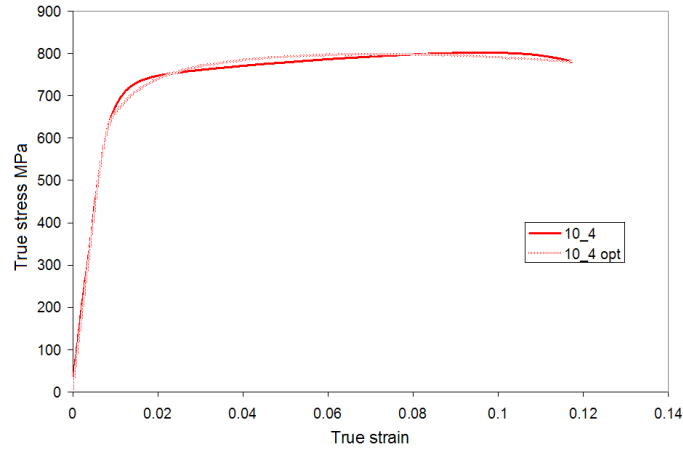


**Figure 7.9:** Experimental (10-4) and numerical (10-4-opt) tensile tests for a strain rate of  $10^{-4} s^{-1}$  on 100%  $\beta$  material. For the numerical test, the parameters are those given in the table in Figure (7.8), except for  $\tau_s$ :  $\tau_s = 323.44$  MPa.

\*) **Third curve:**  $\dot{\epsilon} = 10^{-3} s^{-1}$

For this curve, modifying  $\tau_s$  is not sufficient to obtain a correct fit. Allowing the parameter  $h_0$  to vary no longer optimizes this curve. Consequently, an optimization of all the parameters was tested. The optimized parameters and the corresponding results are presented in Figure (7.10).

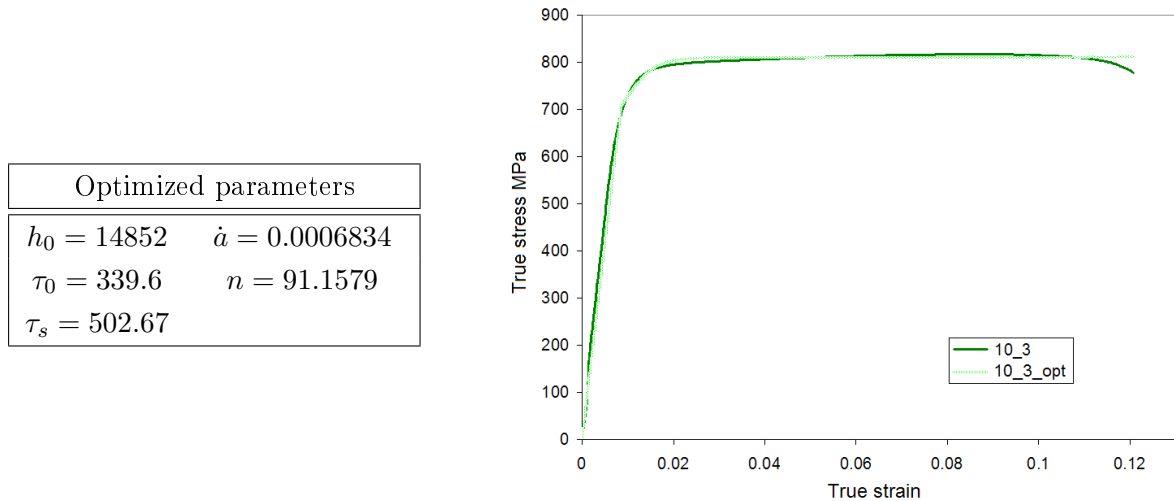


**Figure 7.10:** Optimized parameters for tensile tests performed at  $10^{-3} s^{-1}$ . Experimental (10-3) and numerical (10-3-opt) tensile tests for a strain rate of  $10^{-3} s^{-1}$  on 100%  $\beta$  material.

Consequently, with another set of parameters (far from the parameters corresponding to the

other strain rates), it is possible to model the behavior of the material at a strain rate of  $10^{-3} s^{-1}$ .

\*) **Fourth curve:**  $\dot{\epsilon} = 10^{-2} s^{-1}$

As was performed for the third curve, all parameters were optimized here. Due to the difficulty in obtaining acceptable results, the optimization was performed several times. Each time, different initial parameters were used. In each case, the optimized parameters are different but the general shape of the optimized curve is always approximately the same and far from the experimental behavior (Figure (7.11)). Moreover, softening is never reproduced using this hardening law.

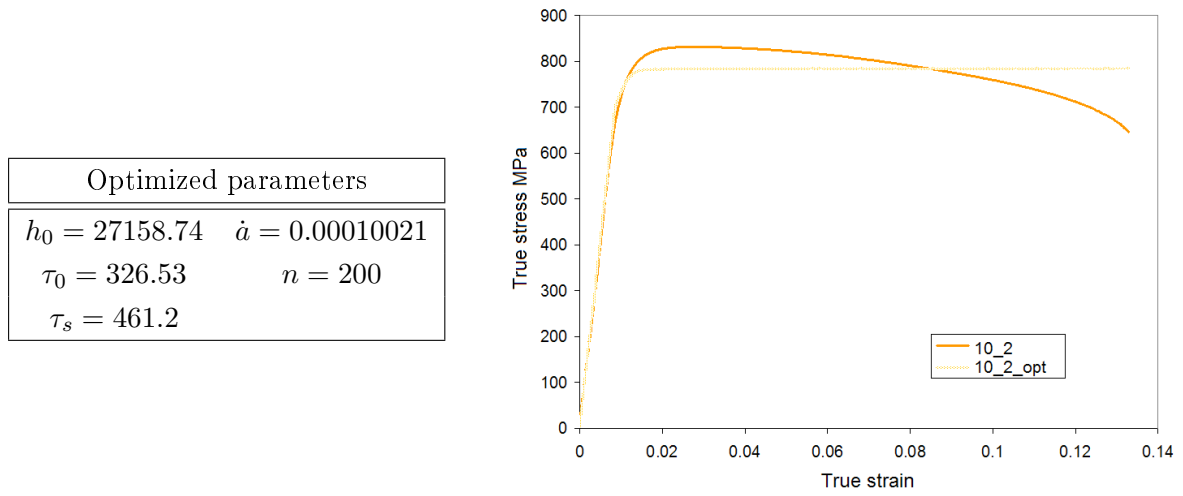


**Figure 7.11:** Optimized parameters for tensile tests performed at  $10^{-2} s^{-1}$ . Experimental (10-2) and numerical (10-2-opt) tensile tests for a strain rate of  $10^{-2} s^{-1}$  on 100%  $\beta$  material.

## Conclusions

Asaro and Pierce's hardening law used to model the behavior of the  $\beta$  phase of Ti-5553 at different strain rates is not adapted to softening models. This behavior was observed for tensile tests performed at high strain rates. Consequently, in the next section, the second hardening law (Bassani and Wu's) will be used to model all the tensile tests performed on 100%  $\beta$  Ti-5553 with one set of parameters.

### 7.4.4 Identification of the $\beta$ phase with the second hardening law

The second hardening law available in the plasticity constitutive law is Bassani and Wu's repeated here:

$$\begin{cases} h_{\alpha\alpha} = \left\{ (h_0 - h_s) \operatorname{sech}^2 \left| \frac{(h_0 - h_s) \gamma^{(\alpha)}}{\tau_s - \tau_0} \right| + h_s \right\} G(\gamma^\alpha; \beta \neq \alpha) \\ h_{\alpha\beta} = qh(\alpha\alpha) \quad (\alpha \neq \beta) \end{cases} \quad (7.8)$$

with

$$G(\gamma^\alpha; \beta \neq \alpha) = 1 + \sum_{\beta \neq \alpha} f_{\alpha\beta} \tanh\left(\frac{\gamma^{(\beta)}}{\gamma_0}\right)$$

where  $h_0$  is the initial hardening modulus,  $\tau_0$  (the initial yield stress) is the initial value of  $g^{(\alpha)}$ ,  $\tau_s$  is the saturation stress and  $h_s$  is the hardening modulus during easy glide within the first stage of hardening.  $\gamma^{(\alpha)}$  is the total shear strain in slip system  $\alpha$ , while "sech" is the hyperbolic secant function.  $\gamma^{(\beta)}$  is the total shear strain in slip system  $\beta$ ,  $\gamma_0$  is the amount of slip after which the interaction between slip systems reaches its peak strength, and each component  $f_{\alpha\beta}$  represents the magnitude of the strength of an interaction between slip systems  $\alpha$  and  $\beta$ . The function  $G$  deals implicitly with cross-hardening that occurs between slip systems.

With this hardening law, for each set of slip systems, 10 parameters must be optimized (if latent hardening (parameter  $q$ ) is not taken into account):  $\dot{\epsilon}$ ,  $n$ ,  $h_0$ ,  $h_s$ ,  $\tau_0$ ,  $\tau_s$ ,  $\gamma_{0\alpha}$ ,  $\gamma_{0\alpha\beta}$ ,  $f_{\alpha\alpha}$  and  $f_{\alpha\beta}$ . As recommended (see Chapter (4) of Part (II)),  $q = 0$  is chosen for each set of slip systems. Moreover, as was performed with the first hardening law, in the numerical simulations of the  $\beta$  phase, the parameters will be the same for each set of slip systems.

To better understand the effect of each parameter of this hardening law, a sensitivity analysis of these parameters was performed. This analysis will also make it possible to model the tensile curve on  $\beta$  Ti-5553 at a strain rate of  $10^{-2} \text{ s}^{-1}$ . Afterwards, from the set of parameters obtained, the other curves will be fitted.

### Sensitivity analysis

#### *\*) Influence of $\tau_0$*

The initial parameters used to perform this analysis are given in Table (7.5). The influence of the parameter  $\tau_0$  is given in Figures (7.12) and (7.13).

Parameter	Value	Parameter	Value
$n$	50	$h_s$	10000
$\dot{\epsilon}$	0.001	$\gamma_{0\alpha}$	0.001
$h_0$	10000	$\gamma_{0\alpha\beta}$	0.001
$\tau_s$	350	$f_{\alpha\alpha}$	15
$\tau_0$	300	$f_{\alpha\beta}$	15

**Table 7.5:** Initial parameters for Bassani and Wu's hardening.

Observations:  $\tau_0$  close to  $\tau_s$  is needed to avoid too large of a plastic modulus. A greater value of  $\tau_0$  leads to a greater yield point and  $\tau_0$  close to 300 MPa seems to be well-adapted in this case.

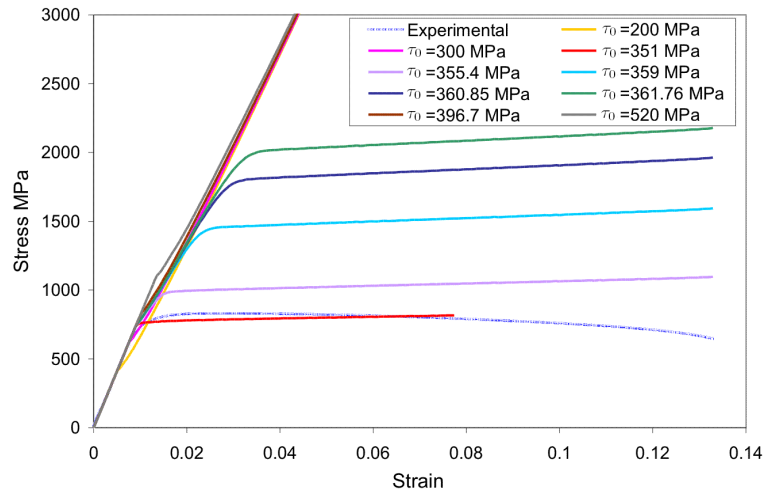


**Figure 7.12:** Experimental and numerical tensile tests with the crystalline plasticity constitutive law and Bassani and Wu's hardening for a strain rate of  $10^{-2} \text{ s}^{-1}$  on 100%  $\beta$  Ti-5553 and for different values of the parameter  $\tau_0$ .

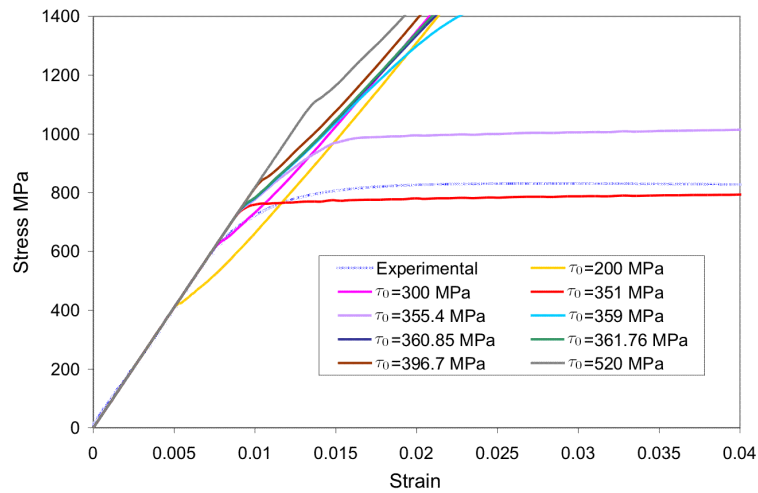


**Figure 7.13:** Experimental and numerical tensile tests with the crystalline plasticity constitutive law and Bassani and Wu's hardening for a strain rate of  $10^{-2} \text{ s}^{-1}$  on 100%  $\beta$  Ti-5553 and for different values of the parameter  $\tau_0$ . Zoom on the yield point.

\*) Influence of  $\tau_s$ 

Parameter	Value
$n$	50
$\dot{a}$	0.001
$h_0$	10000
$\tau_s$	vary
$\tau_0$	300
$h_s$	10000
$\gamma_{0\alpha}$	0.001
$\gamma_{0\alpha\beta}$	0.001
$f_{\alpha\alpha}$	15
$f_{\alpha\beta}$	15

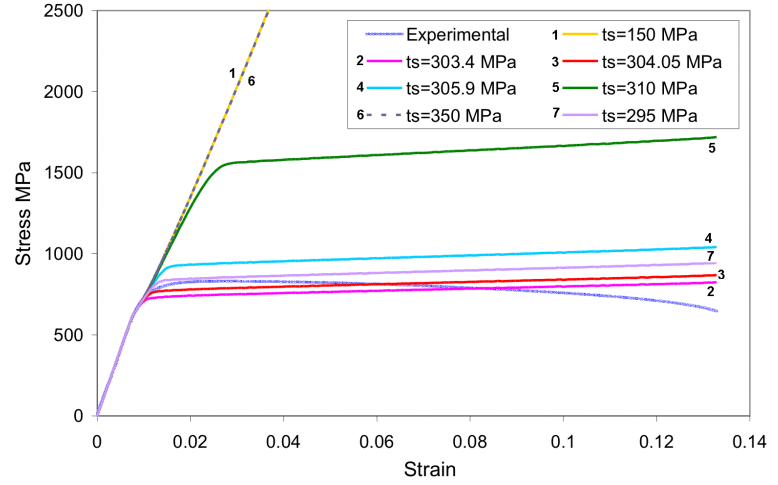


**Figure 7.14:** Experimental and numerical tensile tests with the crystalline plasticity constitutive law and Bassani and Wu's hardening for a strain rate of  $10^{-2} s^{-1}$  on 100%  $\beta$  Ti-5553 and for different values of the parameter  $\tau_s$ .

Observations: As mentioned above,  $\tau_s$  close to  $\tau_0$  is required to avoid too large of a plastic modulus. A small variation in  $\tau_s$  (close to  $\tau_0$ ) leads to an upward shift of the curves, without modification of the yield point and the plastic modulus.

\*) Influence of  $h_0$ 

Parameter	Value
$n$	50
$\dot{a}$	0.001
$h_0$	vary
$\tau_s$	304
$\tau_0$	300
$h_s$	10000
$\gamma_{0\alpha}$	0.001
$\gamma_{0\alpha\beta}$	0.001
$f_{\alpha\alpha}$	15
$f_{\alpha\beta}$	15

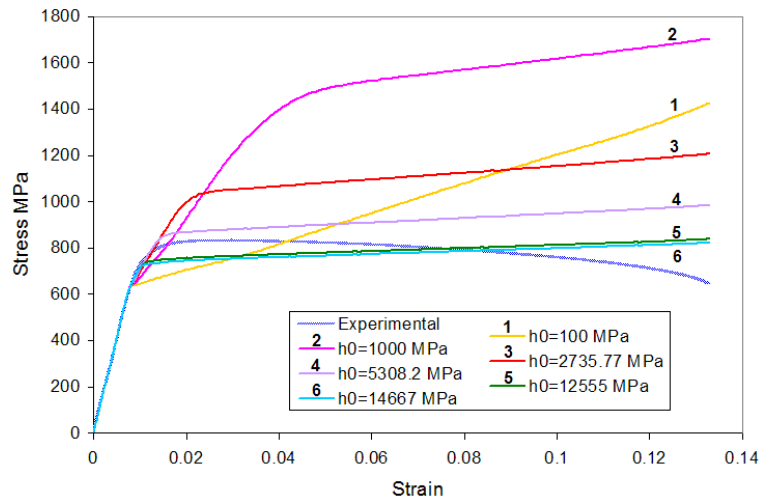


**Figure 7.15:** Experimental and numerical tensile tests with the crystalline plasticity constitutive law and Bassani and Wu's hardening for a strain rate of  $10^{-2} s^{-1}$  on 100%  $\beta$  Ti-5553 and for different values of the parameter  $h_0$ .

Observations: An increase in  $h_0$  leads to an increase in the slope at the yield point. An  $h_0$  value close to 8000 seems to be suitable.

\*) Influence of  $h_s$ 

Parameter	Value
$n$	50
$\dot{a}$	0.001
$h_0$	8000
$\tau_s$	304
$\tau_0$	300
$h_s$	vary
$\gamma_{0\alpha}$	0.001
$\gamma_{0\alpha\beta}$	0.001
$f_{\alpha\alpha}$	15
$f_{\alpha\beta}$	15

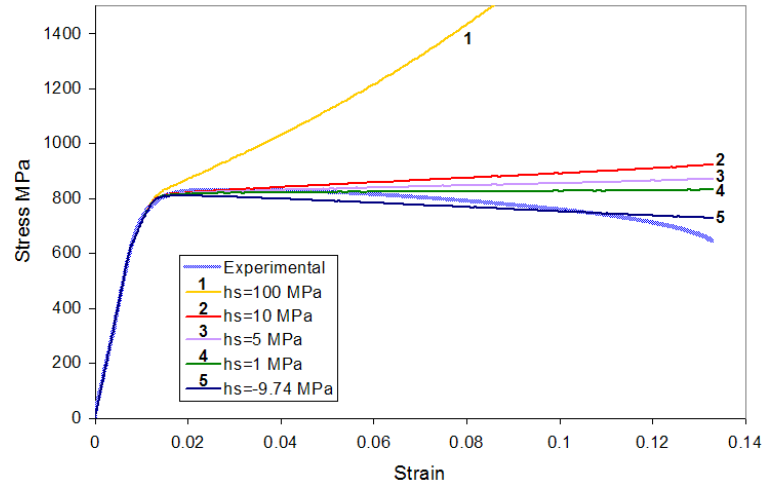


**Figure 7.16:** Experimental and numerical tensile tests with the crystalline plasticity constitutive law and Bassani and Wu's hardening for a strain rate of  $10^{-2} \text{ s}^{-1}$  on 100%  $\beta$  Ti-5553 and for different values of the parameter  $h_s$ .

Observations: An increase in  $h_s$  leads to an increase in the plastic modulus. A negative value of  $h_s$  models softening. An  $h_s$  value close to  $-9.74$  gives an acceptable plastic modulus.

\*) Influence of  $\gamma_{0\alpha}$ 

Parameter	Value
$n$	50
$\dot{a}$	0.001
$h_0$	8000
$\tau_s$	304
$\tau_0$	300
$h_s$	-9.74
$\gamma_{0\alpha}$	vary
$\gamma_{0\alpha\beta}$	0.001
$f_{\alpha\alpha}$	15
$f_{\alpha\beta}$	15

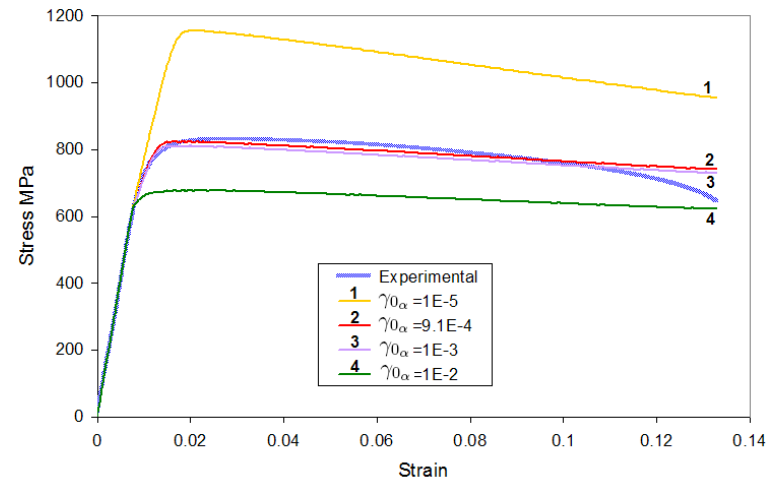


**Figure 7.17:** Experimental and numerical tensile tests with the crystalline plasticity constitutive law and Bassani and Wu's hardening for a strain rate of  $10^{-2} \text{ s}^{-1}$  on 100%  $\beta$  Ti-5553 and for different values of the parameter  $\gamma_{0\alpha}$ .

Observations: An increase in  $\gamma_{0\alpha}$  leads to curves at a lower level and a small value of  $\gamma_{0\alpha}$  increases softening. A  $\gamma_{0\alpha}$  value close to 0.00091 gives a more accurate result.

*Influence of  $\gamma_{0\alpha\beta}$* 

Parameter	Value
$n$	50
$\dot{a}$	0.001
$h_0$	8000
$\tau_s$	304
$\tau_0$	300
$h_s$	-9.74
$\gamma_{0\alpha}$	0.00091
$\gamma_{0\alpha\beta}$	vary
$f_{\alpha\alpha}$	15
$f_{\alpha\beta}$	15

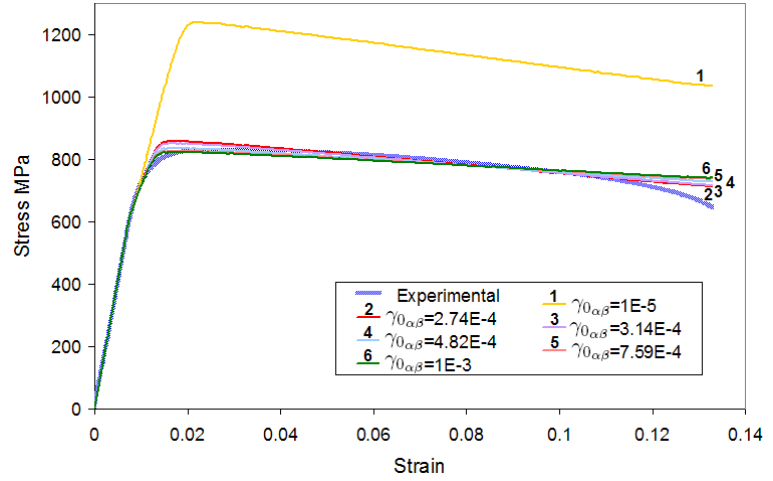


**Figure 7.18:** Experimental and numerical tensile tests with the crystalline plasticity constitutive law and Bassani and Wu's hardening for a strain rate of  $10^{-2} \text{ s}^{-1}$  on 100%  $\beta$  Ti-5553 and for different values of the parameter  $\gamma_{0\alpha\beta}$ .

Observations: An increase in  $\gamma_{0\alpha\beta}$  leads to curves at a lower level and a small value of  $\gamma_{0\alpha\beta}$  increases the amplification of softening. A  $\gamma_{0\alpha\beta}$  value close to 0.000314 gives a more accurate result.

*\*) Influence of  $f_{\alpha\alpha}$* 

Parameter	Value
$n$	50
$\dot{a}$	0.001
$h_0$	8000
$\tau_s$	304
$\tau_0$	300
$h_s$	-9.74
$\gamma_{0\alpha}$	0.00091
$\gamma_{0\alpha\beta}$	0.000314
$f_{\alpha\alpha}$	vary
$f_{\alpha\beta}$	15

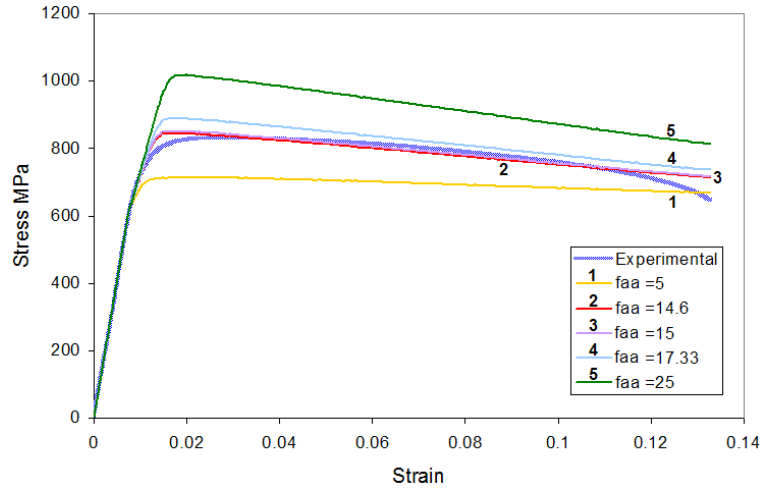


**Figure 7.19:** Experimental and numerical tensile tests with the crystalline plasticity constitutive law and Bassani and Wu's hardening for a strain rate of  $10^{-2} \text{ s}^{-1}$  on 100%  $\beta$  Ti-5553 and for different values of the parameter  $f_{\alpha\alpha}$ .

Observations: An increase in  $f_{\alpha\alpha}$  leads to more elevated curves. An  $f_{\alpha\alpha}$  value close to 14.6 gives a more accurate result.



\*) Influence of  $f_{\alpha\beta}$ 

Parameter	Value
$n$	50
$\dot{a}$	0.001
$h_0$	8000
$\tau_s$	304
$\tau_0$	300
$h_s$	-9.74
$\gamma_{0\alpha}$	0.00091
$\gamma_{0\alpha\beta}$	0.000314
$f_{\alpha\alpha}$	14.6
$f_{\alpha\beta}$	vary

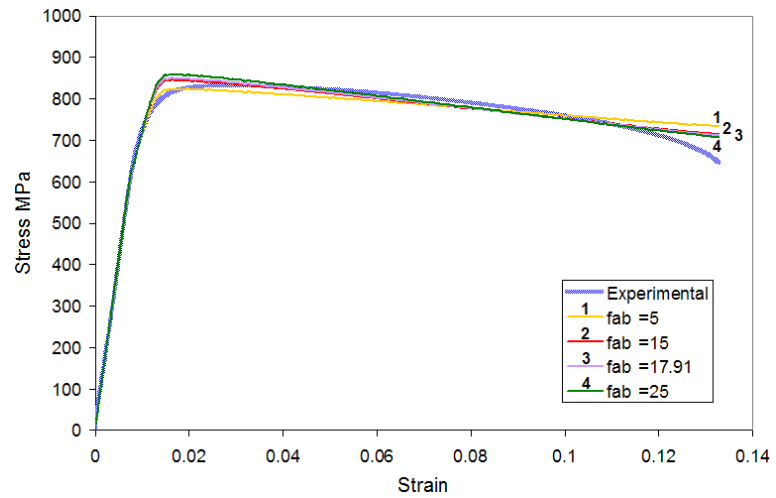


**Figure 7.20:** Experimental and numerical tensile tests with the crystalline plasticity constitutive law and Bassani and Wu's hardening for a strain rate of  $10^{-2} \text{ s}^{-1}$  on 100%  $\beta$  Ti-5553 and for different values of the parameter  $f_{\alpha\beta}$ .

Observations: An increase in  $f_{\alpha\beta}$  leads to higher curves at the yield point and a small amplification of the softening slope. The influence of this parameter is negligible.  $f_{\alpha\beta}$  close to 17.9 gives an acceptable result.

**Optimized parameters for the curve at  $10^{-2} \text{ s}^{-1}$** 

From results obtained in the last section, the optimized parameter set that models the experimental tensile curve at a strain rate of  $10^{-2} \text{ s}^{-1}$  is given in Figure (7.21). The corresponding numerical and experimental tensile curves are also provided.

Parameter	Value
$n$	50
$\dot{a}$	0.001
$h_0$	8000
$\tau_s$	304
$\tau_0$	300
$h_s$	-9.74
$\gamma_{0\alpha}$	0.00091
$\gamma_{0\alpha\beta}$	0.000314
$f_{\alpha\alpha}$	14.6
$f_{\alpha\beta}$	17.9

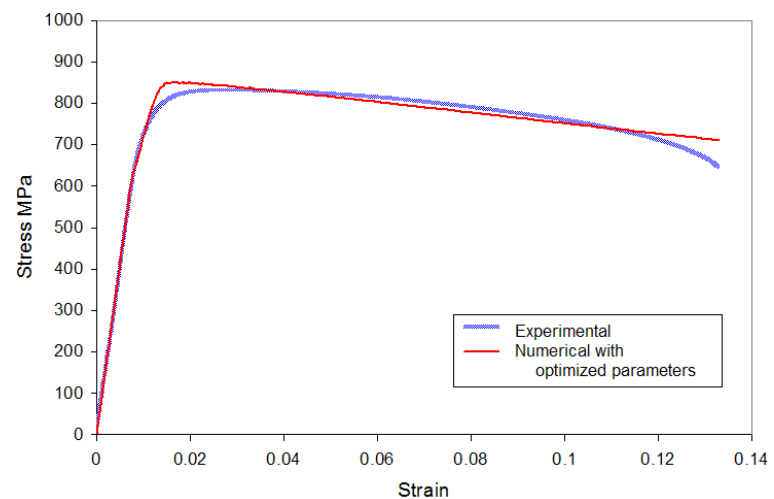


**Figure 7.21:** Experimental and numerical tensile tests with the crystalline plasticity constitutive law and Bassani and Wu's hardening for a strain rate of  $10^{-2} \text{ s}^{-1}$  on 100%  $\beta$  Ti-5553 and for optimized parameters.

Consequently, contrary to Pierce and Asaro's hardening, Bassani and Wu's hardening law can model the softening behavior of Ti-5553 that appears at high strain rates.

### Optimized parameters for all curves

In this paragraph, all curves have been optimized, taking the parameters given in Figure (7.21) into account. First, only the parameters  $h_0$  and  $h_s$  can be modified. From these results, an average value of  $h_0$  was deduced:  $h_0 = 7482$  MPa. A second optimization was then performed using this average value of  $h_0$  for all curves. Consequently, only the parameter  $h_s$  can change from one curve to another. The parameters are provided in Table (7.6) and the corresponding optimized curves are superimposed on experimental ones in Figure (7.22).

Parameter	Value	Strain rate	$h_s$
$n$	50		
$\dot{a}$	0.001		
$h_0$	7482	$10^{-2} (s^{-1})$	-7.42
$\tau_s$	304	$10^{-3} (s^{-1})$	1.019
$\tau_0$	300	$10^{-4} (s^{-1})$	3.8
$\gamma_{0\alpha}$	0.00091	$10^{-5} (s^{-1})$	6.6891
$\gamma_{0\alpha\beta}$	0.000314		
$f_{\alpha\alpha}$	14.6		
$f_{\alpha\beta}$	17.9		

**Table 7.6:** Optimized parameters for tensile tests performed at all strain rates.

The  $h_s$  evolution is given in Figure (7.23) as a function of the strain rate. The evolution of  $h_s$  is not far from a logarithmic progression.

#### 7.4.5 Modifications to optimize the $\beta$ phase

Due to the evolution of  $h_s$  with the strain rate close to a logarithmic progression, this modulus can be approached by an equation of the type:

$$h_s(\dot{\varepsilon}) = A \ln(\dot{\varepsilon}) + B \quad (7.9)$$

where  $A$  and  $B$  are the two constants to be determined (Figure (7.24)).

Consequently, the two new parameters used to simulate the  $\beta$  phase of Ti-5553 for all strain rates are

$$\begin{cases} A = -1.959 \\ B = -14.766 \end{cases} . \quad (7.10)$$

It seems acceptable to choose a logarithmic progression for  $h_s(\dot{\varepsilon})$ . As a result, such a formulation in the finite element simulations requires some modifications in the constitutive law subroutine. More details about these modifications can be found in Appendix (F).

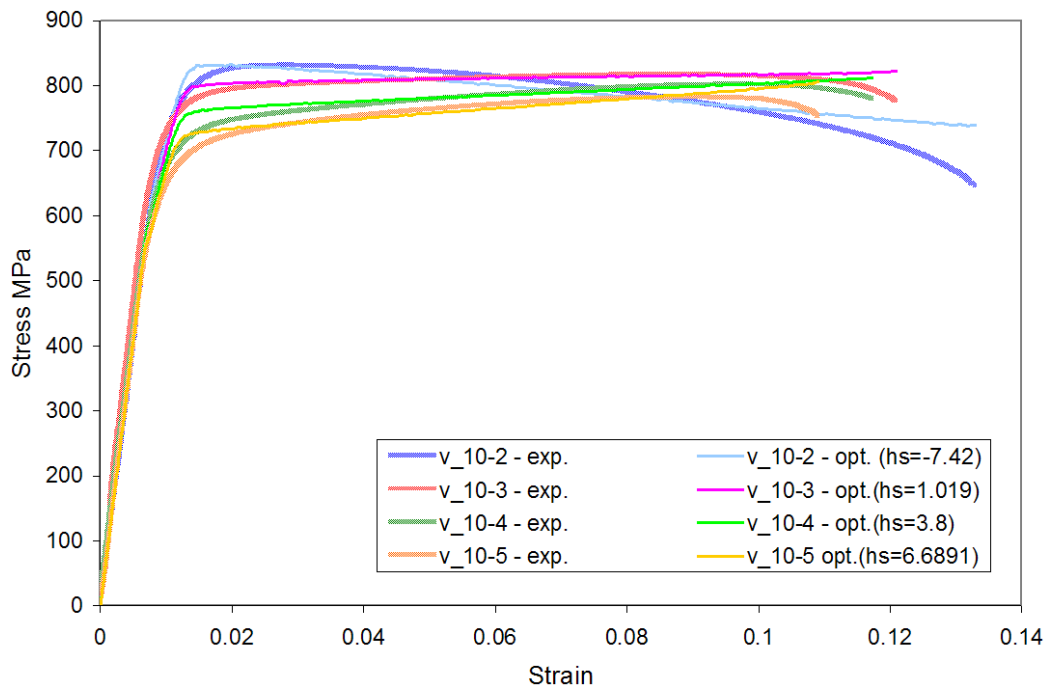


**Figure 7.22:** Experimental and numerical tensile stress versus strain curves with the crystalline plasticity constitutive law and Bassani and Wu's hardening for all strain rates on 100%  $\beta$  Ti-5553 and with the optimized parameters in Table (7.6). Except for  $h_s$ , all other parameters have the same value for each strain rate.

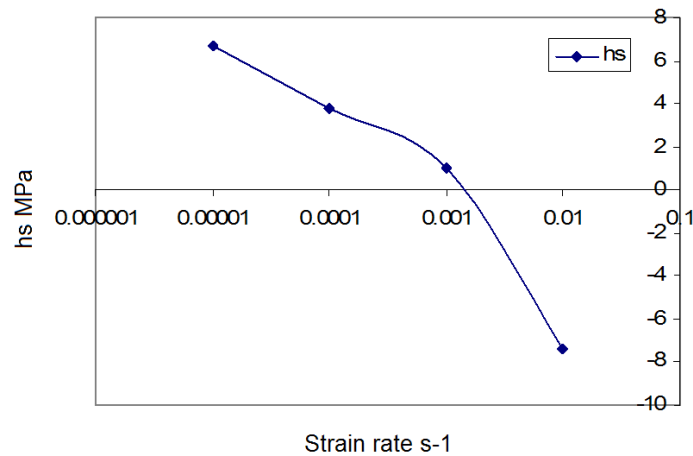


**Figure 7.23:** Evolution of the parameter  $h_s$  optimized for numerical tensile tests as a function of the strain rate of the test (logarithmic scale).

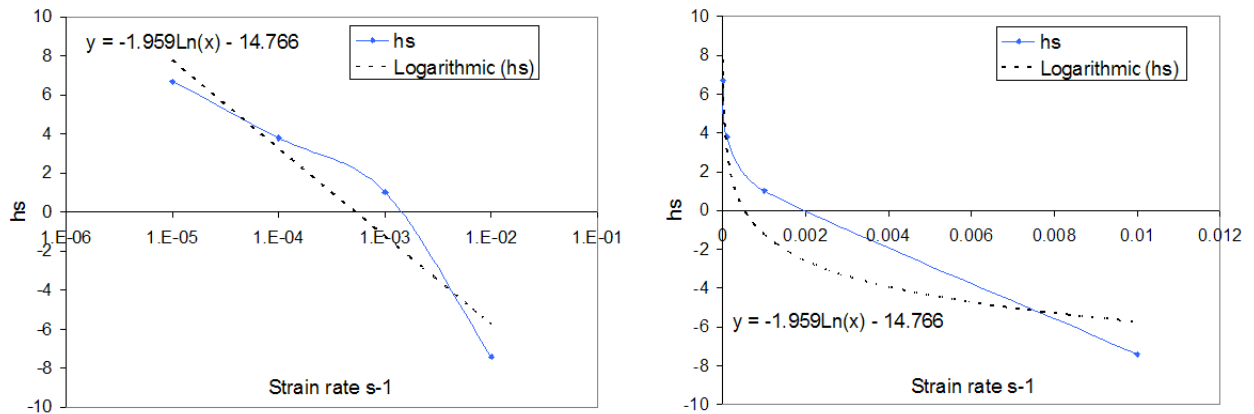


**Figure 7.24:** Identification of the parameters  $A$  and  $B$  from Eqn.(7.9) to simulate  $h_s$ 's evolution. (Left) logarithmic scale and (right) linear scale for the strain rate evolution. Blue dots  $h_s$  correspond to  $h_s$  parameters determined for curves separately identified and the discontinuous black line corresponds to a fit of these linked blue dots by a logarithmic progression.

#### 7.4.6 Tensile test modeling accounting for the evolution of $h_s$

The improvement of the constitutive law was tested on tensile tests with a mesh of one element<sup>8</sup>. Numerical results were then compared to experimental data.

As mentioned earlier, the strain rate cannot be constant during an experimental test, even if it was imposed. Thus, instead of assuming a constant strain rate during the simulation, the experimental rate was used. It was computed from the displacement versus time coordinates. An example of the numerical evolution of the strain rate is given in Figure (7.25) for the tensile test performed at a "constant" strain rate of  $10^{-2} s^{-1}$ . The corresponding  $h_s$  evolution is also given.

The parameters used to obtain the curves shown in Figure (7.26) with the crystalline constitutive law and an evolution law for the parameter  $h_s$  are given in Table (7.7).

$\Rightarrow$  *These results confirm the possibility of modeling the behavior of the  $\beta$  phase of Ti-5553 with only one set of parameters if Bassani and Wu's hardening is chosen with an  $h_s$  evolution.*

<sup>8</sup>The numerical tests were performed with one element and then one grain orientation. It will be shown in Chapter (9) that the grain orientation has very little influence. This result can be explained by the great number of slip systems that can be activated in a BCC material, which results in nearly isotropic behavior.

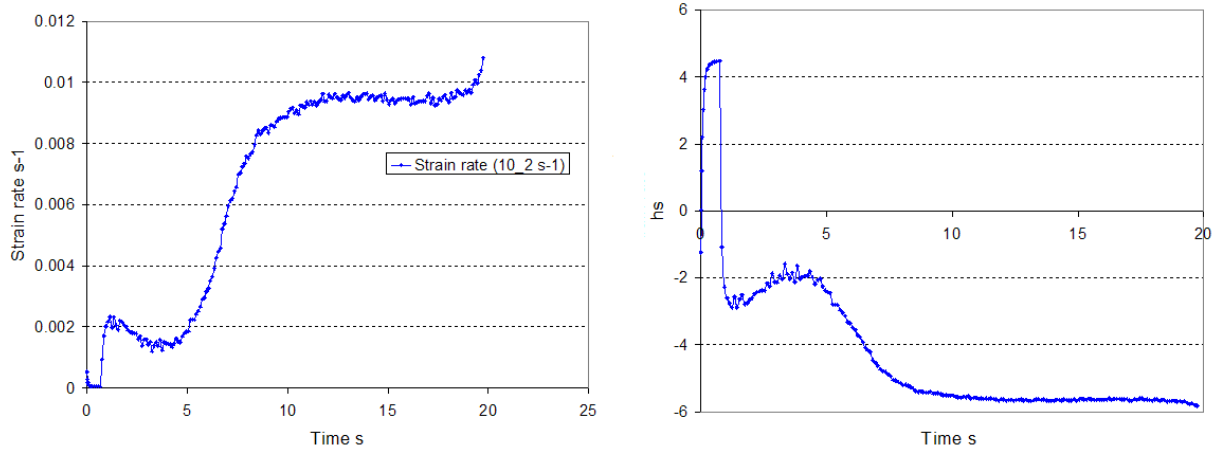


**Figure 7.25:** Tensile tests using the crystalline constitutive law with Bassani and Wu's hardening and  $h_s$  evolution. (left) Strain rate evolution during the test and (right) the corresponding  $h_s$  evolution.

Parameter	Value
$n$	50
$\dot{\alpha}$	0.001
$h_0$	7482
$\tau_s$	304
$\tau_0$	300
$\gamma_{0\alpha}$	0.00091
$\gamma_{0\alpha\beta}$	0.000314
$f_{\alpha\alpha}$	14.6
$f_{\alpha\beta}$	17.9
$A$	-1.959
$B$	-14.766

**Table 7.7:** Optimized parameters for tensile tests performed at all strain rates.

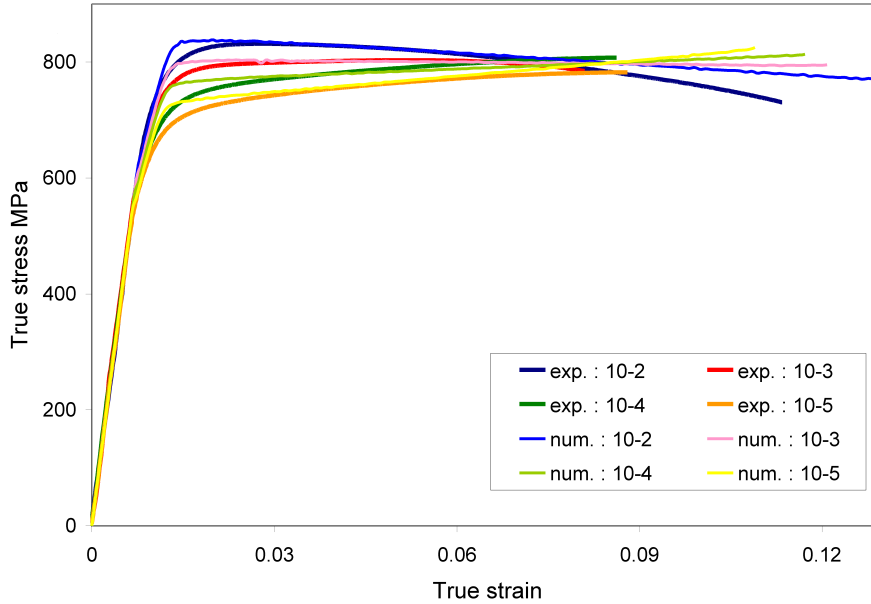


**Figure 7.26:** Tensile tests (at different strain rates) using the crystalline constitutive law with Bassani and Wu's hardening and  $h_s$  evolution. The experimental corresponding ones are superimposed. The parameters used are given in Table (7.7).

## 7.5 Conclusions

The goal of this chapter was to identify the  $\beta$  phase of Ti-5553 from experimental tensile tests performed at different strain rates on 100%  $\beta$  material (Figure (7.1)).

First, a macroscopic Norton-Hoff constitutive law was tested but this method was not successful. In fact, in the range of strain rates studied ( $10^{-5}$  to  $10^{-2} \text{ s}^{-1}$ ), it is not possible to model the behavior of this phase with only one set of parameters. Moreover, the modification of just one of these parameters with the strain rate does not fit all curves.

Secondly, an elastic-viscous-plastic crystalline plasticity-based constitutive law was chosen. It was found that the use of Asaro and Pierce's hardening law did not accurately model the  $\beta$  phase for all strain rates.

Finally, using the microscopic constitutive law with Bassani and Wu's hardening made possible the fitting of the four experimental tensile curves obtained at different strain rates with only one set of parameters. This was possible thanks to a modification in the constitutive law where one parameter ( $h_s$ ) can now vary with the strain rate. This enables the modeling of hardening or softening depending on the strain rate at which the test is performed.

## Chapter 8

# Experimental simple shear tests on Ti-5553 and numerical validation

### 8.1 Introduction

To complete the data set on Ti-5553, simple shear tests were performed on 100 %  $\beta$  and on ( $\alpha + \beta$ ) material.

In this chapter, these experimental shear tests carried out on  $\beta$  samples are presented. Numerical simulations of these tests are performed and the results obtained with Norton-Hoff's constitutive law and with a microscopic plasticity-based constitutive one are presented and discussed. Comparisons have been made with experiments.

Finally, experimental results obtained from shear tests performed on the 100 %  $\beta$  Ti-5553 and the ( $\alpha + \beta$ ) material are compared.

### 8.2 Experimental tests

#### 8.2.1 Experimental device

Experimental shear tests were performed using a bi-axial test machine [FRH05] linked to an Aramis optical measurement system (Figure (8.1)). The sample submitted to shear is presented in Figure (8.2).

For each test, the height between the jaws,  $h$ , is equal to 3 mm and is maintained at this value during the test. The thickness,  $e$ , is always approximately equal to 1.5 mm for these samples and the length,  $l$ , of the shearing zone is close to 30 mm.

#### 8.2.2 Experimental difficulties

In these experimental tests, different error sources are present. The most common ones are given below.

- The slip of the sample in the jaws and their margin.

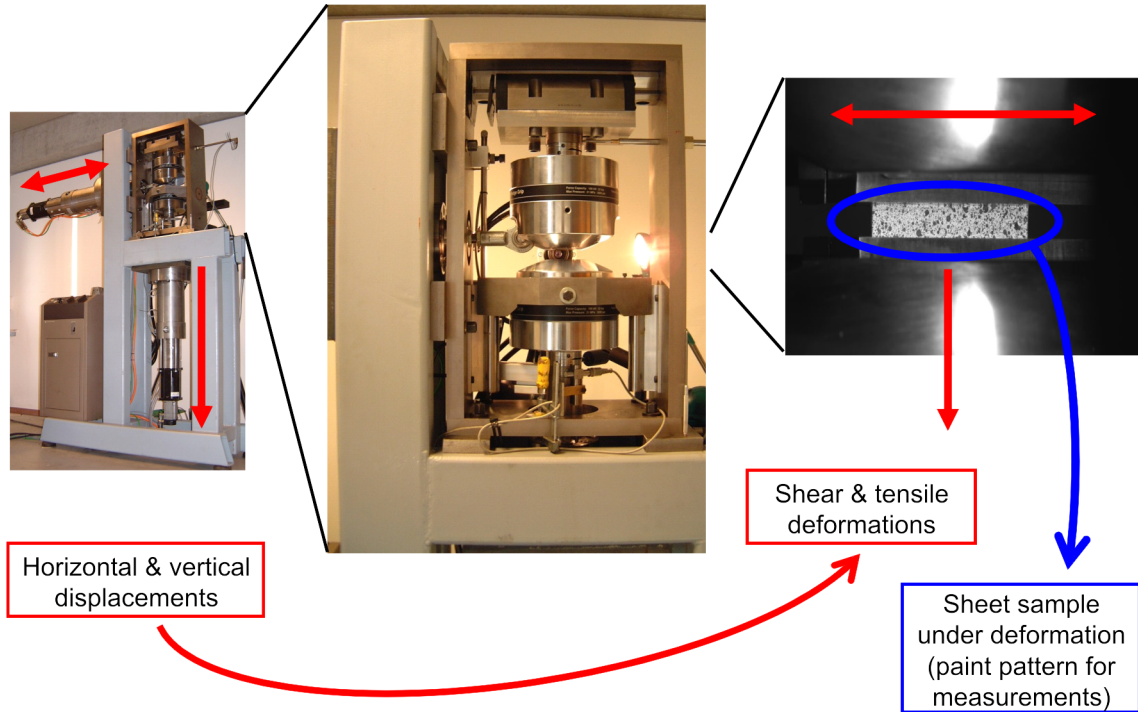


Figure 8.1: Bi-axial test machine used to perform simple shear tests.

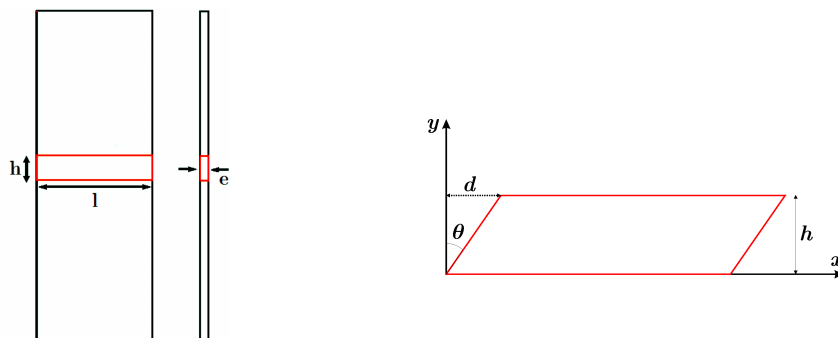


Figure 8.2: Sample submitted to shear. The shearing zone is in red. For these tests,  $h = 3$  mm,  $e = 1.5$  mm and  $l = 30$  mm. The shear strain  $\gamma = \frac{d}{h} = \tan(\theta)$ .



- Luminosity. For the optical measurement system, contrast has to be made by painting the sample. This must be correctly performed for accurate results. Moreover, the camera is not interdependent on the machine. Thus, errors of non-perfect parallelism between the camera and the sample can appear.
- The slight rotation or translation of the sample during the test can also lead to small errors.
- Finally, errors can come from the results analysis by the intermediate of the software.

### 8.2.3 Results

#### Images

An example of experimental results obtained with the optical measurement on 100%  $\beta$  material is presented in Figure (8.3).

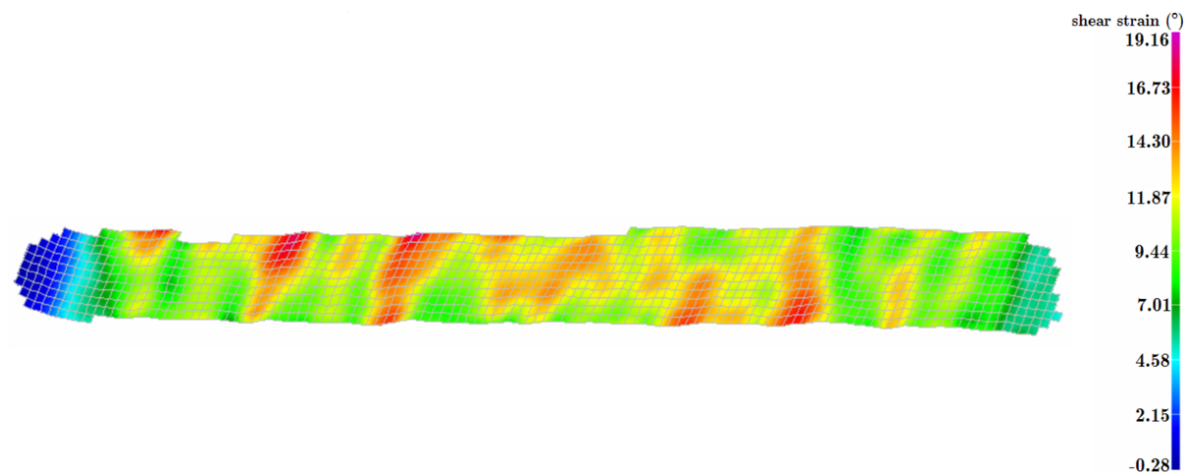


**Figure 8.3:** Shear strain in the material at the end of the shear test. Image from Aramis measurement.

The optical image of a specimen submitted to a shear test is shown in Figure (8.4) for the ( $\alpha + \beta$ ) material and in Figure (8.5) for the 100%  $\beta$  material. In Figure (8.4), the red rectangle encloses the part of the material that is submitted to shear. At the end of the test, the Aramis measure was superimposed on the experimental optical image after the test (Figure (8.4) right). Looking at this figure, it seems that the strain localization zones are linked to the  $\beta$  grains of the material. This observation will be discussed later.

For the 100%  $\beta$  material, the size of the grains is smaller (between 200 and 250  $\mu\text{m}$ ), as shown in Figure (8.5). However, the mechanical behavior is similar to the ( $\alpha + \beta$ ) material (localization zones). From *EBSD*<sup>1</sup> observations, it appears that the new  $\beta$  grains have similar orientations inside a same initial  $\beta$  grain of the material. Thus, there are some "macroscopic zones" with the same size and shape of the initial  $\beta$  grains in which the orientations of the

<sup>1</sup>EBSD = electron backscatter diffraction technique. Observations performed by N. Clement, UCL.

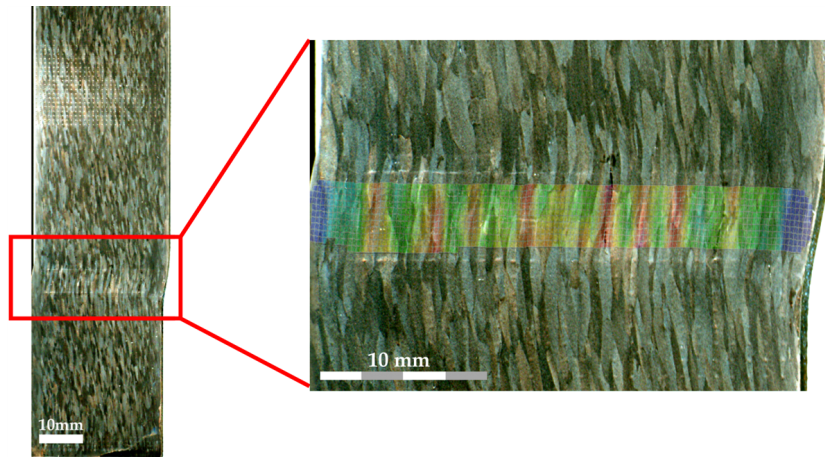


**Figure 8.4:** View of the shearing part of a specimen of  $(\alpha + \beta)$  Ti-5553, at the end of the shear test. On the right, optical image of the shear strain is superimposed on the experimental sheared specimen.

grains are nearly the same. In these zones, the grains deform together. This observation can explain the behavior of the 100%  $\beta$  material.

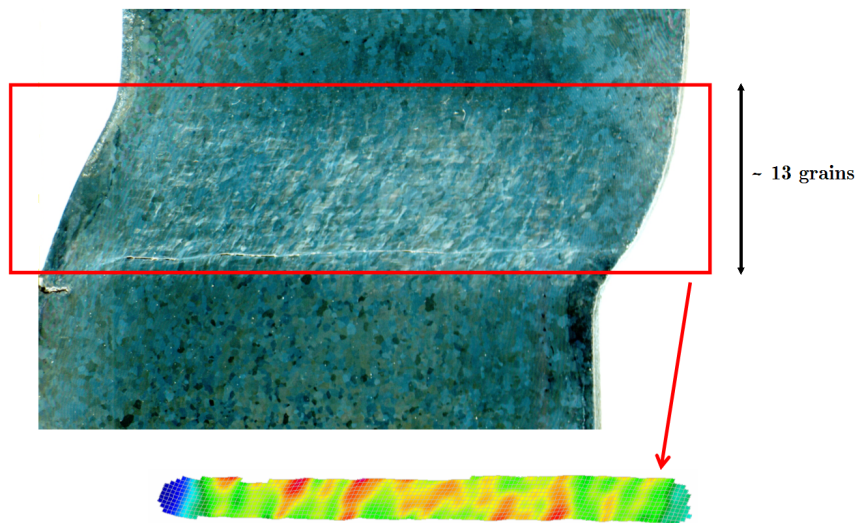


**Figure 8.5:** View of the shearing part of a specimen of 100%  $\beta$  Ti-5553, at the end of the shear test. On the right, optical image of the shear strain is superimposed on the experimental sheared specimen.

### Kinematic hardening

The experimental results of shear in one direction and then in the opposite direction are presented in Figure (8.7). The shear stress is drawn as a function of the shear strain in four different locations in the sample. Each of these results is taken along a horizontal line drawn in the middle of the sample. The locations in the specimen are shown in Figure (8.6).

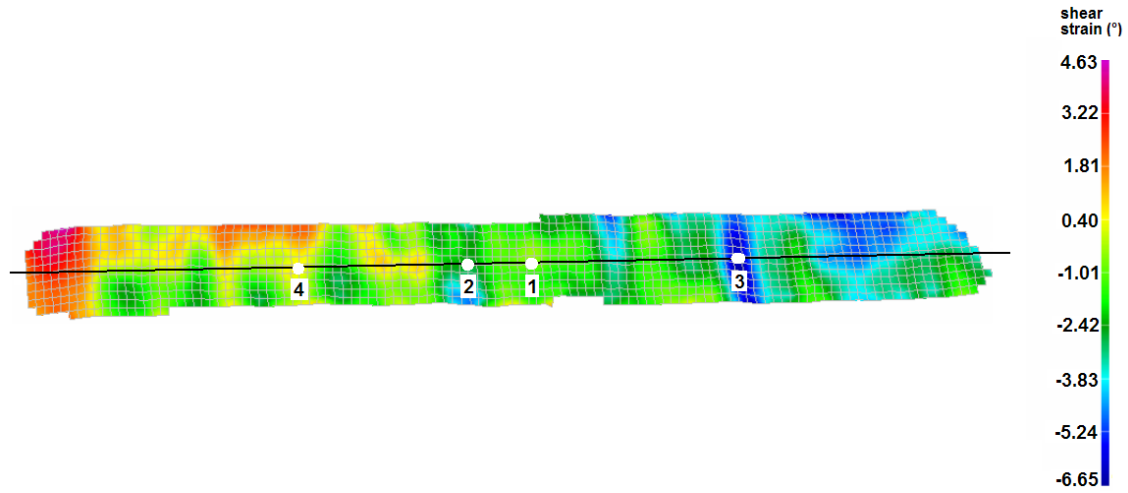


**Figure 8.6:** Shear strain in the material (100%  $\beta$ ) at the end of the shear test (shear in one direction and then in the opposite direction). Image from Aramis measurement. The location of the saved results are shown in the figure.

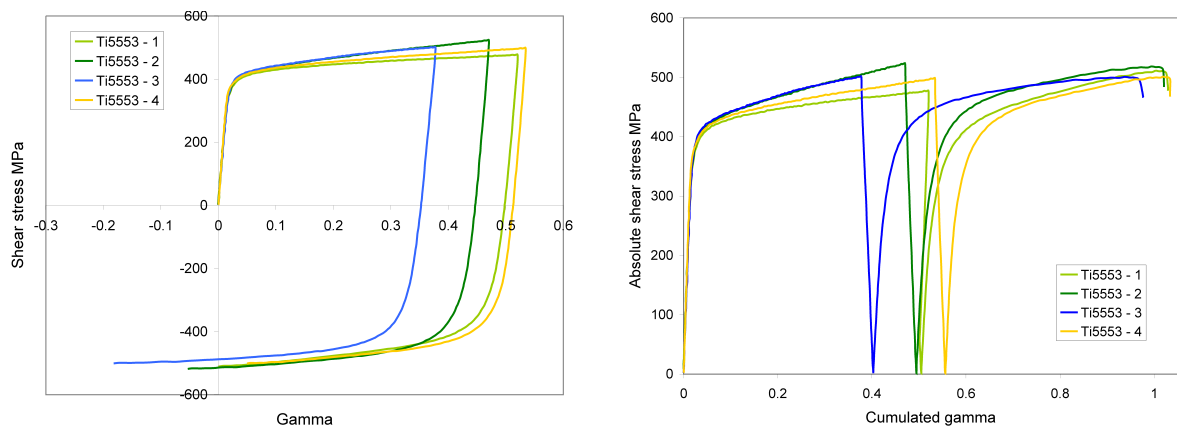


**Figure 8.7:** Shear stress during a shear test performed in one direction and then in the opposite one. On the right, the absolute value of the shear stress (of the same test as the left figure) is drawn as a function of the cumulated gamma, the strain in the shearing direction. The number of the curves correspond to results saved at different parts of the sample (shown in Figure (8.6)).

Looking at these figures, some kinematic hardening seems to be present but it is difficult to reach any conclusions due to the inhomogeneous aspect of the strain.

## 8.3 Numerical tests

### 8.3.1 Simulations with Norton-Hoff's constitutive law

#### A. Reminder

As described in Chapter (5) of Part (II), Norton-Hoff's constitutive law used can be written like this:

$$\bar{\sigma} = \bar{\varepsilon}^{p_4} \exp(-p_1 \bar{\varepsilon}) p_2 \sqrt{3} (\sqrt{3} \bar{\varepsilon})^{p_3} \quad (8.1)$$

with the 4 parameters  $p_1$ ,  $p_2$ ,  $p_3$  and  $p_4$ .

#### B. First set of parameters optimized

For tensile tests performed at  $10^{-4}$  and  $10^{-5} s^{-1}$ , the parameters optimized<sup>2</sup> (Table (7.2) of Chapter (7) in Part (III)) on experimental curves are repeated in Table (8.1):

$p_1$	$p_2$	$p_3$	$p_4$
2.140885	910.5649	0.014817	0.149774

**Table 8.1:** First set of Norton-Hoff's parameters.

Simulations of shear tests are performed with these parameters. The simulations begin at time  $t = 0$  until  $t = 535$  seconds. The final displacement is set to be 2.6 mm, as experimentally. Two meshes of 3D eight-node brick elements (BWD3D element, briefly described in Appendix (E)) were used to simulate this shear test. The first one contains 90 elements and the second one, 707 elements. Each mesh has only one layer of elements along the thickness. The lower face of the sample is fixed (horizontal and vertical displacements) and no vertical displacement of the upper face is allowed.

#### *Simulations with mesh 1 (90 3D elements)*

At the end of the simulation, the distribution of  $\sigma_{12}$  in the material sheared is presented in Figure (8.8). The same result obtained after smoothing of  $\sigma_{12}$  is shown in Figure (8.9).

#### *Simulations with mesh 2 (707 3D elements)*

After 432 seconds, corresponding to a displacement of 2.1 mm, the distribution of  $\sigma_{12}$  in the material is given in Figure (8.10).

<sup>2</sup>In this case, the parameter  $p_1$  is greater than zero, and then linked to softening. Physically, as shown in Figure (7.4), these strain rates imply small hardening and no softening.

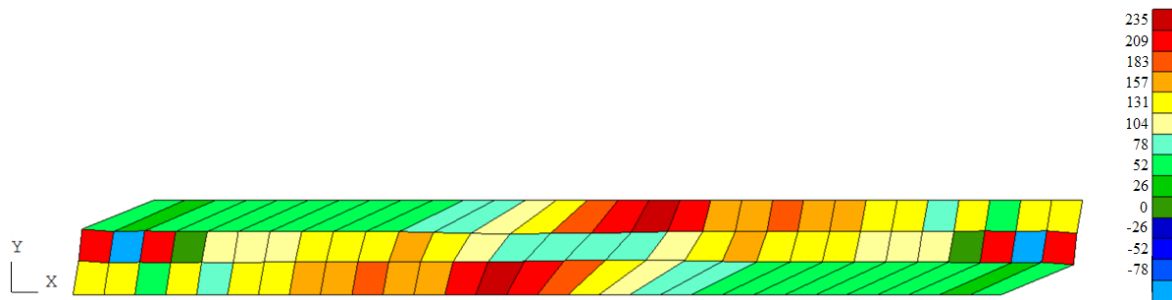


**Figure 8.8:** Numerical simulation of shear test with Norton (1st set of parameters) - 90 FE - Distribution of  $\sigma_{12}$  (MPa) in each element after a displacement of 2.6 mm.

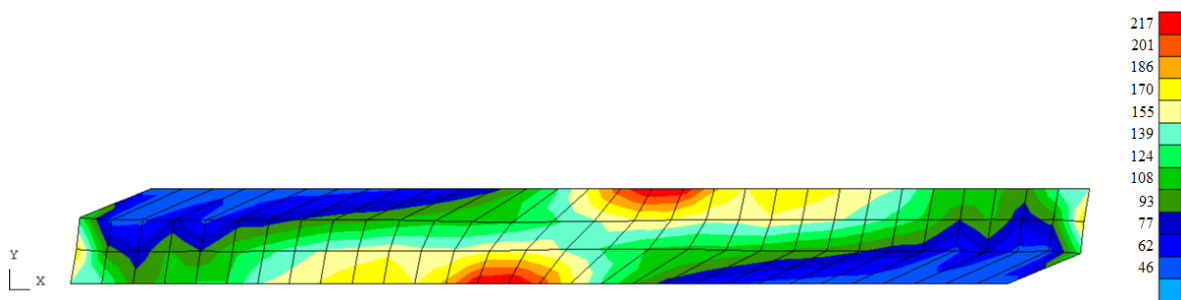


**Figure 8.9:** Numerical simulation of shear test with Norton (1st set of parameters) - 90 FE - Smoothed distribution of  $\sigma_{12}$  (MPa) in each element after a displacement of 2.6 mm.

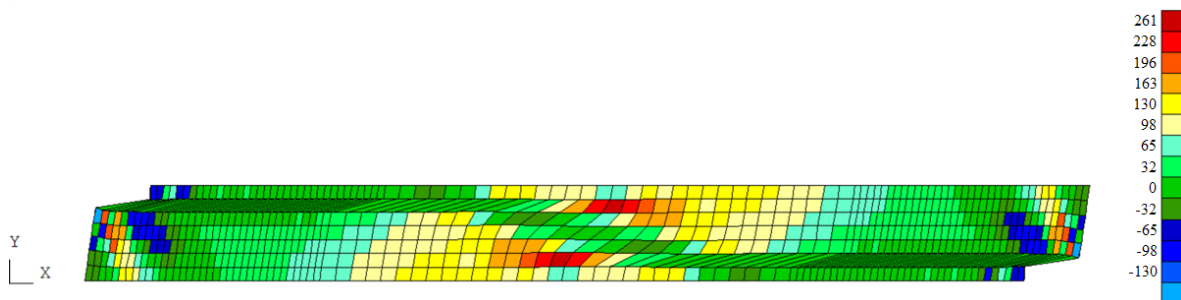


**Figure 8.10:** Numerical simulation of shear test with Norton (1st set of parameters) - 707 FE - Distribution of  $\sigma_{12}$  (MPa) in each element after a displacement of 2.1 mm.

From the results obtained with the two meshes, it is clear that Norton-Hoff's constitutive law with a softening parameter is not suitable to model the shearing behavior of this material. A strong localization of the shear strain appears connected to the mesh and not to any physical phenomenon. The shear distribution is significantly far from the one related to the grains (which is expected for a macroscopic model not modelling the grains) but also from any homogeneous strain distribution as observed when no softening exists (well known test, [Flo06]).

### C. Second set of parameters

For tensile tests performed at  $10^{-4}$  and  $10^{-5} s^{-1}$ , another set of parameters can be optimized, imposing  $p_1 = 0$  to avoid softening. The optimization was done using *Excel* optimizer. These parameters are presented in Table (8.2) and the corresponding curves are shown in Figure (8.11).

$p_1$	$p_2$	$p_3$	$p_4$
0.0	649.5	0.0153	0.07343

**Table 8.2:** Second set of Norton-Hoff's parameters.

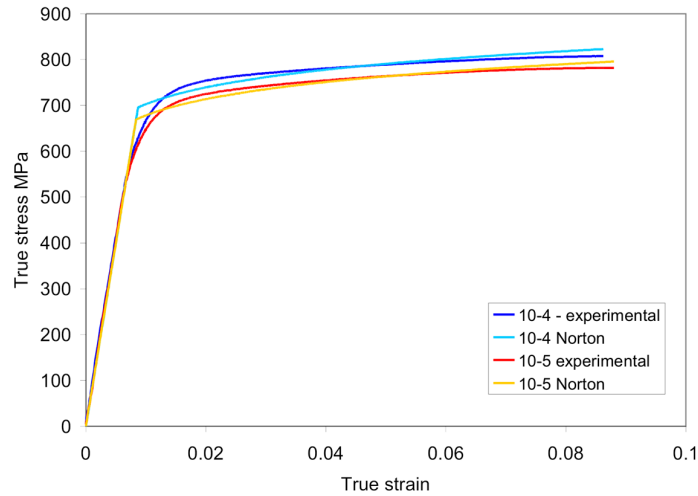


**Figure 8.11:** Tensile tests on Ti-5553 100%  $\beta$  - strain rate =  $10^{-4}$  and  $10^{-5} s^{-1}$ .

This set of parameters is more realistic from a physical point of view.

### *Simulations with mesh 1 (90 3D elements)*

For this simulation, the total time was 535 seconds for a final displacement of 2.6 mm. The results of the variable  $\sigma_{12}$  are given in Figure (8.12) without smoothing and in Figure (8.13) with smoothing.

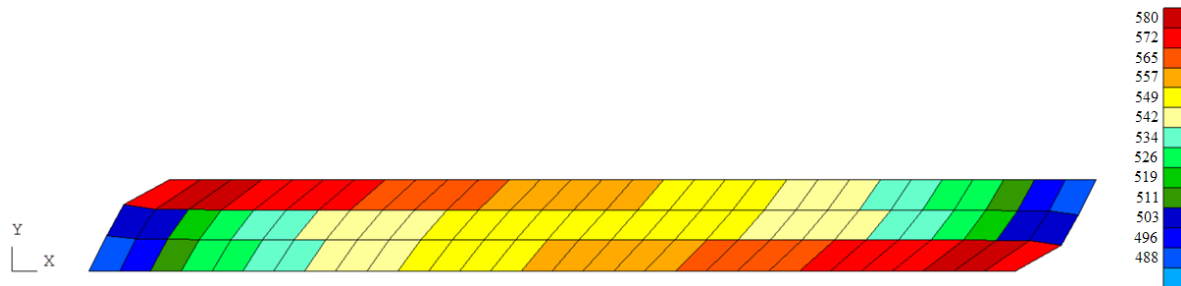


**Figure 8.12:** Numerical simulation of shear test with Norton (second set of parameters) - 90 FE - Distribution of  $\sigma_{12}$  (MPa) in each element after a displacement of 2.6 mm.

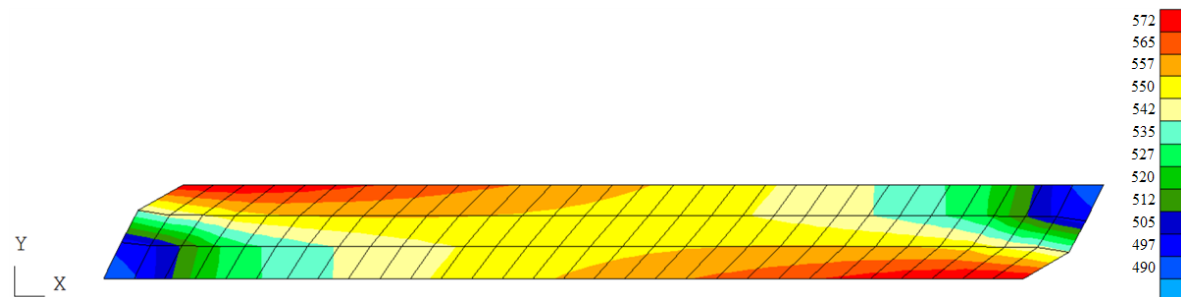


**Figure 8.13:** Numerical simulation of shear test with Norton (second set of parameters) - 90 FE - Distribution of  $\sigma_{12}$  (MPa) in each element after a displacement of 2.6 mm.

### Simulations with mesh 2 (707 3D elements)

For this simulation, the total time was 432 seconds for a final displacement of 2.1 mm. Results are given in Figure (8.14).



**Figure 8.14:** Numerical simulation of shear test with Norton (second set of parameters) - 707 FE - Distribution of  $\sigma_{12}$  (MPa) in each element after a displacement of 2.6 mm.

In conclusion, without softening, shear tests can be modelled by a fine mesh but without being able to see the localization of the shear strain according to the grains.

### 8.3.2 Crystal plasticity-based constitutive law for $\beta$ Ti-5553

Localization bands appear in the material during the experimental test, as shown in Figure (8.15) at the end of the simulation by the optical measurement system. The width of the localization zones seems to be linked to the size of the grains. Consequently, the goal now is to check the possibility of reproducing this experimental behavior, using the microscopic constitutive law presented in Chapter (4) of Part (II).

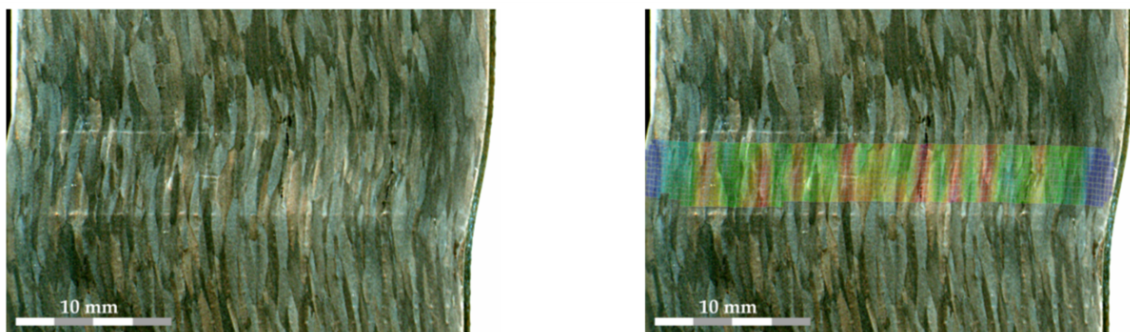


**Figure 8.15:** View of the shearing part of a Ti-5553 specimen, at the end of the shear test. On the right, optical image of the shear strain in a  $(\alpha + \beta)$  material is superimposed on the experimental specimen.

With this constitutive law, the orientation of the  $\beta$  grains can be taken into account. The



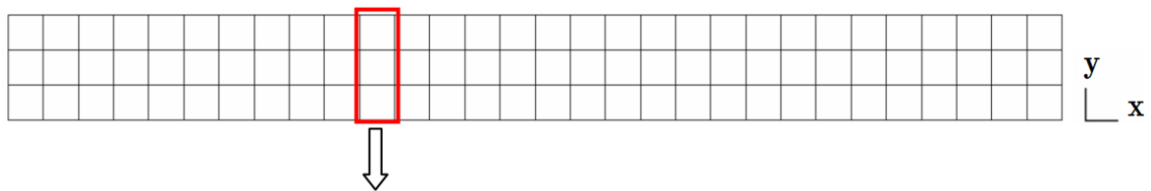
parameters used for this constitutive law (Table (8.3)) are those optimized<sup>3</sup> to model the  $\beta$  phase of Ti-5553 at all strain rates.

$n$	$\dot{a}$	$h_0$	$\tau_s$	$\tau_0$	$\gamma_{0\alpha\alpha}$	$\gamma_{0\alpha\beta}$	$f_{\alpha\alpha}$	$f_{\alpha\beta}$	$A$	$B$
50	0.001	7482	304	300	0.00091	0.000314	14.6	17.9	-1.959	-14.766

**Table 8.3:** Parameters of the microscopic constitutive law for  $\beta$  Ti-5553.

### Simulations with mesh 1 (90 3D elements)

The orientations of the elements were all similar but not exactly the same. The size of the grains (rectangular shape of the total specimen height) in the mesh is shown in Figure (8.16).



1 rectangle along the "x" direction = 1 grain ( $\sim 1$  mm wide, as experimentally)  
= 1 orientation

**Figure 8.16:** 90 FE mesh. "Definition" of the shape of the grains.

The orientations of the different grains of the sample were not measured before the tests. Consequently, in these simulations, random<sup>4</sup> orientations for the different grains were chosen instead of true ones.

With this mesh, the results are (after a displacement of 2.2 mm) shown in Figure (8.17) and in Figure (8.18).

<sup>3</sup>See Chapter (4) of Part (II) for more details about the constitutive law and the hardening law used. For the optimization of the parameters for the  $\beta$  phase of Ti-5553, see Chapter (7) of Part (III).

<sup>4</sup>A random orientation is chosen but without a great difference between the grains. These orientations are given in Appendix (G).

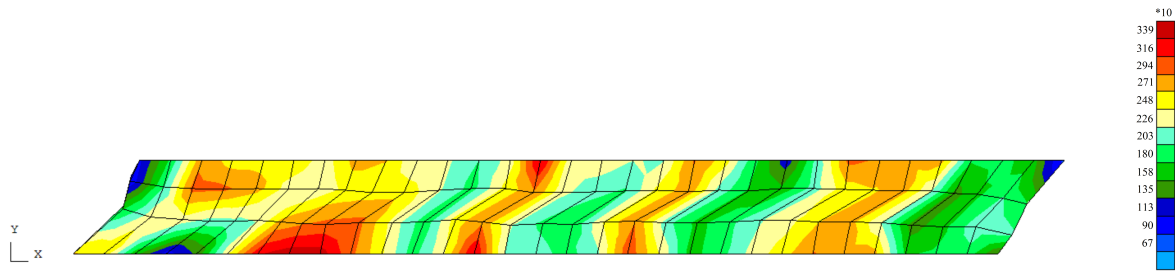


**Figure 8.17:** Numerical simulation of shear test with the microscopic constitutive law - 90 FE - Smoothed distribution of  $\sigma_{12}$  (MPa) in each element.

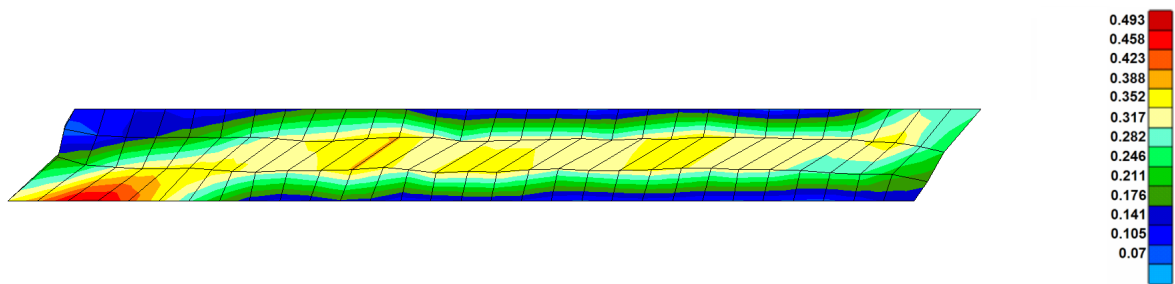


**Figure 8.18:** Numerical simulation of shear test with the microscopic constitutive law - 90 FE - Distribution of  $\epsilon_{12}$  in each element.

Thus, despite the use of hypothetical orientations of the grains in the material, localization bands normal to the direction of loading appeared. This result is qualitatively the same as the experimental one.

### *Simulations with mesh 2 (707 3D elements)*

The second mesh and the size of the grains are illustrated in Figure (8.19).

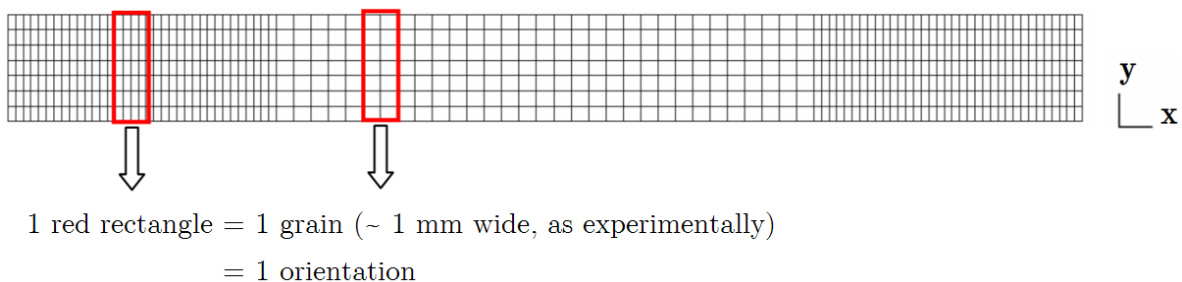


**Figure 8.19:** 707 FE mesh. "Definition" of the shape of the grains.

The numerical results are given in Figure (8.20), after a horizontal displacement of 1.8 mm. Also in this case, localization bands appear.

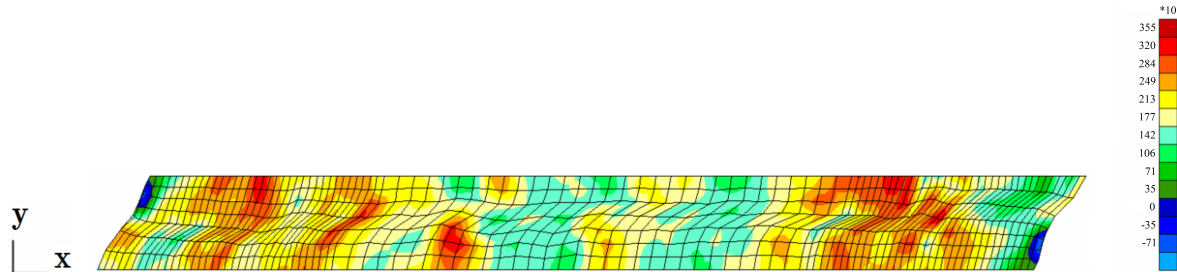


**Figure 8.20:** Numerical simulation of shear test with the microscopic constitutive law (second set of parameters) - 707 FE - Distribution of  $\sigma_{12}$  (MPa).

To refine the numerical results, experimental tests should be performed on samples for which the grain orientations have been measured. In this case, the true grain orientations can be imposed on the corresponding numerical elements associated with these grains. It was decided to perform such experimental tests with grain orientation measurements in the sample before and after the test and to simulate the corresponding shear tests numerically. However, due to time delay between each step of the experimental procedure (cut of the material, thermal treatments, manufacturing, measures and tests), it was not possible to obtain the data before the end of this work.

## 8.4 Comparison between the $\beta$ and $(\alpha + \beta)$ materials

Experimental shear test results on 100 %  $\beta$  material and on  $(\alpha + \beta)$  material will now be compared.

### 8.4.1 Reminder of the two microstructures

In the as-received material, both  $\alpha$  and  $\beta$  phases are present. The size of the  $\beta$  grains is of the order of the  $mm$ . For the  $\alpha$  phase, it is important to distinguish the globular  $\alpha$  ( $\sim 2 - 3 \mu m$ ) and the very small  $\alpha$  ( $\sim nm$ ) that are present everywhere. Here, for the  $(\alpha + \beta)$  material, a thermal treatment<sup>5</sup> was imposed to eliminate the minor  $\alpha$  precipitates. Consequently, the microstructure is composed of  $\beta$  and globular  $\alpha$  grains.

### 8.4.2 Stress versus strain results

The shear stress versus strain results are given in Figure (8.21) for the  $\beta$  material and in Figure (8.22) for the  $(\alpha + \beta)$  material.

<sup>5</sup>From the as-received material, a three hours annealing is performed at  $800^\circ C$ , followed by a water quench.

Due to the great heterogeneity of the results, each curve was obtained from an average of the values measured at different points of the material (see Section (8.2.3)). The first test was performed until fracture. The "till A" legend means that the test was performed until a point "A", near but before the fracture. The point "B" is another point (different from "A") also near the fracture. Finally, the term "return" means that the shear test was performed in one direction and then in the opposite direction.

In the figures, the appearance of the shear localization zones is mentioned. This appearance was detected by visual observation of the plots of the shear strains measured by Aramis when homogeneity was lost. For each, a picture of the distribution of the shear strain in the sample at the end of the test is also superimposed, showing once again the discrepancy of the values.

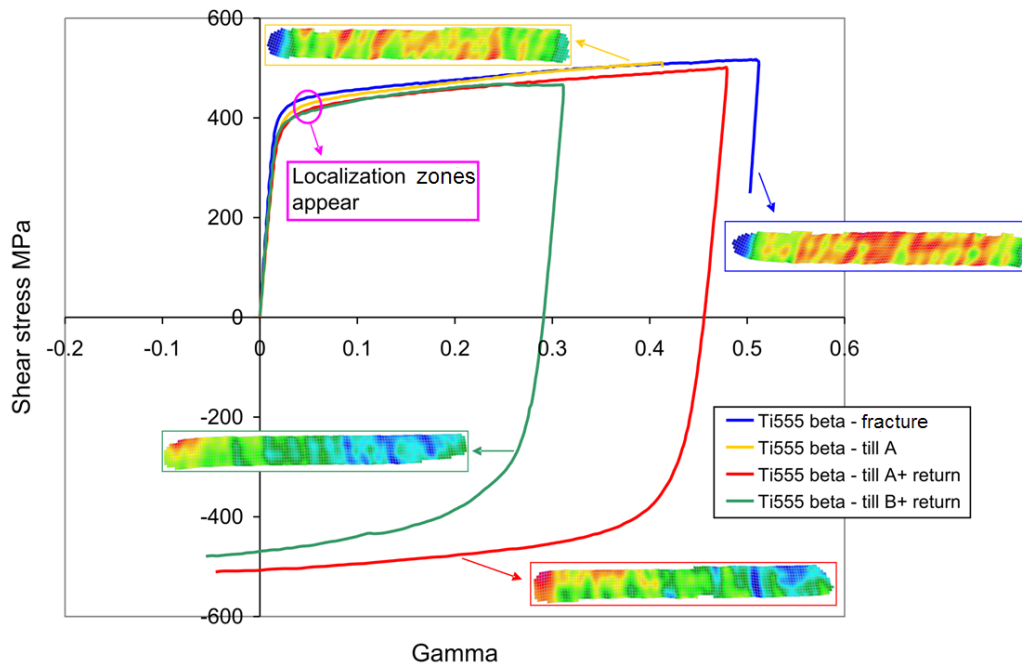


**Figure 8.21:** Experimental shear tests on the  $\beta$  material. Shear stress versus strain curves.

In Figure (8.23), the results obtained with the two materials are superimposed. For identical values of gamma, the  $(\alpha + \beta)$  curves have a shear stress approximately 10% greater than the  $\beta$  ones but in the former case the fracture happens earlier.

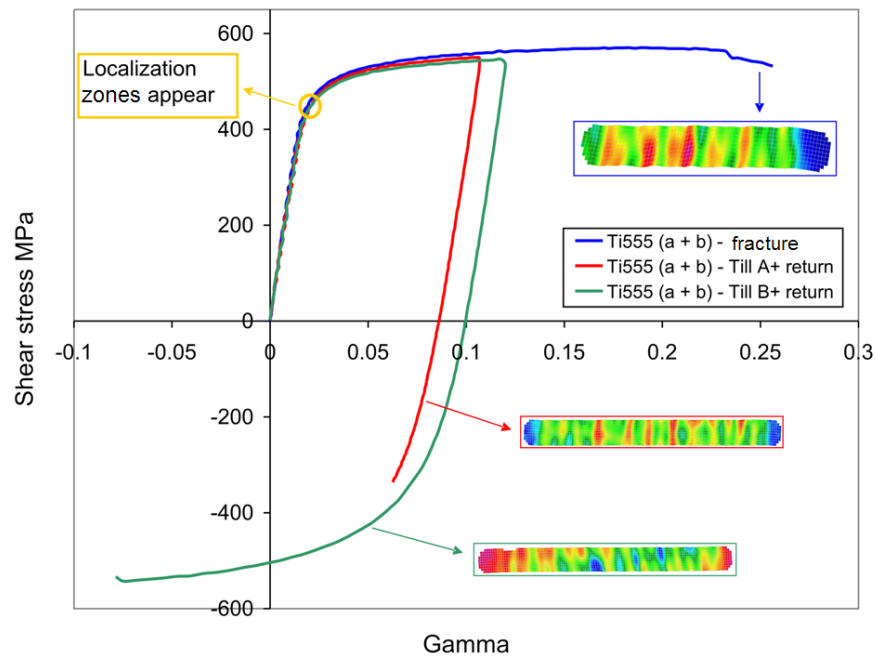


**Figure 8.22:** Experimental shear tests on the  $(\alpha + \beta)$  material. Shear stress versus shear strain curves.

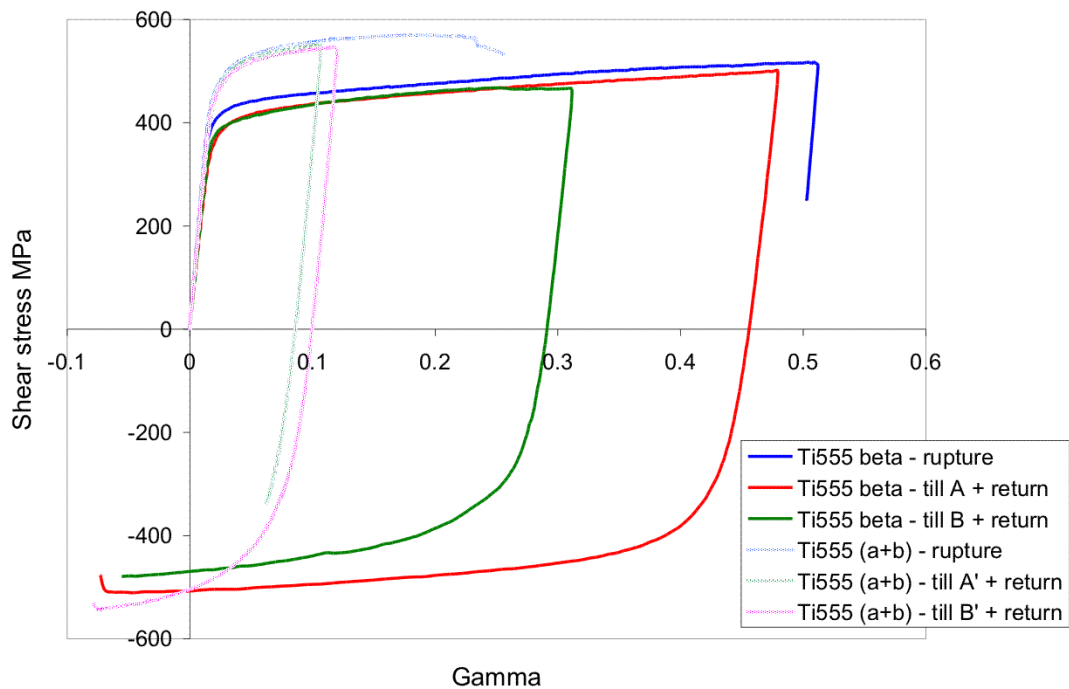


**Figure 8.23:** Experimental shear tests on  $\beta$  and  $(\alpha + \beta)$  materials. Shear stress versus shear strain.

### 8.4.3 Load versus displacement curves

The load versus displacement curves obtained in experimental shear tests on the two materials are superimposed in Figure (8.24).

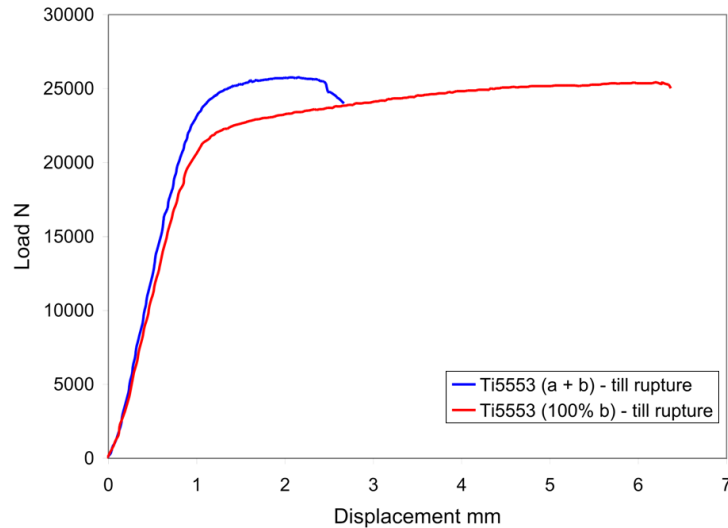


**Figure 8.24:** Experimental shear tests on  $\beta$  and  $(\alpha + \beta)$  materials. Load versus displacement curves.

The  $(\alpha + \beta)$  material had a higher maximum load but cracked earlier than the  $\beta$  material. This observation is the same as the one obtained from tensile tests performed on  $(\alpha + \beta)$  and 100%  $\beta$  materials. These tensile tests are provided in Figure (8.25) for different strain rates ( $\dot{\epsilon} = 10^{-5} s^{-1}$  until  $10^{-2} s^{-1}$ ).

The qualitative behavior is the same for tensile and simple shear tests: the  $(\alpha + \beta)$  material had a higher yield stress but cracked earlier than the  $\beta$  material. In practice, the  $(\alpha + \beta)$  material is not the same in each case. For the tensile test, the  $(\alpha + \beta)$  material was the as-received one. For the shear test, a thermal treatment was imposed on the material to avoid the small  $\alpha$  precipitates that have a hardening effect.

## 8.5 Conclusions

This chapter presented experimental simple shear tests on 100%  $\beta$  Ti-5553 and their numerical modeling. These tests have shown a particular behavior. In fact, in all experiments, localization bands appear, perpendicular to the shearing direction.

First, a macroscopic Norton-Hoff's law was applied to model this behavior. However, as was the case for tensile tests, this constitutive law is not sufficient to model this material correctly. With such a law, it is not possible to see the localization bands that appear in the experimental shear tests.

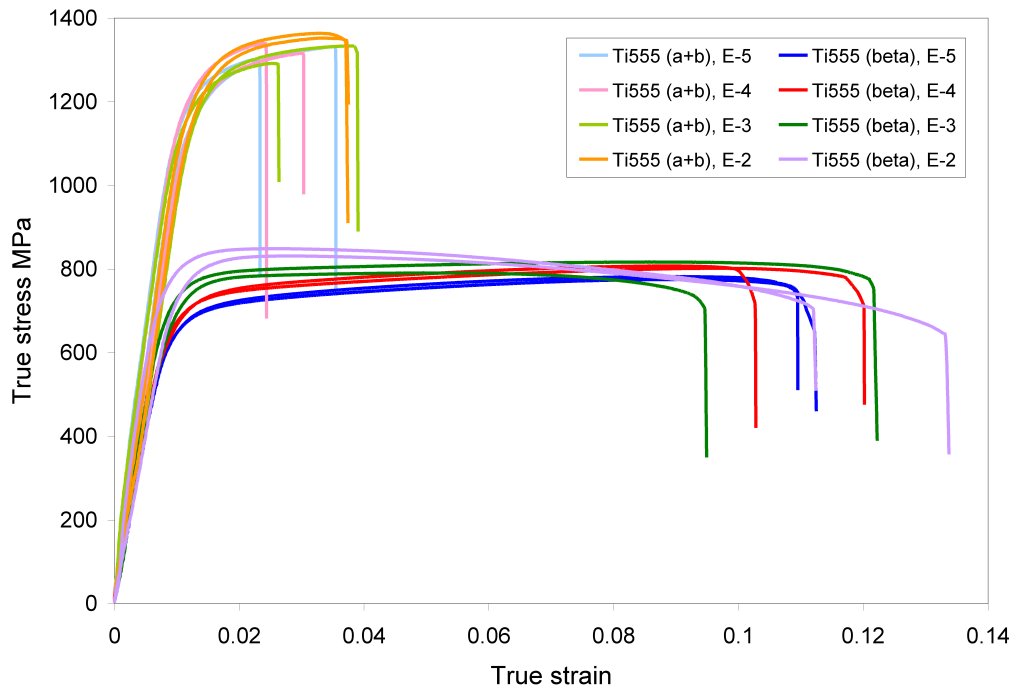


**Figure 8.25:** Experimental tensile tests on the tempered (100%  $\beta$ ) and the as-received ( $\alpha + \beta$ ) materials at different strain rates ranging from  $\dot{\epsilon} = 10^{-5} \text{ s}^{-1}$  until  $10^{-2} \text{ s}^{-1}$ . True stress versus true strain curves. Each test was performed twice.

Secondly, the crystalline plasticity-based constitutive law was applied. In this case, localization bands could appear, similar to experimental tests. Results obtained were only qualitative due to the lack of experimental measurement of the grain orientations before and after the shearing tests.

Finally, a comparison between experimental shear tests performed in the ( $\alpha + \beta$ ) and in the 100%  $\beta$  materials shows that the ( $\alpha + \beta$ ) material is less ductile and has a higher yield stress than the 100%  $\beta$  one.





## Chapter 9

# Limitations and interest of nanoindentation for bulk multiphase material identification. Application on $\beta$ phase of Ti-5553.

### 9.1 Introduction

Nanoindentation is a widely used technique to measure the mechanical properties of thin films [LN06], [CV01] and small volumes of materials [Pel05] [WRKR04], [LGS<sup>+</sup>96], [HP07].

For a long time, nanoindentation has been used to determine Young's modulus ( $E$ ) and hardness ( $H$ ) of materials. Some authors [SN02], [CV01], [CLZ<sup>+</sup>07] present methods based on the *Doerner and Nix* [DN86] and *Oliver and Pharr* [OP92] studies to extract  $E$  and  $H$  from the unloading part of the nanoindentation curve. These methods are briefly described in Appendix (L).

Nowadays, with the utilization of finite element methods, nanoindentation can also be used to identify other parameters of the material studied. This is the case of [SYFT04], who performs inverse modeling on load versus displacement curves to identify elastic orthotropic parameters ( $E_1$  and  $\nu_{12}$  along the thickness and  $E_2$ ,  $\nu_{22}$  for the surface plane) of films. [YKC07] also uses inverse modeling of the indentation curve, in order to determine plastic parameters of the material (the yield stress ( $\sigma_y$ ) and the strain sensitivity parameter ( $n$ )). [LWY<sup>+</sup>05] focuses on using nanoindentation and inverse modeling to obtain stress versus strain relations of thin films. [Pel05] identifies equations for the loading and unloading parts of the nanoindentation load versus displacement curve and then, uses it to identify the elastic and plastic parameters of the material ( $E$ ,  $\nu$ ,  $E_T$ ,  $n$ , ...).

Many authors have performed finite element simulations of nanoindentation with 2D axisymmetric meshes and a simple elastic-plastic constitutive law [MP06], [PKCM00], [YKC07], [XL08]. This formulation is sufficient for the identification of usual parameters of the material. However, to study the influence of other parameters, such as grain orientation, this methodology is not sufficient. A 3-D FE mesh is necessary and a crystalline plasticity law is needed. Such a law is presented and used for copper single crystal in [WRKR04]. These authors work on the dependence of nanoindentation pile-up patterns and micro textures on the crystallographic orientation. [ZRS<sup>+</sup>06] studies the microstructure and texture below a

conical indenter. An approach incorporating a mesoplastic constitutive model to determine the material properties of copper single crystal was developed by [LWY<sup>+</sup>05].

Nanoindentation experiments have been physically studied by several authors. The grain size of the material affects the results. It is observed by [MP06] that the grain size has a high effect on  $H$  measurements, and [LN06] demonstrates that the results are different when the material is constituted of large coarse grains or finer ones.

The orientation of the grain affects the hardness  $H$  but also the number of pile-ups and their symmetries as presented by [WRKR04] for copper. Moreover, [LVM<sup>+</sup>08] mentions that the symmetry characteristics and the size of the plastic zone depend strongly on the crystal orientation.

Some authors have tried to predict the appearance of pile-up or sink-in patterns near the indented imprint. [CV01], [ZRS<sup>+</sup>06], [FM05], [CLZ<sup>+</sup>07] relate the appearance of pile-up and sink-in patterns to hardening properties. For [LWY<sup>+</sup>05], the amount of pile-up is greater when the radius of the spherical indenter used is larger but, for [WRKR04], the prediction of pile-up or sink-in patterns is not so obvious. According to this article, they are due to the crystallography and the orientation of the grain indented. In one article, [ACO08], the numerical appearance of pile-up or sink-in patterns around the contact boundary is linked to the hardening description assumed in the crystal plasticity model.

Friction also affects the appearance of pile-up or sink-in patterns. Indeed, as mentioned by [BSFM03], [LWY<sup>+</sup>05] and [BBM05], when the friction coefficient is greater, the height of the pile-up patterns decreases.

Even though the friction influences the patterns near the indented imprint, this coefficient is generally considered to be "zero" by many authors. In fact, friction does not significantly affect the nanoindentation load versus displacement curves. This result is observed by [LWY<sup>+</sup>05] and by [WRKR04] for a range of friction coefficients that go from 0 to 0.3 or 0.4.

[Tab51] physically explains this result. He proposes an analytical model to describe the evolution of the normal force as a function of the included angle of the indenter tip (see figure (9.1)) and the friction coefficient, for a conical indenter<sup>1</sup>. The contact pressure,  $p$ , is assumed to be constant at the interface and independent of the shape of the indenter. The shear stress,  $\tau$ , is equal to  $\mu p$ , where  $\mu$  is Coulomb's friction coefficient that models the friction between the indenter and the surface of the material. The normal force  $F$  is equal to

$$F = \pi p R_c^2 \left( 1 + \frac{\mu}{\tan(\theta)} \right) \quad (9.1)$$

where  $R_c$  is the contact radius and  $\theta$  is the included angle, as shown in Figure (9.1). From this equation, it is clear that the friction term is always negligible with respect to "1" if the included angle is sufficiently high. Thus, the effect of friction is small for indenters with a large angle (like Berkovich and Vickers) but this effect is more significant when the angle,  $\theta$ ,

<sup>1</sup>More details about the effect of the friction coefficient on nanoindentation load versus displacement results are given in Appendix (I).

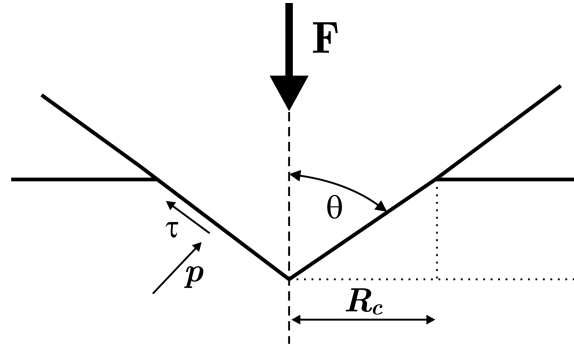


**Figure 9.1:** Schematic drawing of a conical indentation.  $\tau$  and  $p$  represent the tangential and normal stresses, respectively, at each contact point.

of the indenter is less than  $60^\circ$ . This result is also reported by [KSM<sup>+</sup>07] and [BSFM03].

To compare experimental and corresponding numerical nanoindentation results, it is important to reflect the experimental problem accurately in numerical simulations. Indeed, the geometry of the indenter tip must be rigorously reproduced because it has a high effect on  $H$  measurements, as depicted by [MP06], and it significantly affects the load versus displacement results. On the micro- or nanoscale, the finite (albeit minuscule) tip radius of a real sharp tip cannot be neglected [GCD<sup>+</sup>07]. [YKC07] shows that an increase in the included angle leads to an increase in the maximum force obtained for the same indentation depth. Note that, as mentioned above, [LWY<sup>+</sup>05] finds a larger pile-up for a greater included angle.

Similarly, the curvature of the tip must be accurate. [PKCM00] shows that the numerical modeling of the curvature of the indenter tip has an influence on load versus displacement curves. He finds that a more realistic modeling of that curvature leads to results in better agreement with experimental ones.

In several finite element nanoindentation curves, some bumps occur. [LWY<sup>+</sup>05] observes that the curve oscillations are more present and pronounced for simulations carried out with a coarser mesh. This observation, also mentioned by [BBM05], can be explained by the finite element contact model. A smoother curve is obtained with a finer mesh. Consequently, the choice of the mesh is still a compromise between accuracy and calculation cost.

The goal of this chapter is to determine the material parameters and the geometrical choices that must be known to a high degree of accuracy in order to simulate the nanoindentation experimental tests performed in the  $\beta$  phase of Ti-5553 as well as possible. Moreover, the set of material parameters optimized for the  $\beta$  phase in the above chapters will be validated by these simulations.

In the next section, the experimental nanoindentation tests are briefly described. Afterwards, numerical aspects are introduced. The constitutive laws and the meshes used for nanoindentation numerical modeling are briefly presented. In the last section, the results of the sensitivity analysis are presented. The reference parameters used to perform the numerical simulations

are those optimized for the BCC  $\beta$  phase of the Ti-5553 alloy. Parameters such as the geometrical, elastic or plastic ones are studied. The results are commented on and compared with experimental ones and with results obtained by other authors on this subject.

## 9.2 Nanoindentation experimental tests

### 9.2.1 Principle

The nanoindentation principle is depicted in Figure (9.2). A diamond indenter is fixed to a support that can move vertically. Once the indenter has made contact with the specimen surface, it gradually penetrates into the surface of the sample and then, the tip is removed.

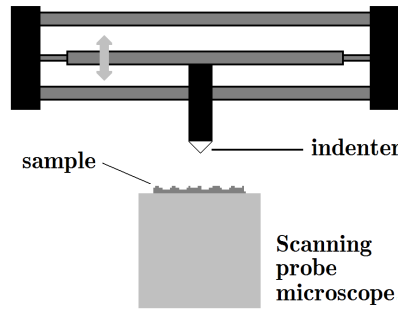


**Figure 9.2:** Nanoindentation principle.

During the test, the indentation load and the penetration depth into the material are simultaneously recorded and a load versus penetration depth curve can be plotted, as shown in Figure (9.3). The imprint of the indenter in the sample can be analyzed using microscopy techniques.

The experimental nanoindentation tests used in this thesis were performed by N. Clement<sup>2</sup> using a three-sided diamond Berkovich pyramidal indenter tip (Figure (9.5)). The total included angle of such a tip is equal to  $142.3^\circ$ , as shown in Figure (9.4).

As mentioned by several authors such as [PKCM00] and [YKC07], indentations using a Berkovich indenter result in the same force versus displacement curve as a conical indenter with a half apex angle  $\theta = 70.3^\circ$ . This is the reason why several authors prefer to simplify numerical modeling using a 2D axisymmetric mesh with a conical indenter instead of a 3D Berkovich one. However, this approximation does not permit researchers to study the influence of the grain orientation indented, for example.

In the simulations, the indenter is modeled as a rigid tool. This is justified because the diamond indenter has a Young's modulus of about 1000 GPa [LVM<sup>+</sup>08], [BSM08], an order higher than Ti-5553, for which the Young's moduli are in the range of 80 GPa for the  $\beta$  phase and 115 – 125 GPa for the  $\alpha$  phase.

<sup>2</sup>N. Clement from IMAP department, UCL.

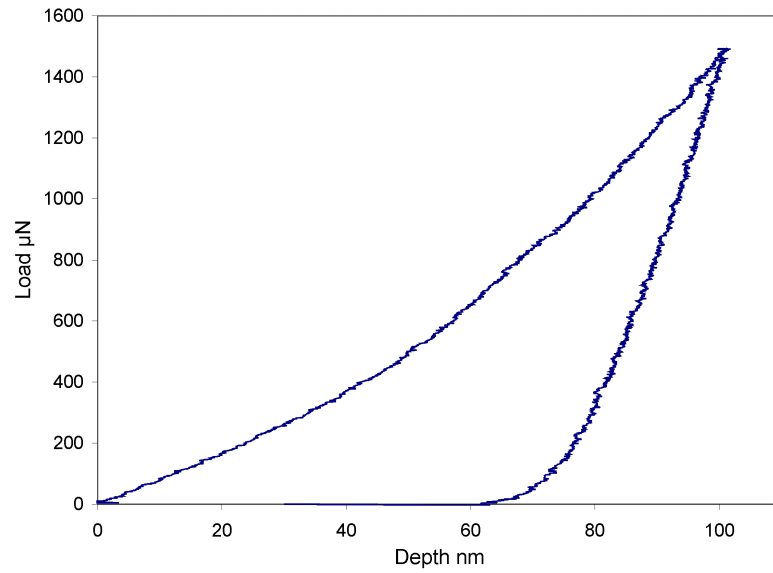


**Figure 9.3:** Experimental load versus displacement nanoindentation curve. Example of a test performed in a  $\beta$  grain.

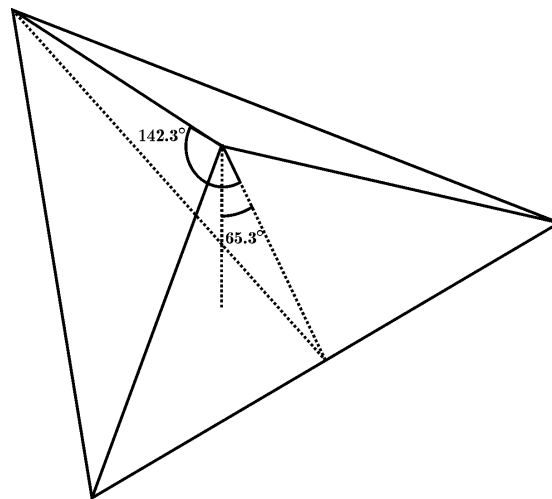


**Figure 9.4:** Three-sided Berkovich indenter tip. Included angle.

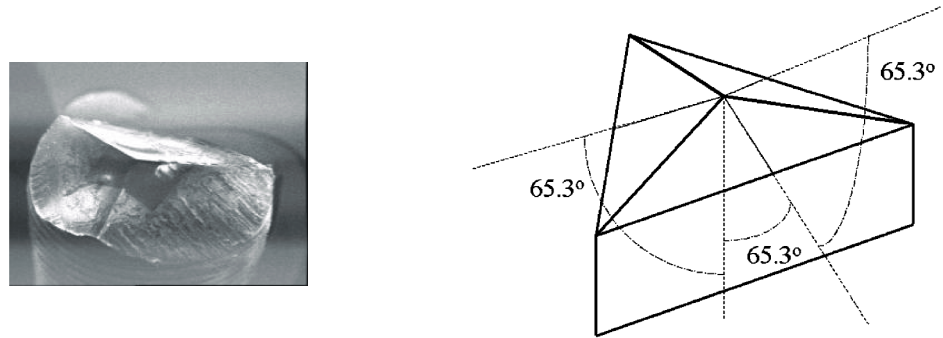


**Figure 9.5:** Berkovich indenter. The right figure comes from [Gia06].

### 9.2.2 Experimental tests

Experimental nanoindentation tests were performed in several  $\beta$  grains<sup>3</sup> of Ti-5553 material. For each test, the orientation of the grain indented was measured (Figure (9.6)). The grain numbers are indicated in the picture and the corresponding orientations are given in Table (9.1) by their Euler's angles  $(\varphi_1, \phi, \varphi_2)$ <sup>4</sup>.

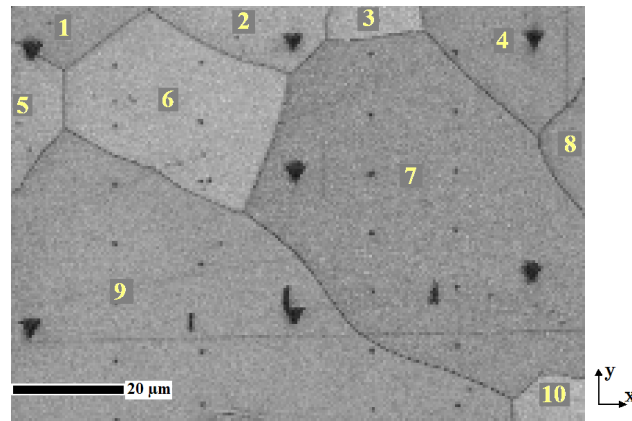


**Figure 9.6:** Sample of indented 100%  $\beta$  Ti-5553. The numbers of the grains are indicated and the corresponding orientations are given in Table (9.1).

<sup>3</sup>These tests were carried out by Nicolas Clement at the IMAP department of the University of Louvain, in January 2007.

<sup>4</sup>See Appendix (H) for numerical details.

Grain number	$\varphi_1$ [°]	$\phi$ [°]	$\varphi_2$ [°]
1	232.69	39.16	22.43
2	37.89	32.53	56.27
3	37.68	34.5	71.26
4	89.59	39.34	86.67
5	51.75	41.29	60.66
6	207.75	43.16	65.16
7	247.87	39.3	34.85
8	147.45	44.78	78.28
9	203.77	35.16	83.83

**Table 9.1:** Orientation of the indented  $\beta$  grains illustrated in Figure (9.6).

### 9.3 Numerical models

The numerical nanoindentation simulations were achieved using the *Lagamine* finite element code [DHC92] and two constitutive laws: a Von Mises' elastic-plastic constitutive law and an elastic-viscous-plastic microscopic crystal law. The first one is shortly recalled in the next section and the second one has been described in Chapter (4) of Part (II). Then, the finite element meshes and the material used to perform the simulations will be presented.

#### 9.3.1 Constitutive laws

The first law used is a Von Mises' elastic-plastic (EP) constitutive law. The hardening law is given by

$$\begin{cases} \sigma = \varepsilon E & \sigma \leq \sigma_{y1} \\ \sigma = \varepsilon E_T & \sigma \geq \sigma_{y2} \end{cases} \quad (9.2)$$

with  $E$ , the Young's modulus and  $E_T$ , the plastic modulus. Between  $\sigma_{y1}$  and  $\sigma_{y2}$ , the transition is given by stress - strain coordinates, as illustrated in Figure (9.7). The advantage of such a law is its simplicity. Thus, numerical modelings with this law are generally faster than those performed with a more complicated constitutive law.

The second constitutive law used in this chapter is the elastic-viscous-plastic (EVP) microscopic crystal plasticity law described earlier (in Chapter (4) of Part (II)). In this kind of constitutive law, the crystal orientation and the activated slip systems are taken into account.

#### 9.3.2 Finite element meshes

Many authors used 2D axisymmetric finite element meshes because the calculation cost is considerably reduced and it makes the characterization of usual parameters of the material possible. However, to study the influence of other parameters such as grain orientation, this

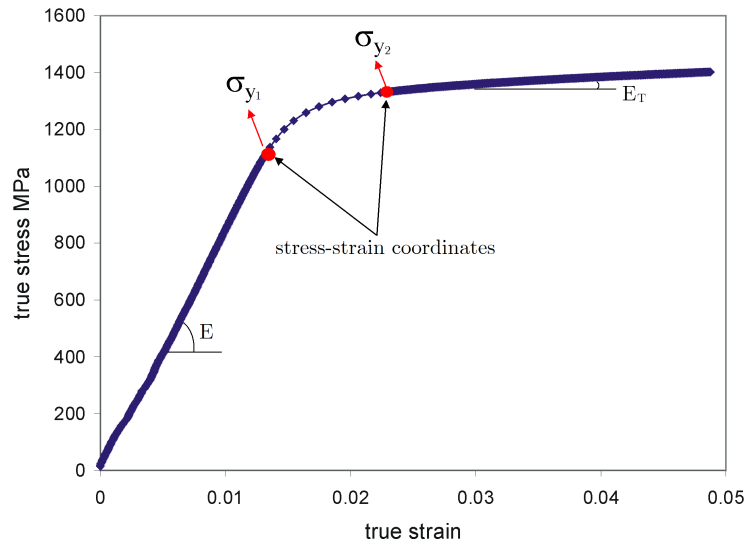


**Figure 9.7:** Stress versus strain curve. Illustration of the parameters of the EP constitutive law.

methodology is not sufficient. In this case, a 3D mesh is necessary.

To perform numerical simulations of nanoindentation, several 3D meshes were defined. They are shown in Figures (9.8) and (9.9).

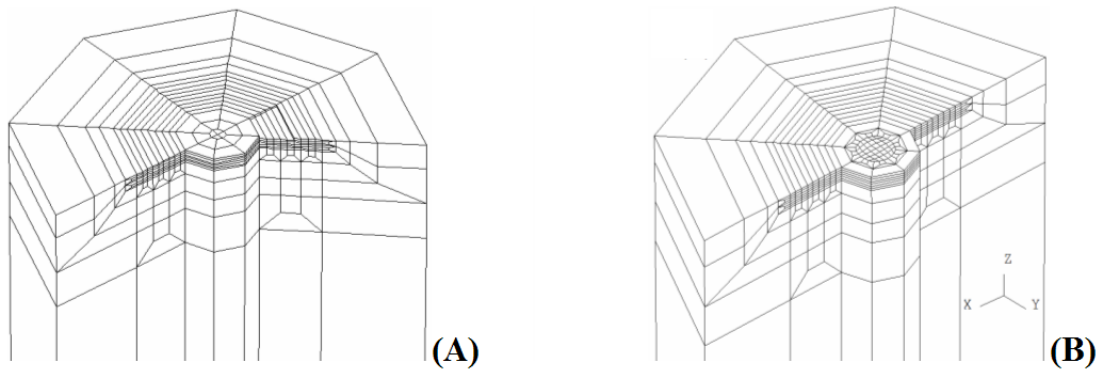


**Figure 9.8:** Parts of meshes used for nanoindentation simulations: (A) 1044 elements, (B) 1772 elements.

The difference between the three meshes presented is principally due to the number of elements at the center of the mesh, where the tip enters the material. The first mesh, the coarser one, contains 1044 eight-node brick<sup>5</sup> elements (Figure (9.8 (A))). The second one, more refined, is composed of 1772 elements. This mesh is entirely shown in Figure (9.10) and partially in Figure (9.8 (B)). A top view of the mesh and a cross section along the plane ( $x = 0$ ) are also provided (Figure (9.11)) where graduations (in  $10^{-8}$  m) are superimposed.

<sup>5</sup>This element is described more in Appendix (E).



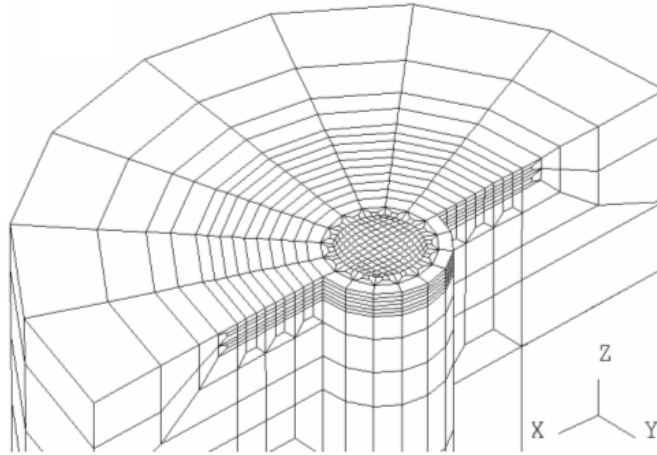


**Figure 9.9:** Part of the third mesh used for nanoindentation simulations: 4544 elements.

The third and last mesh, well refined in the indented region, contains 4544 elements and is shown in Figure (9.9).

In each mesh, contact elements [HC98] with 9 integration points are placed in the central zone of the top surface of the mesh and the indenter is considered to be a rigid tool.

### 9.3.3 Material and parameters

The material studied in this chapter is the body-centered cubic (BCC)  $\beta$  phase of Ti-5553. The parameters of this phase for the elastic-plastic constitutive law are given in Table (9.2). These parameters were optimized using inverse modeling on tensile tests performed on 100 %  $\beta$  material [GCJ<sup>+</sup>07]. This was carried out using the program *Optim* of the *Lagamine* FE code based on Levenberg Marquardt's algorithm [Lev44], [Mar63].

$E$ (MPa)	$\nu$	$\sigma_y$ (MPa)	$E_T$ (MPa)	$\mu$
85000	0.31	595	1388.9	0.2

**Table 9.2:** Parameters optimized for the  $\beta$  phase of Ti-5553: Elastic modulus  $E$ , Poisson's ratio  $\nu$ , plastic strength  $\sigma_y$ , tangent modulus  $E_T$  and friction coefficient  $\mu$ .

A first result is presented hereafter. Nanoindentation tests in the  $\beta$  phase obtained experimentally and numerically with the EP constitutive law are compared in Figure (9.12). Despite the relative simplicity of this constitutive law, the numerical results are in good agreement with experimental ones.

The microscopic plasticity-based constitutive law is also used in several simulations in the next section. The reference elastic parameters are given hereafter:

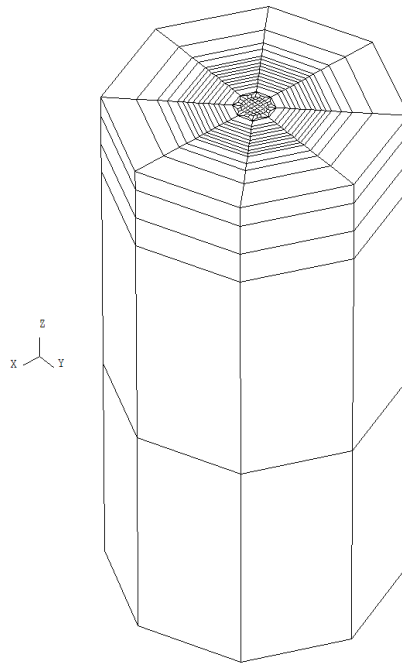


Figure 9.10: Second mesh, composed of 1772 elements.

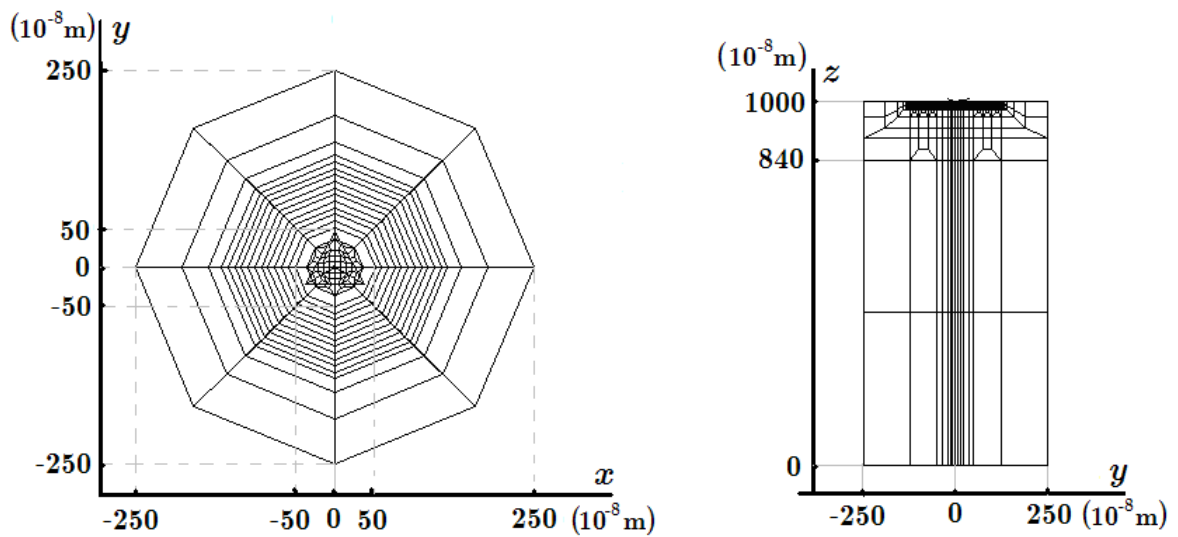
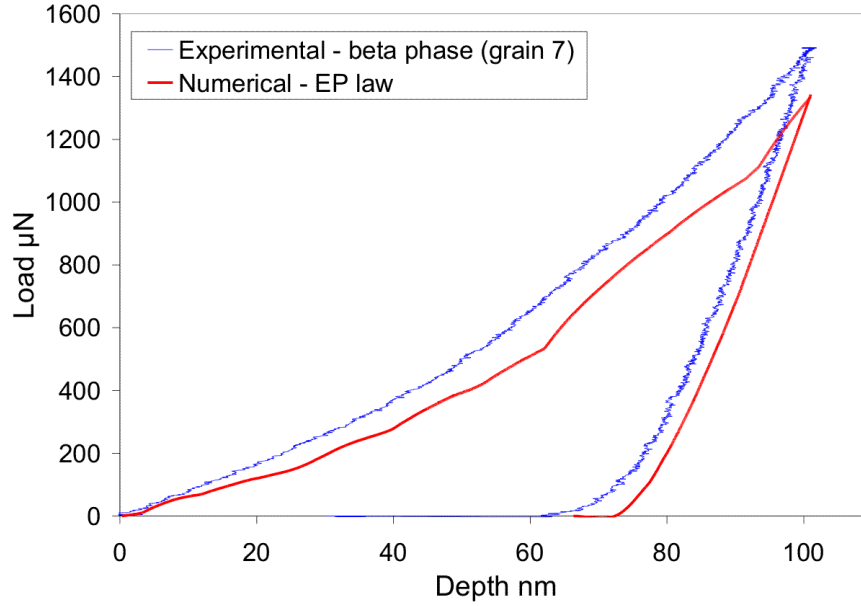


Figure 9.11: Second mesh with graduations in  $10^{-8}$  m. (Left) Top view and (right) cross section in the plane  $x = 0$ . The Berkovich indenter tip is also shown, in the middle.



**Figure 9.12:** Nanoindentation in a  $\beta$  grain of Ti-5553. Comparison between experimental results and numerical ones obtained with the EP constitutive law for which parameters were optimized from tensile tests on 100 %  $\beta$  material.

$$\begin{cases} E = 85000 \text{ MPa} \\ \nu = 0.35 \end{cases}$$

Using Pierce, Needleman and Asaro's hardening law (Eqn.(4.18)), the reference parameters used are provided in Table (9.3). Using Bassani and Wu's hardening law (Eqn.(4.20)), the parameters used are given in Table (9.4).

$h_0$ (MPa)	$\tau_0$ (MPa)	$\tau_s$ (MPa)	$n$	$\dot{a}$ ( $s^{-1}$ )
13120	300	353	19.3	0.0001

**Table 9.3:** Parameters of Pierce, Needleman and Asaro's hardening model, for the  $\beta$  phase of Ti-5553.

$n$	$\dot{a}$	$h_0$	$\tau_s$	$\tau_0$	$\gamma_{0\alpha\alpha}$	$\gamma_{0\alpha\beta}$	$f_{\alpha\alpha}$	$f_{\alpha\beta}$	$A$	$B$
50	0.001	7482	304	300	0.00091	0.000314	14.6	15	-1.959	-14.766

**Table 9.4:** Parameters of Bassani and Wu's hardening model for the  $\beta$  phase of Ti-5553.

In the next section, a sensitivity analysis is performed, using the material parameters optimized for the  $\beta$  phase of Ti-5553 as reference parameters. The influence of some parameters are studied and commented on. The final goal of this study, in which the influence of certain parameters is investigated, is to help determine or validate the parameters of a chosen material. Indeed, to ensure the relevance of the set of optimized parameters, it is important to test

if a slight variation in one of them significantly influences the nanoindentation results.

Thus, hereafter, results obtained with variations of some parameters such as the geometrical, the elastic or the plastic ones are observed. As will be shown, some parameters must be known to be accurate to avoid large mistakes.

## 9.4 Sensitivity analysis

### 9.4.1 Mesh refinement

In any finite element calculation, the discretization chosen is a compromise between the conflicting requirements of accuracy and computational cost-effectiveness. To choose the appropriate mesh that reaches this compromise, numerical simulations with the three meshes presented above (Figures (9.8) and (9.9)) were performed, using the crystalline plasticity-based constitutive law with Pierce, Needleman and Asaro's hardening model (Eqn.(4.18)). For each numerical simulation, the parameters of the law (Table (9.3)), the geometry of the sample, the Berkovich indenter and the imposed penetration depth of the tip are exactly the same. Load versus displacement nanoindentation curves obtained with the three meshes are presented in Figure (9.13).

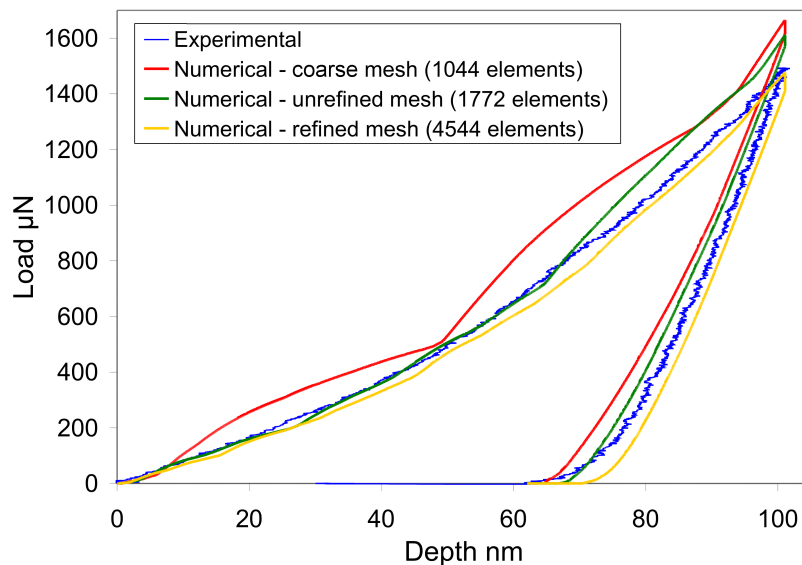


**Figure 9.13:** Numerical nanoindentation simulations with three different meshes.

With a small number of elements in the indented zone, bumps in the loading curve were more pronounced. Similar nonsmooth loading curves in numerical indentations were also reported by [LWY<sup>+</sup>05] and [BBM05]. Similarly, [LWY<sup>+</sup>05] observed that, with a coarser mesh, more and larger oscillations appear in the load versus displacement curve. As mentioned in [GCJ<sup>+</sup>06], these bumps can be linked to the new integration points that enter into contact. This result is shown in Figure (9.14). In this figure, for different times, the central part of the mesh, just under the tip of the indenter, is shown. In these meshes, red arrows define the pressure applied

by the indenter at the integration points of the contact elements<sup>6</sup>. The central node of these meshes corresponds to the node just under the tip of the indenter. Indeed, there is a correlation between the new integration points that enter into contact and the bumps in the curves.

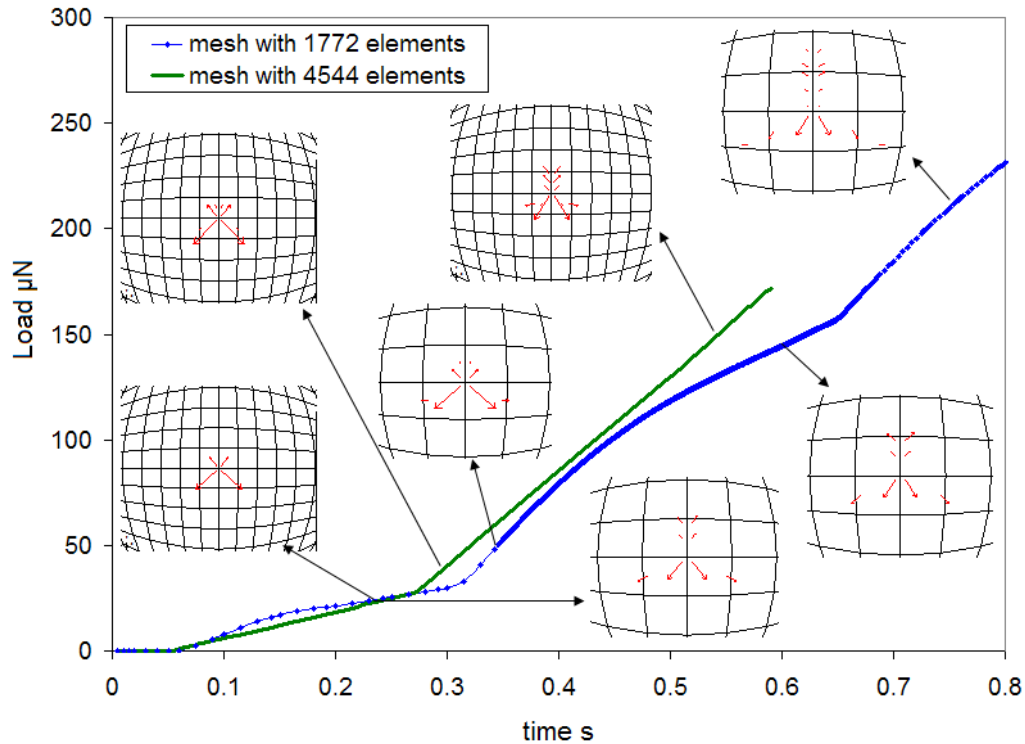


**Figure 9.14:** Nanoindentation numerical load versus time curves obtained with meshes (B) and (C) and with the EP constitutive law. Red arrows show the pressure applied by the indenter at the integration points of the contact elements under the tip.

For some authors [BBM05], these oscillations in the numerical nanoindentation curves reflect model errors associated with the computer simulation of the moving contact. Nevertheless, all these comments agree with the same conclusions. When the mesh refinement is increased, the oscillation amplitude in the numerical load versus displacement nanoindentation curves is reduced and the response tends to a smoother line.

In Figure (9.13), it appears that the number of elements in the finite element mesh also influences the maximum load obtained for an imposed indentation depth. The maximum load is reduced when the number of elements increases. Contact is better localized when more degrees of freedom allow the material surface to follow the indent shape better.

For the next numerical nanoindentation simulations in this chapter, the second mesh will be used because it corresponds to a good compromise between accuracy and calculation cost.

<sup>6</sup>Contact elements [HC98] with nine integration points are put in the central zone, where the material is indented. More details about the contact in finite element simulations is given in Appendix (E).

### 9.4.2 Geometry of the indenter tip

Experimental indenter tips are never geometrically flawless. In an ideal case, the experimental Berkovich indenter tip should be perfectly sharp. In practice, it is impossible to construct such a tip: it always presents some curvature. The imperfections lead to questions about the accuracy of the simulations. It is necessary to understand the importance of the curvature and of the included angle of the tip.

To study these imperfections, numerical simulations were performed using the simple EP constitutive law (Eqn.(9.2) and the parameters of Table (9.2)), in order to compare the results obtained for small modifications of the indenter geometry.

In Figure (9.15), the influence of the included angle of the Berkovich tip is studied. A numerical simulation was performed with the usual values of the total included angle of a Berkovich pyramidal indenter ( $65.3^\circ + 77^\circ = 142.3^\circ$ ), and another one was performed with a slightly more open angle ( $71^\circ + 80.23^\circ = 151.23^\circ$ ). Both tips are shown in Figure (9.15).

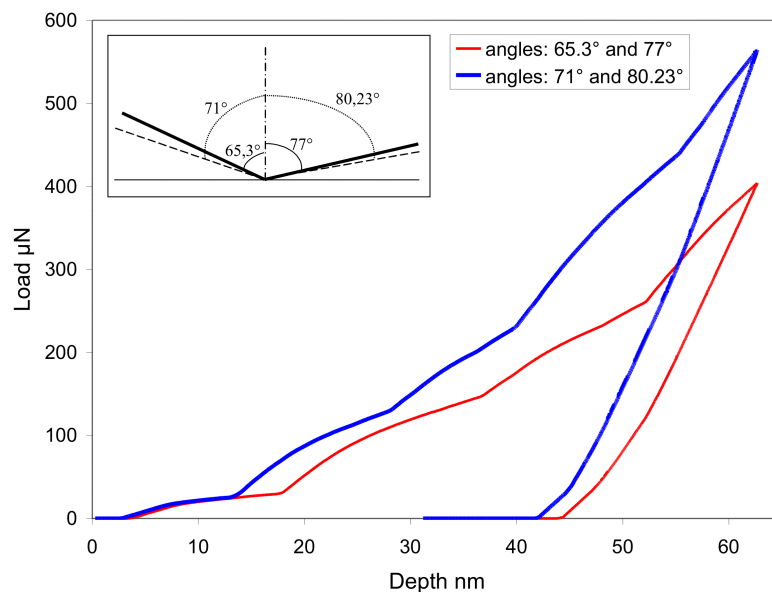


**Figure 9.15:** Numerical nanoindentation simulations: influence of the opening angle of the tip.

An increase of about 6 % of the included angle induces an increase of more than 30 % of the maximum load, for the same indentation depth. [YKC07] also observed that increasing the included angle of the tip leads to a greater load for the same indentation depth. Similarly, [KM08] mentioned that the geometry of the indenter has a high influence on the response of the investigated model.

The influence of the curvature always present at the bottom of the indenter tip will now be discussed. To understand the influence of this curvature, three different indenter tips, drawn in Figure (9.16), were used and the load versus displacement curves have been compared.

The first tip (A) is composed of four nodes. The edges of this indenter are supposed to be perfectly linear without curvature of the tip. The second one (B) is composed of seven nodes. The three additional nodes are used to change the slope of the edges near the bottom of the tip in order to simulate the natural curvature of the tip better. The third one (C) is composed of ten nodes. The three new nodes are also added to better simulate the curvature. Here, two changes in the slope of the edges are present near the bottom of the tip to smooth the geometrical changes compared to the perfect and non realistic tip (A). These tip geometries are drawn in Figure (9.16): on the right, a perspective view of the three tips, and on the left, a view of each of them in the plane ( $x = 0$ ).

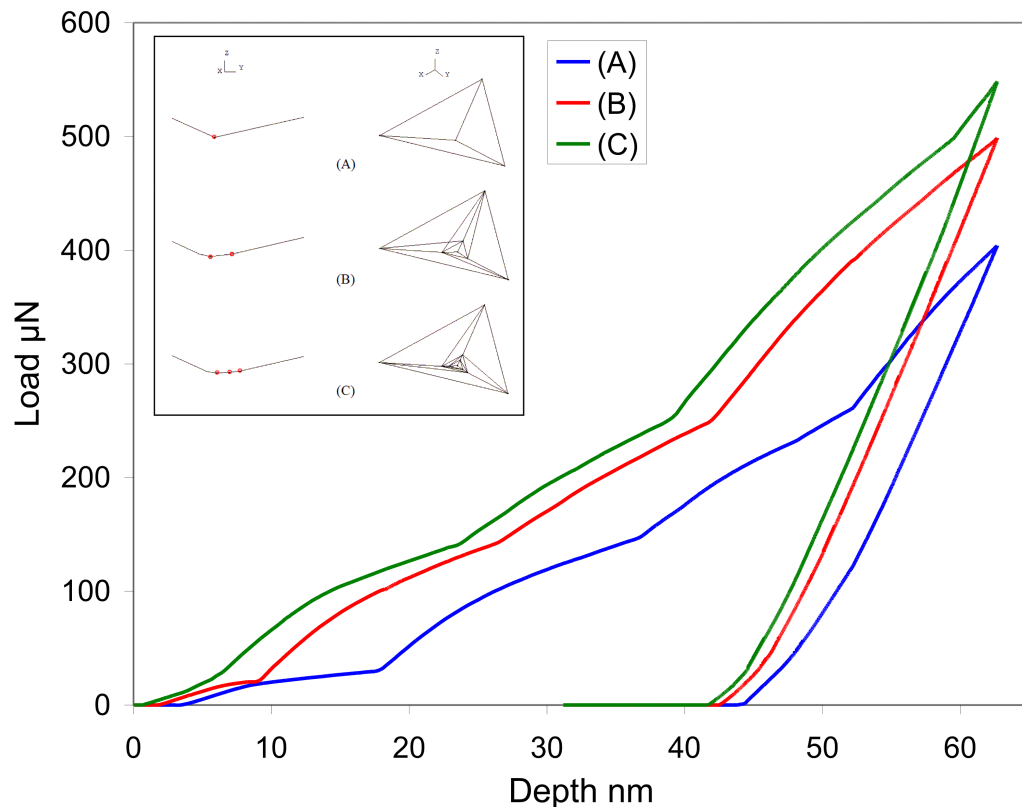


**Figure 9.16:** Influence of the curvature of the tip on load versus displacement curves. (A) Tip without curvature, (B) 3 more nodes and (C) 6 more nodes to better simulate the real curvature of the indenter.

From the load versus displacement results obtained with these three tips (Figure (9.16)), it appears that a decrease in the sharpness of the simulated indenter tip provides an increase in the maximum load, for the same indentation depth. [PKCM00] have also shown the necessity of taking the curvature into account to better simulate the experimental results.

### 9.4.3 Positioning of the indenter tip

Experimentally, the indenter tip is fixed vertically to the nanoindentation device but nothing is present to check the accuracy of its position<sup>7</sup>. However, to analyze the imprint of the tip into the material indented, a sufficient knowledge of the position of the indenter is needed. To study the influence of a defect of the tip's verticality in a nanoindentation test, simulations were performed with the EP constitutive law and different positions of tips composed of four nodes (tip (A) of Figure (9.16)). The first one has its axis along the  $z$  direction (nodes 1, 2, 3 and 4 of Figure (9.17)), the second has its nodes (1', 2', 3' and 4') rotated by  $5^\circ$  around the  $x$  axis and the third one is rotated by  $5^\circ$  around an axis placed at  $30^\circ$  from the  $x$  direction, in the  $xy$  plane. These three tips, the coordinates of their corners and the position of these indenters are described in Appendix (J).

The load versus displacement results obtained with these three indenters are shown in Figure (9.17).

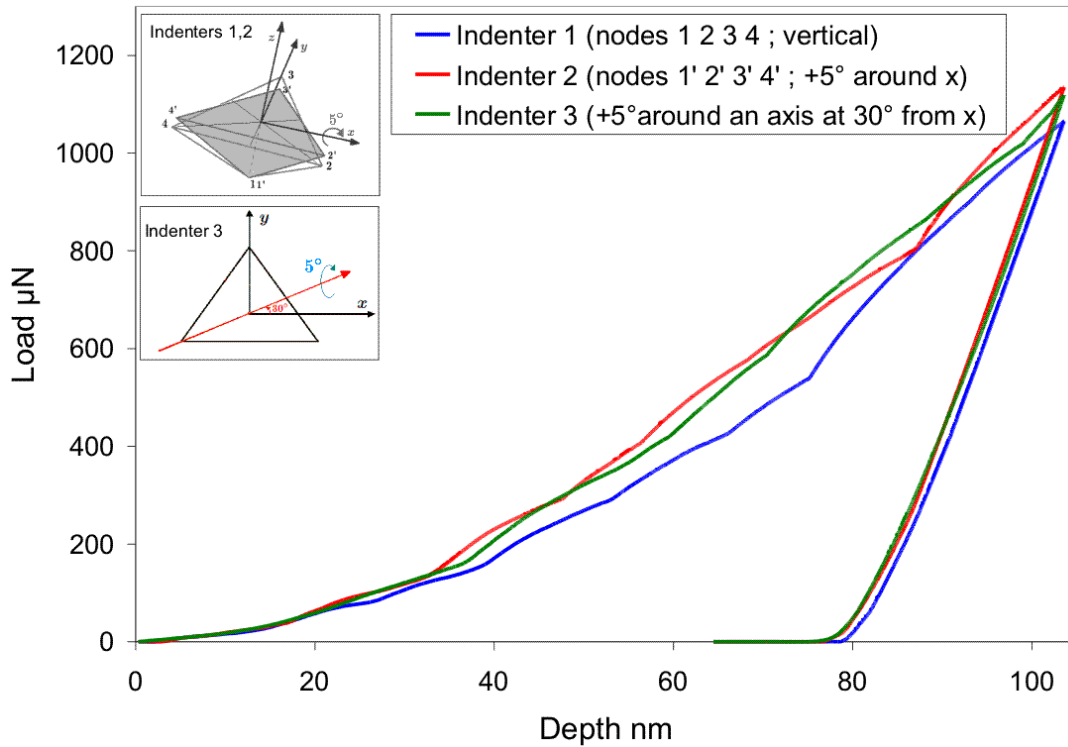


**Figure 9.17:** Numerical nanoindentation simulations: influence of the positioning of the tip.

For small indentations (indentation depth lower than 20-25 nm), results are the same for all tips studied. When the indentation depth increases, the load is slightly greater for the second and the third tip and, at the maximum indentation depth, the load difference between the first and the second tips (1 and 2) is about 6 %. The change in load between the second

<sup>7</sup>The vertical displacement is parallel to the  $z$  axis (Figure (9.17)).



and the third tips for the same indentation depth is negligible. Thus, the axis around which the tip is rotated does not significantly affect the corresponding load versus displacement curve.

Nevertheless, despite the small effect of the tip positioning on the load versus displacement results, it is still interesting to study this defect on the pile-up patterns to better understand the shape of the pile-ups that appear in experimental nanoindentation results. In the set of experimental nanoindentation tests performed<sup>8</sup> in the  $\beta$  phase, pile-up patterns around the indenter often exhibit a similar, non-symmetrical aspect, as shown in Figure (9.18).

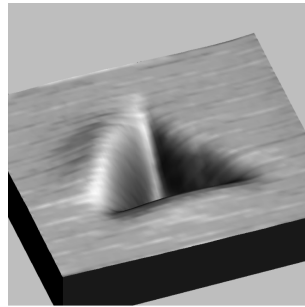


**Figure 9.18:** Imprint in a  $\beta$  grain of Ti-5553 after an indentation test.

A non-negligible pile-up was observed on a first side, a smaller one was observed on the second side and no pile-up appeared on the third one. This qualitative result was perceived on several samples of different orientations.

The numerical results obtained with different tip positioning are given in Appendix (K). From this study, it was shown that a verticality defect of the indenter tip does not significantly change the geometry of the patterns. Thus, the strange shape observed in the experimental pile-up patterns provided by the UCL cannot be explained in this way.

#### 9.4.4 Elastic parameters

In this paragraph, the effect of Young's modulus and Poisson's ratio are studied. Numerical simulations with the EP constitutive law were performed using different values of these parameters. The results are presented in Figure (9.19) for different Young's moduli and in Figure (9.20) for several Poisson's ratios.

As shown in Figure (9.19), Young's modulus does not have to be known accurately because its influence on the increasing load versus displacement curve is not very high. However, a good approximation of the value of this parameter is important to prevent too large an error. Nevertheless, the value of Young's modulus strongly influences the slope of the unloading part of the nanoindentation load versus displacement curve. Indeed, using a Young's modulus of 70 or 90 GPa leads to a change of 20% in the slope of the unloading nanoindentation curves.

---

<sup>8</sup>Nanoindentation tests performed by N. Clement from UCL.

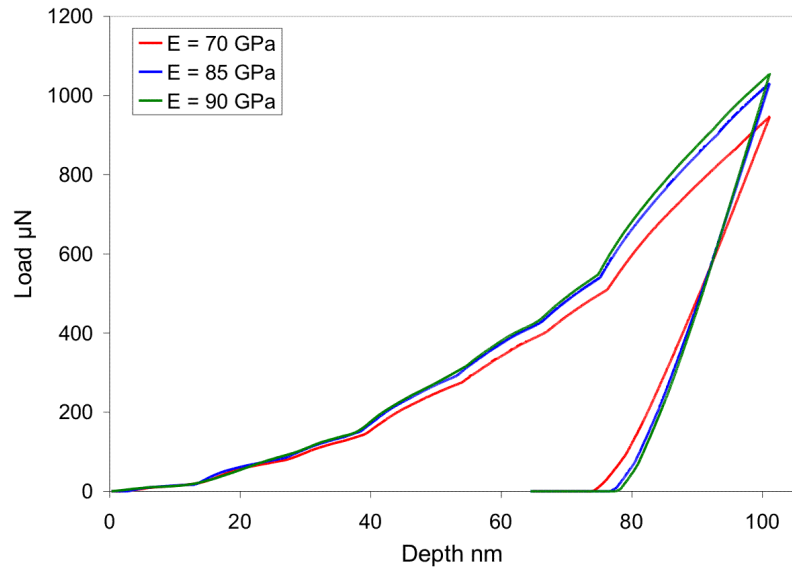


**Figure 9.19:** Influence of Young's modulus on numerical nanoindentation simulations.

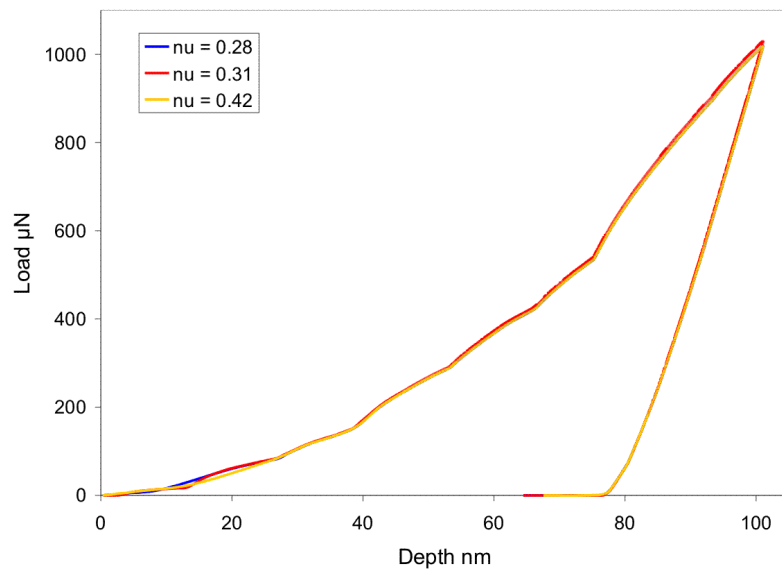


**Figure 9.20:** Influence of Poisson's ratio on numerical nanoindentation curves.

On the other hand, as shown in Figure (9.20), a rough estimate of Poisson's ratio is enough to simulate this type of test. Poisson's ratio has a very small effect on the numerical nanoindentation curves. The slight influence of this parameter was also reported by [FM05]. They observed that, over a reasonable range of Poisson's ratio values for metals, between 0.27 to 0.37, the load versus displacement indentation curves displayed only a small variation of less than 3 % at the maximum indentation load.

### 9.4.5 Tangent modulus and yield strength

When the EP constitutive law is used to perform numerical nanoindentation simulations, two other parameters can also be modified. The first one,  $E_T$ , represents the slope of the plastic part of the stress versus strain curve. The second,  $\sigma_{y1}$ , is linked to plasticity onset. Nanoindentation simulations obtained with the modification of both parameters are presented in Figures (9.21) and (9.22). From Figure (9.21), it appears that a multiplication by a factor of two of the tangent modulus hardly affects the nanoindentation curve. On the other hand, as shown in Figure (9.22), when the yield strength is modified, changes in the load for the same indentation depth are important. In his study, [FM05] performed simulations of indentation using a series of yield strengths. The influence he reports is close to the one observed in Figure (9.22).

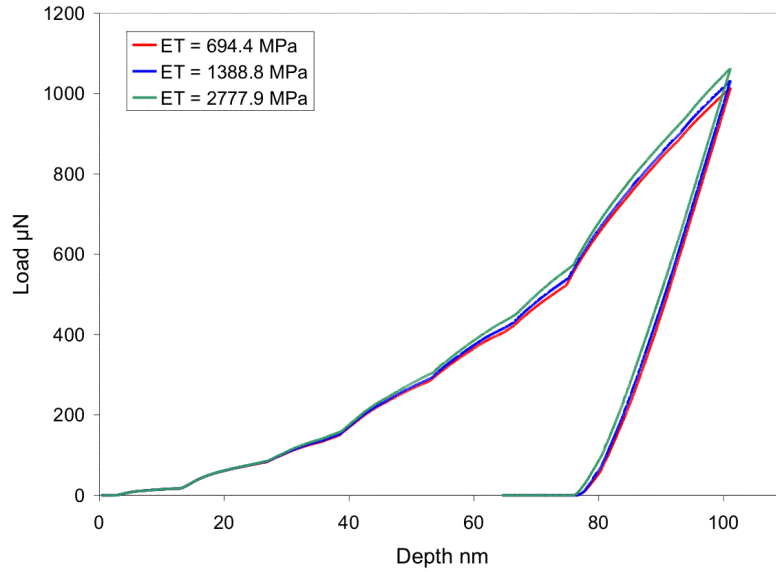


**Figure 9.21:** Influence of the tangent modulus on nanoindentation load versus displacement curves.

### 9.4.6 Friction coefficient

To analyze the role of the friction coefficient,  $\mu$ , on the load versus displacement nanoindentation curves, numerical simulations were performed using different values of this coefficient. The results presented in Figure (9.23) were obtained with the microscopic crystal plasticity-based constitutive law and friction coefficients from 0.02 to 0.2. For better visibility, only results obtained with extreme values of  $\mu$  are shown in figure (9.23). It appears that the friction coefficient has nearly no effect on numerical nanoindentation curves. This result was also observed by [LWY<sup>+</sup>05], [WRKR04] and is explained by [Tab51]. In fact, the equivalent conical indenter of Berkovich's pyramid has an included angle  $\theta$  of  $70.3^\circ$ , as written by [BSFM03]. This angle is represented in Figure (9.1). Eqn.(9.1), recalled here, is used to explain this phenomenon:

$$F = \pi p R_c^2 \left( 1 + \frac{\mu}{\tan(\theta)} \right)$$

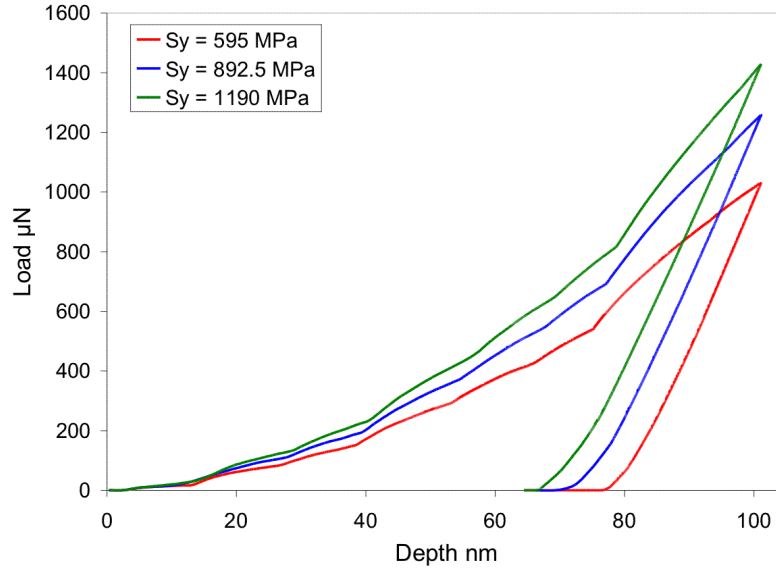


**Figure 9.22:** Influence of the yield strength on nanoindentation load versus displacement curves.

where  $F$  is the normal force. The shear stress,  $\tau$ , is equal to  $\mu p$ , where  $\mu$  is Coulomb's friction coefficient that models the friction between the indenter and the surface of the material.  $R_c$  is the contact radius. With such an included angle ( $\theta = 70.3^\circ$ ), the friction part,  $\frac{\mu}{\tan(\theta)}$ , of this equation is insignificant with regards to the factor of 1 for realistic values of the parameter  $\mu$ <sup>9</sup>.

However, if this coefficient does not affect the numerical results, the computation time varies greatly from one coefficient to another. An example is given in Table (9.5) for two numerical simulations performed with identical parameters except for friction coefficient. The computation time is about 25 times greater when a friction coefficient of 0.02 is chosen compared to a coefficient of 0.5.

$\mu$	Computation time
0.02	$\sim 840$ h
0.5	$\sim 34$ h

**Table 9.5:** Comparison of the computation time of two numerical simulations. These simulations are exactly the same except for friction coefficient.

Moreover, some authors such as [LWY<sup>+</sup>05] and [BSFM03] found that, while the introduction of friction does not change the nanoindentation load versus displacement relationship, it changes the indent surface pile-up profiles. They observed that an increase in the friction

<sup>9</sup>In fact, for a friction coefficient  $\mu = 0.02$ ,  $\frac{\mu}{\tan(\theta)} \simeq 0.00716 \ll 1$ . Similarly, for a friction coefficient  $\mu = 0.2$ ,  $\frac{\mu}{\tan(\theta)} \simeq 0.0716 \ll 1$ .

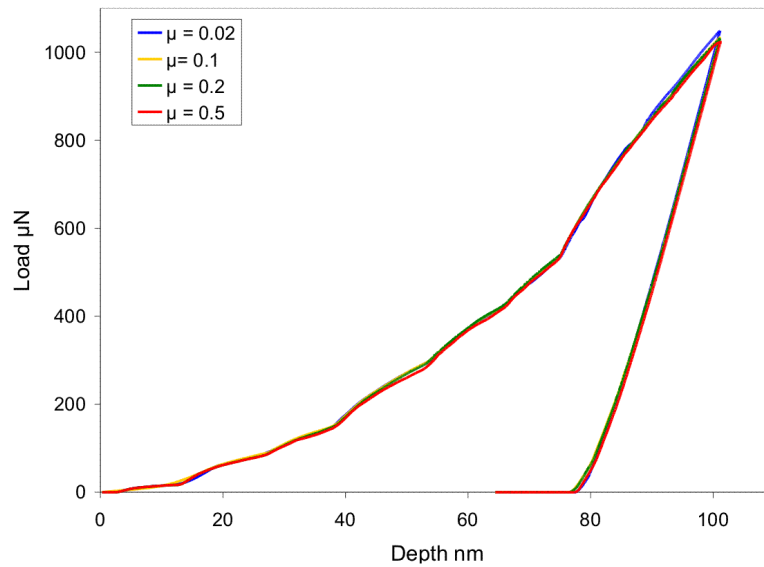


**Figure 9.23:** Influence of the friction coefficient on nanoindentation load versus displacement curves.

coefficient leads to a reduction of the height of the pile-up patterns. [LWY<sup>+</sup>05] observed this phenomenon up to a friction coefficient of  $\mu = 0.4$ . For greater values of this coefficient, no further reduction of pile-up heights was perceived.

The influence of the friction coefficient on the appearance of pile-up patterns in numerical nanoindentation simulations is studied in the next paragraph, dedicated to the study of sink-in or pile-up pattern appearance.

### 9.4.7 Pile-up or sink-in patterns

#### Literature review

Several authors have tried to predict the appearance of pile-up or sink-in patterns near the indented imprint. As mentioned in the previous section, the friction coefficient can influence the height of pile-ups [LWY<sup>+</sup>05], [BSFM03] and [BBM05].

Other authors, like [LWY<sup>+</sup>05], have observed that the number of pile-up patterns is greater the larger the radius of the spherical indenter used is.

Furthermore, [CV01], [FM05], [CLZ<sup>+</sup>07] and [XL08] link the appearance of pile-up and sink-in patterns to hardening properties. For [XL08], who works on elastic-perfectly plastic materials, an  $E/\sigma_y$  ratio of 14.4 corresponds to a "hard" material, leading to sink-in patterns under indentation. An  $E/\sigma_y$  ratio of 240 corresponds to a "soft" material for which pile-up patterns appear under indentation.

[CV01] gave a definition of "soft" and "hard" material, for elastic perfectly plastic materials. Similarly to [XL08], the distinction is linked to the  $E/\sigma_y$  ratio but in this case, the half apex angle,  $\alpha$ , of a rigid cone used as the indenter also has its influence. This angle is shown in

Figure (9.24).

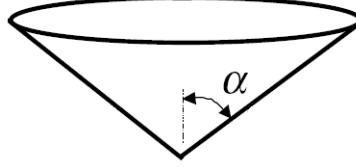


**Figure 9.24:** Half apex angle of a rigid cone indenter.

Thus, for [CV01] and if  $\beta_0 = (90^\circ - \alpha)$ , a material is<sup>10</sup>:

- "soft" for  $\frac{E \tan(\beta_0)}{\sigma_y} > 36$
- "hard" for  $\frac{E \tan(\beta_0)}{\sigma_y} < 36$

Looking at the experimental result of Figure (9.18), pile-up patterns appeared. Numerically, pile-up patterns would also be expected. Indeed, from the material parameters of the EP constitutive law optimized for the  $\beta$  phase of Ti-5553 and given in Table (9.2), the  $\sigma_y$  value is equal to 595 MPa, for a Young's modulus of 85000 MPa and  $\alpha = 70.3^\circ$ . In this case,  $\frac{E \tan(\beta_0)}{\sigma_y} = 51 > 36$  and from [CV01], pile-up patterns should occur.

[CLZ<sup>+</sup>07] has also observed that pile-ups decrease when  $\sigma_y$  increases.

Other authors such as [FM05] explain the effect of strain hardening on patterns. When a material exhibits a high degree of ductility and low strain hardening, material displaced by the indentation pushes out at the surface and forms a pile-up. In contrast, for a high strain hardening material, the indentation is accommodated by far field elastic displacement that results in sink-in patterns. The amount of elastic deformation relative to plastic deformation depends to a large extent on the relationship between the elastic modulus and the yield stress; a low elastic modulus relative to the yield stress will result in primarily elastic deformation and will enhance sink-in, whereas a high elastic modulus relative the yield stress will result in primarily plastic deformation and will enhance pile-up.

Nevertheless, in practice, the appearance of pile-up patterns is not so easy to predict. As mentioned by [WRKR04], the pile-up or sink-in appearances are also due to the crystallography and the orientation of the indented grain.

<sup>10</sup>Thus, for an indentation with an indenter with a half apex angle  $\alpha = 70.3^\circ$  and on a material for which  $E = 85000$  MPa, the material is "soft" if  $\sigma_y < 845.4$  MPa and "hard" if  $\sigma_y > 845.4$  MPa.

### Numerical simulations with the simple elastic-plastic (EP) constitutive law

To better understand the appearance of pile-up or sink-in patterns and the influence of parameters like the friction coefficient or  $E/\sigma_y$  ratio, numerical simulations were performed with a Young's modulus of 85000 MPa, the EP constitutive law and a refined mesh (shown in Figure (9.8 (B))). First, a  $\sigma_y$  value of 6000 MPa was chosen, corresponding to a  $E/\sigma_y$  ratio of 14.17. In this case and from literature results, after unloading, sink-in patterns should appear at the surface of the indented material. Results obtained with a friction coefficient of 0.2 and 0.05 are shown in Table (9.6). For each value of the friction coefficient, two cross sections in the material indented are shown, after tip removal. These cross sections are presented in Figure (9.25).

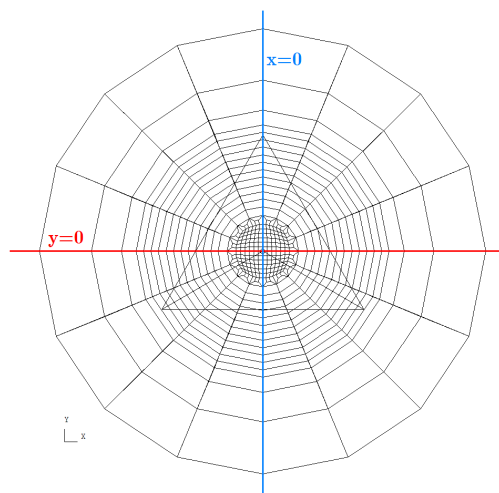


**Figure 9.25:** Top view of the indented material and the Berkovich indenter. Cross sections of the material.

From these results, it is clear that a modification of the friction coefficient applied does not significantly influence the shape of the indented material.

Then, similar simulations were performed using a  $\sigma_y$  value of 354 MPa, corresponding to a  $E/\sigma_y$  ratio of 240. In this case, according to [CV01] and [XL08], pile-up patterns should appear and should be greater with the lower value of the friction coefficient. Like the case  $\sigma_y = 6000$  MPa, for each value of the friction coefficient, two cross sections in the material indented are shown in Table (9.7). In this case, the results were saved before tip removal.

Although the literature predicts the appearance of pile-up patterns with such a value of the yield strength and greater pile-up patterns for lower friction coefficients, numerical simulations obtained with  $\sigma_y = 354$  MPa and with two values of the friction coefficient show no pile-up pattern around the material indented.

Consequently, with the simple elastic-plastic constitutive law and the numerical parameters chosen, it was not possible to simulate pile-up patterns around the material indented. This result was obtained with different values of the yield strength and the friction coefficient.

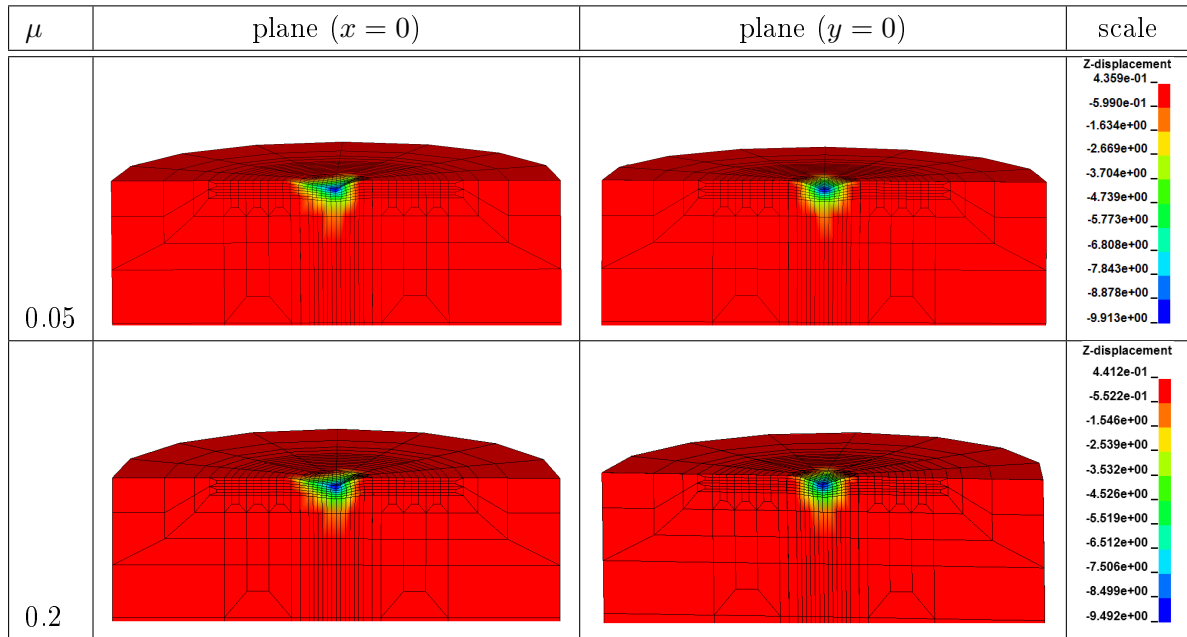


**Table 9.6:** Numerical nanoindentation simulations. Cross sections in the unloaded material ( $\sigma_y = 6000$  MPa). Cross sections along the planes ( $x = 0$ ) and ( $y = 0$ ). The scale (in  $10^{-10}$  m) represents the Z-displacement of the material indented.

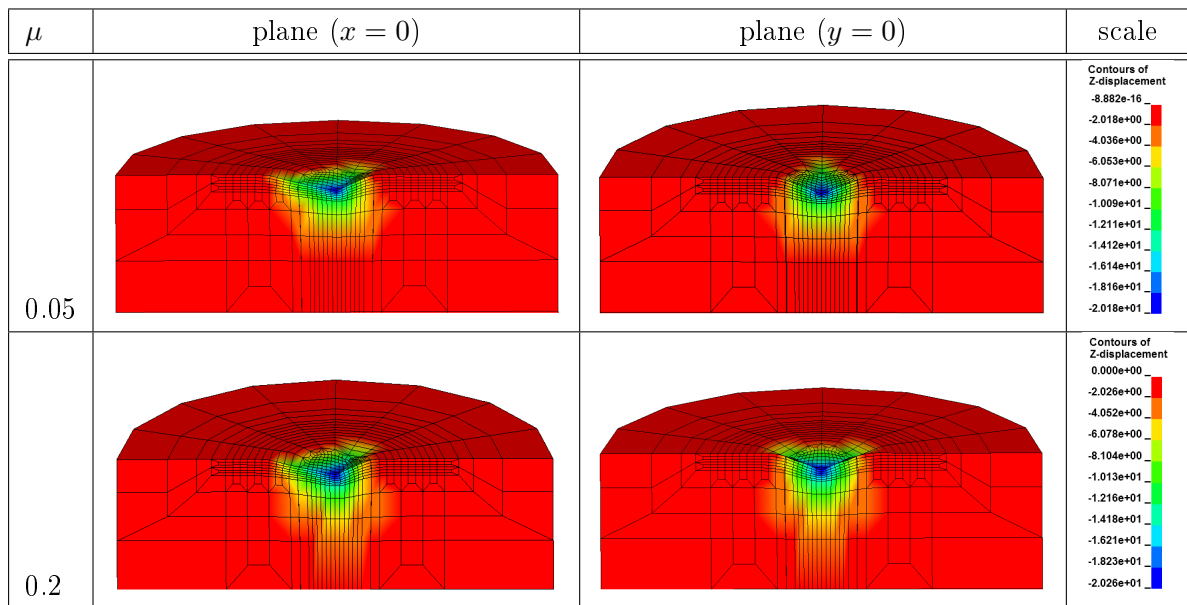


**Table 9.7:** Numerical nanoindentation simulations. Results are shown after a penetration depth of 200 nm. Cross sections in the material indented ( $\sigma_y = 354$  MPa) before tip removal. Cross sections along the planes ( $x = 0$ ) and ( $y = 0$ ). The scale (in  $10^{-10}$  m) represents the Z-displacement of the material indented.



### Numerical simulations with the crystalline constitutive law

Finally, two other numerical simulations were performed using the crystalline constitutive law with Pierce, Needleman and Asaro's hardening model. The parameters used are those given in Table (9.3) except for  $\tau_0$  and  $\tau_s$ , which are given in Table (9.8) for the two simulations.

Parameter (MPa)	Simulation 1	Simulation 2
$\tau_0$	30	3000
$\tau_s$	35	3500

**Table 9.8:** Parameters  $\tau_0$  and  $\tau_s$  of the PAN model for the two numerical simulations performed with the microscopic constitutive law.

The friction coefficient is equal to 0.2 in both cases. Results obtained after a penetration depth of approximately 180 nm are given in Figures (9.26) for simulation 1 and in Figures (9.27) for simulation 2. From literature results based on elastic-plastic materials, pile-up patterns should appear in the first simulation when the material deforms plastically rapidly. Thus, only the positive displacements are shown in Figures (9.26) in order to visualize the pile-up patterns. As mentioned earlier, using a small value of the yield strength leads to pile-up patterns around the imprint of the indenter tip in the material.

For the second simulation performed with a greater value of the yield strength, the material should present sink-in patterns around the indent. Results obtained after an indentation depth of approximately 180 nm are shown in Figures (9.27). As expected, no pile-up pattern appeared in this case.

Consequently, unlike the elastic-plastic constitutive law, with the crystalline constitutive law, it is possible to simulate pile-up patterns around the indented material. Moreover, as is generally the case experimentally (for which an example was shown in Figure (9.18)), the size of the pile-up patterns are not the same along the three sides. Therefore, the orientation of the indented grain has an effect on the pile-up shape. This point is investigated in the next section.

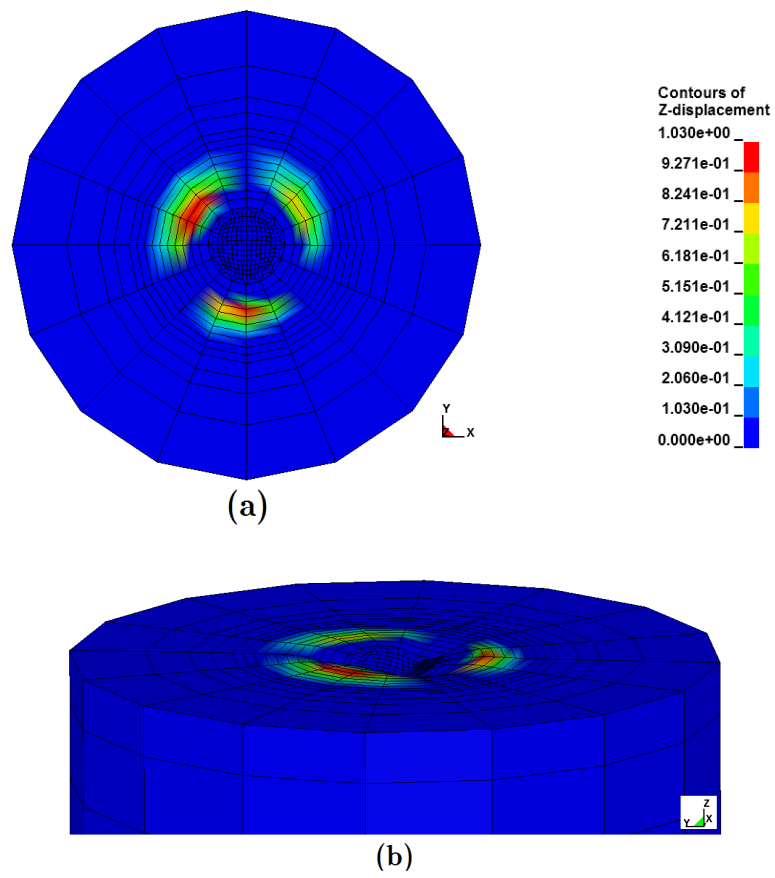


**Figure 9.26:** Contours of Z-displacement (in  $10^{-8}$  m) in the material indented after a penetration depth of approximately 180 nm. (a) Top view and (b) 3D view of the top of the material indented. Just the positive displacements are shown in the legend to visualize the pile-up patterns.

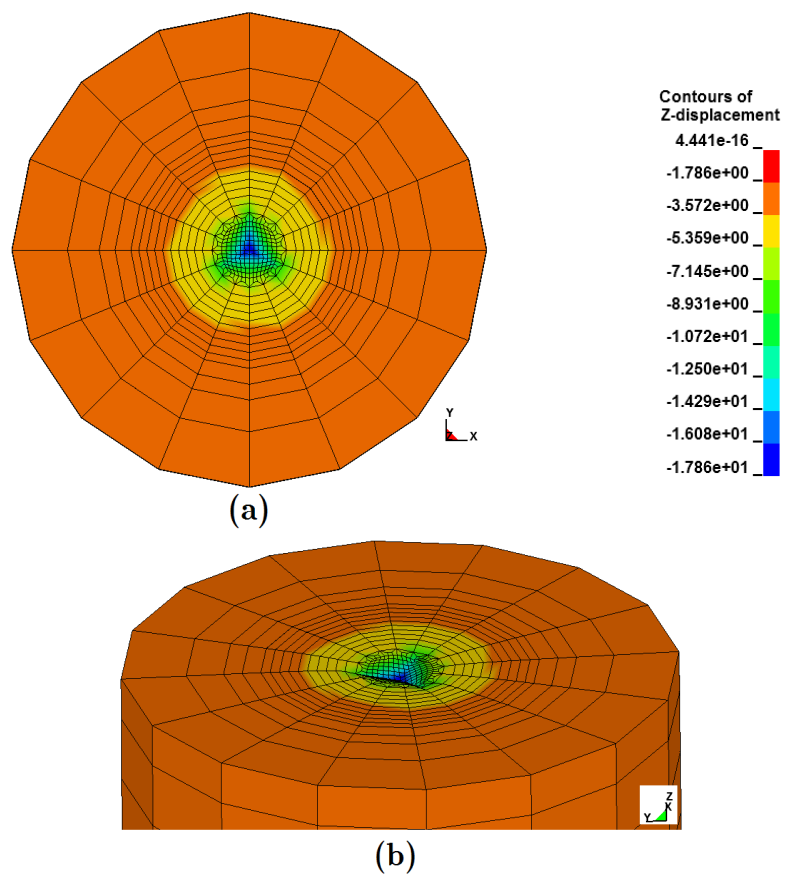


**Figure 9.27:** Contours of Z-displacement (in  $10^{-8}$  m) in the material indented after a penetration depth of approximately 180 nm. (a) Top view and (b) 3D view of the top of the material indented.

### 9.4.8 Grain orientation

Finally, from a microscopic point of view, it is important to study the role of the grain orientation on load versus displacement curves. Experimentally, it is possible to locate the grain indented and to measure its orientation. Numerically, with the microscopic plasticity-based constitutive law, the orientation of the grain is also taken into account. As a consequence, the numerical results obtained in a grain orientation can be compared to the corresponding experimental ones.

As mentioned earlier, the influence of the grain orientation was also studied by [WRKR04] for copper, a face-centered cubic (FCC) material. They observed that pile-up patterns around the imprint of the indent are linked to the orientation of the grain. Similar simulations were performed with the Lagamine code on FCC Aluminium material on different grain orientations, with a conical indenter. The goal of such tests was also to validate the implementation of the constitutive law and check the possibilities of such a law. The numerical results obtained on different grain orientations of FCC materials are given in Appendix (M). They demonstrate the ability of the model chosen to predict similar patterns to the ones observed and predicted by other authors.

In this paragraph, numerical nanoindentation simulations in the BCC  $\beta$  phase of Ti-5553 were performed on different grain orientations using the microscopic constitutive law and the set of parameters optimized from tensile tests performed on 100 %  $\beta$  material. The 1772 FE mesh and the indenter tip (C) in Figure (9.16) were used for these numerical simulations. These nanoindentation tests should validate the set of parameters optimized in the previous chapter for the  $\beta$  phase (Table (9.4)). In such crystals, slip systems are supposed to have all the same critical shear stresses to initiate slipping. Results obtained for this validation are presented in Figure (9.28), where experimental and numerical indentations in grains 6, 7 and 9 are compared. The orientations of these three grains are recalled in Figure (9.28). The location of the grains in the indented material is also shown in Figure (9.28).

The numerical nanoindentation results correspond well to experimental ones for the three grain orientations. The minor differences between the various grains are probably due to the great number of slip systems that can be activated in a BCC crystal. Thus, a rotation of the grain does not imply drastic modification of the behavior.

The experimental patterns corresponding to these three grain orientations are given in Figure (9.29) after tip removal. The qualitative behavior is the same for the three grains, as mentioned earlier.

Figures (9.30) and (9.31) give the variation depth and Von Mises' stress profiles after an indentation of 117 nm (and after tip removal), for three different grain orientations. These simulations were performed with the 1772 FE mesh. There were few differences in pile-up patterns and stress profile between grains of different orientations. However, it is important to keep in mind that the indenter tip is a Berkovich one and not a conical one. Thus, the geometry of the tip also influences the shape of the patterns.

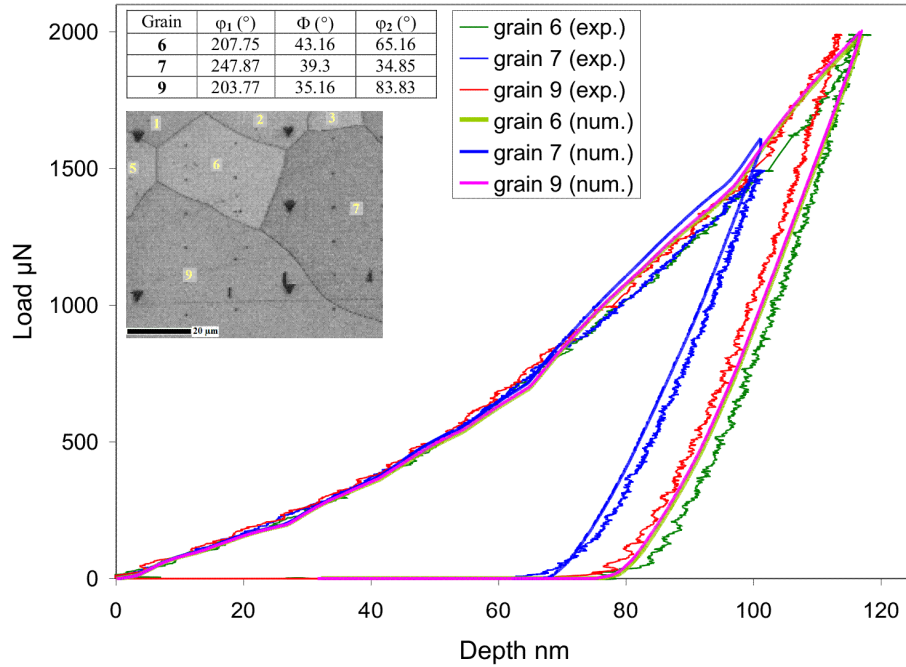


**Figure 9.28:** Influence of the orientation of the BCC  $\beta$  grain (of a Ti-5553 alloy) indented on load versus displacement indentation curve. The orientation of the grains indented and their positions in the material are superimposed.

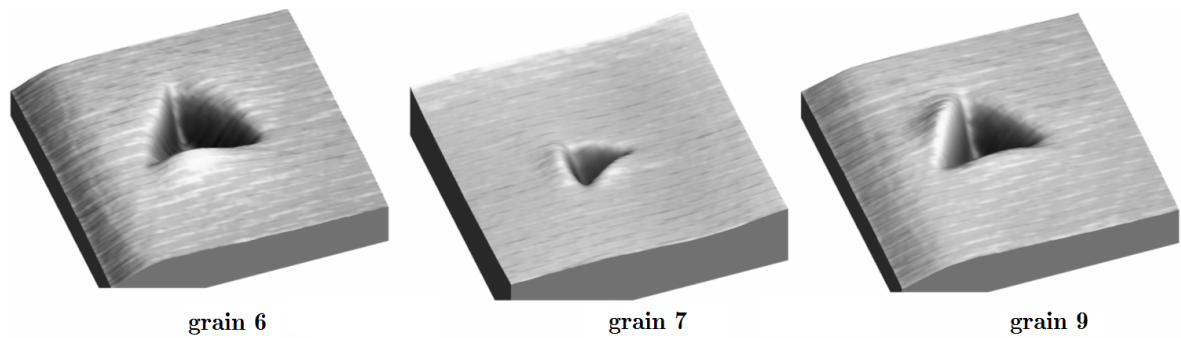


**Figure 9.29:** Experimental patterns obtained after indentation in three different grain orientations.

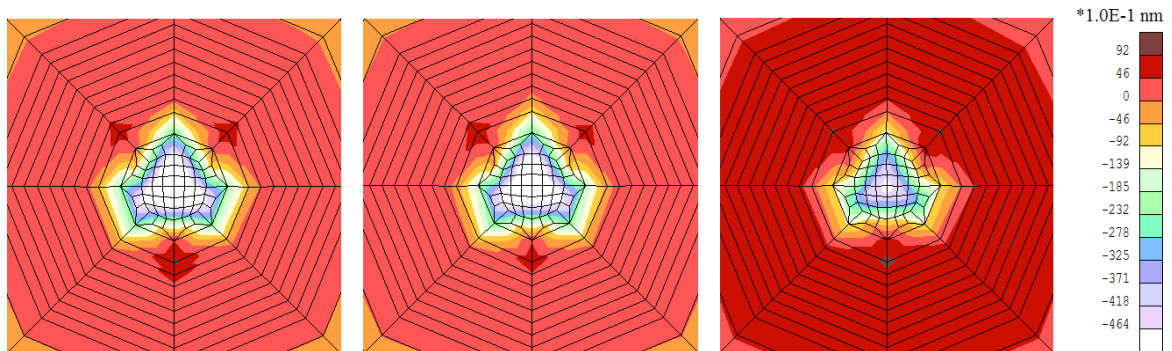


**Figure 9.30:** Variation depth profile after an indentation of 117 nm (and after tip removal) of the indented surface for 3 grain orientations corresponding to grains 6, 7 and 9. Simulations performed with the 1772 finite element mesh.

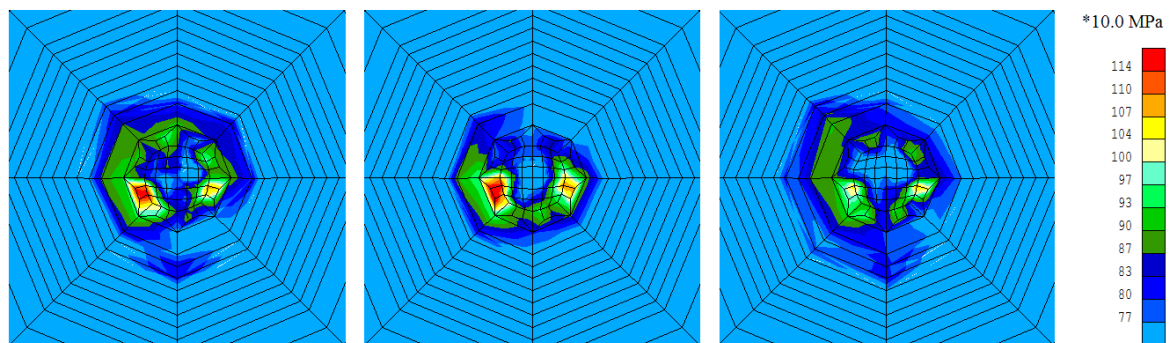


**Figure 9.31:** Stress profile after an indentation of 117 nm (and after tip removal) of the indented surface for 3 grain orientations corresponding to grains 6, 7 and 9. Simulations performed with the 1772 finite element mesh.

## 9.5 Conclusions

In this chapter, numerical nanoindentation tests were presented. It is worth noting that several months were sometimes necessary to obtain available numerical nanoindentation results.

A sensitivity analysis was performed and the main conclusions are summarized in Table (9.9).

Influence of	on loading curves	on unloading curves
<b>Meshes</b>	Only bumps	Large
<b>Elastic parameters</b>		
E	Small	Large
$\nu$	No	No
<b>Yield strength (<math>S_y</math>)</b>	Large	No
<b>Plastic modulus (<math>E_T</math>)</b>	No (very small)	No
<b>Friction coefficient</b>	No	No
<b>Indenter tip</b>		
opening angle	Large	Large
curvature	Large	Large
positioning	Very small	No
<b>Grain orientation</b>	Very small	No

**Table 9.9:** Sensitivity analysis about nanoindentation in the  $\beta$  phase of Ti-5553. Concluding results.

The parameters that influence the unloading part of the nanoindentation curves are limited to the refinement of the mesh, the geometry of the indenter (the opening angle and the curvature) and Young's modulus.

In this chapter, the difficulty obtaining pile-up patterns was presented. From the literature, the parameters that influence their appearance and their size are generally the hardening parameters, the friction coefficient and the orientation of the indented grain. Some changes of these parameters were performed and corresponding numerical results were analyzed. It was found that the occurrence of pile-up or sink-in patterns is not so obvious. It was not possible to visualize pile-up patterns with the EP constitutive law and with an appropriate choice of the yield strength and the friction coefficient. However, pile-up patterns appeared with the crystalline constitutive law and appropriate parameters. Simulations were validated by the ability to predict FCC case from literature. However, the experimental sink-in and pile-up patterns from UCL were not predicted at all.

Finally, it was observed that the orientation of the indented BCC  $\beta$  grain does not significantly influence the load versus displacement nanoindentation curves. Results correspond well to the experimental ones, for three different grain orientations.





## Part IV

# Identification of the $\alpha$ phase of Ti-5553



## Chapter 10

# Identification of the $\alpha$ phase using nanoindentation

### 10.1 Introduction

This chapter focuses on the identification of the  $\alpha$  phase of Ti-5553. Compared to the identification of the  $\beta$  phase, the difficulty in studying the  $\alpha$  phase is the impossibility of finding a thermal treatment leading to a 100%  $\alpha$  material. Consequently, experimental macroscopic tests could not be performed on this phase only.

It is possible to perform macroscopic tests on ( $\alpha + \beta$ ) materials. Yet, even though the  $\beta$  phase has been identified, it is complicated to deduce the material parameters of the  $\alpha$  phase from such tests. The results obtained were not conclusive, the reason lying in several arguments. First, the percentage of  $\alpha$  phase in the ( $\alpha + \beta$ ) material was not accurately known; the percentage of  $\alpha$  phase was nevertheless known to be small (10 - 20 %) compared to the  $\beta$  phase and thus, the global behavior was principally dictated by the  $\beta$  phase. Secondly, the numerical modeling was not accurate enough. In fact, one  $\alpha$  grain was modeled with one brick element and thus, the shape of the grain was coarsely modeled. To achieve better results, each grain should be modeled using a greater number of finite elements such that the real shape of the grains will be taken into account as well as their distribution within  $\beta$  grains. However, such modeling requires a large amount of elements and is not realistic in the frame of the present work.

Thus, nanoindentation appeared to be the best adapted available experimental test to identify the  $\alpha$  phase. Indeed, a nanoindentation test is performed in a single  $\alpha$  grain, and so, it removes the problem due to the presence of  $\beta$  grains in the sample. Moreover, the orientation of the indented grain can also be measured and then used in numerical tests.

In this chapter, the experimental nanoindentation tests performed in  $\alpha$  grains are first presented. Some of these were chosen to identify the parameters of the  $\alpha$  phase. Interactions between both phases exist at the ( $\alpha - \beta$ ) boundary but, in the present work, only tests providing stable results inside the  $\alpha$  grains were chosen. The indent is far from the grain boundary and the effect of surrounding  $\beta$  grains can be neglected. Thus, a few simplifications were brought to the experimental curves. They will be shown in detail and their applicability will be checked.

To identify the elastic parameters of this phase, the basis of the theory is first recalled and then, numerical simulations performed to optimize these parameters are presented.

The task is more complicated for the identification of the plastic parameters of the microscopic plasticity-based constitutive law used in the present work. This constitutive law [Hua91] was presented in Chapter (4) of Part (II). Using the best set of elastic parameters found in the previous step and the values of the plastic parameters collected from the literature, a first numerical model was generated. These parameters were then modified in order to better fit the experimental results of the  $\alpha$  phase. Finally, the different procedures used to identify this phase will be presented.

## 10.2 Experimental data

Experimental nanoindentation tests were performed at a UCL laboratory [IMA] in several  $\alpha$  grains. To obtain sufficiently large  $\alpha$  grains, Ti-5553 was put in solution in the  $\beta$  domain (875°C) for 30 minutes. Then, the sample was slowly cooled down to 800°C over 24 hours and the microstructure was set by water quenching. The sample was finally prepared and polished before nanoindentation tests. The zone of the sample where nanoindentations in  $\alpha$  grains were performed is shown in Figure (10.1).

Two sets of experimental tests were performed (Figure (10.1)): the first one, with white numbers, and the second one, with dark numbers, providing a total of more than 130 experiments. These indentations were performed on  $\alpha$  grains of different orientations; those orientations were measured and several indentations were performed in the same grain when it was possible.

For each indentation on an  $\alpha$  grain, the nanoindentation *depth* and the corresponding *load* and *time* were recorded.

## 10.3 Choice of the experimental nanoindentation curves

The first step in studying the  $\alpha$  phase is the choice of the experimental curves to model. For this purpose, the indented grains and their orientations were identified. Then, the indentation tests performed on the same grain were compared. Several curves corresponding to reproducible results and performed on different grain orientations were retained<sup>1</sup>. The label of these indentations (numbers of the black set of Figure (10.1)) and the corresponding orientations (Euler angles) are provided in Table (10.1).

An example of an experimental nanoindentation curve performed on an  $\alpha$  grain is presented in Figure (10.2).

---

<sup>1</sup>For a large number of experimental nanoindentation tests performed, the variation between results obtained for the same grain is generally not greater than 15%. For the curves chosen here, the maximum difference between two nanoindentation curves never exceeds 7%.

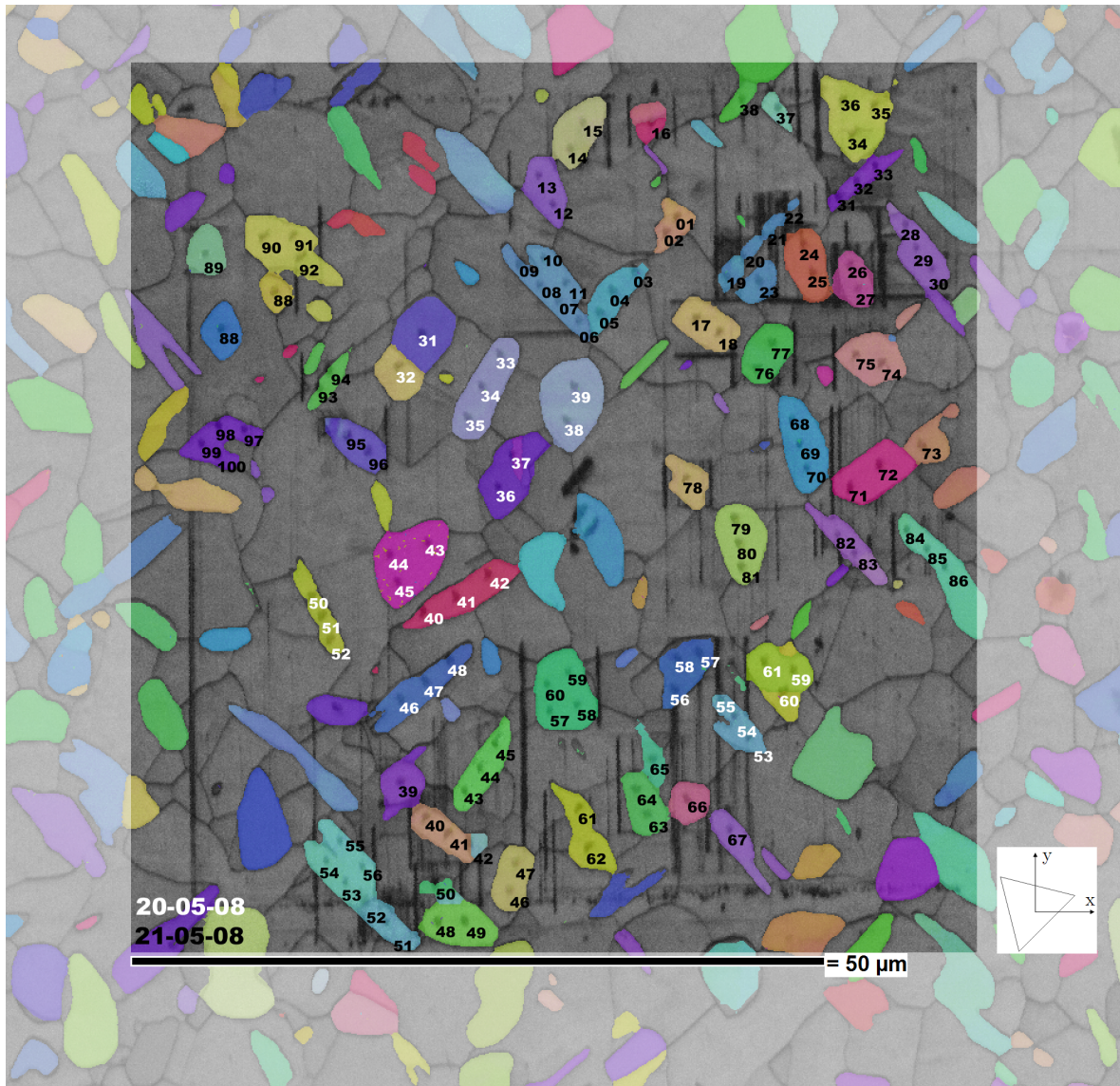


**Figure 10.1:** EBSD image of the indented material. Indentations were performed in  $\alpha$  grains. Each number corresponds to one indentation. The white numbers correspond to the first set of indentations and the black ones to the second set.

indentation number	Euler angles		
	$\varphi_1$	$\Phi$	$\varphi_2$
12	80.53	26.8	33.23
31	92.85	27.99	28.05
43	159.08	138.52	8.44
52	161.25	136.25	2.07
58	7.11	44.43	35.47
98	89.85	25.48	30.83

**Table 10.1:** Euler angles of indentations chosen (indentation number of the black set from Figure (10.1)).

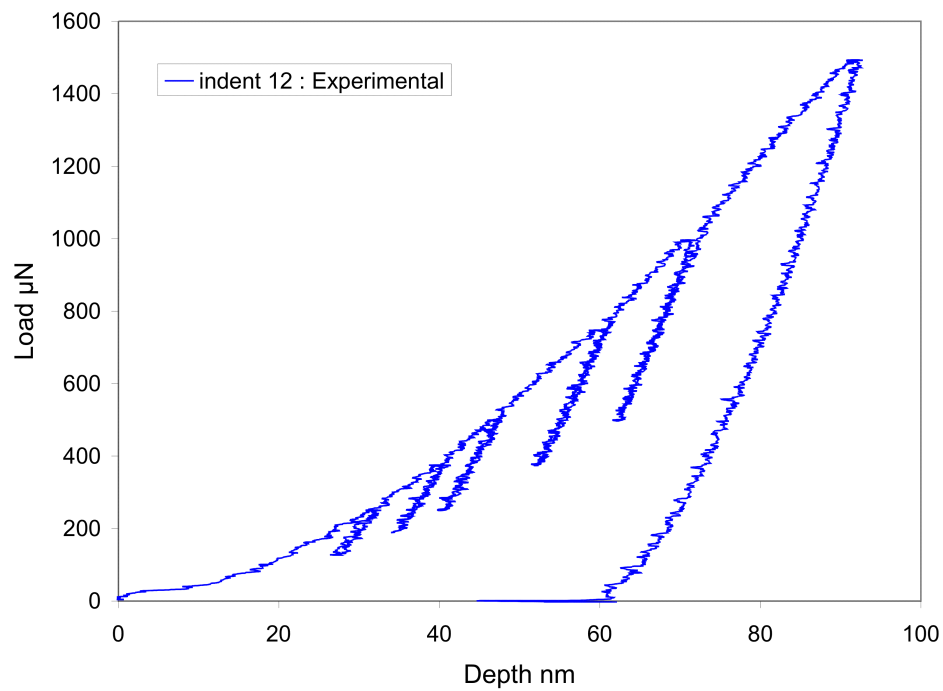


**Figure 10.2:** Nanoindentation experiment in  $\alpha$  grain: load versus displacement (number 12 of Figure (10.1)).

## 10.4 Effect of intermediate unloading during nanoindentation experiment

As shown in Figure (10.2), several intermediate stages unloading were performed during each experimental nanoindentation test. These intermediate phases were ignored in the numerical simulations presented in the next sections because they would have been time-consuming and uninteresting. It was nevertheless important to check that the intermediate unloading did not affect the other parts of the curve.

For that purpose, numerical curves obtained with and without intermediate unloading during the loading part of the nanoindentation curves were compared. The parameters used were not optimized since the goal of these simulations is to compare a numerical curve obtained with the exact experimental loading and a second with simplified loading in which all the intermediate unloading parts are not taken into account. The results obtained for the two cases are presented in Figure (10.3).

It is clear that the simplification of the loading does not affect the load versus displacement curve. It is worth noting that the slight difference between the two numerical curves at the maximum loading is linked only to numerical records. Consequently, in the next sections, to identify the parameters of this phase from nanoindentation curves, the simplified loading will be used and thus, significant reduction in the computing time will be achieved.

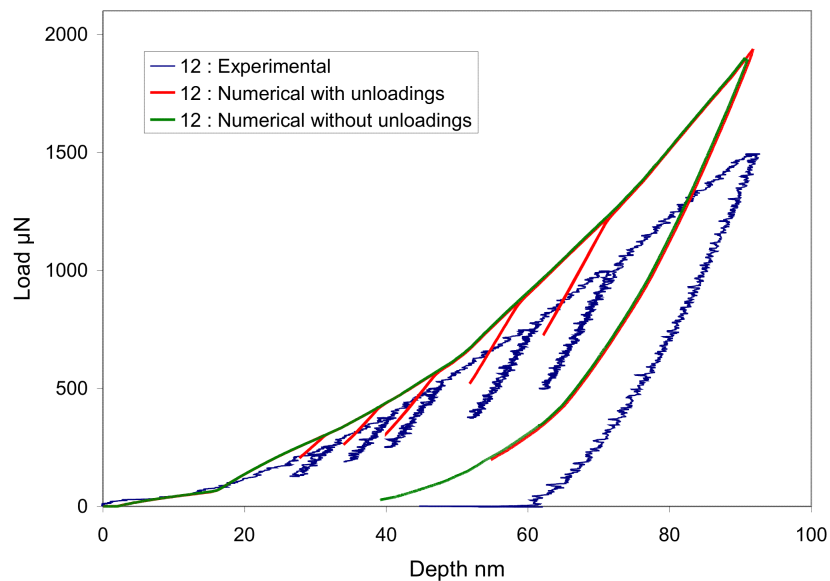


**Figure 10.3:** Nanoindentation in  $\alpha$  grain (12th indentation of Figure (10.1)): load versus displacement curves. Comparison between numerical results with and without unloading. The corresponding experimental result is superimposed.

## 10.5 Identification of the elastic parameters

In this section, the elastic parameters of the  $\alpha$  phase will be identified. The appropriateness of an elastic matrix or just a Young's modulus and a Poisson's ratio will be discussed.

For each simulation presented herein, the plastic parameters used are given in Table (10.2). Three sets of slip systems<sup>2</sup> can be activated: the *basal* ((0001) $\langle 11\bar{2}0 \rangle$ ) ones, the *prismatic* ((10 $\bar{1}0$ ) $\langle 11\bar{2}0 \rangle$ ) ones and the *pyramidal*  $\langle \mathbf{a} \rangle$  ((10 $\bar{1}1$ ) $\langle 11\bar{2}0 \rangle$ ) ones. The choice of the plastic parameters is briefly explained in the third column of this table.

Parameter	Value	Origin
$n$	50	same as $\beta$ phase
$\dot{a}$	0.001	same as $\beta$ phase
$h_0$	7482	same as $\beta$ phase
$\tau_0$	206.9 (basal) 275.8 (prismatic) 248.2 (pyramidal $\langle \mathbf{a} \rangle$ )	values from [Cha04]
$\tau_s$	217.8 (basal) 290.3 (prismatic) 261.3 (pyramidal $\langle \mathbf{a} \rangle$ )	$\frac{\tau_0}{\tau_s} = 0.95$
$h_s$	3	constant value, intermediate compared to $\beta$ phase
$\gamma_{0\alpha}$	0.00091	same as $\beta$ phase
$\gamma_{0\alpha\beta}$	0.000314	same as $\beta$ phase
$f_{\alpha\alpha}$	14.6	same as $\beta$ phase
$f_{\alpha\beta}$	15.0	same as $\beta$ phase

**Table 10.2:** Plastic parameters used in this section for the identification of the elastic parameters.

### 10.5.1 The elastic matrix of hexagonal materials

In the elastic part, the strain ( $\boldsymbol{\varepsilon}$ ) and the stress ( $\boldsymbol{\sigma}$ ) tensors of a crystal are generally linked by Hooke's linear law:

$$\sigma_{ij} = \sum_{k,l=1}^3 C_{ijkl} \varepsilon_{kl} \quad (10.1)$$

where  $C_{ijkl}$  are the elastic moduli and

$$\boldsymbol{\varepsilon} = \begin{pmatrix} \varepsilon_{11} & \varepsilon_{12} & \varepsilon_{13} \\ \varepsilon_{21} & \varepsilon_{22} & \varepsilon_{23} \\ \varepsilon_{31} & \varepsilon_{32} & \varepsilon_{33} \end{pmatrix} \quad \text{and} \quad \boldsymbol{\sigma} = \begin{pmatrix} \sigma_{11} & \sigma_{12} & \sigma_{13} \\ \sigma_{21} & \sigma_{22} & \sigma_{23} \\ \sigma_{31} & \sigma_{32} & \sigma_{33} \end{pmatrix} .$$

<sup>2</sup>These slip systems are illustrated in Figure (10.16).



The symmetries of the strain and stress tensors make it possible to reduce their representations to a vector of 6 components (Voigt's notation, [Tri06]). Consequently,  $C_{ijkl}$  becomes  $C_{ij}$  with the transformations of the indices in Table (10.3).

Tensor notation	11	22	33	23	32	13	31	12	21
Matrix notation	1	2	3	4	4	5	5	6	6

**Table 10.3:** Corresponding indices between notations of  $C_{ijkl}$ .

Similarly, the stress tensor becomes  $\sigma_i$  where

$$\boldsymbol{\sigma} = \begin{pmatrix} \sigma_{11} & \sigma_{12} & \sigma_{13} \\ \sigma_{21} & \sigma_{22} & \sigma_{23} \\ \sigma_{31} & \sigma_{32} & \sigma_{33} \end{pmatrix} = \begin{pmatrix} \sigma_1 & \sigma_6 & \sigma_5 \\ \sigma_6 & \sigma_2 & \sigma_4 \\ \sigma_5 & \sigma_4 & \sigma_3 \end{pmatrix} . \quad (10.2)$$

Similarly, the strain tensor  $\varepsilon_i$  is

$$\boldsymbol{\varepsilon} = \begin{pmatrix} \varepsilon_{11} & \varepsilon_{12} & \varepsilon_{13} \\ \varepsilon_{21} & \varepsilon_{22} & \varepsilon_{23} \\ \varepsilon_{31} & \varepsilon_{32} & \varepsilon_{33} \end{pmatrix} = \begin{pmatrix} \varepsilon_1 & \varepsilon_6 & \varepsilon_5 \\ \varepsilon_6 & \varepsilon_2 & \varepsilon_4 \\ \varepsilon_5 & \varepsilon_4 & \varepsilon_3 \end{pmatrix} \quad (10.3)$$

and thus,

$$\sigma_i = \sum_{j=1}^6 C_{ij} \varepsilon_j . \quad (10.4)$$

For a crystal with a hexagonal symmetry<sup>3</sup>, the elastic tensor can be simplified and rewritten [Nye61] as:

$$\mathbf{C} = \begin{pmatrix} C_{11} & C_{12} & C_{13} & 0 & 0 & 0 \\ C_{12} & C_{11} & C_{13} & 0 & 0 & 0 \\ C_{13} & C_{13} & C_{33} & 0 & 0 & 0 \\ 0 & 0 & 0 & C_{44} & 0 & 0 \\ 0 & 0 & 0 & 0 & C_{44} & 0 \\ 0 & 0 & 0 & 0 & 0 & C_{66} \end{pmatrix} \quad (10.5)$$

where

$$C_{66} = \frac{1}{2}(C_{11} - C_{12}) . \quad (10.6)$$

<sup>3</sup>The  $\mathbf{e}_3$  axis must be assumed to be perpendicular to the basal (0001) plane of the crystal. Since the plane perpendicular to  $\mathbf{e}_3$  is isotropic, the orientation of  $\mathbf{e}_1$  and  $\mathbf{e}_2$  is arbitrary.

The deformation energy of the crystal<sup>4</sup> must be positive to avoid crystal instability. Consequently, for hexagonal materials, restrictions on  $C_{ij}$  are required [Nye61]:

$$\begin{cases} C_{44} > 0 \\ C_{11} > |C_{12}| \\ (C_{11} + C_{12})C_{33} > 2C_{13}^2 \end{cases} . \quad (10.7)$$

### 10.5.2 Literature review

Some authors ([Del05], [FPC97], [Cha04]) give only Young's modulus,  $E$ , and Poisson's ratio,  $\nu$ , as elastic parameters to characterize the  $\alpha$  phase of titanium. According to these works, the values of these parameters are in the range:

$$\begin{cases} E \sim 115 - 125 \text{ GPa} \\ \nu \sim 0.3 - 0.36 \end{cases} . \quad (10.8)$$

Other authors give the value of the parameters included in Eqn.(10.5), as shown in Table (10.4).

Reference	material	$C_{11}$	$C_{12}$	$C_{13}$	$C_{33}$	$C_{44}$	$E$ (Average)
[Tri06]	Ti $\alpha$	$\sim 210$	$\sim 76$	$\sim 95$	$\sim 203$	$\sim 37.5$	114.7
[BD05] (experimental values)	Ti $\alpha$	162.4	92	69	180.7	46.7	111.17
[BD05] (calculated values)	Ti $\alpha$	219.3	73.1	36.51	215.08	37.1	114.73

**Table 10.4:** Values of elastic parameters (in GPa) for the  $\alpha$  phase of titanium from the literature. The last column gives an idea of the corresponding Young's modulus (computed from an average of the anisotropic coefficients).

### 10.5.3 Experimental point of view

Looking at the curves provided in Figure (10.4), there is no influence of the grain orientation on the experimental nanoindentation unloading slope. Thus, the choice of the author to define an isotropic elastic behavior determined only by  $E$  and  $\nu$  seems to be well-adapted. Moreover, in Chapter (9) of Part (III), the sensitivity analysis on nanoindentation simulations in  $\beta$  grains showed that Poisson's ratio has no influence on the load versus displacement curves. Consequently, there is no means of accurately determining  $\nu$  by nanoindentation; only Young's modulus can be identified.

It was also shown in Chapter (9) of Part (III) that the unloading part of the nanoindentation curve is affected by:

<sup>4</sup>In [Nye61], the deformation energy of a crystal is defined as  $\frac{1}{2}C_{ij}\varepsilon_i\varepsilon_j$ .

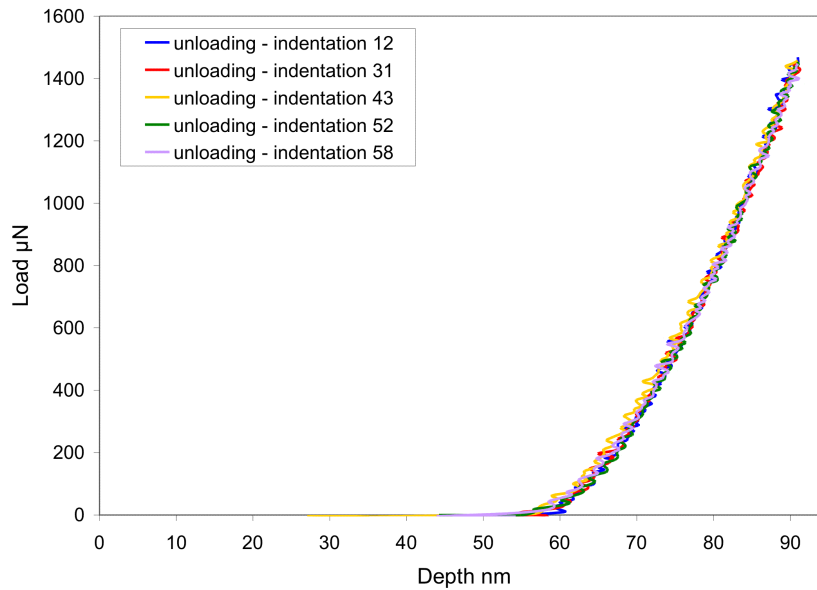


**Figure 10.4:** Nanoindentation: load versus displacement curves. Grain numbers of black set from Figure (10.1).

- Young's modulus,
- the mesh refinement,
- the indenter's geometry.

In the present work, the influence of the refinement of the mesh is not taken into account. The best compromise between accuracy and CPU time is used (1772 FE, mesh (B) in Figure (9.8)). The influence of Young's modulus and the geometry of the tip will be studied.

### Influence of Young's modulus on the unloading slope

As mentioned earlier, for some authors, Young's modulus in the  $\alpha$  phase is in the range of 115 - 125 GPa. The numerical results for these values of Young's modulus are presented in Figure (10.5) together with the results for three other  $E$ : 140, 150 and 160 GPa. In all cases, Poisson's ratio is chosen to be constant:  $\nu = 0.33$ . The numerical values of the slopes are also provided in the figure. The goal is not to obtain the exact same slope. These values are mentioned merely to help the comparison. It can be deduced from these results that an isotropic elastic matrix with usual value of Young's modulus in the range of [115, 125 GPa] is not appropriate to model the unloading part of the nanoindentation curve correctly. It is thus necessary to study if the influence of this modulus together with the tip geometry (curvature, opening angles) would obtain close numerical results with a Young's modulus in a physical range of [115, 125 GPa]. This was the aim, as described in the next paragraph.

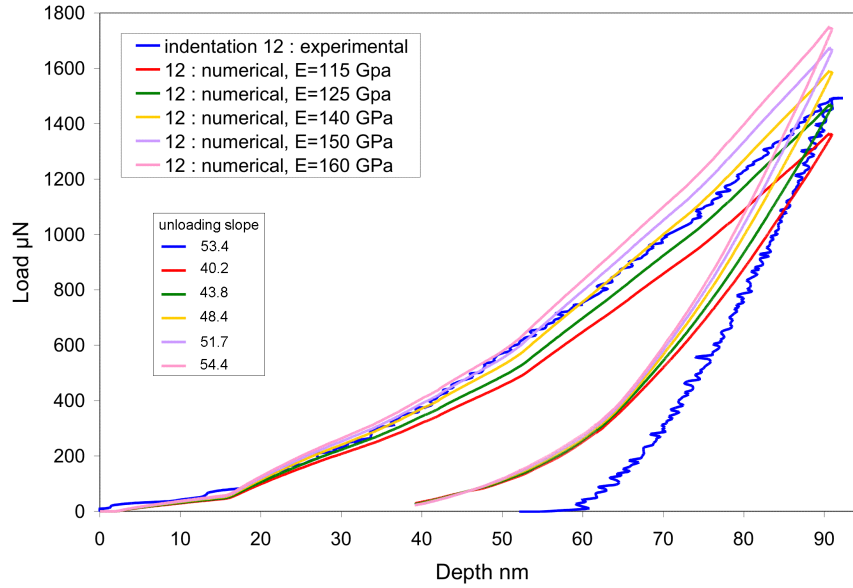


**Figure 10.5:** Nanoindentation: load versus displacement curves for different Young's moduli. Grain numbers of black set from Figure (10.1). Unloading slopes in  $\mu N/nm$ .

### Influence of the tip geometry on the unloading slope

A top view of a Berkovich indenter with the superimposed axes is shown in Figure (10.6) while Figure (10.7) shows four indenter geometries in the plane ( $X = 0$ ). The characteristics of these tips are provided below:

- A "perfect" indenter, without curvature at the bottom of the tip with the included angle of a Berkovich tip (total included angle of  $142.3^\circ$ ).
- Tip 1, a more realistic indenter with the same included angle as the previous one but with a relatively small curvature at the bottom of the tip.
- Tip 2, similar to tip 1 but with a slightly more pronounced curvature at the bottom of the tip.
- Tip 3, with the same curvature as tip 1 but with a slightly greater included angle (+3%).
- Tip 4, with the same curvature as tip 2 and the same included angle as tip 3.

Figures (10.8) and (10.9) present the numerical results obtained using the five different tips in Figure (10.7) with Young's modulus being chosen first equal to 115 GPa (Figure (10.8)) and then equal to 125 GPa (Figure (10.9)). For these curves, the maximum indentation depth is less than before in order to reduce computation time. An indication of value of the unloading slopes are given. The goal here is not to reproduce the exact slope of the unloading part of the curve but rather to understand how to approach the experimental value.

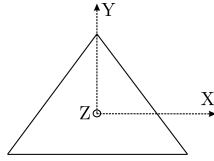


**Figure 10.6:** Top view of a Berkovich indenter in the  $XYZ$  axes.

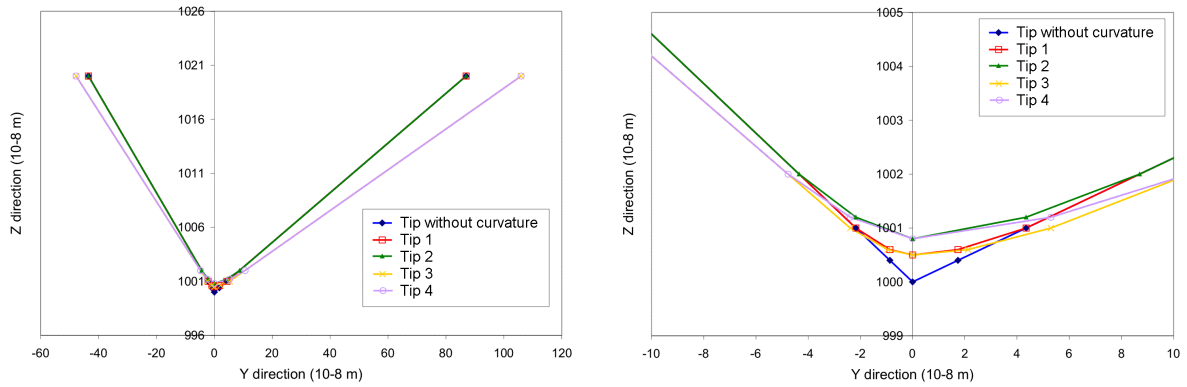


**Figure 10.7:** Different indenter geometries in the plane ( $X = 0$ ) used to perform simulations: on the right, zoom on the tip of the indenters shown in whole on the left figure.

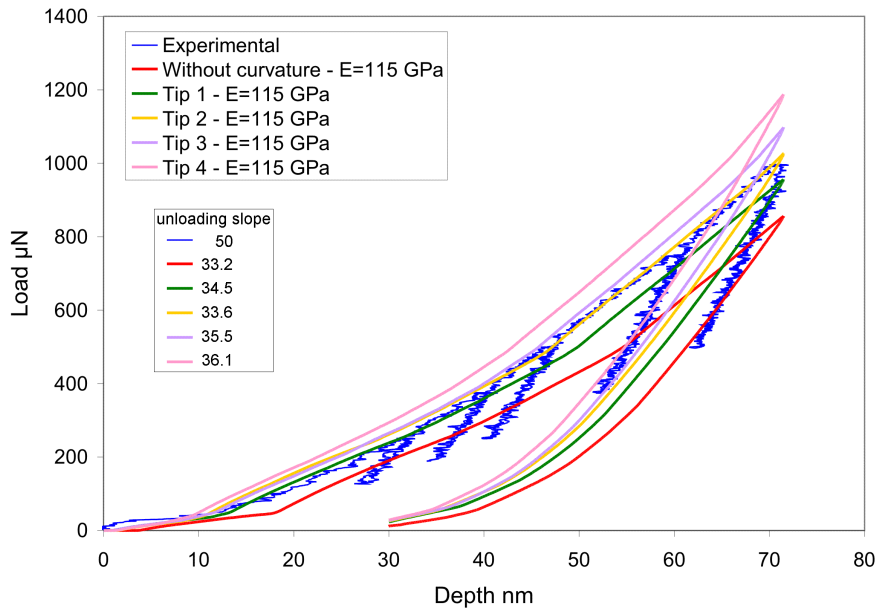


**Figure 10.8:** Nanoindentation: load versus displacement curves for different tip geometries (Figures (10.7)) and for a Young's modulus equal to 115 GPa. Unloading slopes in  $\mu N/nm$ .

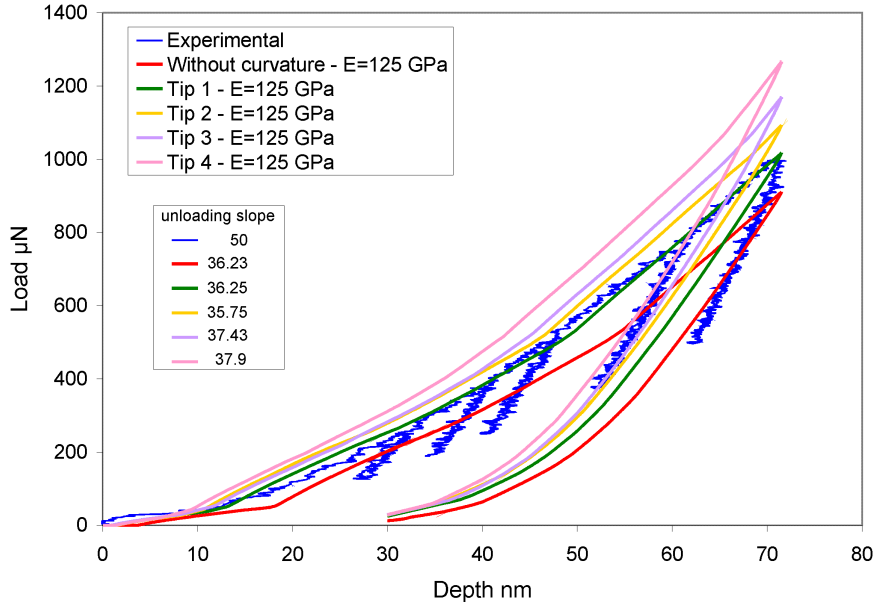


**Figure 10.9:** Nanoindentation: load versus displacement curves for different tip geometries (Figures (10.7)) and a Young's modulus equal to 125 GPa. Comparison with the experimental curve. Unloading slopes in  $\mu N/nm$ .

Looking at the results obtained with two values of Young's modulus, the closest results with respect to the experimental slope of the unloading part of the nanoindentation curve were predicted with the fourth tip (Tip 4). However, this numerical result is still far from the experimental value. Figure (10.10) shows the results obtained with this tip and the two values of Young's modulus.

Young's modulus values of 140 to 160 GPa are not considered due to their great difference compared to the usual values of this modulus found in the literature. A value of 125 GPa and the use of the fourth indenter tip provided the closest physical value to the experimental results. Consequently, it is reasonable to use these parameters for the next numerical simulations.

In order to check the influence of the grain orientation, similar simulations with the fourth tip and a Young's modulus of 125 GPa were performed on two other grains (indentations 43 and 58 in Figure (10.1)). Figure (10.11) shows a comparison of these numerical results with the experimental results of indentation 12. With these assumptions, similar to the experimental case (Figure (10.4)), there is a negligible influence of the grain orientation on the load versus displacement curves for numerical unloading.

#### 10.5.4 Numerical point of view

The results shown above demonstrate that two elastic parameters ( $E$  and  $\nu$ ) can model the unloading behavior. However, experimentally, indentations performed on different grain ori-

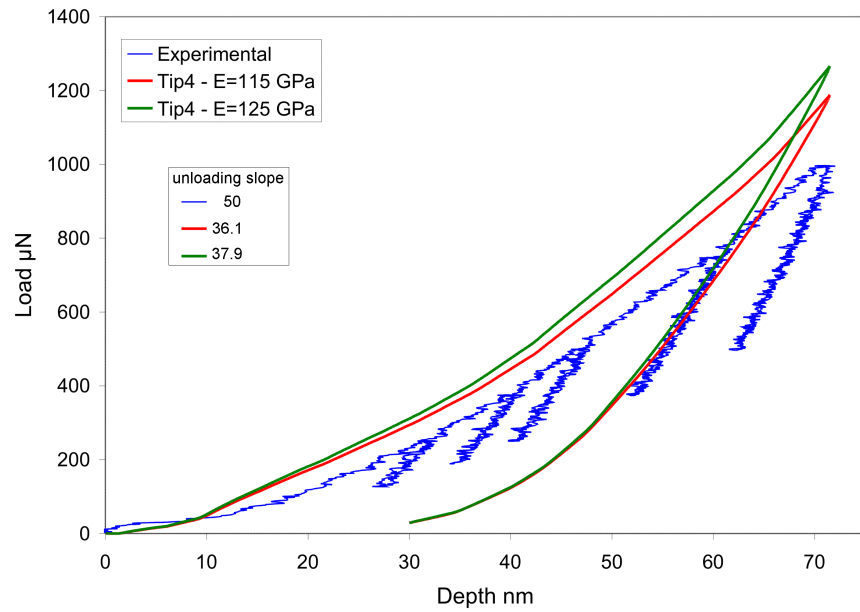


**Figure 10.10:** Nanoindentation: load versus displacement curves for Tip 4 (Figures (10.7)) and Young's modulus equal to 115 and 125 GPa. Comparison with the experimental curve. Unloading slopes in  $\mu N/nm$ .

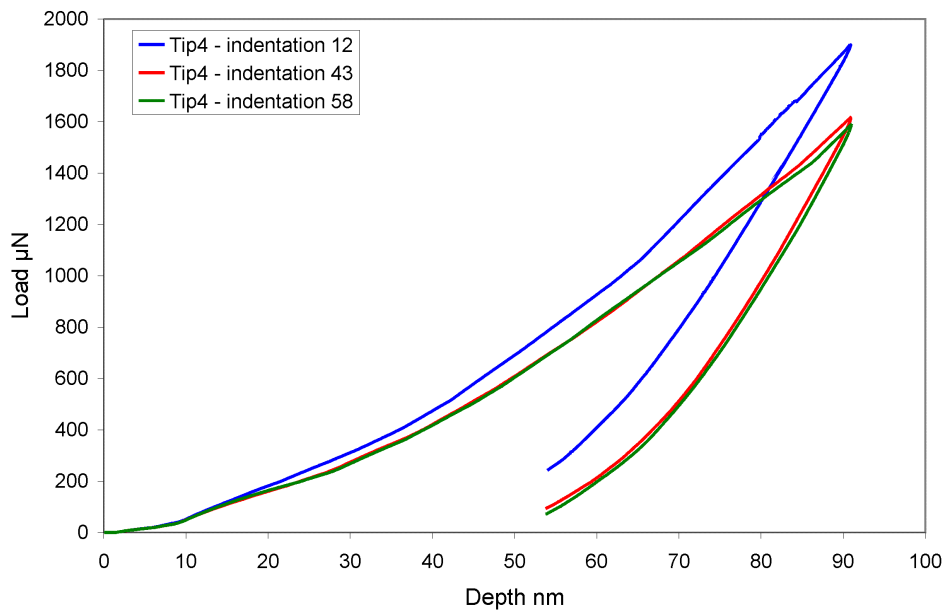


**Figure 10.11:** Nanoindentation: load versus displacement performed with Tip 4 (Figures (10.7)) and  $E = 125$  GPa on different grain orientations.

entations produce strongly different nanoindentation curves (Figure (10.12)) and it is not clear whether these differences are caused by the plastic anisotropy (CRSS) parameters or by the elastic anisotropy, or by a combination of the two.

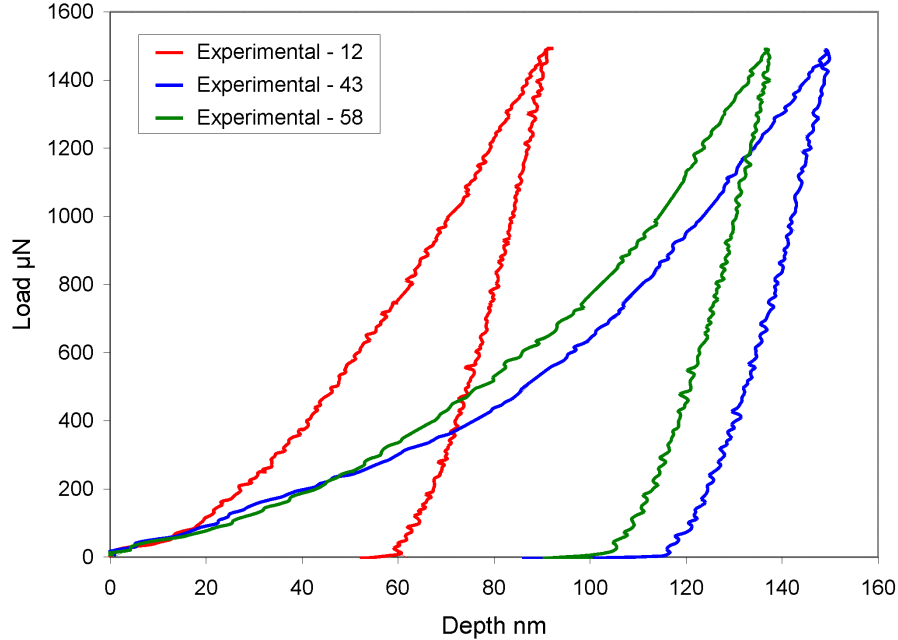


**Figure 10.12:** Nanoindentation: Experimental load versus displacement curves performed in different grain orientations (Indentations 12, 43 and 58 of Figure (10.1)).

To observe the influence of the elastic parameters of the  $C$  matrix on different grain orientations, numerical simulations with anisotropic elastic parameters were performed. Different sets of elastic parameters were tested (parameters from [Tri06], [BD05] and different multiplying factor of these parameters). Only the results obtained with the elastic parameters of [Tri06] all multiplied by 1.31 are presented here. This constitutes the best set of anisotropic elastic parameters tried to optimize the unloading part of the curve. The anisotropic plastic parameters from Table (10.2) were still used in the numerical simulations as in all the previous ones. The simulations were then compared to the corresponding experimental ones (12, 43 and 58). These results are depicted in Figure (10.13).

Compared to the results obtained with isotropic elastic parameters (Figure (10.11)), the influence of the grain orientation is larger here, with the anisotropic elastic parameters. This result is even more obvious in Figures (10.14) and (10.15), where the plastic parameters used to perform these simulations are those from Table (10.2) except for parameters  $\tau_0$  and  $\tau_s$  corresponding to the activated slip systems (see Table (10.5)). In Figure (10.14), the isotropic elastic parameters chosen were  $E = 125$  GPa and  $\nu = 0.33$ . In Figure (10.15), the anisotropic elastic parameters are those from [Tri06] (Table (10.4)) multiplied by 1.31<sup>5</sup>.

<sup>5</sup>The corresponding Young's modulus is approximately equal to 150 GPa.



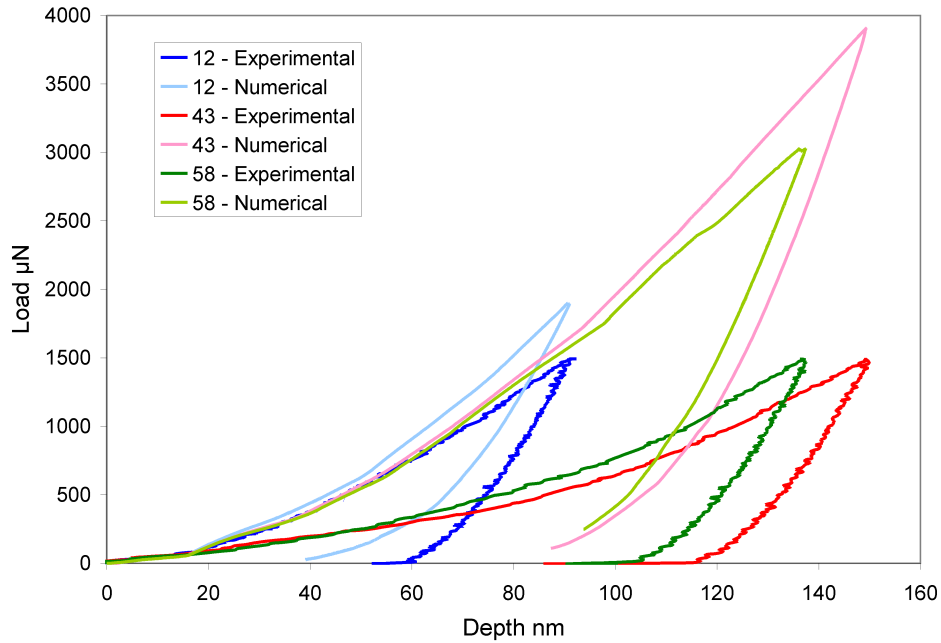


**Figure 10.13:** Nanoindentation: Load versus displacement curves obtained with the elastic anisotropic parameters from [Tri06], all multiplied by 1.31, and with the plastic parameters from Table (10.2). Indentations in 3 grains corresponding to indentation 12, 43 and 58.

Parameter	Value
$\tau_0$	200 (prismatic) 350 (1st pyramidal $\langle c+a \rangle$ )
$\tau_0/\tau_s$	0.98

**Table 10.5:** Plastic parameters used in this section where only elastic parameters are identified.

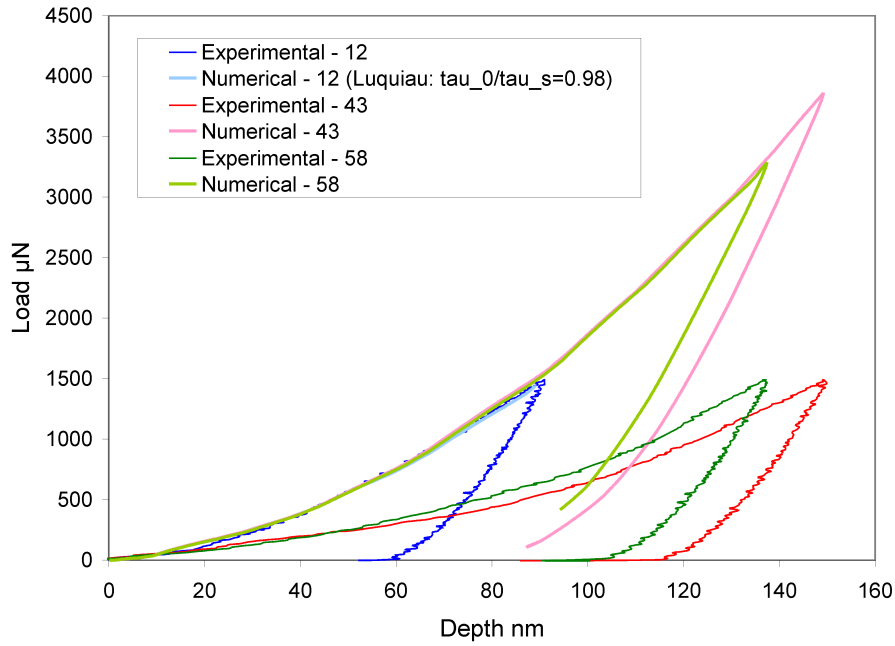


**Figure 10.14:** Nanoindentation: load versus displacement curves performed with  $\tau_0$  parameters from Luquiau (Table (10.5)),  $\tau_0/\tau_s = 0.98$  for the 12th (for which only the loading part is shown), 43rd and 58th indentations. The isotropic elastic parameters are  $E = 125$  GPa and  $\nu = 0.33$ . Comparison with experimental results.

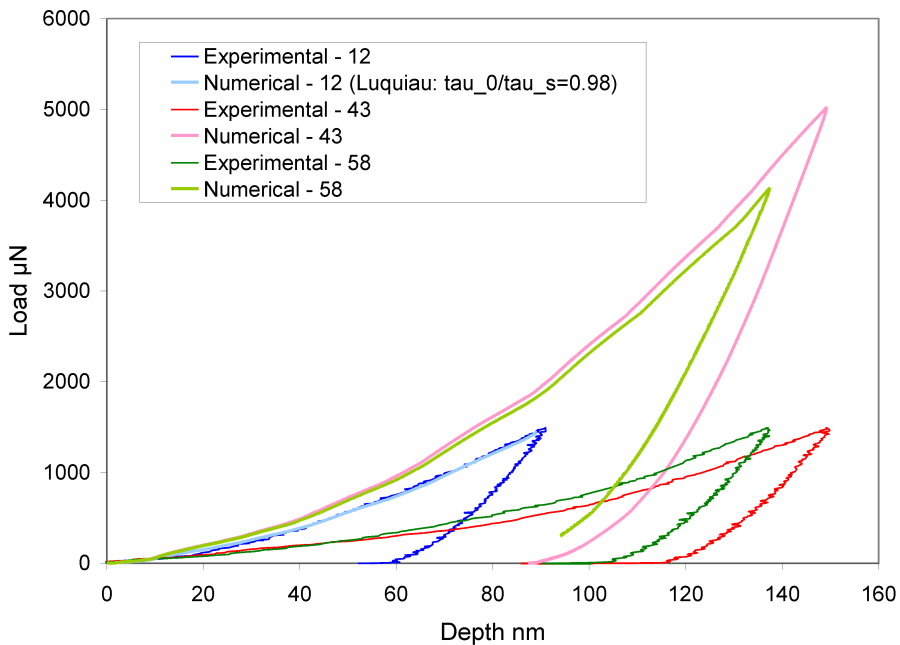


**Figure 10.15:** Nanoindentation: Numerical load versus displacement curves performed with  $\tau_0$  parameters from Luquiau (Table (10.5)),  $\tau_0/\tau_s = 0.98$  for the 12th (only the loading part), 43rd and 58th indentations. The elastic anisotropic parameters chosen are those from [Tri06], all multiplied by 1.31. Comparison with experimental results.

From Figure (10.14), where the isotropic elastic parameters are used, in contrast to what was observed during the experiments, numerical nanoindentation results seem to be unaffected by the grain orientation as already shown in Figure (10.11), while in Figure (10.15), it is observed that, using the anisotropic elastic parameters, numerical identification results are in fact affected by grain orientation.

### 10.5.5 Conclusions

By looking at the unloading part of the nanoindentation curves, the identification of isotropic elastic parameters ( $E$  and  $\nu$ ) is sufficient to model this section accurately. Nevertheless, it seems that these parameters are not adapted to model the loading part correctly since there was no effect of the grain orientation on numerical predictions.

In the next section, in which the plastic parameters are optimized, the isotropic elastic parameters are used. This choice was essentially guided by the experimental results in Figure (10.4) showing an identical unloading curve for all the indented grains and by the excessive and physically inappropriate elastic modulus ( $E_{average} \simeq 150$  GPa) necessary to model the experimental curve with anisotropic elastic parameters. These parameters correspond to the ones obtained by [Tri06] multiplied by 1.31. In the literature, the elastic modulus found for the  $\alpha$  phase is in the range of [115 - 125 GPa]. Moreover, the average Young's modulus obtained at UCL from 782 nanoindentation experimental tests on  $\alpha$  grains is equal to 102 GPa with a standard deviation of 31 GPa. This result seems to be underestimated<sup>6</sup> but it agrees with the choice of a moderate Young's modulus. Consequently, in the next section, a Young's modulus of 125 GPa will be used.

## 10.6 Identification of the plastic parameters

### 10.6.1 Literature review

#### Crystallographic slips in hexagonal materials

The different slip planes and slip directions commonly activated in HCP materials<sup>7</sup> are depicted in Table (10.6) and illustrated in Figure (10.16).

#### Activated slip systems and critical resolved shear stresses (CRSS)

It is not easy to find relative CRSS values for the slip systems of the  $\alpha$  phase of titanium. Usually, the values found in the literature for these relative CRSS are very different, as mentioned by [Dic06] for the  $\alpha$  phase of Ti6Al4V, where the author tried to explain these discrepancies by the differences in the purity of the alloy used, the supplementary treatments applied to the alloy, the history of fabrication and, particularly, the method used to identify the slip systems.

<sup>6</sup>Indeed, Young's modulus of the  $\beta$  phase is close to 80 GPa. For bimodal Ti-5553, Young's modulus obtained from macroscopic tests is equal to 115 GPa.

<sup>7</sup>For titanium, the  $c/a$  ratio has the value  $c/a = 1.587$  [BA02].

Slip systems	Number	Slip plane	Slip direction
Basal	3	(0001)	$\langle 11\bar{2}0 \rangle$
Prismatic	3	$\{10\bar{1}0\}$	$\langle 11\bar{2}0 \rangle$
Pyramidal $\langle \mathbf{a} \rangle$	6	$\{10\bar{1}1\}$	$\langle 11\bar{2}0 \rangle$
1st order Pyramidal $\langle \mathbf{c} + \mathbf{a} \rangle$	12	$\{10\bar{1}1\}$	$\langle 11\bar{2}\bar{3} \rangle$
2nd order Pyramidal $\langle \mathbf{c} + \mathbf{a} \rangle$	6	$\{11\bar{2}\bar{2}\}$	$\langle 11\bar{2}\bar{3} \rangle$

Table 10.6: Slip systems in HCP materials.

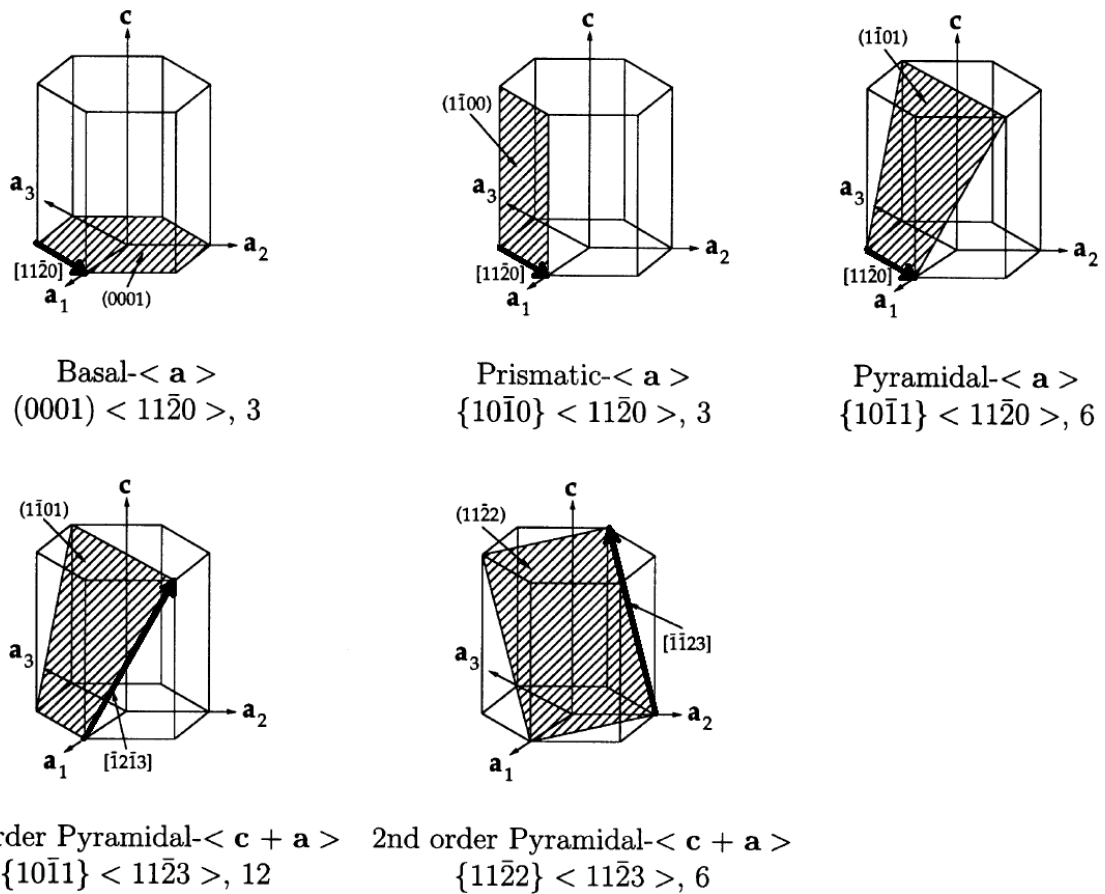
Figure 10.16: Basal  $\langle \mathbf{a} \rangle$ , prismatic  $\langle \mathbf{a} \rangle$ , pyramidal  $\langle \mathbf{a} \rangle$  slip systems, and first- and second-order pyramidal  $\langle \mathbf{c} + \mathbf{a} \rangle$  slip systems in HCP materials. Figure collected from [BA02].

Table (10.7) provides the reviewed values of CRSS of different HCP materials regarding the activated slip system.

Reference	Material	$\tau_c^{prism.<a>}$ (MPa/rel.)	$\tau_c^{basal<a>}$ (MPa/rel.)	$\tau_c^{pyram.<a>}$ (MPa/rel.)	$\tau_c^{pyram.<c+a>}$ (MPa/rel.)
Chan [Cha04]	Ti8Al1Mo1V	206.9	275.8	248.2	
Luquiau [Del05]	Ti10.2.3	200			1°: 350
Feaugas [FPC97]	Ti6246	380			1°: 615
Dick [Dic06]	Ti6Al4V	380	400		1°: 640
Fundenberger [FPWE97]	Ti6Al4V	1	3-6	3-6	1°: 4-10
Perilla [PS95]	Ti6Al4V	1	~ 1	~ 1	1°: ~ 1.4
Balasubramanian [BA02]	titanium (750°C)	1	1	1	1°: 10 2°: 10
Sanchez [SPCB01]	zirconium	1.0	4.0	2.0	1°: 8.0

**Table 10.7:** Initial CRSS (in MPa or relative values) of HCP materials collected in the literature. In the last column, values labelled "1°" correspond to initial CRSS of 1st order pyramidal <c+a> slip systems and values labelled "2°" correspond to initial CRSS of 2nd order pyramidal <c+a> slip systems. These slip systems are illustrated in Figure (10.16).

It is worth mentioning that in the implemented constitutive law subroutine<sup>8</sup>, only three sets of slip systems can be simultaneously activated. This is the reason why, in the next sections, no more than three sets of slip systems will be defined for a material.

### 10.6.2 First identification procedure of the plastic parameters

To identify the plastic parameters of the  $\alpha$  phase of Ti-5553 from nanoindentation curves, the following procedure is applied:

1. First identifications:

- Identification compared to the 12th experimental results (Figure (10.1)).
- The isotropic elastic parameters are those obtained in the previous section ( $E = 125$  GPa,  $\nu = 0.33$ ).
- The fourth indenter of Figure (10.7) is used.
- The plastic parameters found in the literature (Table (10.7)) are tried and predicted results are compared to experimental ones.

2. Some parameters will be optimized in order to obtain more accurate results for the grain orientation under consideration.

<sup>8</sup>Microscopic plasticity-based constitutive law subroutine written by Huang and modified by Kysar [Hua91]. This subroutine is further described in Chapter (4) of Part (II).

3. The optimized set of parameters will be compared against other indentation results performed on other grain orientations.
4. If necessary, the set of parameters will be adapted once again.

### 10.6.3 Simulations to identify the plastic parameters

Except for parameters  $\tau_s$  and  $\tau_0$ , plastic parameters used are those presented in Table (10.2). Several indentations were performed using the  $\tau_0$  parameter values provided in Table (10.7). For each slip system, a  $\tau_0$ -to- $\tau_s$  ratio of 0.95 is chosen, thus providing the value of  $\tau_s$ . The load versus displacement curves obtained with these parameters are presented in Figure (10.17) together with the experimental results of indentation 12. For these first simulations, the elastic parameters used are:

$$\begin{cases} E = 125 \text{ GPa} \\ v = 0.33 \end{cases} .$$

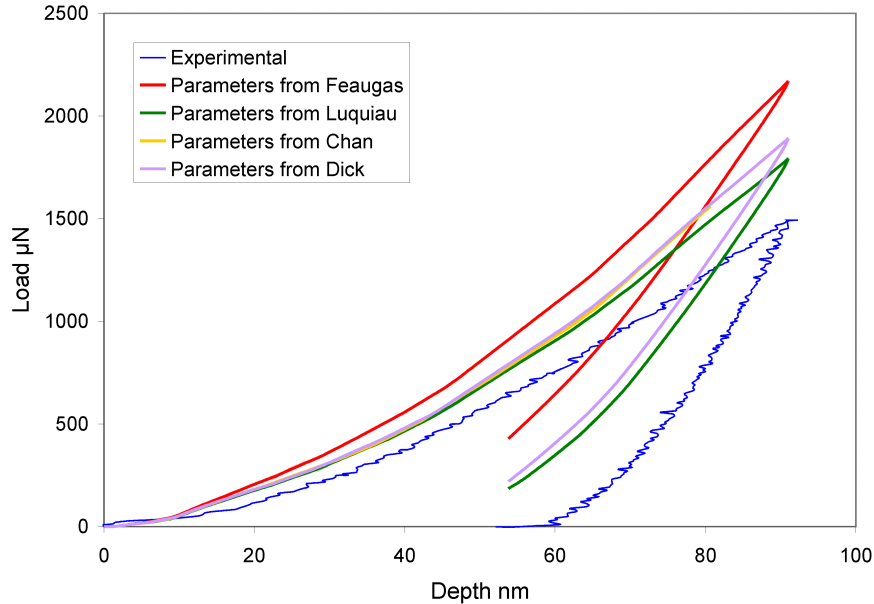


**Figure 10.17:** Load versus displacement nanoindentation curves performed with  $\tau_0$  parameters from literature (Table (10.7)) and comparison with experimental results of indentation 12.

It can be seen in Figure (10.17) that Luquiau's set of parameters provides better results in comparison to the experimental ones. Consequently, it was decided to perform a simulation using the activated slip systems and the corresponding  $\tau_0$  values of Luquiau with  $\tau_0/\tau_s = 0.98$  instead of the ratio of 0.95, used in Figure (10.17). Modifying this ratio was influenced by the sensitivity analysis performed in Chapter (7) of Part (III). The resulting load versus displacement curves (experimental and numerical ones) are provided in Figure (10.18).

The numerical results obtained with these parameters show an excellent correlation with the experimental ones for the 12th indentation. This set of parameters was then tested considering other grain orientations with the isotropic elastic parameters. The obtained results are

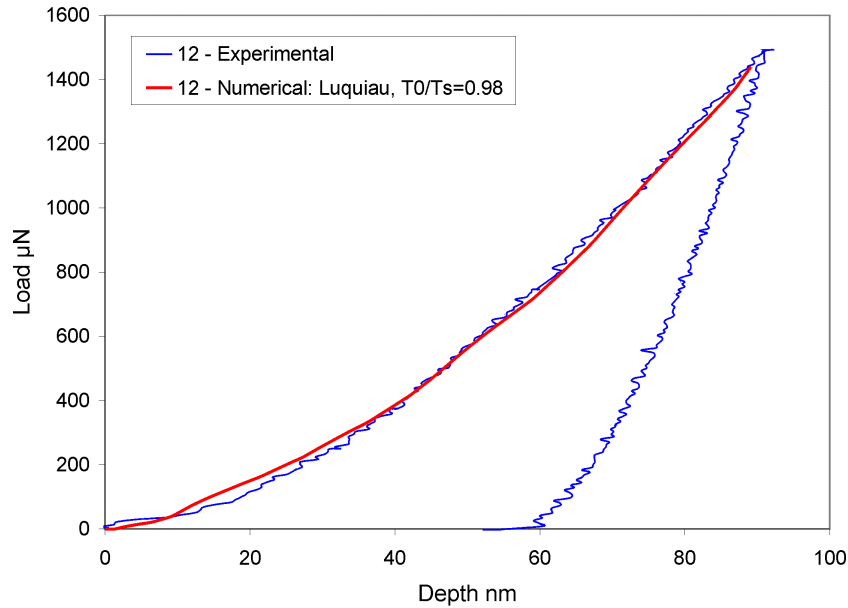


**Figure 10.18:** Load versus displacement nanoindentation curves performed with Luquiau's  $\tau_0$  parameters (Table (10.7)) and  $\tau_0/\tau_s = 0.98$ . Comparison with experimental curve 12.

presented in Figure (10.19).

It can be seen from Figure (10.19) that, contrary to the experimental curves, the numerical nanoindentation results seem to be unaffected by the grain orientations. Moreover, the numerical results for grains 43 and 58 do not correspond well with the experimental ones. This is the reason why another procedure of identification is investigated in the next section.

#### 10.6.4 Second identification procedure of the plastic parameters

The objective of this second procedure is to identify the slip systems activated in priority for each grain orientation. The numerical simulations were also performed with the isotropic elastic parameters ( $E = 125$  GPa and  $\nu = 0.33$ ). For that purpose, the following steps were followed:

1. The simulations were performed on three grain orientations. Three sets of slip systems were arbitrarily chosen to be activated (all with the same initial CRSS and saturation values). All the other parameters of the hardening law were the same as in each previous set of slip systems.
2. Using the numerical results, the activated slip systems were detected for each grain orientation.
3. These results were then used to choose the initial CRSS for each set of slip systems in order to improve the modeling of all grain orientations.

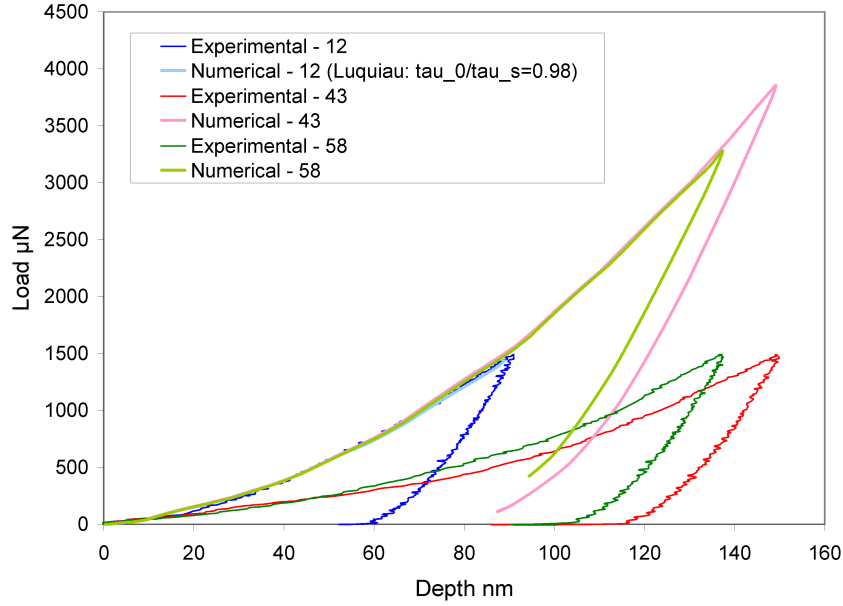


**Figure 10.19:** Load versus displacement nanoindentation curves performed with Luquiau's  $\tau_0$  parameters (Table (10.7)) and  $\tau_0/\tau_s = 0.98$  for 12th, 58th and 43rd indentations. The elastic parameters are  $E = 125$  GPa and  $\nu = 0.33$ . Comparison with experimental results.

### Application

The set of slip systems that could be active in each simulation are given in Table (10.8). These simulations were performed for three different grain orientations, corresponding to indentations 12, 43 and 58, for a total of nine simulations.

Simulation	Sets of slip systems
1	Basal, prismatic and pyramidal $\langle a \rangle$
2	Basal, prismatic and pyramidal $\langle c+a \rangle$
3	Basal, pyramidal $\langle a \rangle$ and pyramidal $\langle c+a \rangle$

**Table 10.8:** Set of slip systems that could be activated in simulations 1, 2 and 3.

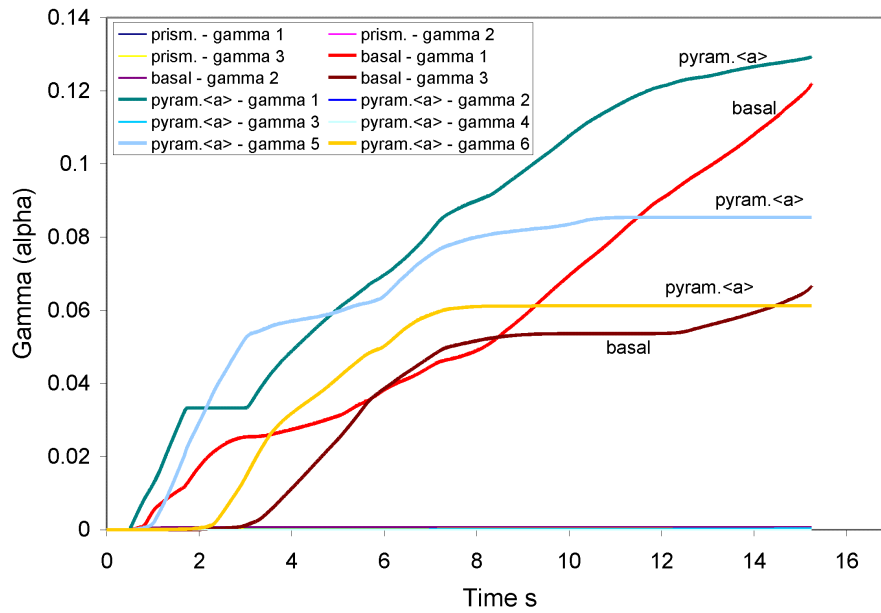
During the loading of these nanoindentation simulations, the shear strain of each slip system was recorded. An example of the results obtained is shown in Figure (10.20) for indentation number 12 and for the basal, prismatic and pyramidal  $\langle a \rangle$  slip systems<sup>9</sup>. The other curves are given in Appendix (N).

For each simulation, the observations are summarized below and illustrated in Table (10.9).

1. For simulation 1,

<sup>9</sup>The results were obtained from one element under the indenter tip.















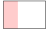
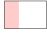


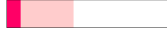






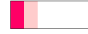





**Figure 10.20:** Indentation 12. Shear strain on each slip system that can be activated during the loading of a nanoindentation test. The slip systems that can be activated are the 3 basal systems, the 3 prismatic systems and the 6 pyramidal  $\langle a \rangle$  systems.

- the pyramidal  $\langle a \rangle$  slip systems were highly active in the three grains. In indentations 43 and 58, this is clearly the most active set of slip systems;
  - the basal slip systems were also highly activated in the 12th indentation;
  - the prismatic slip systems were somewhat activated in indentation 43 and slightly more in indentation 58.
2. For simulation 2,
    - In indentation 12, the pyramidal  $\langle c+a \rangle$  slip systems were the most activated, followed by the basal ones;
    - For indentations 43 and 58, the basal slip systems were the most activated. The pyramidal  $\langle c+a \rangle$  ones were also activated but to a lesser degree.
  3. For simulation 3,
    - In indentation 12, the pyramidal  $\langle c+a \rangle$  slip systems were the most activated, followed by the basal ones and, thirdly, the pyramidal  $\langle a \rangle$  ones;
    - For indentation 43, the three slip systems were similarly activated but with one more slip for the pyramidal  $\langle a \rangle$  ones at high values of  $\gamma^{(a)}$ ;
    - For indentation 58, the basal slip systems were the most activated, followed by the pyramidal  $\langle a \rangle$  ones and, finally, the pyramidal  $\langle c+a \rangle$  ones.

In Table (10.9), each rectangle represents the set of slip systems that could be activated. The size of the rectangles is linked to the maximum number of slip systems in a corresponding

set. The colors in the rectangles are linked to the number of slip systems activated during the test. Red color corresponds to a highly activated slip system (high shear strain), pink represents the slip systems activated in a second position, and finally, white means that the corresponding slip systems were not activated during this test.

Simulation	Set of slip systems	indent 12	indent 43	indent 58
1	Basal (3)			
	Prismatic (3)			
	Pyramidal $\langle a \rangle$ (6)			
2	Basal (3)			
	Prismatic (3)			
	Pyramidal $\langle c+a \rangle$ (12)			
3	Basal (3)			
	Pyramidal $\langle a \rangle$ (6)			
	Pyramidal $\langle c+a \rangle$ (12)			

**Table 10.9:** Summary of the number of slip systems activated for the three simulations in three orientations. Red color means that the corresponding number of slip systems in one set are highly activated, pink is associated with corresponding slowly activated slip systems and white is for slip systems that were not activated.

The corresponding load versus indentation depth curves obtained from the numerical simulations performed with the different slip systems (simulations 1, 2, 3) are provided in Figure (10.21).

From this figure, it is clear that the differences in the results (regarding different grain orientations) were higher when the prismatic, basal and pyramidal  $\langle a \rangle$  sets of slip systems (simulation 1) could be activated. Indeed, the blue, red and green curves are considerably different. However, the other sets of slip systems lead to nearly the same results for different grain orientations.

### Basal - prismatic - pyramidal $\langle a \rangle$ slip systems with different values of $\tau_0$

As depicted above in Figure (10.21), only the choice of the basal, prismatic and pyramidal  $\langle a \rangle$  sets of slip systems shows results that are greatly affected regarding different grain orientation, as observed experimentally.

Thanks to this observation, this set of slip systems capable of being activated was chosen. Several simulations were performed with different  $\tau_0$ -to- $\tau_s$  ratios using these sets of slip systems. Some<sup>10</sup> of the tested ratios are given in Table (10.10) and the corresponding results can be found in Figures (10.22), (10.23), (10.24) and (10.25). These values were selected from the range observed in Table (10.7) but also for exploration purposes and as determined by the

<sup>10</sup>Other parameters tested can be found in Appendix (P).

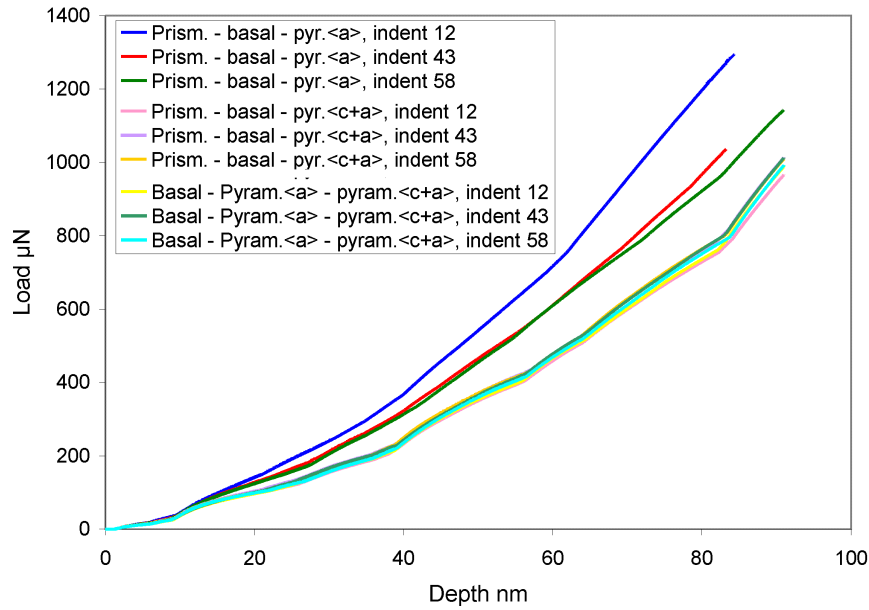


**Figure 10.21:** Load versus displacement nanoindentation curves (loading only) in three different grain orientations and with different slip systems that could be activated (all with the same initial and saturation shear stresses).

first results.

	$\tau_{0_{prism.}}$	$\tau_{0_{basal}}/\tau_{0_{prism.}}$	$\tau_{0_{pyram.<a>}}/\tau_{0_{prism.}}$
Param. 1	200	1	0.25
Param. 2	250	1	0.18
Param. 3	50	4	2
Param. 4	45	6.666	1.111
Param. 5	45	6.666	3.333
Param. 6	20	20	5
Param. 7	10	50	12

**Table 10.10:** Ratio of the CRSS between the different sets of slip systems to identify the  $\alpha$  phase of Ti-5553.

Some parameters provide quite accurate results but never accurately model the three curves. It seems to be necessary to choose between an accurate modeling of indentation 12 or an accurate modeling of indentations 43 and 58. In the end, parameters set 3 was chosen as the best compromise to model experimental results.

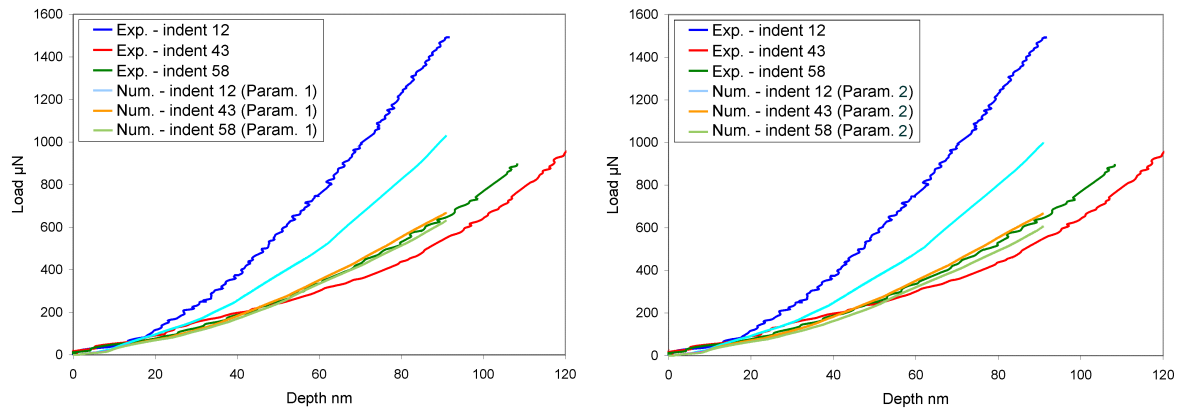


**Figure 10.22:** Simulation of nanoindentations (loading phase only) 12, 43 and 58 and comparison with experiments. The CRSS of slip systems (basal, prismatic and pyramidal  $\langle a \rangle$ ) are provided in Table (10.10).

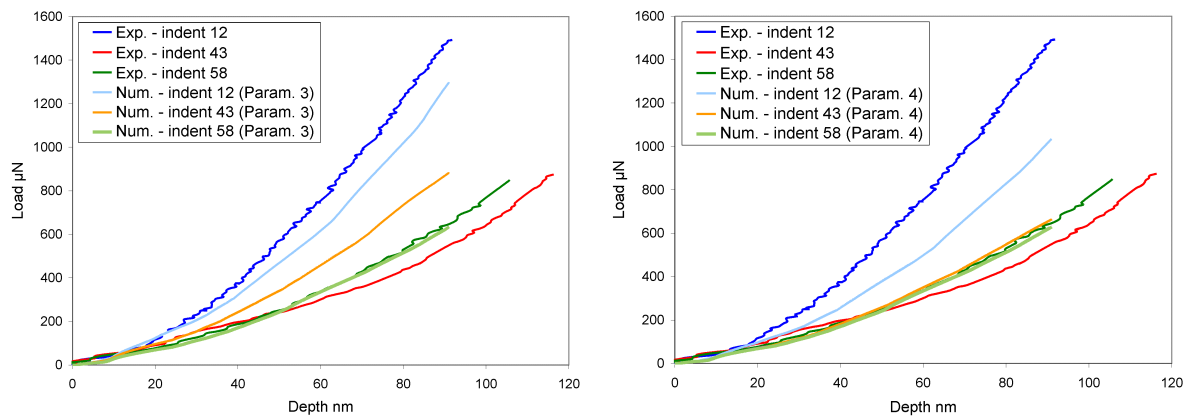


**Figure 10.23:** Simulation of nanoindentations (loading phase only) 12, 43 and 58 and comparison with experiments. The CRSS of slip systems (basal, prismatic and pyramidal  $\langle a \rangle$ ) are provided in Table (10.10).

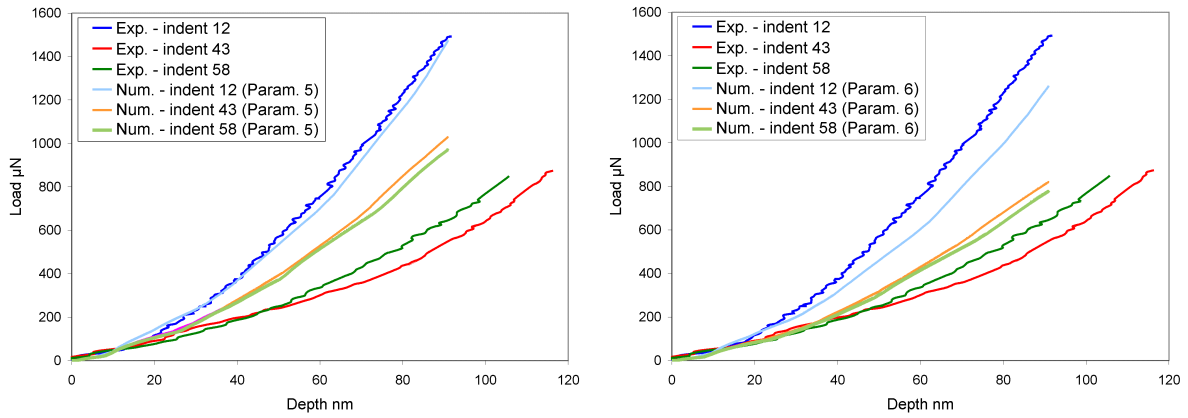


**Figure 10.24:** Simulation of nanoindentations (loading phase only) 12, 43 and 58 and comparison with experiments. The CRSS of slip systems (basal, prismatic and pyramidal  $\langle a \rangle$ ) are provided in Table (10.10).

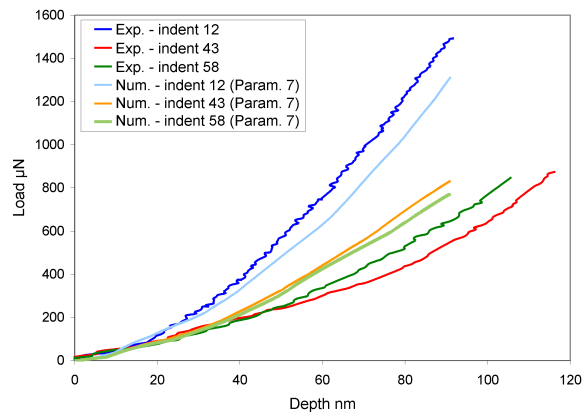


**Figure 10.25:** Simulation of nanoindentations (loading phase only) 12, 43 and 58 and comparison with experiments. The CRSS of slip systems (basal, prismatic and pyramidal  $\langle a \rangle$ ) are provided in Table (10.10).

In Appendix (O), different values of CRSS were also tested for the basal, pyramidal  $\langle a \rangle$  and pyramidal  $\langle c+a \rangle$  sets of slip systems. As observed above in Figure (10.21), the influence of the grain orientation is nearly non-existent. Thus, it seems impossible to model the experimental behavior with these combined sets of slip systems.

Consequently, a set of parameters providing satisfactory results against all grain orientations is chosen. These parameters are given in Table (10.11).

Parameters		Value		
<b>Elastic parameters</b>	$E$ (GPa)	125		
	$\nu$	0.33		
<b>Plastic parameters</b> <i>for all slip systems</i>	$n$	50		
	$\dot{a}$	0.001		
	$h_0$	7482		
	$h_s$	3		
	$\gamma_{0\alpha}$	0.00091		
	$\gamma_{0\alpha\beta}$	0.000314		
	$f_{\alpha\alpha}$	14.6		
	$f_{\alpha\beta}$	15.0		
<b>Plastic parameters</b> <i>by set of slip systems</i>	$\tau_0$	200 (basal)	50 (prism.)	100 (pyr. $\langle a \rangle$ )
	$\tau_s$	202 (basal)	50.5 (prism.)	101 (pyr. $\langle a \rangle$ )

**Table 10.11:** Elastic and plastic parameters optimized to characterize the  $\alpha$  phase of Ti-5553. The three sets of slip systems that can be activated are the basal, the prismatic and the pyramidal  $\langle a \rangle$  ones.

The results obtained with this set of parameters are shown in Figure (10.26); there, the results are also shown for a fourth orientation (indentation 31 of Table (10.1)). The numerical simulations provide a relatively accurate description of the experimental curves for all grain orientations, although none of these curves is predicted to an acceptable level.

## 10.7 Conclusions

This chapter presents the procedure and the results obtained to identify the  $\alpha$  phase of Ti-5553. Due to the difficulty in using typical experimental macroscopic tests (such as tensile tests or shear tests) to identify this phase, nanoindentation experimental tests were performed on several  $\alpha$  grains of different orientations.

Firstly, the experimental tests used for the identification were selected from a set of more than 130 experiments considering the orientation of the grain to be indented and the reproducibility of the results.

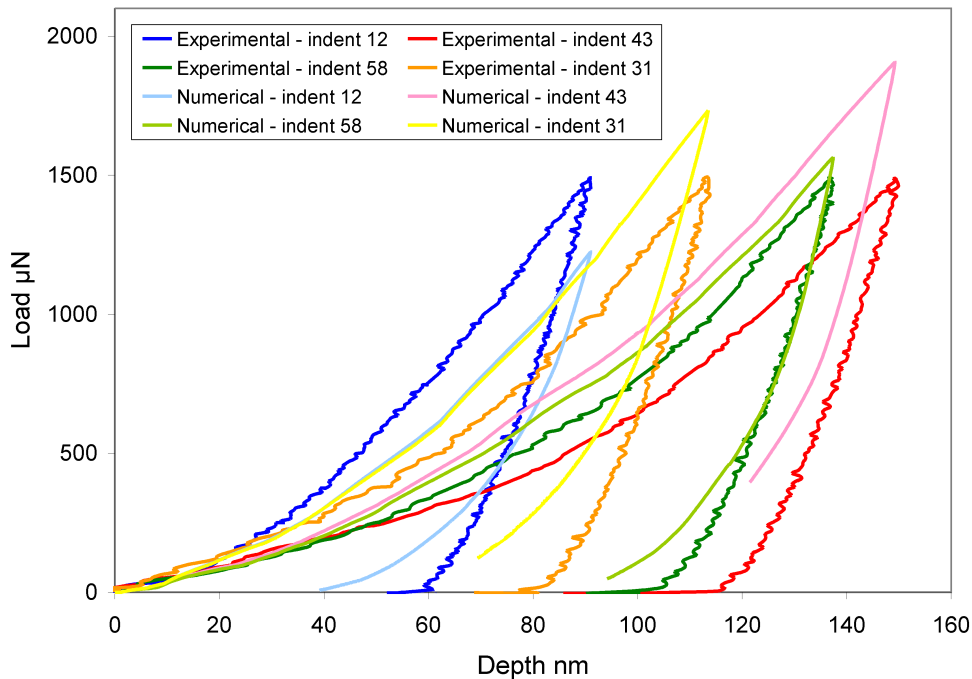


**Figure 10.26:** Experimental and numerical nanoindentation load versus displacement curves in four different grain orientations (numbers 12, 31, 43 and 58 of Table (10.1)). Numerical tests were performed with the parameters from Table (10.11).

The next stage served to identify the elastic parameters using the unloading curves. The influence of the tip geometry on the unloading curves was studied as well as the use of isotropic or anisotropic elastic parameters. Looking at the elastic unloading part of the nanoindentation experimental curves, the identification of the isotropic elastic parameters ( $E$  and  $\nu$ ) was demonstrated to be sufficient. Moreover, the values chosen ( $E = 125$  GPa,  $\nu = 0.33$ ) correspond to those usually found in the literature.

Finally, the complicated characterization of the plastic parameters was conducted. A first procedure was tested using the parameters collected in the literature as reference parameters. Due to the inefficiency of this method, another procedure proposed by the author was conducted. In this method, for each grain orientation, the slip systems activated were detected. These systems were then used to determine the corresponding parameters (CRSS) leading to the closest representation of the experimental results.

A great number of sets of parameters were tested and only a few of them are presented in this chapter. None of them has been able to characterize the experimental nanoindentation curves obtained for several grain orientations in an accurate way. As a consequence of this, the author has chosen another set of parameters that represent the three curves in a relatively satisfactory way. This set of parameters will be used in the next section, in which simulations will be performed on  $(\alpha + \beta)$  representative cells.





Part V

Representative cells of Ti-5553



## Chapter 11

# Representative cells of Ti-5553 - Choice and modeling

### 11.1 Introduction

The main goal of this chapter consists in using the results obtained in the previous chapters concerning the identification of the  $\alpha$  and the  $\beta$  phases in order to numerically simulate representative cells of Ti-5553 containing these two phases.

To carry out such simulations, the periodic homogenization technique described in Chapter (6) of Part (II) is used. The parameters of the microscopic constitutive law for the  $\alpha$  and the  $\beta$  phases are those obtained from the material characterization of these two phases (Part (III) and Part (IV)). No interface elements between the  $\alpha$  and the  $\beta$  phase were defined, as the continuity of the field displacement is total. No sliding or decohesion modeling is possible in these simulations.

The final goal of these modelings is to study the influence of several parameters on the mechanical behavior of the representative material and, thus, to determine the most appropriate microstructure for a particular application.

In this context, two microstructures of the ( $\alpha + \beta$ ) material were chosen. Firstly, these microstructures are described, after which the corresponding simplified meshes are presented and compared. In the next section, numerical simulations of these representative cells are considered. To begin this discussion, the presence of the  $\alpha$  and the  $\beta$  phases or only the  $\beta$  phase in the representative cell is studied. Secondly, numerical simulations on representative cells containing different shapes of the  $\alpha$  phase inside the  $\beta$  matrix are compared. After that, the influence of the loading direction on two microstructures is commented upon and, finally, the influence of the orientation of the  $\alpha$  phase in the cell is studied. Throughout the discussion, results obtained are presented and compared in this chapter.

## 11.2 Choice of the microstructures to define representative cells

### 11.2.1 First microstructure

#### Characteristic

The first microstructure was obtained with the thermal treatment depicted in Figure (11.1). The sample was quickly heated just below  $T_\beta$  and was maintained for 30 minutes at this temperature. After that, the sample was quenched.

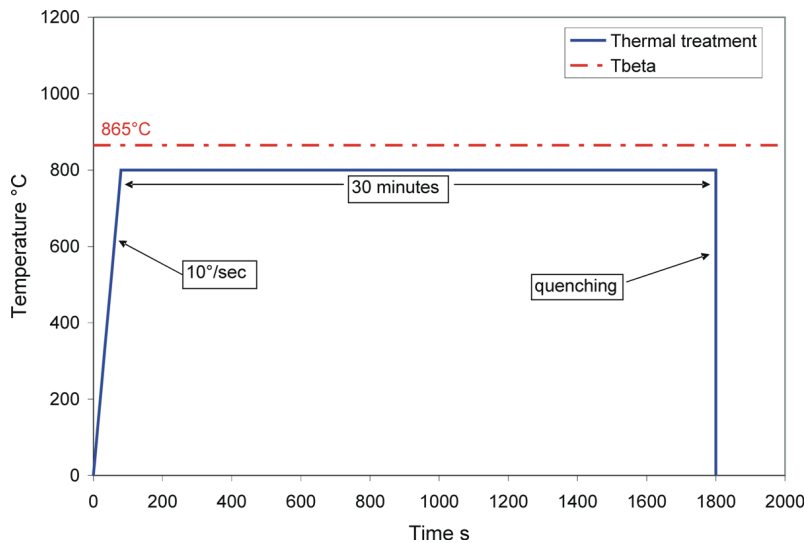


**Figure 11.1:** Thermal treatment (n°1) used to obtain the first microstructure.

This thermal treatment provides the microstructure seen in Figure (11.2), with globules of  $\alpha$  phase within the  $\beta$  phase. The diameter of these globules is between 1 and 3  $\mu\text{m}$ . This microstructure contains 11% of  $\alpha$  phase.

#### Mesh

The first microstructure was simplified to a globular  $\alpha$  phase inside the  $\beta$  matrix. The total volume of the 3D cubic shape representative cell is  $5\ \mu\text{m} * 5\ \mu\text{m} * 5\ \mu\text{m}$ . The spherical  $\alpha$  phase was meshed with 2401 elements and the  $\beta$  phase with 1176 elements for a total of 3577 eight-node brick elements<sup>1</sup> in the total representative cell. The elements of the external boundary of the mesh of the representative cell are shown in Figure (11.3) and views of the internal mesh are shown in Figures (11.4). The first one (a) is a cross section along a plane ( $z = \text{constant}$ ), showing the spherical  $\alpha$  phase inside the  $\beta$  matrix. The two other figures ((b) and (c)) are parts of the same mesh. The elements associated with each phase are represented.

Numerically, the different characteristics of the two phases are taken into account by the definition of two sets of constitutive law parameters. Initially, the elements associated with one particular phase have the same crystallographic orientation.

<sup>1</sup>See element BWD3D, Appendix (E).

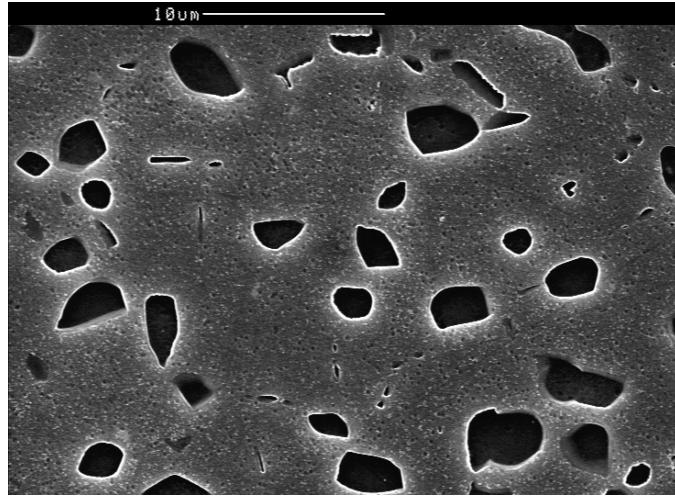


**Figure 11.2:** First microstructure, obtained with the thermal treatment of Figure (11.1).

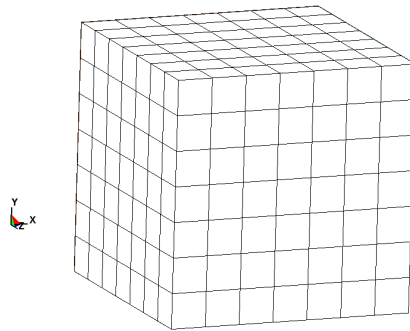


**Figure 11.3:** Mesh of the representative cell of the first microstructure: one globular  $\alpha$  grain in a  $\beta$  matrix.

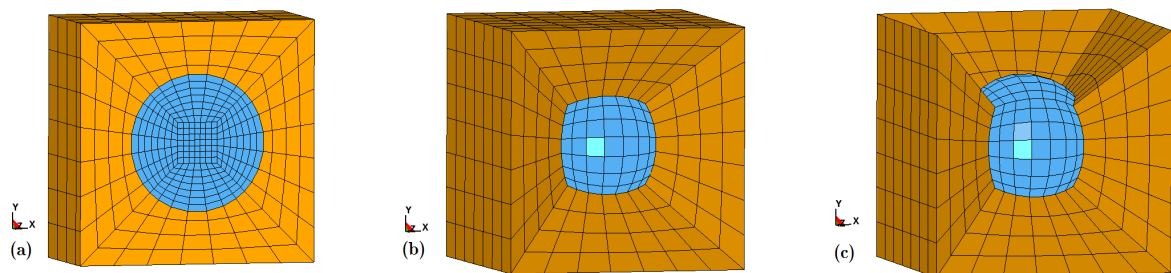


**Figure 11.4:** Representative cell of the first microstructure: one globular  $\alpha$  grain inside a  $\beta$  matrix. (a) Cross section along a ( $z = \text{constant}$ ) plane that shows the mesh inside the cell. (b),(c) Parts of the mesh: the  $\alpha$  phase in the (blue) globular part, in the middle, and the surrounding  $\beta$  phase (in orange).

## 11.2.2 Second microstructure

### Characteristic

The second microstructure was obtained with the thermal treatment described in Figure (11.5). The sample was slowly heated up to a temperature just above  $T_{\beta}$  and was maintained for 30 minutes at this temperature. Then, it was slowly cooled to  $600^{\circ}\text{C}$  and was finally quenched.

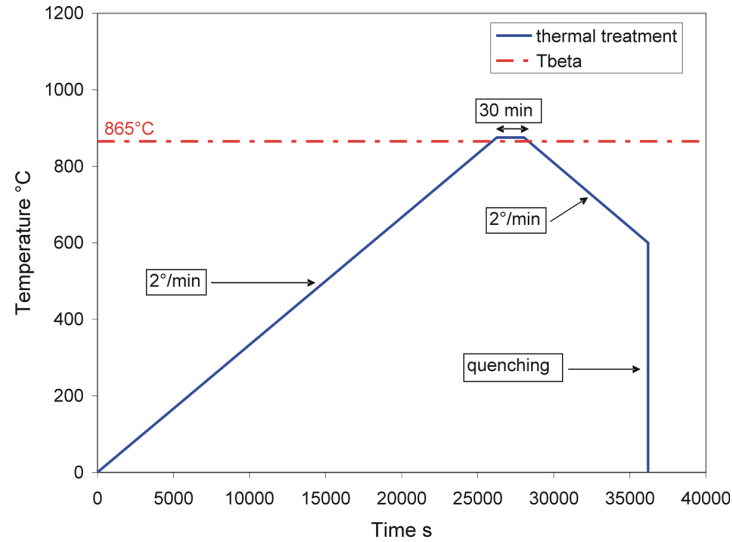


**Figure 11.5:** Thermal treatment ( $n^{\circ}2$ ) used to obtain the second microstructure.

This microstructure (Figure (11.6)) is composed of thin  $\alpha$  plates inside the  $\beta$  matrix.

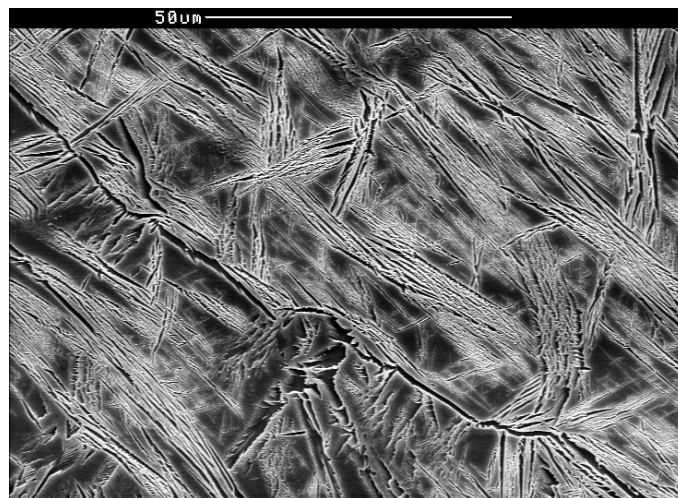


**Figure 11.6:** Second microstructure, obtained with the thermal treatment described in Figure (11.5).

## Mesh

The modeling of the exact shape of the two phases seen in Figure (11.6) containing  $\alpha$  plates inside the  $\beta$  matrix is not possible with the available mesh generator and computer at the author's immediate access. The representative microstructure was simplified to one elongated  $\alpha$  grain in the  $\beta$  matrix. The influence of the shape of the  $\alpha$  phase in the representative cell will be studied. The corresponding mesh is shown in Figure (11.7). The  $\alpha$  phase was meshed with 2232 elements and the  $\beta$  phase with 1248 elements, for a total of 3480 eight-node brick elements in the representative cell. As in the previous case, the proportion of  $\alpha$  phase is 11% of the cell.

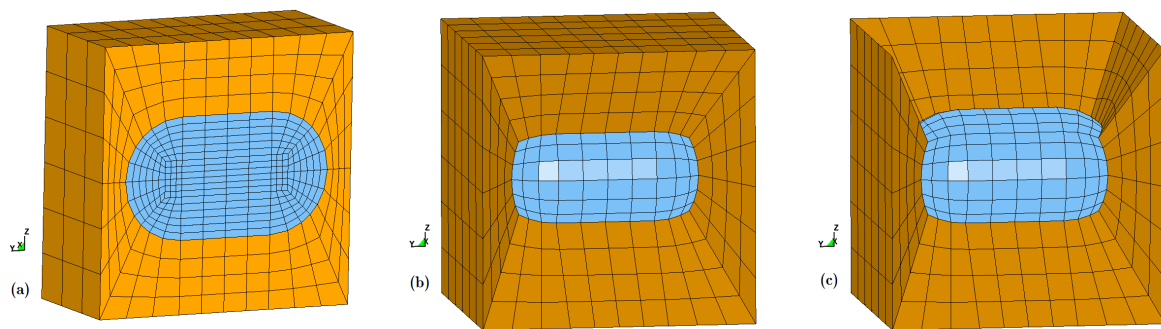


**Figure 11.7:** Representative cell of the second microstructure: an elongated  $\alpha$  phase inside a  $\beta$  matrix. (a) Cross section along a  $x$  plane that shows the mesh inside the cell. (b),(c) Parts of the mesh: the  $\alpha$  phase in the (blue) part, in the middle, and the surrounding  $\beta$  phase (in orange).

### 11.2.3 Comparison between the two meshes

The two images in Figure (11.8) show a cross section at the center of the two meshes presented above. The volume of the internal  $\alpha$  part is 11% of the total volume of the representative cell in each case. Moreover, the external size of the cells is the same for the two meshes in each direction and the total number of elements in each mesh is nearly identical (3577 vs 3480). The ratios between the length and the height of the inclusion are noted in Table (11.1).

Mesh	$L/l$ ratio
(a) globular $\alpha$	1
(b) elongated $\alpha$	1.78

**Table 11.1:** Ratios between the greatest length ( $L$ ) of the inclusion and the smallest one ( $l$ ) for the two meshes in Figure (11.8).

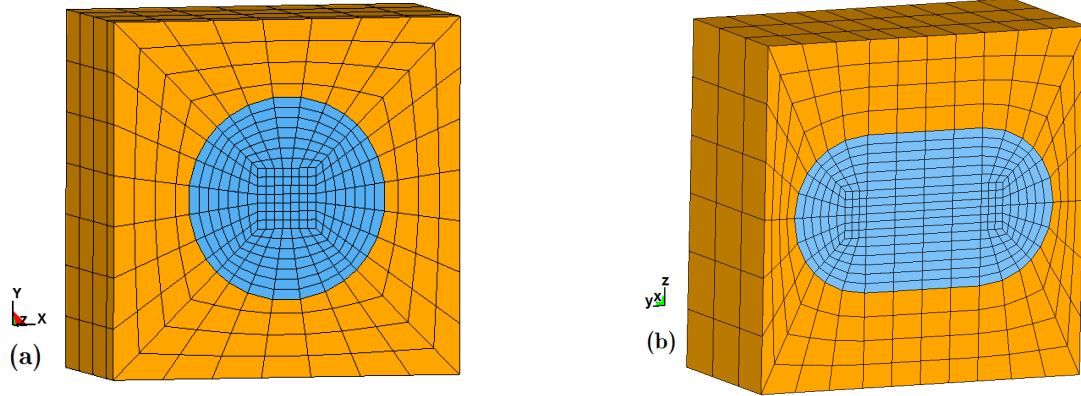


**Figure 11.8:** Cross sections in the representative cells of the two microstructures. (a) Globular  $\alpha$  and (b) coarse plate  $\alpha$ .

### 11.3 Numerical simulations of representative cells: presentation of the tests

Numerical simulations were performed to study the effect of the appearance of the  $\alpha$  phase in the  $\beta$  matrix and the influence of the former's orientation and shape.

The microstructures used for numerical simulations were described in the section above. In this section, the loading phases on the structures and the orientations of the phases are presented.

Two macroscopic loading phases were defined. For the first loading phase, the macroscopic velocity gradient  $\mathbf{L}$  is defined by<sup>2</sup>

$$\mathbf{L}_1 = \begin{pmatrix} -0.3 & 0 & 0 \\ 0 & 0.6 & 0 \\ 0 & 0 & -0.3 \end{pmatrix}. \quad (11.1)$$

This loading corresponds to a tensile test in the  $Y$  direction. The second loading corresponds to a tensile test in the  $X$  direction:

$$\mathbf{L}_2 = \begin{pmatrix} 0.6 & 0 & 0 \\ 0 & -0.3 & 0 \\ 0 & 0 & -0.3 \end{pmatrix}. \quad (11.2)$$

Each loading was applied for one second in the numerical simulations. The constitutive law used was microscopic plasticity-based constitutive and the parameters used for both phases were those optimized in previous chapters<sup>3</sup>.

<sup>2</sup>For a simulation performed for one second, this corresponds to a macroscopic strain of 60% in the tensile direction.

<sup>3</sup>For the  $\beta$  phase, this consists of the parameters found in Table (7.7) in Chapter (7) of Part (III), and for the  $\alpha$  phase, those in Table (10.11) in Part (IV).



The periodic conditions were imposed as follows:

- One node is fixed to avoid rigid-body motion. In this case, one corner is imposed (position  $(0, 0, 0)$ ) at which there is no displacement.
- Due to periodic relations, the periodic displacement of the other corner nodes is imposed to be equal to that of the first node (i.e. no periodic displacement).
- The corresponding nodes on the faces and on the edges<sup>4</sup> have the same periodic displacement.

Moreover, two orientations of the  $\alpha^5$  grain compared to that of  $\beta$  were defined in order to study the orientation effect on the representative cell's behavior (Table (11.2)). The difference introduced between the two grain orientations is that the  $\vec{c}$  axis of the hexagonal phase is along the global  $Z$  direction in the first case and along the  $Y$  direction in the second case (see Figure (11.9)).

Phase	First local axis	First global axis	Second local axis	Second global axis
$\beta$	(100)	(100)	(0 10)	(0 10)
$\alpha$ (1)	(100)	(100)	(0 10)	(0 10)
$\alpha$ (2)	(100)	(100)	(0 0 1)	(0 10)

**Table 11.2:** Orientations of the phases in the representative cell: the  $\beta$  matrix and two orientations for the  $\alpha$  phase. Two local and corresponding global (macroscopic) axes are given.

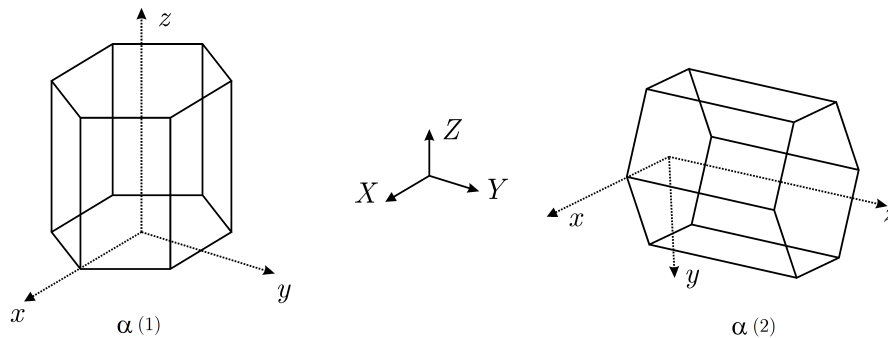


**Figure 11.9:** Orientation of the  $\alpha$  phase ( $\alpha(1)$  and  $\alpha(2)$ ) in the global  $(XYZ)$  axes.

## 11.4 Results and comparison

To compare the different representative cells, it was decided to inspect Von Mises' stress and strain and to compare the qualitative behavior of the cells.

<sup>4</sup>See Chapter (6) in Part (II) for further explanations.

<sup>5</sup>Generally, for a hexagonal material, four components are given, but these four dependent components can be expressed in the orthogonal axes as was illustrated previously (see Figure (4.5) of Chapter (4) in Part (II)).

### 11.4.1 Influence of the presence of the $\alpha$ phase in the representative cell

In this paragraph, two numerical simulations are examined to study the presence of the  $\alpha$  phase in the cell. In the first one, the sample was composed of only the  $\beta$  phase. In the second one, the representative cell was composed of the two phases (corresponding to the first microstructure). These numerical simulations were performed with the first loading phase presented in the section above and the orientation of the  $\alpha$  phase is the first one of Table (11.2).

Von Mises' strain and stress are given inside the samples in Figures (11.10) and (11.11). In the figures on the left, the sample is composed only of the  $\beta$  phase. In the figures on the right, the globular elements of the first microstructure correspond to the  $\alpha$  phase and the others are  $\beta$ .

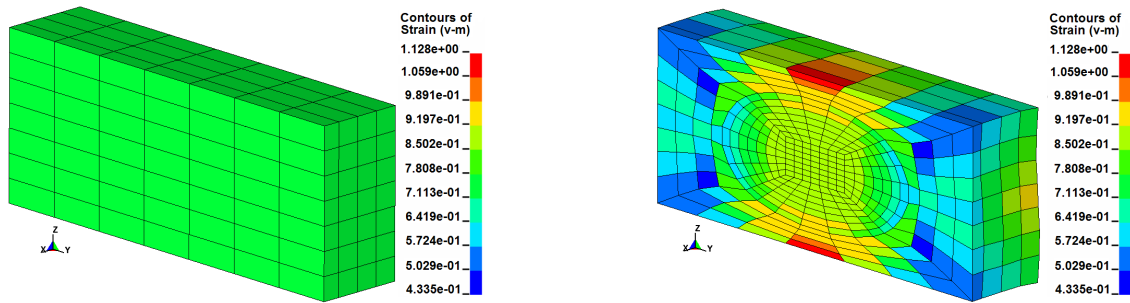


**Figure 11.10:** Von Mises' strain in the deformed configuration and the first loading. (Left) 100%  $\beta$  sample, (right) globular  $\alpha$  inside the  $\beta$  matrix.

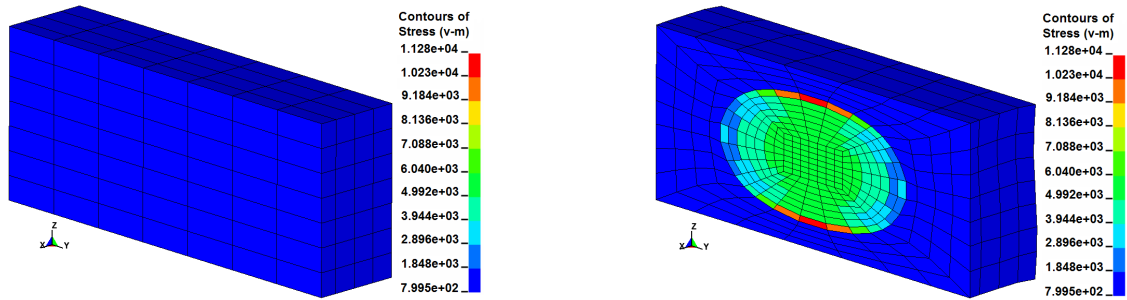


**Figure 11.11:** Von Mises' stress (MPa) in the deformed configuration and the first loading. (Left) 100%  $\beta$  sample, (right) globular  $\alpha$  inside the  $\beta$  matrix.

As expected, results were homogeneous in the 100 %  $\beta$  sample, which was not the case in the ( $\alpha + \beta$ ) representative cell in which  $\alpha$ 's presence leads to a stress concentration.

Figure (11.12) provides Von Mises' stress versus strain in both samples. These were obtained from the macroscopic stress and strain made available with the periodic homogenization technique.

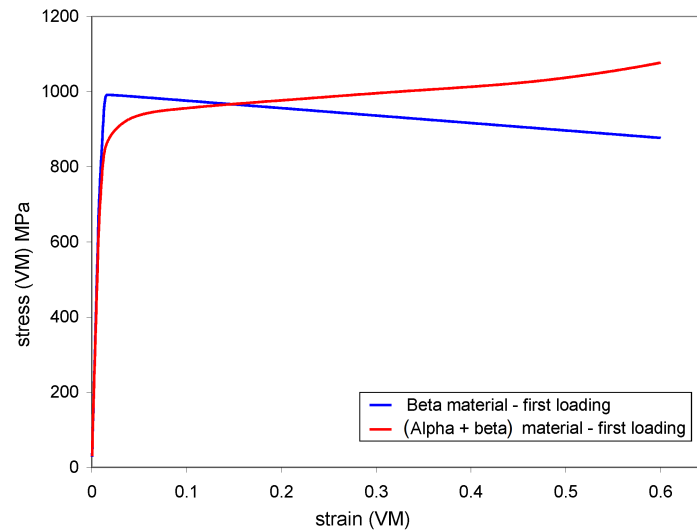


**Figure 11.12:** Von Mises' macroscopic stress versus strain for the 100%  $\beta$  and  $(\alpha + \beta)$  samples.

Just as experimental conditions (see Figure (11.13)) during a simple tensile test on a 100 %  $\beta$  sample with a sufficiently high strain rate (here,  $0.6 \text{ s}^{-1}$ ), the numerical simulation of a  $\beta$  material presents a softening behavior. By contrast, in the case of an  $(\alpha + \beta)$  representative cell, the material hardens.

This behavior is not surprising. Indeed, as shown in Figure (11.14) for a tensile test performed with one finite element and with the parameters of the  $\alpha$  phase, the material hardens.

However, the change in ductility observed experimentally between these two materials was not reproduced numerically. This is due to the lack of damage and rupture criterion in the model. Moreover, the yield strength obtained numerically was different from the experimental one. Indeed, experimentally, the yield stress of the  $(\alpha + \beta)$  materials was higher than for the  $\beta$  material. Numerically, there is not a great difference between the yield stress of the two materials and the  $\beta$  material gives the greatest value of this parameter. However, the next sections show the importance of the orientation of the  $\alpha$  phase compared to that of  $\beta$  in the results.

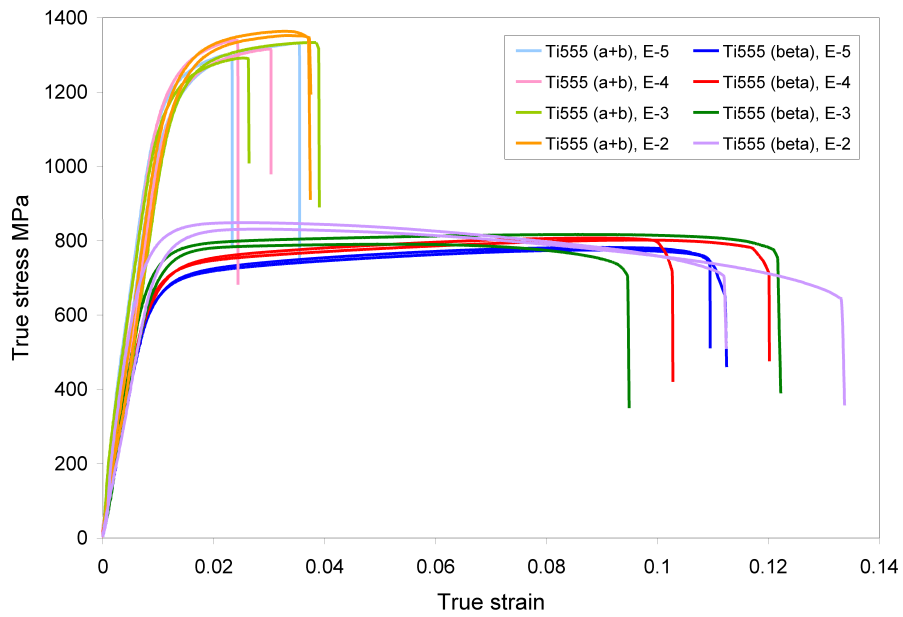


**Figure 11.13:** Experimental tensile tests on the tempered (100%  $\beta$ ) and the as-received ( $\alpha + \beta$ ) materials at different strain rates ranging from  $\dot{\epsilon} = 10^{-5} \text{ s}^{-1}$  up to  $10^{-2} \text{ s}^{-1}$ . True stress versus true strain curves. Each test was performed twice.

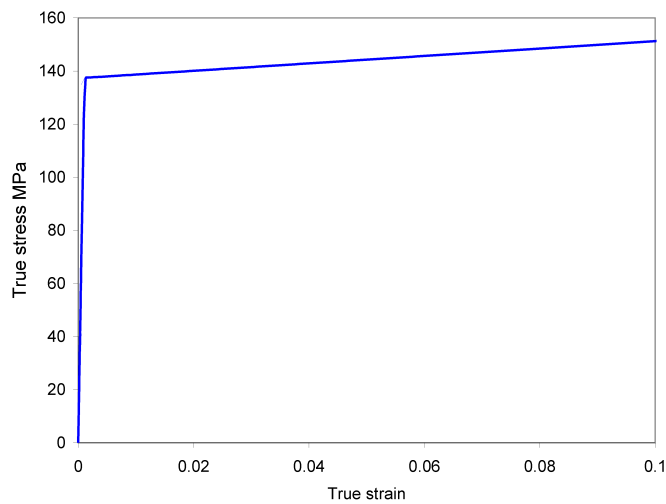


**Figure 11.14:** Numerical tensile test performed with one element, with the orientation  $\alpha(1)$  and with the parameters of the  $\alpha$  phase (Table (10.11) in Part (IV)). Strain rate  $\dot{\epsilon} = 0.6 \text{ s}^{-1}$ .

### 11.4.2 Influence of the shape of the $\alpha$ phase

In this paragraph, numerical simulations are examined for two representative cells. The first one contains a globular  $\alpha$  phase inside the  $\beta$  matrix (first microstructure) and the second contains an elongated  $\alpha$  phase inside the  $\beta$  matrix (second microstructure). The numerical simulations were performed with the first loading phase (Eqn.(11.1)).

Von Mises' strain and stress are given within the samples in Figures (11.15) and (11.16). The first microstructure was used in the figures on the left and the second microstructure was used in the ones on the right.

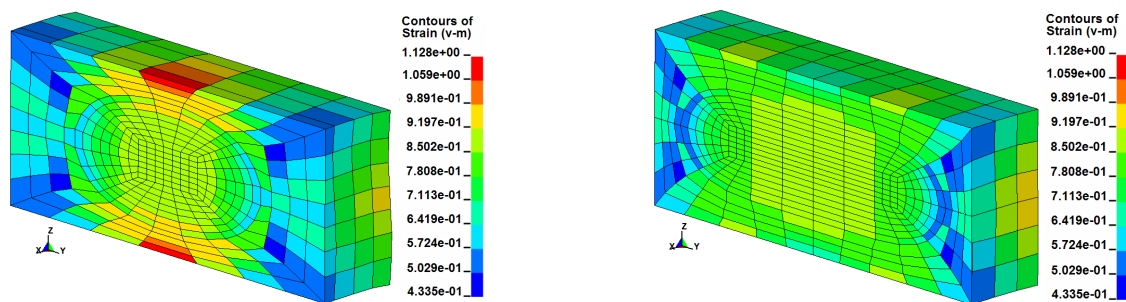


**Figure 11.15:** Von Mises' strain in the two microstructures in the deformed configuration and submitted to the first loading phase. (Left) first microstructure, (right) second microstructure.

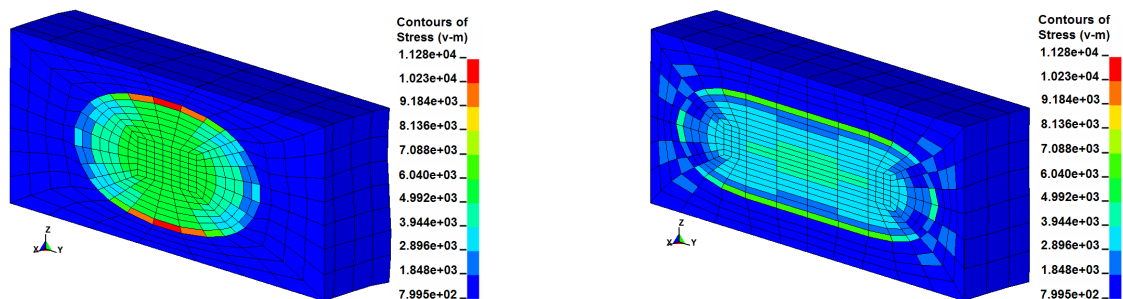


**Figure 11.16:** Von Mises' stress (MPa) in the two microstructures in the deformed configuration and submitted to the first loading phase. (Left) first microstructure, (right) second microstructure.

The scales are the same for the two microstructures to make a straightforward comparison between the results. From these figures, it is clear that, for this loading phase, the second microstructure leads to a more homogeneous behavior than the first one.

Figure (11.17) provides Von Mises' stress versus strain in the two microstructures submitted to the first loading phase.

There is very little difference between the stress versus strain obtained from these two microstructures. This result is not so amazing. Intrinsicly, the properties of the globular and

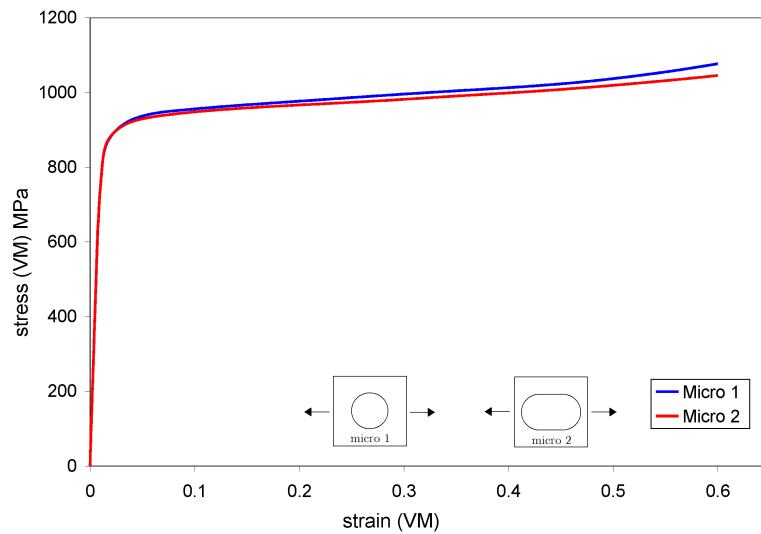


**Figure 11.17:** Von Mises' stress versus strain for the two microstructures.

the lamellar  $\alpha$  phase are similar. Moreover, the characteristic size of the  $\alpha$  particles compared to the deformation mechanisms should affect the results but here, the size of the  $\alpha$  particles in the two representative cells are not significantly different. A considerably larger  $\alpha$  particle should help to visualize different behaviors.

### 11.4.3 Influence of the loading phase

Now, the influence of the macroscopic loading imposed on the representative cells will be studied. For each of the two microstructures, two numerical simulations were performed: one with the first loading phase (Eqn.(11.1)) and one with the second loading phase (Eqn.(11.2)). The orientation of the  $\alpha$  phase corresponds to  $\alpha_1$  in Table (11.2).

#### First microstructure

First, the deformed samples are given at the end of both loading phases (Eqn.(11.1) and Eqn.(11.2)). Figure (11.18) provides the periodic displacement added to the initial configuration and Figure (11.19) shows the total (periodic and macroscopic) displacement.

The deformed samples were not identical in these two cases. This difference could be due to the orientation of the grain compared to the loading direction.

Figure (11.20) provides the periodic displacement in three dimensions for two corresponding nodes. These nodes, numbered 362 and 382, were labelled in Figure (11.18). As expected for such nodes, the corresponding periodic displacements were identical, which demonstrates the efficiency of the implementation of the periodic homogenization theory.

Then, Von Mises' stress and strain were given in each element of the deformed sample, at the end of the simulation. Figure (11.21) represents the contours of Von Mises' strain in the

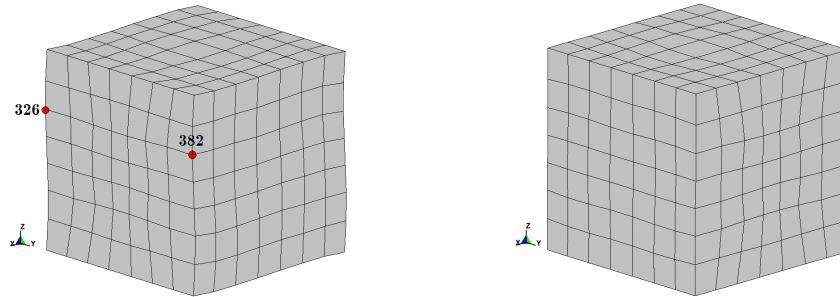


Figure 11.18: Plot of the final periodic displacement in the initial configuration.

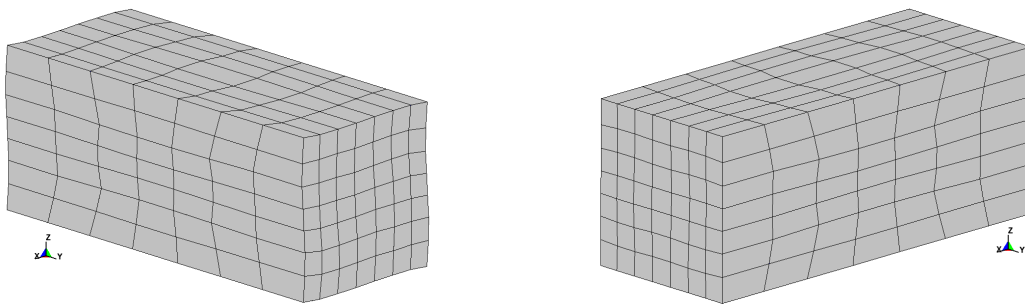


Figure 11.19: First microstructure in the deformed configuration. (Left) first loading phase, (right) second loading phase.

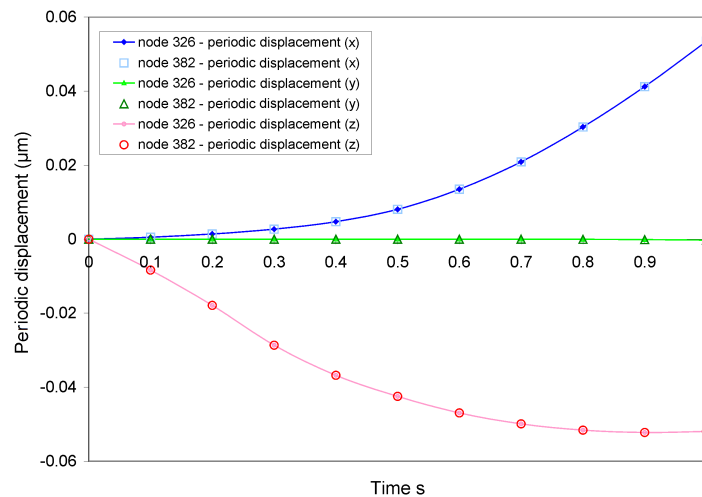
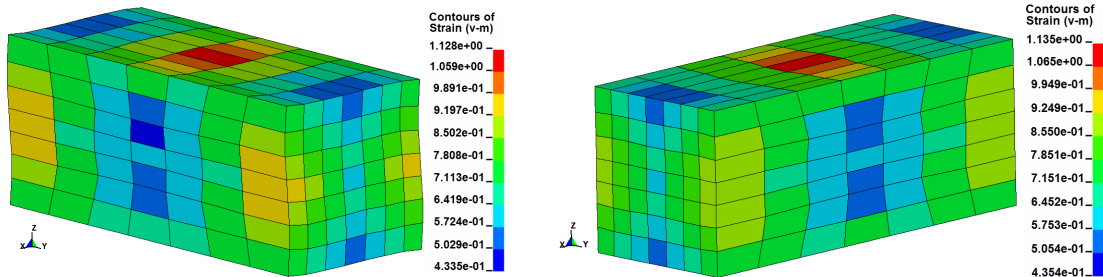
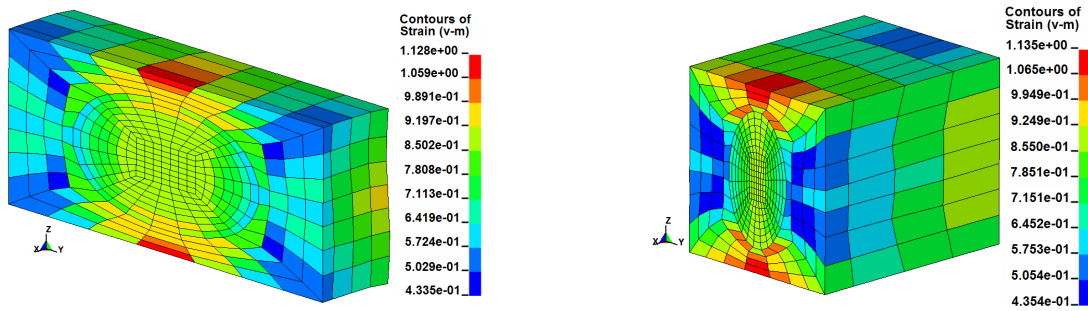


Figure 11.20: Periodic displacement during the test for two corresponding nodes: nodes 326 and 382 (shown in Figure (11.18)).

deformed sample for both loading phases. In Figures (11.22) and (11.23), the same strains are given inside the mesh.



**Figure 11.21:** Von Mises' strain of the first microstructure in the deformed configuration. (Left) first loading phase, (right) second loading phase.



**Figure 11.22:** Von Mises' strain of the first microstructure in a part of the deformed configuration. (Left) first loading phase, (right) second loading phase.

The scale of Von Mises' strain was slightly different for the two loading phases but the distribution was similar: the strains inside the sample along the direction of maximum loading ( $Y$  direction for the first loading phase (Figure (11.22), left) and  $X$  for the second loading phase (Figure (11.23), right)) were similarly distributed.

Figures (11.24) and (11.25) give Von Mises' stress for the first microstructure and both loading phases.

The conclusions are the same as for the strain obtained with both loading phases.

Von Mises' stress versus strain for both loading phases on the first microstructure are shown in Figure (11.26). There is only a slight divergence between curves at the end of the loading. Consequently, for the first microstructure, there is hardly any effect of the loading direction on macroscopic stress versus strain curves when such orientations of the  $\alpha$  and  $\beta$  phases are chosen compared to the loading imposed. This result is not surprising. Indeed, for this microstructure, the  $\vec{c}$  axis is along the  $Z$  direction. Thus, a tensile test along the  $X$  or the  $Y$  direction should be similar.



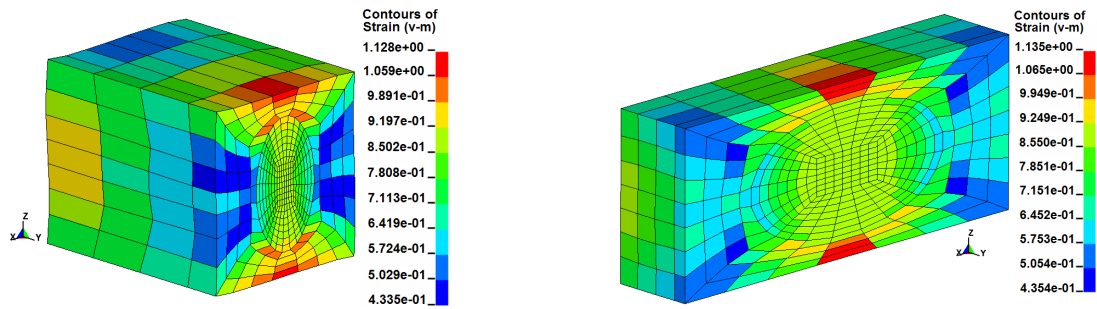


**Figure 11.23:** Von Mises' strain of the first microstructure in a part of the deformed configuration. (Left) first loading phase, (right) second loading phase.

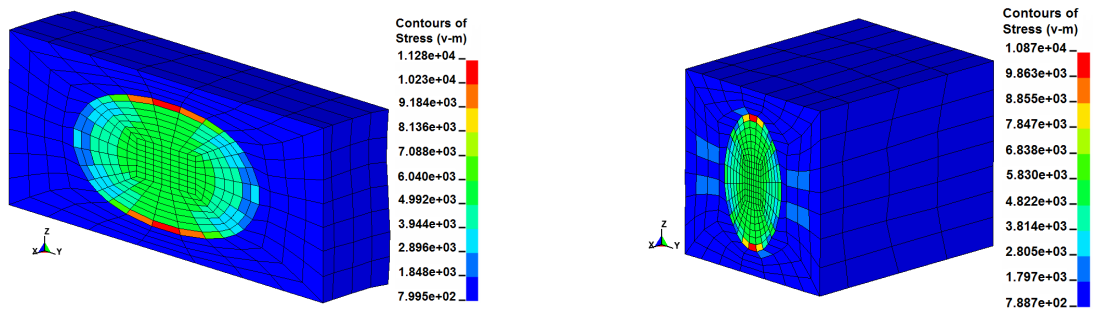


**Figure 11.24:** Von Mises' stress (MPa) of the first microstructure in a part of the deformed configuration. (Left) first loading phase, (right) second loading phase.

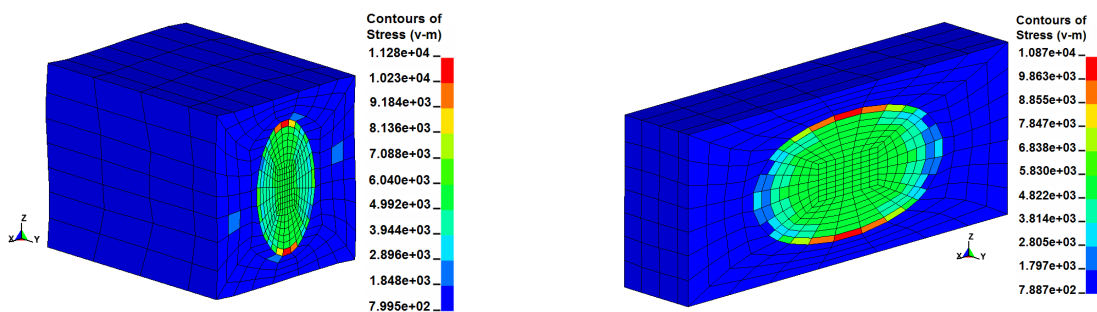


**Figure 11.25:** Von Mises' stress (MPa) of the first microstructure in a part of the deformed configuration. (Left) first loading phase, (right) second loading phase.

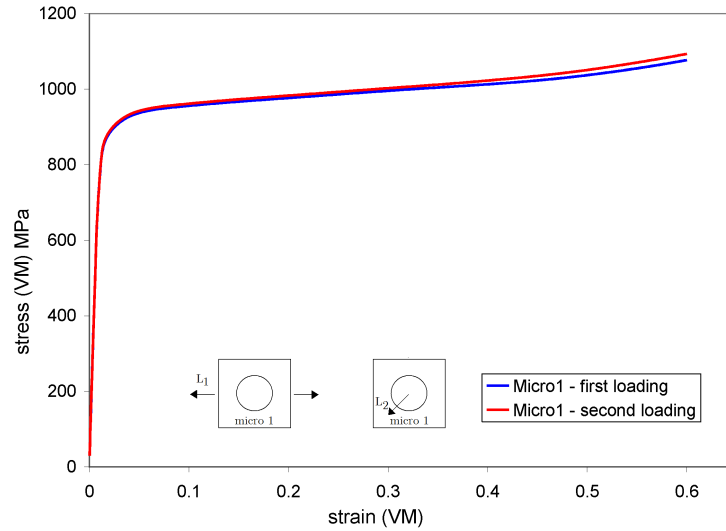


**Figure 11.26:** Von Mises' stress versus strain for the two loading phases on the first microstructure.

### Second microstructure

The same numerical simulations were performed using the second microstructure. Von Mises' stress and strain are given in each element of the deformed sample, at the end of the simulation. Figures (11.27) represent Von Mises' strain in the deformed sample for the two loading phases. In Figures (11.28) and (11.29), Von Mises' strains are given inside the mesh.

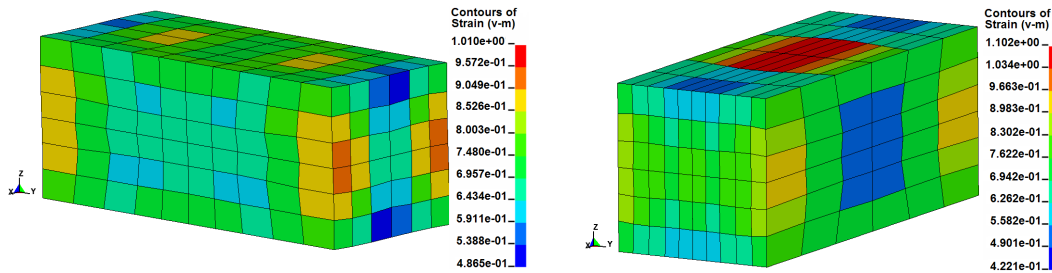


**Figure 11.27:** Von Mises' strain of the second microstructure in the deformed configuration. (Left) first loading phase, (right) second loading phase.

Contrary to the first microstructure, results are not similar with the two loading phases as was expected due to the shape of the  $\alpha$  grain in the representative cell. The strain is greater in the  $\alpha$  phase when the maximum loading is in the direction of the elongated  $\alpha$  phase.

Figures (11.30) and (11.31) give Von Mises' stress for the second microstructure and both loading. Once again, the stress was greater in the  $\alpha$  phase than in the  $\beta$  matrix.

Von Mises' stress versus strain curves for the two loadings and for the second microstructure are shown in Figure (11.32).

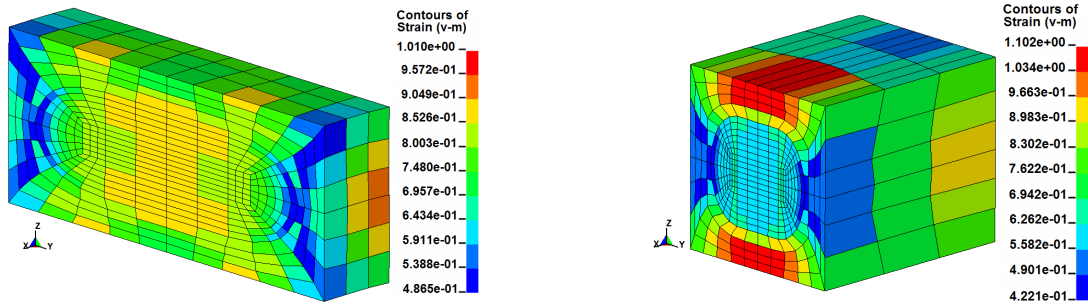


**Figure 11.28:** Von Mises' strain of the second microstructure in a part of the deformed configuration. (Left) first loading phase, (right) second loading phase.

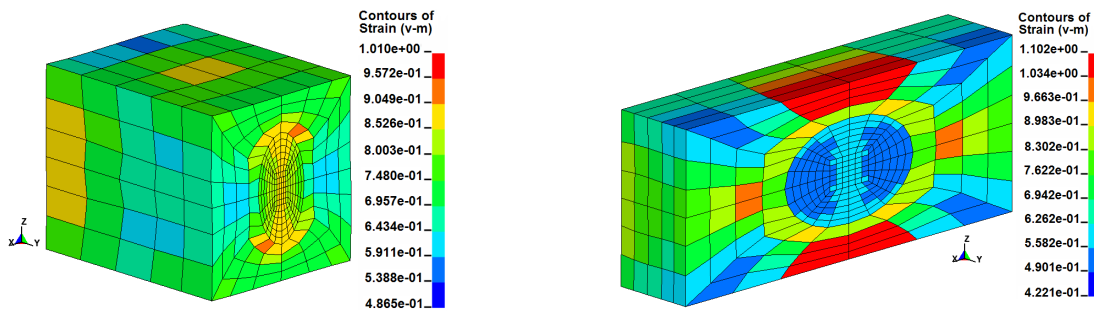


**Figure 11.29:** Von Mises' strain of the second microstructure in a part of the deformed configuration. (Left) first loading phase, (right) second loading phase.

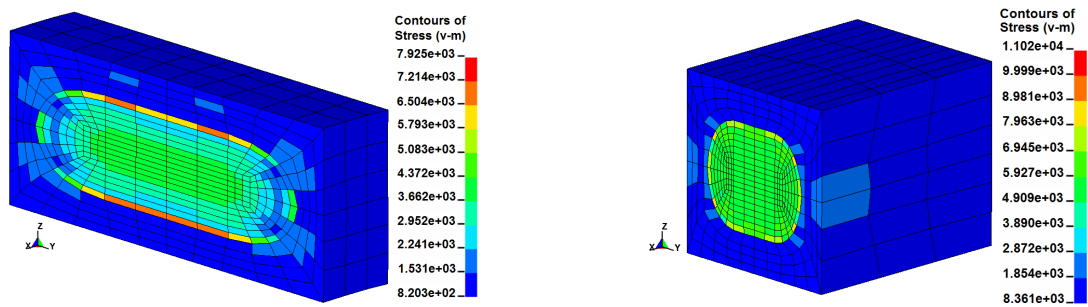


**Figure 11.30:** Von Mises' stress (MPa) of the second microstructure in a part of the deformed configuration. (Left) first loading phase, (right) second loading phase.

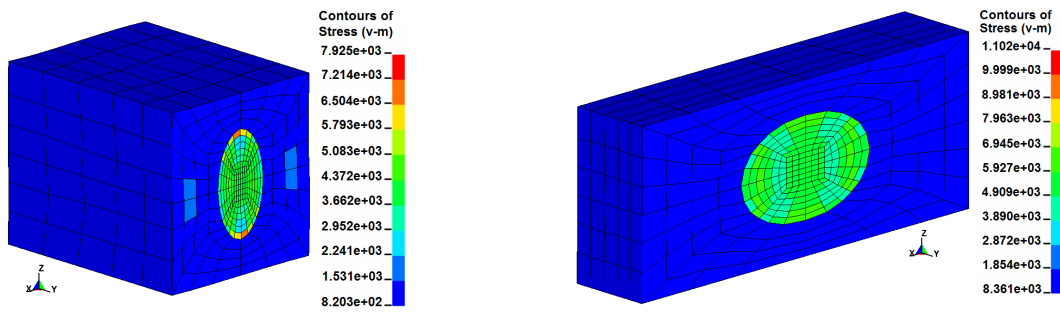


**Figure 11.31:** Von Mises' stress (MPa) of the second microstructure in a part of the deformed configuration. (Left) first loading phase, (right) second loading phase.

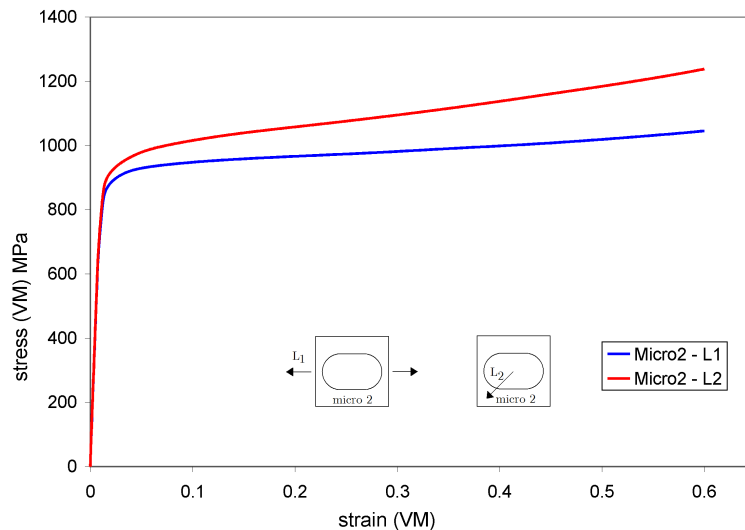


**Figure 11.32:** Von Mises' stress versus strain curves for the two loading phases on the second microstructure.

Contrary to the first microstructure, loading has an influence on the macroscopic stress versus strain curves for the second microstructure. Indeed, Von Mises' stress is greater for the second loading phase, when the maximum load is applied along the  $X$  axis, perpendicular to the length of the elongated  $\alpha$ .

#### 11.4.4 Influence of $\alpha$ orientation in the cell

Tests were performed on the first microstructure, the globular  $\alpha$ , with the first loading phase and two  $\alpha$  grain orientations. Results are given on the left for the first orientation and on the right for the second orientation. Figures (11.33) and (11.34) provide the strain and Figures (11.35) and (11.36) provide the stress inside the material.

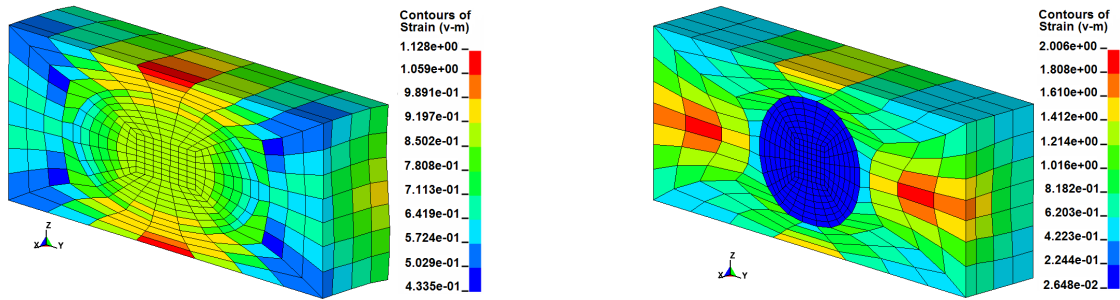


**Figure 11.33:** Von Mises' strain (MPa) of the first microstructure, submitted to the first loading phase and with (left) the first  $\alpha$  orientation and, (right) the second  $\alpha$  orientation in a part of the deformed configuration.

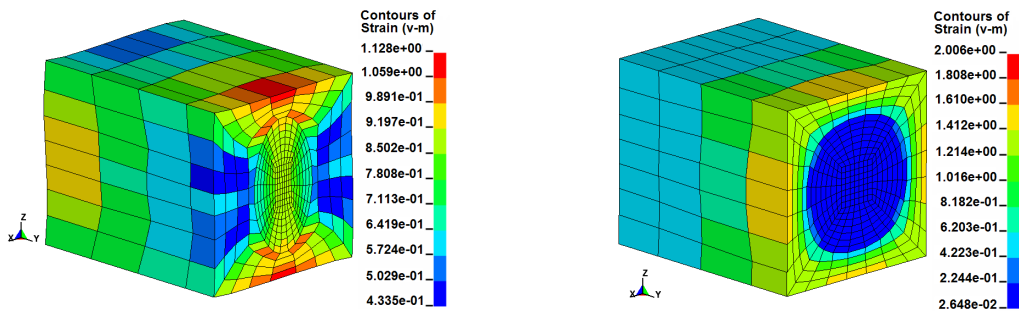


**Figure 11.34:** Von Mises' strain (MPa) of the first microstructure, submitted to the first loading phase and with (left) the first  $\alpha$  orientation and, (right) the second  $\alpha$  orientation in a part of the deformed configuration.

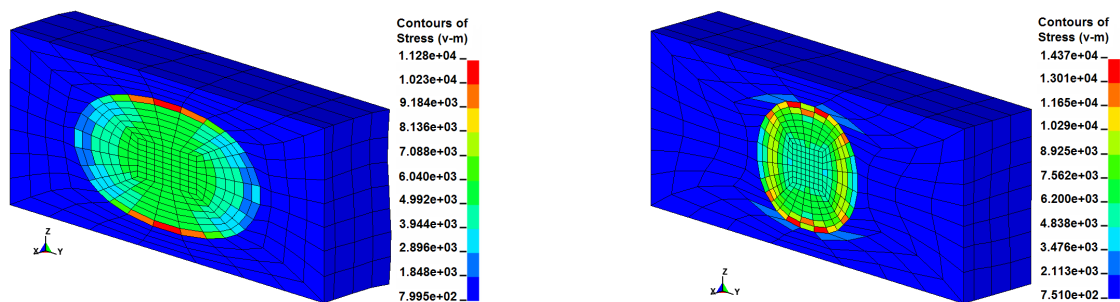


**Figure 11.35:** Von Mises' stress (MPa) of the first microstructure, submitted to the first loading phase and with (left) the first  $\alpha$  orientation and, (right) the second  $\alpha$  orientation in a part of the deformed configuration.

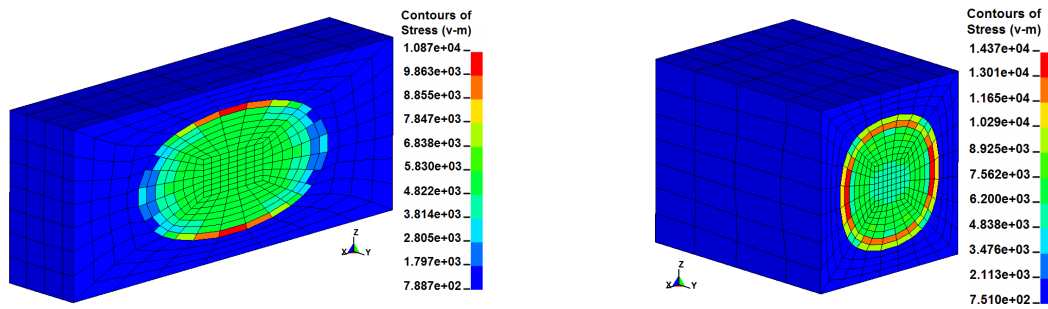


**Figure 11.36:** Von Mises' stress (MPa) of the first microstructure, submitted to the first loading phase and with (left) the first  $\alpha$  orientation and, (right) the second  $\alpha$  orientation in a part of the deformed configuration.

The behavior of representative cells with the same microstructure, submitted to the same loading but with a different orientation of the globular  $\alpha$  phase inside the matrix, is quite different. For example, the strain in the  $\alpha$  phase with the second orientation is smaller than with the first orientation. Moreover, with the second orientation, the globular  $\alpha$  phase at the end of the test is less extended than with the first orientation.

Von Mises' stress versus strain curves in the first representative cell submitted to the first loading phase are shown in Figure (11.37) for the two  $\alpha$  grain orientations.

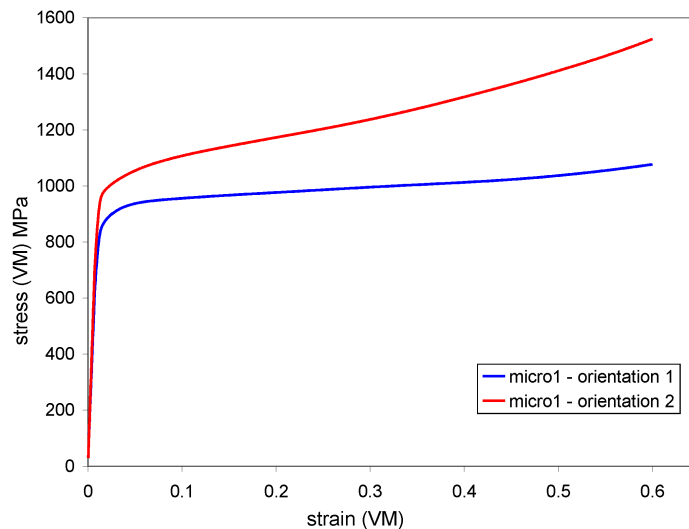


**Figure 11.37:** Von Mises' stress versus strain curves for the first microstructure submitted to the first loading phase and for the two  $\alpha$  grain orientations.

Looking at the stress versus strain curves, significant changes in the behavior appear due to the orientation of the  $\alpha$  phase. Most notably, an increase in the stress for the same strain can be observed for the second microstructure.

Nevertheless, it is worth noting that some orientation relationships exist between the two phases,  $\alpha$  and  $\beta$ , known as Burgers' relationships [Len07]:

$$\{110\}_{\beta} // \{0001\}_{\alpha}$$

$$\langle 111 \rangle_{\beta} // \langle 11\bar{2}0 \rangle_{\alpha} .$$

Indeed, as shown in Figure (11.38), it is possible that the body-centered cubic form becomes hexagonal by a slight displacement (smaller than interatomic distance) of a few atoms and by their slight rearrangement. This is the allotropic transformation  $\beta \leftrightarrow \alpha$  of titanium [Pri00], [Rob07].

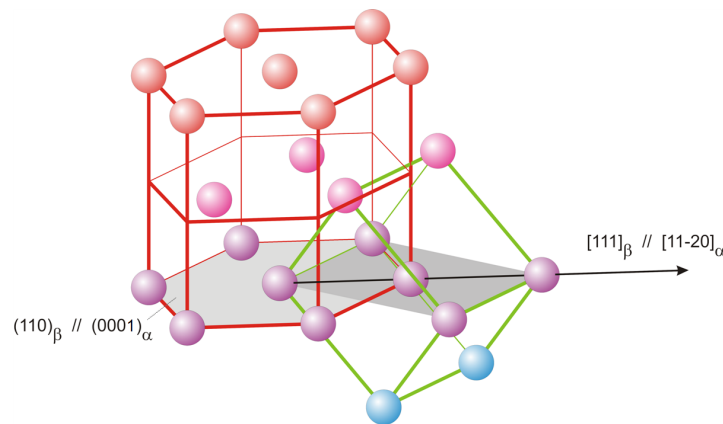


**Figure 11.38:** Schematic representation of the allotropic transformation  $\beta$  (BCC)  $\rightarrow$   $\alpha$  (HCP).

This relation between the phases will now be tested (orientation 3). The corresponding stress versus strain results are given in Figure (11.39), for the first microstructure, and are compared to the two previous orientations tested.

These results show once again the importance of the relative orientation between the two phases and of the loading direction.

## 11.5 Conclusions

This chapter focused on the numerical simulations of representative cells of Ti-5553. The main goal of these simulations was to study the general behavior of such representative cells. The microstructures of two representative cells were chosen from experimental EBSD pictures. These pictures were then simplified in order to mesh basic microstructures. Representative cells containing only the  $\beta$  phase or containing this phase and the  $\alpha$  phase (globular (micro 1) or elongated (micro 2)), were compared.

Experimentally, some global tendencies can be observed. Concerning hardness, N. Clement from UCL observed that the hardness of the  $\alpha$  phase is less than the hardness of the  $\beta$  phase and these are in turn smaller than the hardness of the  $(\alpha + \beta)$  materials. Moreover, it is clear

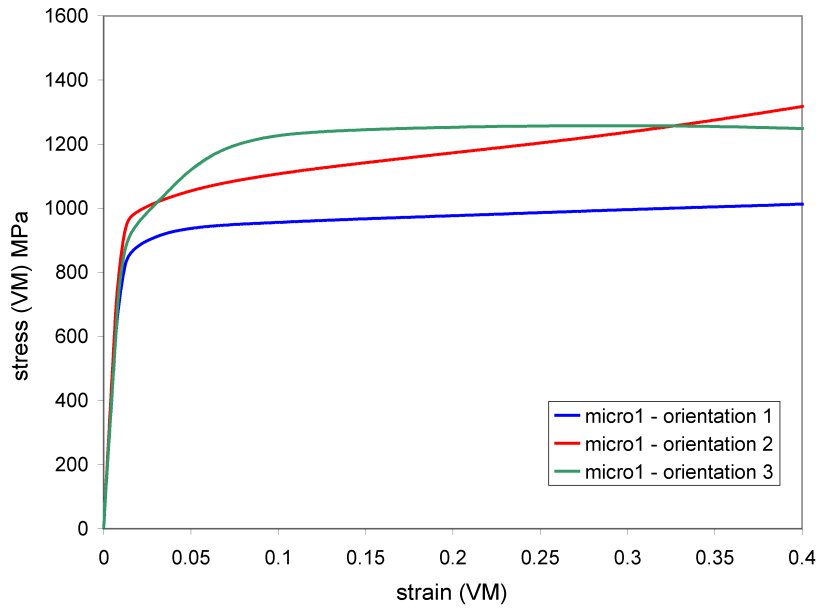


**Figure 11.39:** Von Mises' stress versus strain curves for the first representative cell submitted to the first loading phase and for three  $\alpha$  grain orientations.

that the ductility of the  $\beta$  material is higher than the ductility of an  $(\alpha + \beta)$  material (cf results of Figure (11.13)). [Len07] showed that, for the Ti-LCB alloy, the ductility of the material composed of lamellar  $\alpha$  is less than a material with globular  $\alpha$ . Finally, as mentioned by N. Clement, intrinsically, the properties of the lamellar and globular  $\alpha$  should be comparable but the characteristic size of the  $\alpha$  phase with respect to the deformation mechanism should have an effect on the behavior of the cell<sup>6</sup>.

Table (11.3) summarizes the tests performed in this chapter and the corresponding macroscopic Von Mises' stress versus strain results are superimposed in Figure (11.40).

In terms of yield point, it is only slightly influenced by the presence and shape of the  $\alpha$  phase in the matrix. However, the orientation of the  $\alpha$  grain can have an influence on the yield point.

Results obtained show that, when the  $\alpha$  phase is present within the cell, hardening behavior appears, whereas when only the  $\beta$  phase is present, softening behavior is observed. This result was also observed experimentally.

The shape of the  $\alpha$  phase inside the matrix was also studied with only two shape ratios. Results obtained on the globular  $\alpha$  phase showed a slight influence of the loading direction but a greater influence of the orientation of the  $\alpha$  phase with respect to the  $\beta$  phase on the results. Modifying the orientation or the loading gives another result but the most important remark is that the orientation of the  $\alpha$  phase with respect to the loading direction influences the results, beginning from the yield strength. For the lamellar  $\alpha$ , it appeared that the loading

<sup>6</sup>For example, interfaces adjacent to each other in thin plates will stop dislocations more efficiently.



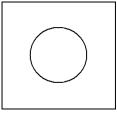
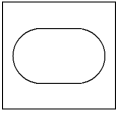
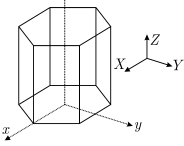
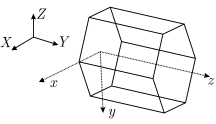
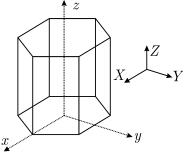
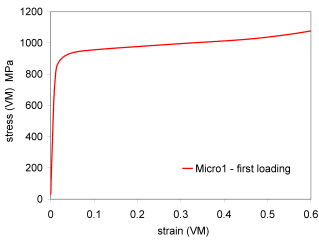
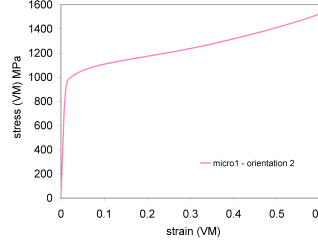
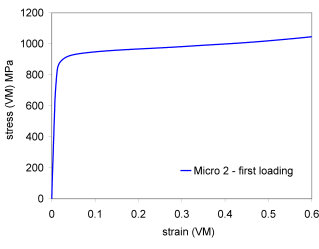
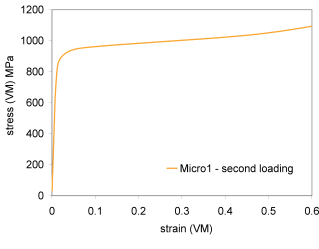
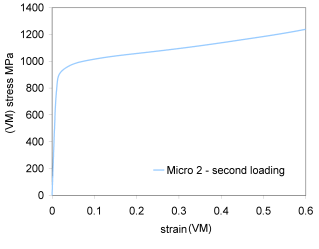
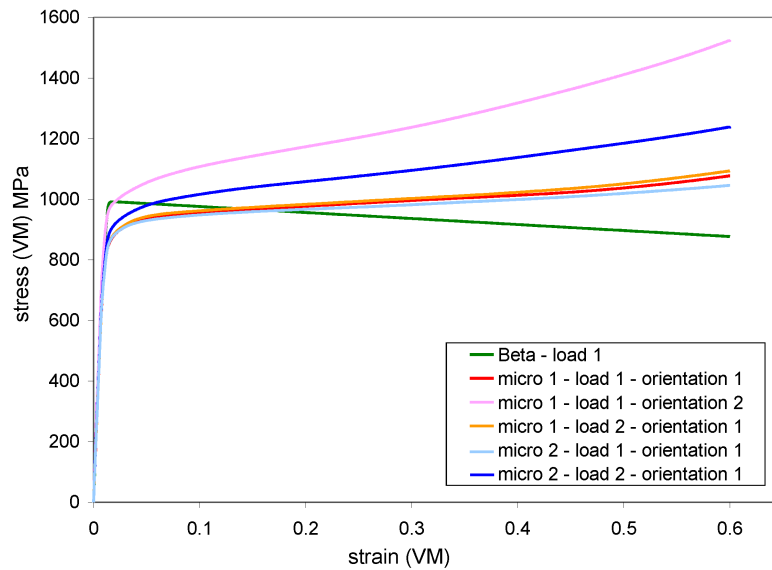
	Microstructure 1		Microstructure 2
			
<b>Loading</b>	<b>Orientation 1</b> 	<b>Orientation 2</b> 	<b>Orientation 1</b> 
<b>L<sub>1</sub></b> $\begin{pmatrix} -0.3 & 0 & 0 \\ 0 & 0.6 & 0 \\ 0 & 0 & -0.3 \end{pmatrix}$			
<b>L<sub>2</sub></b> $\begin{pmatrix} 0.6 & 0 & 0 \\ 0 & -0.3 & 0 \\ 0 & 0 & -0.3 \end{pmatrix}$		/	

Table 11.3: Summary of the tests performed in this chapter.



**Figure 11.40:** Von Mises stress versus strain for all the microstructures, loadings and orientations studied.

direction strongly influences the results. This conclusion was expected due to the different orientations between the elongated  $\alpha$  and the loading direction.

In the end, these results do not give information about ductility, which can be very different from one microstructure to another and which is also an important factor for practical applications.

Instead, this chapter provided information about the tensile behavior of Ti-5553 using representative cells. To improve modeling of this material, other behavioral aspects need to be studied. For example, the effect of the proportion (the size, the shape and the interdistance of the  $\alpha$  phase inside the  $\beta$  matrix) of the  $\alpha$  phase inside the  $\beta$  matrix should be investigated. For the same shape, the size of the  $\alpha$  phase with respect to the deformation mechanism should have a non-negligible effect on the total behavior of the cell. Moreover, to better model the behavior of the macroscopic material, it may be worthwhile to create representative cells containing several  $\alpha$  grains of appropriate orientations. In these cells, the effect of the respective size of the  $\alpha$  grains, the relative orientation and the interdistance between them will also be worth investigating. Finally, the addition of interface elements between the  $\alpha$  and the  $\beta$  phases should also improve the results.

## Part VI

# Conclusions and perspectives



## Conclusions and perspectives

The overall goals of this thesis were to characterize the titanium alloy Ti-5553 from a material perspective and, thanks to this characterization, to optimize the alloy's microstructure for aeronautical applications.

The identification of this alloy was performed using the *Lagamine* finite element code. Several numerical tools had to be implemented or developed in order to characterize the material more suitably. Of those tools, the constitutive laws used to model the behavior of this alloy were described, and the periodic homogenization theory used to perform numerical simulations of representative cells of Ti-5553 was introduced in Part (II).

The first step in characterizing the Ti-5553 alloy was to study its body-centered cubic (BCC)  $\beta$  phase (Part (III)). The study of this phase was facilitated by the possibility of obtaining a 100%  $\beta$  material with an adapted thermal treatment. Moreover, experimental tensile, shear and nanoindentation tests were already available for this phase. From numerical simulations of the macroscopic uniaxial tensile tests, results yield the conclusion that a macroscopic elastic-viscous-plastic Norton-Hoff constitutive law was not well adapted to this material, due to the significant changes in the hardening behavior of this  $\beta$  phase with modifications of the strain rate. However, these tests served to identify and optimize the parameters of a crystalline plasticity-based constitutive law with a Bassani and Wu's hardening model. This constitutive law makes the modeling of this phase possible for a large range of strain rates. The numerical simulations of the simple shear tests performed on the  $\beta$  material have confirmed the necessity of using such a law. In fact, contrary to the macroscopic constitutive law, with the microscopic one, localization bands can appear during the numerical simple shear test, as in experiments. Finally, the set of parameters optimized for this phase was validated by nanoindentation tests in  $\beta$  grains of different orientations.

During the numerical nanoindentation study on the  $\beta$  material (Chapter (9), Part (III)), a sensitivity analysis was performed. It showed that some parameters, notably the friction coefficient or Poisson's ratio, have hardly any influence on load versus displacement nanoindentation curves. On the other hand, other parameters, such as the geometry of the indenter or the yield strength should be known to a high degree of accuracy because of their great influence on nanoindentation results.

The next part (Part (IV)) focused on characterizing the hexagonal close packed (HCP)  $\alpha$  phase of Ti-5553. As a consequence of the difficulty in using typical experimental macroscopic tensile or shear tests to identify this phase, nanoindentation experimental tests were used. The identification of the slip systems activated in this hexagonal phase and of the corresponding

critical resolved shear stresses was accurately performed for one grain orientation. However, correctly identifying the material's behavior for several grain orientations with the same set of parameters was considerably more laborious. Finally, a set of parameters that characterize the  $\alpha$  phase satisfactorily in three grain orientations was chosen and tested on a fourth orientation.

Finally, the numerical modeling of representative cells of Ti-5553 using the periodic homogenization theory, the crystalline elastic-viscous-plastic constitutive law and the parameters of the  $\alpha$  and  $\beta$  phases optimized in the preceding sections was the main goal of Part (V). These cells were chosen from experimental microstructures and, then, simplified to be meshed. Several parameters, including the appearance of the  $\alpha$  phase in the representative cell, the shape or the orientation of this  $\alpha$  phase or the macroscopic loading imposed, were tested and analyzed. It is worth noting that the generation alone of representative cells with different phase proportions, different orientations and different shapes can be a research subject in and of itself. This is in fact the case of an international project carried out by the group MSR, with the aim of modeling recrystallization using a multi-scale approach (DigiMat project)<sup>7</sup>. It is also the case of a series of works and theses of G. Cailletaud's team, such as the N. Osipov[Osi07]'s thesis. In the present thesis, different approaches are presented for microstructure mesh generation<sup>8</sup>. In the beginning, the objectives of this chapter on representative cells were more ambitious, hoping to model different additional representative cells, ones closer to reality and with a greater number of different loading phases. However, the time spent identifying the  $\alpha$  and  $\beta$  phases and implementing the periodic homogenization tools did not allow for a more widespread exploitation of the established model. In this work, therefore, the investigation was limited to single cases in order to show the model's potential.

Several of the areas mentioned above can be focused on for future research. With regards to the characterization of the  $\alpha$  phase, it is clear that improvement should be possible. For one, very little data were available to identify the material parameters of this phase. To improve the identification, texture measurements should be carried out before and after experimental tests in order to validate the model. The procedure of these experimental tests had begun but was not finished before the end of this work. Moreover, the measurement of neutron diffraction should also help to identify which slip systems are more or less activated. Concerning this phase, it would also be interesting to study the nanoindentation patterns appearing around indented  $\alpha$  grain and to reproduce these patterns for different grain orientations.

This study could also be improved by the numerical simulations of representative cells in which different proportions between phases or in which several  $\alpha$  grains of different orientations in the  $\beta$  matrix are present. A better approximation of the (longer and narrower) extended  $\alpha$  phase can also be made to match the experimental results. A better choice would be a similar extended  $\alpha$  but one with its axis along the greatest diagonal of the cubic representative cell. Such a choice would enhance the modeling of a more extended  $\alpha$  phase. It would also aid the

---

<sup>7</sup>R. Logé, M. Bernacki, Y. Chastel, Mechanical and physical modelling at the microstructure scale, Metallurgy, Structure, Rheology team, CEMEF, Paris.

<sup>8</sup>The generation of the parent phase, the generation of the resulting phase and the generation of the whole microstructure with a parent phase which is subdivided into several parts, in order to describe appearance of a new phase inside a parent phase.

study of the effect of the size of the  $\alpha$  particles. Nevertheless, such shapes involve significantly more complicated meshing.

Nowadays, numerical simulations of representative cells are only performed using macroscopic velocity gradient loading. In practice, the possibility of imposing macroscopic stress loading or imposing some components of the macroscopic velocity gradient and some components of the macroscopic stress should be available. To impose such loading phases on representative cells, modifications in the finite element code used are needed (see Appendix (D)).

Another area for improvement is the numerical modeling of the boundaries between the grains in the representative cell. Sliding or decohesion could be simulated if one added interface elements and corresponding constitutive laws. The ductility of the global material is a function of the damage strength of each phase and a function of the interface between these phases. Without too many additional developments, it would be possible to associate a fracture criterion (for example, Rice and Tracy's criterion, based on critical void growth ratio [KSK09]) and a tensile limit in the normal direction to the interface and to investigate the behavior of several microstructures submitted to different loading conditions. Only time has limited such applications.

It would also be useful to check and change, if necessary, the properties of the phases when they appear together in the representative cell. In fact, the properties of the  $\beta$  phase alone in a material or the properties of this phase in an  $(\alpha + \beta)$  material can be different. These  $\beta$  phases are obtained from different thermal treatments, which can lead to different properties. For example, one thermal treatment triggers the appearance of the  $\omega$  phase in the  $\beta$  matrix.

In this research, only the static behavior of Ti-5553 was studied. Therefore, another area that can be followed in future research is the study of the fatigue properties of this alloy. In fact, this fatigue behavior is a general dimensioning criterion in aerodynamic fields and, to date, few works have been dedicated to this aspect of the alloy.

Finally, the influence of temperature on the material's behavior is also interesting to study for aeronautical applications. In fact, some parts are submitted to medium to high temperatures and it is important to understand and predict their consequence on the material's behavior.





Part VII

Appendix



## Appendix A

### Ti-5553 as-received: thermal treatment

The thermal treatments of the Ti-5553 samples used for experimental tests are given in Figure (A.1). Only the low oxygen material was used.

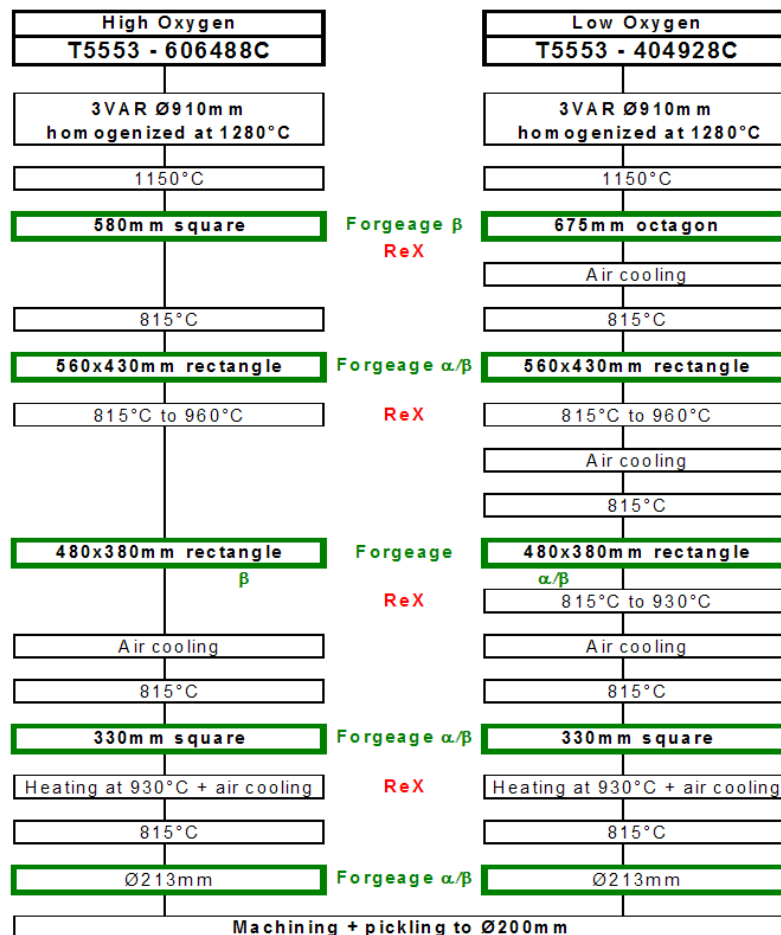


Figure A.1: Geometry of a general unit cell.



## Appendix B

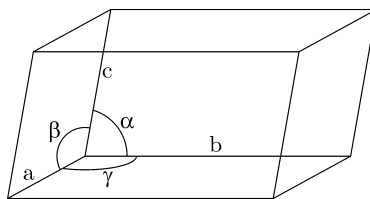
# Crystalline structure and crystal defects

### B.1 Introduction

Some bases of crystallography are summarized in this appendix.

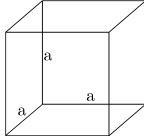
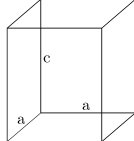
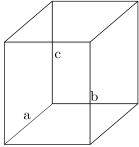
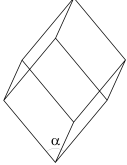
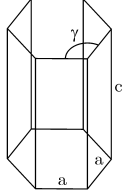
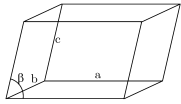
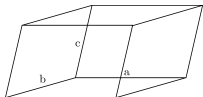
A crystal is a regular, repeating arrangement of atoms or molecules. The majority of solids, including all metals, adopt a crystalline arrangement because the amount of stabilization is at its greatest when the particles adopt regular (rather than random) arrangements. In the crystalline arrangement, the particles pack together efficiently to minimize the total intermolecular energy.

The crystal structure is determined by the *lattice* structure and the configuration of the *unit cell* [FA08], shown in Figure (B.1). The length of a unit cell's edges and the angles between crystallographic axes are referred to as *lattice parameters*.



**Figure B.1:** Geometry of a general unit cell.

The location of all the particles in the crystal are determined by multiplying identical unit cells in three directions. All possible structures are reduced to a small number of basic unit cell geometries. Indeed, only 7 crystal systems (Table (B.1)) and 14 crystal lattices, also called *Bravais lattices* (Table (B.2)), exist. The crystal lattices are obtained by several dispositions of the atoms to fill the 3D microstructure of the 7 systems.

System	Axial length and angles	Unit cell geometry
Cubic	$a = b = c, \alpha = \beta = \gamma = 90^\circ$	
Tetragonal	$a = b \neq c, \alpha = \beta = \gamma = 90^\circ$	
Orthorhombic	$a \neq b \neq c, \alpha = \beta = \gamma = 90^\circ$	
Rhombohedral	$a = b = c, \alpha = \beta = \gamma \neq 90^\circ$	
Hexagonal	$a = b \neq c, \alpha = \beta = 90^\circ, \gamma = 120^\circ$	
Monoclinic	$a \neq b \neq c, \alpha = \gamma = 90^\circ \neq \beta$	
Triclinic	$a \neq b \neq c, \alpha \neq \beta \neq \gamma \neq 90^\circ$	

**Table B.1:** The seven crystal systems. Figure inspired from [Sha96] and from [FA08].

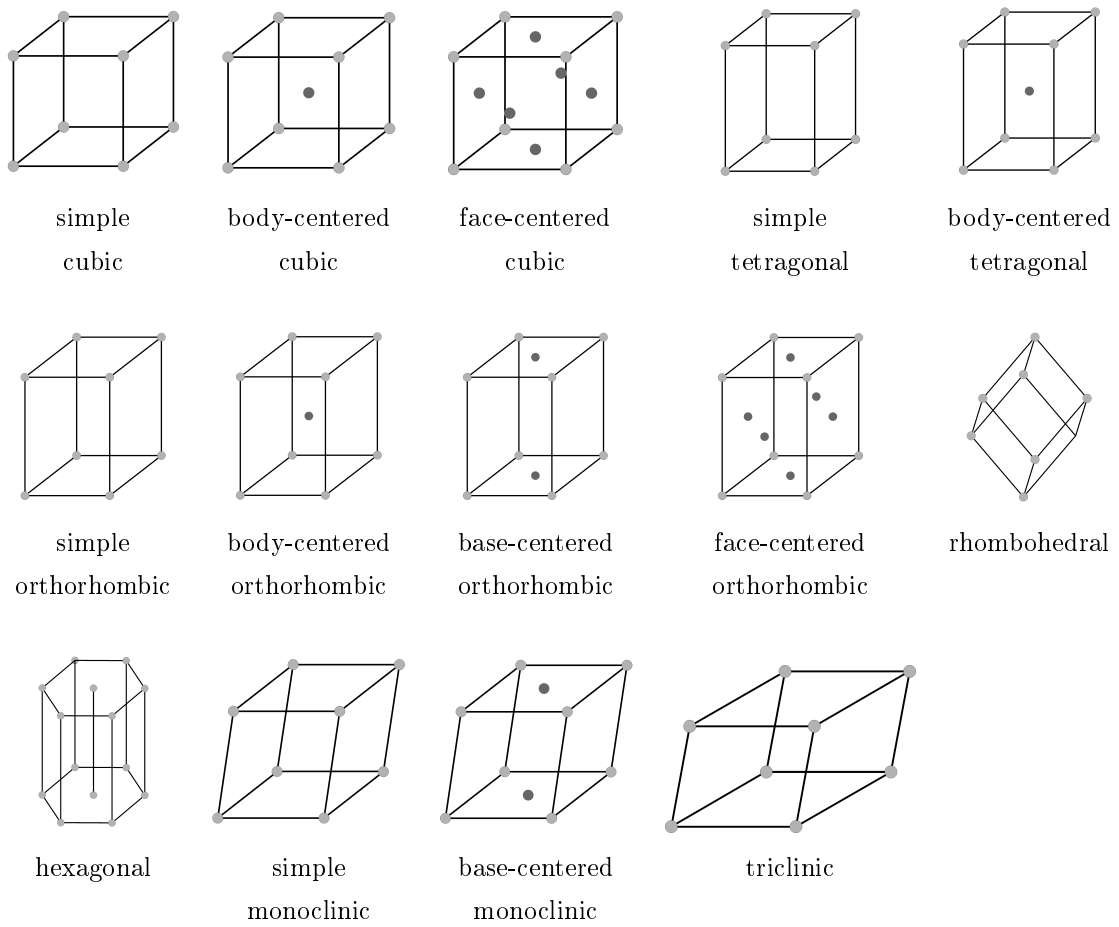


**Table B.2:** The fourteen crystal Bravais lattices. Figure inspired from [Sha96].

## B.2 Lattice positions, directions and planes

**Lattice positions** are expressed as fractions (or multiples) of unit cell dimensions. The three fundamental vectors, or vectors of the unit cell,  $\vec{a}$ ,  $\vec{b}$ , and  $\vec{c}$  are shown in Figure (B.2). The translation of all the nodes of the lattice can be deduced from these vectors. The distance of a node  $M$ , from another one,  $O$ , chosen as the origin, is given by the relation

$$O\vec{M} = n_1\vec{a} + n_2\vec{b} + n_3\vec{c}$$

where  $n_1$ ,  $n_2$ , and  $n_3$  are integers.

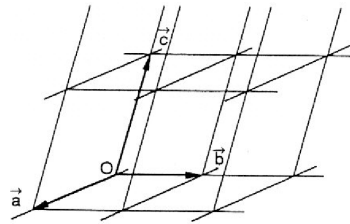


**Figure B.2:** Fundamental vectors of a lattice.

A **lattice plane** is defined by three integers, known as *Miller indices*. These indices are simply obtained from A, B and C, which are the intersections between the plane and the coordinate axes (Figure (B.3)). A, B and C are, respectively, equal to  $D/h$ ,  $D/k$  and  $D/l$ , where D is the smallest common denominator of A, B and C. A crystal plane is thus written

$$(hkl) = \left( \frac{D}{A} \frac{D}{B} \frac{D}{C} \right)$$

with  $hkl$  being the integers called Miller indices.

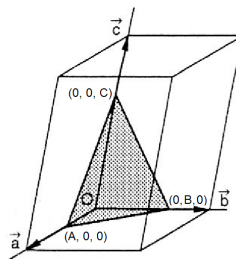


**Figure B.3:** Lattice planes - Miller indices.

Figure (B.4) provides examples of lattice planes defined in a cubic lattice. A negative index is expressed by a bar above the corresponding integer. A plane is designated by parentheses,  $(\mathbf{h} \mathbf{k} \mathbf{l})$ , and the indices of a family of equivalent planes are enclosed in braces,  $\{\mathbf{h} \mathbf{k} \mathbf{l}\}$ .

The **lattice directions** are expressed as sets of three integers:  $u$ ,  $v$  and  $w$ . These integers are proportional to the components of the unit vector of the direction on the three fundamental



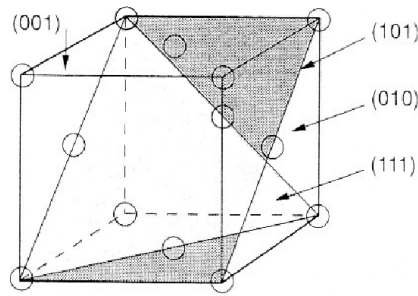


**Figure B.4:** Lattice planes - Miller indices.

axes. In the notation of a direction, the integers are enclosed by square brackets,  $[u \ v \ w]$ . A family of directions is designated by angular brackets,  $\langle u \ v \ w \rangle$ . An example of body diagonals in a cubic system is

$$\langle 111 \rangle = [111], [\bar{1}11], [1\bar{1}1], [11\bar{1}], [\bar{1}\bar{1}\bar{1}], [\bar{1}1\bar{1}], [1\bar{1}\bar{1}], [1\bar{1}\bar{1}] .$$

Some directions in a cubic system are shown in Figure (B.5).

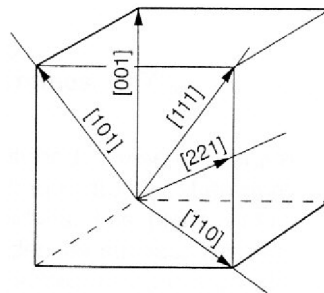


**Figure B.5:** Lattice directions - Cubic system.

As mentioned above, the general notation for Miller indices is  $(hkl)$ . It can be used for any of the seven crystal systems. Nevertheless, the hexagonal system is conveniently represented by four axes: a vertical axis and three coplanar axes in the basal plane, at  $120^\circ$  from one another (Figure (B.6)). Consequently, a four-digit set of Miller-Bravais indices  $(hkli)$  is defined. Since only three axes are necessary to define the three-dimensional geometry of a crystal, one of the integers in the Miller-Bravais system is redundant. The fourth index reflects symmetry and is obtained from two other ones:

$$i = -(h + k) .$$

## B.3 Metal structures

As mentioned above, there are 14 different types of crystal unit cell structures or lattices found in nature. However, most metals and many other solids have unit cell structures described

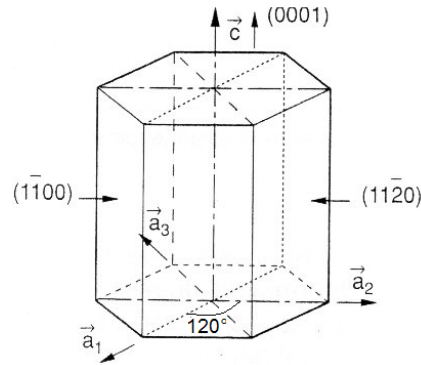


**Figure B.6:** Hexagonal system.

as body-centered cubic (BCC), face-centered cubic (FCC) or hexagonal close packed (HCP). Only these three structures will be shortly described hereafter.

### B.3.1 Body-centered cubic (BCC) structure

Figure (B.7) shows the body-centered cubic structure. There is one atom at the  $\frac{1}{2}\frac{1}{2}\frac{1}{2}$  position and one eight-atom at each unit cell corner (each corner atom is shared by eight adjacent unit cells). The BCC arrangement does not allow the atoms to pack together as closely as the FCC or HCP arrangements. The volume of atoms in a cell per the total volume of a cell is called the packing factor. The BCC unit cell has a packing factor of 0.68.

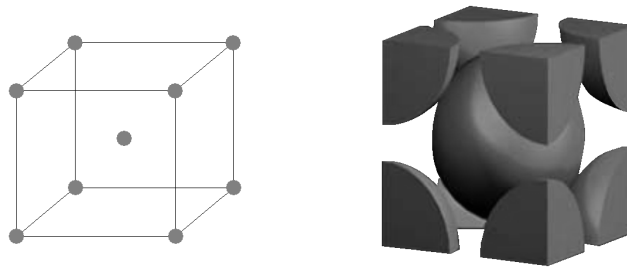


**Figure B.7:** Body-centered cubic structure.

### B.3.2 Face-centered cubic (FCC) structure

The face-centered cubic (FCC) structure is shown in Figure (B.8). There is one half-atom in the center of the unit cell face and one eighth-atom at each unit cell corner, for a total of four atoms in each FCC unit cell. The atomic packing of this structure is 0.74.

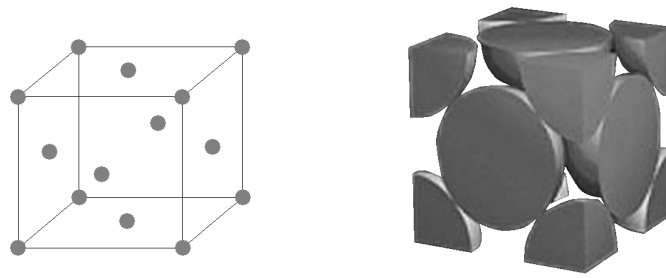


**Figure B.8:** Face-centered cubic structure.

### B.3.3 Hexagonal close packed (HCP) structure

The hexagonal close packed (HCP) structure is shown in Figure (B.9). There are six atoms in the HCP unit cell<sup>1</sup>. The atomic packing of this structure is 0.74, as for FCC structures.

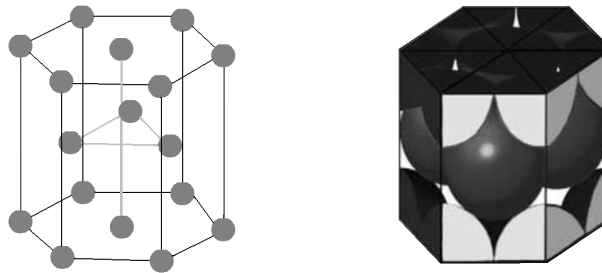


**Figure B.9:** Hexagonal close packed structure.

### B.3.4 Similarities and differences between FCC and HCP structures

FCC and HCP structures both have a packing factor of 0.74. They consist of closely packed planes of atoms. The difference between FCC and HCP is the stacking sequence. As can be seen in Figure (B.10), the HCP structure contains only two types of planes with an alternating ABAB ... arrangement. The atoms of the third plane are exactly in the same position as the atoms in the first plane. However, the FCC structure contains three types of planes with an ABCABC ... arrangement. The atoms in rows A and C are no longer aligned.

## B.4 Crystal defects

A material cannot be prepared without some degree of chemical impurity. Moreover, there are numerous structural flaws that represent a loss of crystalline perfection. These flaws can

<sup>1</sup>Each of the 12 atoms in the corners of the top and bottom layers contribute 1/6 atom to the unit cell, the two atoms in the center of the hexagon of both the top and bottom layers each contribute 1/2 atom and each of the three atoms in the middle layer contribute 1 atom.

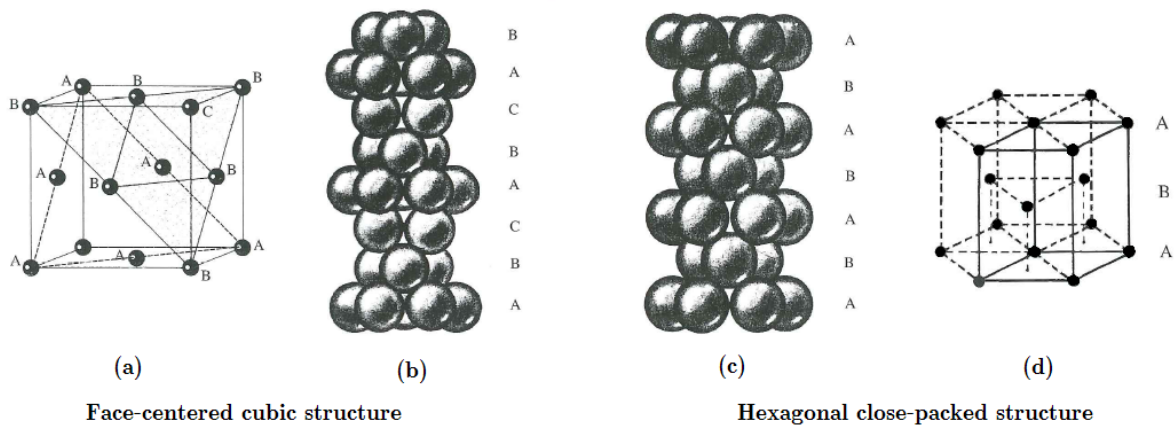


**Figure B.10:** (a) Stacking sequence of some parallel atomic (111) planes in an FCC structure. Only one atom of the parallel C plane is shown. (b) Stacking sequence of parallel atomic (111) planes in the FCC structure. The positions of the A, B and C layers are all different and repeat periodically. (c) Stacking sequence of the atomic planes in an HCP structure. (d) HCP structure, A and B planes alternate. Figures reproduced from [FA08].

be classified like this:

- Zero-dimensional imperfections (**point defect**). For example, there can be a missing atom (a vacancy), an interstitial atom, a Frenkel or a Schottky defect.
- One-dimensional imperfections (**linear defects, or dislocations**). There are edge dislocations (the defect runs along the edge of the extra row atom), screw dislocations (spiral stacking of crystal planes around the dislocation line) or mixed dislocations that have both edge and screw characters.
- Two-dimensional imperfections (**planar defects**). For example, there may be a twin boundary that separates two crystalline regions that are, structurally, mirror images of each other, or the grain boundary.

For more details about these defects, consult [Sha96] or [FA08]. Here, just dislocation will be shortly described.

Plastic deformation of crystalline solids is difficult without dislocations. In fact, the theoretical shear strength of a crystal, calculated assuming that the shear is homogeneous (the entire crystal shears simultaneously on one plane, as shown in Figure (B.11)), is very large (many orders of magnitude greater than usual  $\text{CRSS}^2$  values).

Nevertheless, the assumption of homogeneous shear is wrong. Plastic deformation in crystals normally occurs by the movement of the dislocations, which are usually present in large numbers. Figure (B.12) illustrates the role a dislocation can play in the shear of a crystal along a

<sup>2</sup>CRSS = Critical Resolved Shear Stress.

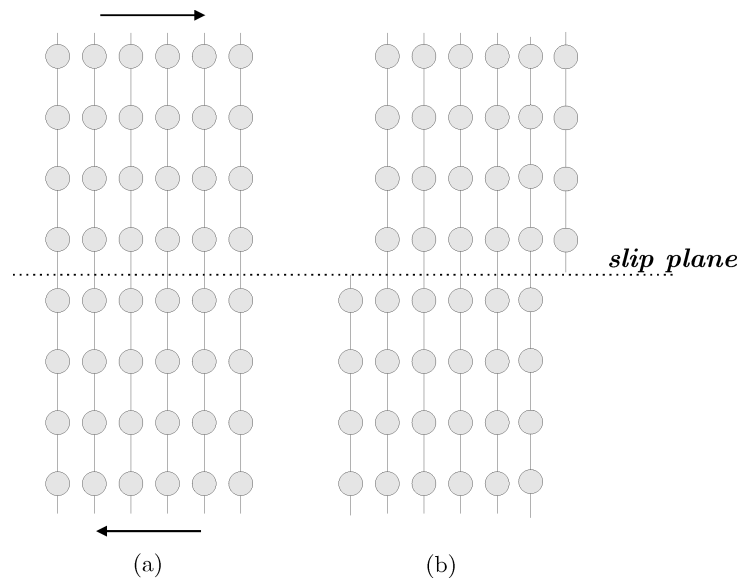


**Figure B.11:** Sliding of one plane of atoms past an adjacent one. This high-stress process is necessary to plastically (permanently) deform a perfect crystal. Figure inspired from [Sha96].

slip plane. Only a relatively small shearing force needs to operate and only in the immediate vicinity of the dislocation in order to produce a step-by-step shear that eventually yields the same overall deformation as the high stress mechanism (Figure (B.11)).

In general, the micromechanical mechanism of slip (dislocation motion) occurs in high-atomic-density planes and in high-atomic-density directions. A combination of families of crystallographic planes and directions corresponding to dislocation motion is referred to as a slip system. Examples of slip systems that can be activated in BCC and in HCP materials are summarized in Table (B.3). They are illustrated in Figures (B.13) and (B.14).

Crystal structure	Slip plane	Slip direction	Number of slip systems
BCC	$\{101\}$	$\langle 11\bar{1} \rangle$	12
	$\{112\}$	$\langle 11\bar{1} \rangle$	12
	$\{123\}$	$\langle 11\bar{1} \rangle$	24
HCP	(0001)	$\langle 11\bar{2}0 \rangle$	3 (basal)
	$\{10\bar{1}0\}$	$\langle 11\bar{2}0 \rangle$	3 (prismatic)
	$\{10\bar{1}1\}$	$\langle 11\bar{2}0 \rangle$	6 (pyramidal $\langle \mathbf{a} \rangle$ )
	$\{10\bar{1}1\}$	$\langle 11\bar{2}3 \rangle$	12 (1st order pyramidal $\langle \mathbf{c} + \mathbf{a} \rangle$ )
	$\{11\bar{2}2\}$	$\langle 11\bar{2}3 \rangle$	6 (2nd order pyramidal $\langle \mathbf{c} + \mathbf{a} \rangle$ )

**Table B.3:** Major slip systems in BCC and HCP metal structures.

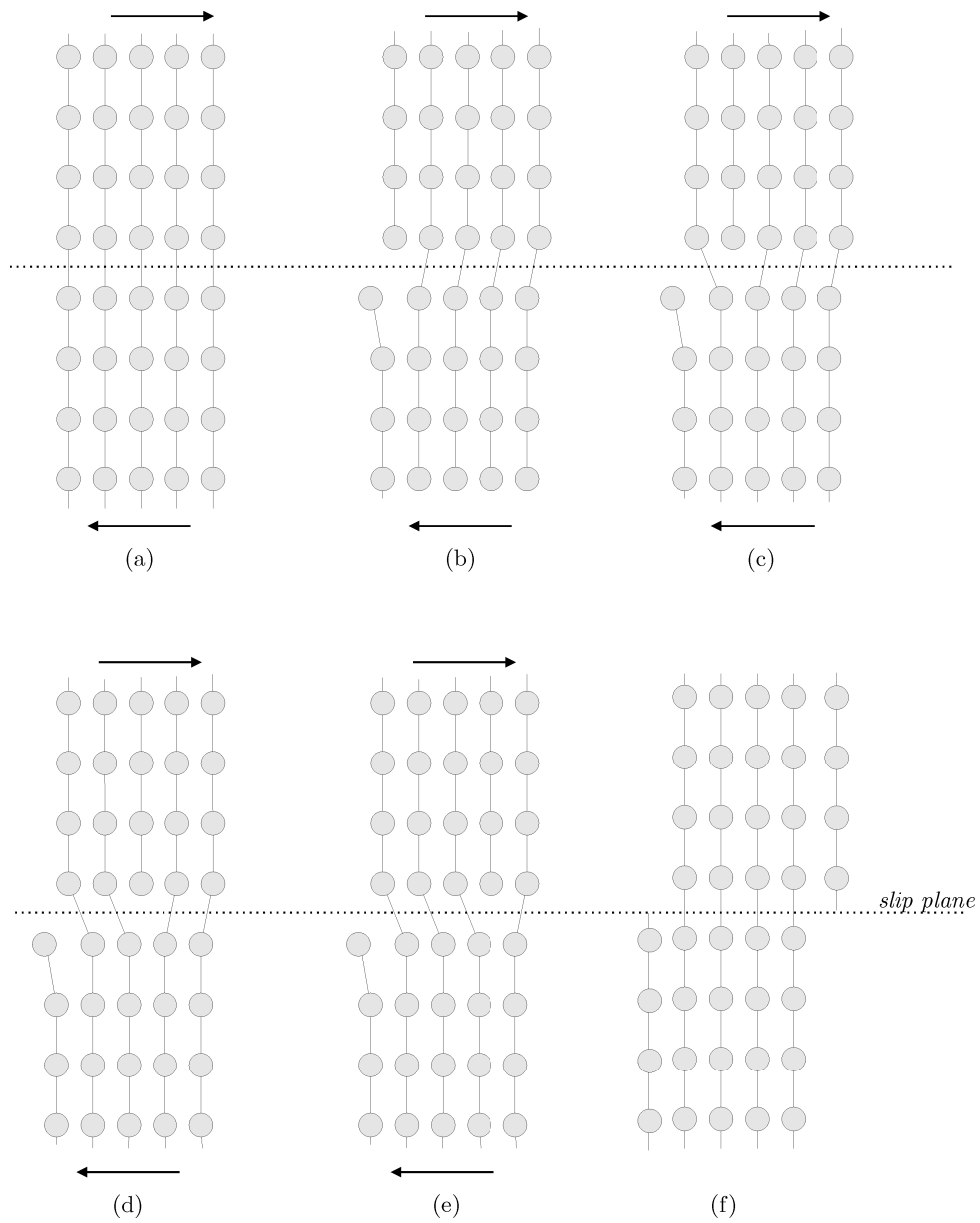


**Figure B.12:** A low-stress alternative for plastically deforming a crystal involves the motion of a dislocation along a slip plane. Figure inspired from [Sha96].

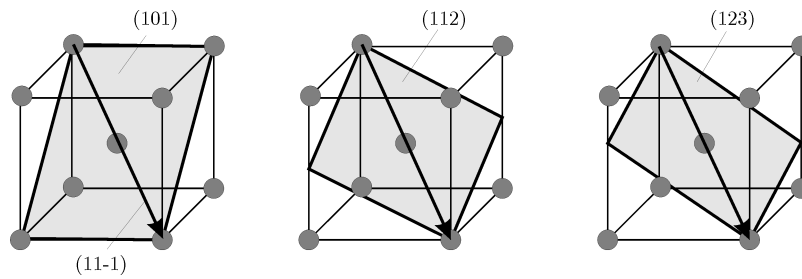


Figure B.13: Slip systems in BCC materials. Information from [LW07].

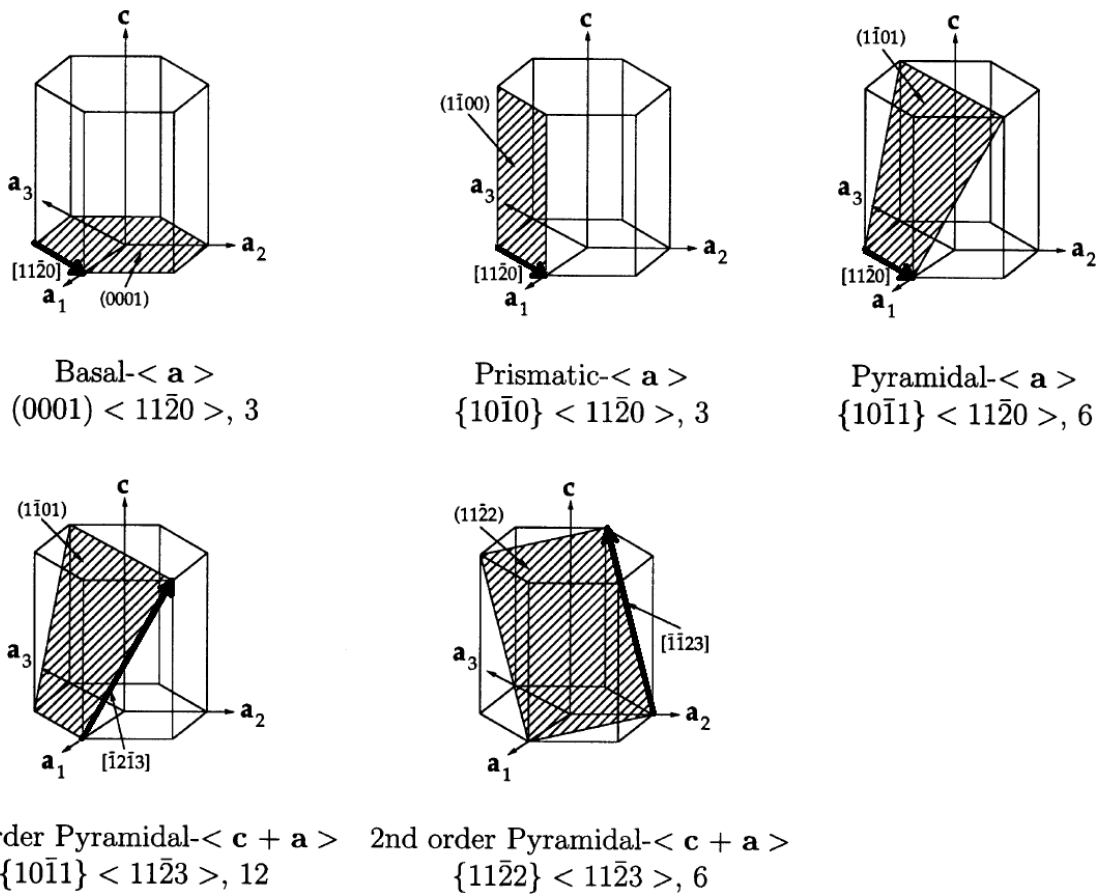


Figure B.14: Basal  $\langle \mathbf{a} \rangle$ , prismatic  $\langle \mathbf{a} \rangle$ , pyramidal  $\langle \mathbf{a} \rangle$  slip systems, and first- and second-order pyramidal  $\langle \mathbf{c} + \mathbf{a} \rangle$  slip systems in HCP materials. Figure collected from [BA02].





## Appendix C

# Periodic homogenization - Validation of the implementation

### C.1 Introduction

To validate the periodic homogenization implemented in the *Lagamine* finite element code, simple tests were performed using the  $3*3*3$  finite element (BWD3D<sup>1</sup>) mesh presented in Figure (C.1).

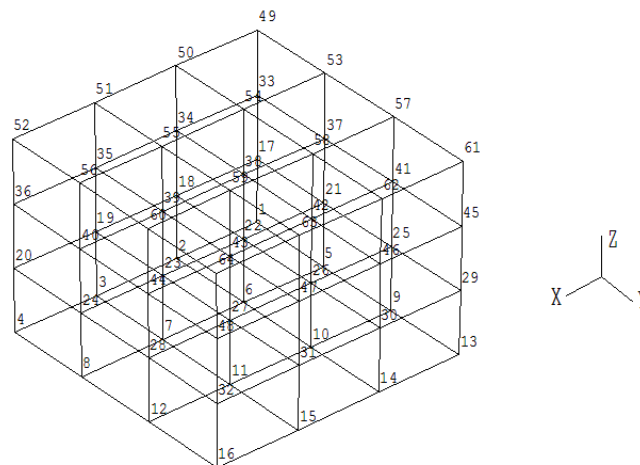


**Figure C.1:** FE mesh of 27 elements composed of eight nodes. The nodes are numbered.

Using this FE mesh, the periodic conditions are imposed on the IDMAT<sup>2</sup> matrix as followed:

- One node is fixed to avoid rigid-body motion. In this case, it is one corner (node 1) at which no displacement is imposed.

---

<sup>1</sup>A short description of this element is provided in Appendix (E).

<sup>2</sup>As explained in Chapter (6) of Part (II), this matrix is defined in the data file. It is used to specify which degree of freedom is free or fixed and which ones are imposed to move jointly.

- Due to periodic relations, the periodic displacement of the other corner nodes is imposed to be equal to that of the first node (no periodic displacement).
- The corresponding nodes<sup>3</sup> have the same periodic displacement (for example: nodes 21 and 24; nodes 2, 14, 50 and 62).

In this chapter, an elastic homogeneous sample at which macroscopic loading is imposed was first tested. Secondly, an elastic-plastic homogeneous sample is examined. The next section is dedicated to a heterogeneous elastic material and finally, this validation chapter ends with numerical modeling of elastic-plastic heterogeneous samples.

## C.2 Elastic homogeneous case

A first validation was performed in the elastic domain on the homogeneous mesh presented in the above section. Young's modulus and Poisson's ratio used here are:

$$\begin{cases} E = 100000 \text{ MPa} \\ \nu = 0.3 \end{cases} . \quad (\text{C.1})$$

Macroscopic loading is provided by the constant macroscopic velocity gradient  $\mathbf{L}$ , in three additional macroscopic fictive nodes (65, 66 and 67). In this case, the macroscopic velocity gradient imposed during the simulation ( $t = 0$  sec until  $t = 1$  sec) is

$$\mathbf{L} = \begin{pmatrix} 0.6 & 0 & 0 \\ 0 & -0.3 & 0 \\ 0 & 0 & -0.3 \end{pmatrix} \quad (\text{C.2})$$

corresponding to an expansion test in the first direction. This loading will be also used in Sections (C.3), (C.4) and (C.5).

### C.2.1 Updated coordinates

#### Theory - exact integration

The updated position of a node at time  $t$  is computed using the equation provided in [BB06]:

$$\dot{\mathbf{x}}^t = \mathbf{L}\mathbf{x}^t + \mathbf{v}_{per} . \quad (\text{C.3})$$

The exact integration of this equation leads to

$$\mathbf{x}^{t+\Delta t} = e^{\Delta t \mathbf{L}} \mathbf{x}^t + \boldsymbol{\lambda}^{-1} (e^{\Delta t \mathbf{L}} - \mathbf{I}) \mathbf{v}_{per} , \quad (\text{C.4})$$

where  $\boldsymbol{\lambda}$  is the matrix that contains the eigenvalues of the  $\mathbf{L}$  matrix.

---

<sup>3</sup>See Chapter (6) of Part (II) for further explanations.

### Application

For node 6 of initial coordinates (1,1,0), the updated coordinates after  $t = 1$  second are analytically computed using Eqn.(C.4):

$$\mathbf{x}^{t+\Delta t} = \begin{pmatrix} 1.8221188 \\ 0.740818 \\ 0 \end{pmatrix} . \quad (\text{C.5})$$

The results obtained from numerical modeling are exactly the same. Moreover, as was checked, there is no influence of the time step on these results.

### C.2.2 Microscopic velocity gradient

The evolution of the diagonal components of the microscopic velocity gradient matrix is given in Figure (C.2).

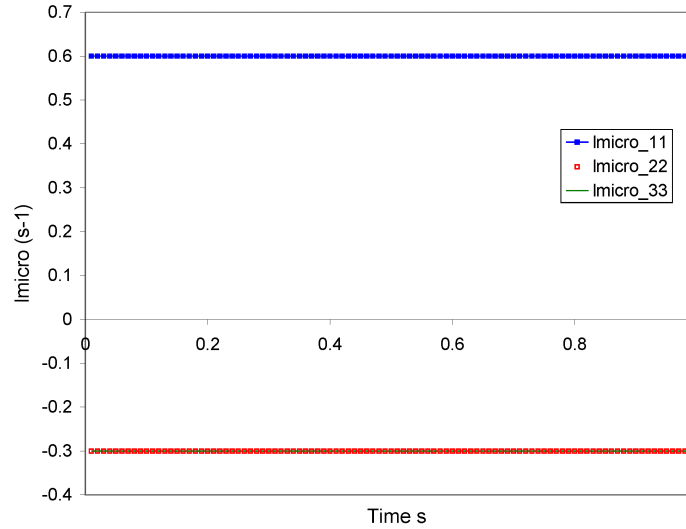


**Figure C.2:** Evolution of the microscopic velocity gradient (in the three directions) in one element of the mesh.

This figure shows that the microscopic velocity gradient matrix is the same as the macroscopic one and does not change during the test, as was expected. It was also proved that the same result is obtained in each element.

### C.2.3 Macroscopic and microscopic stresses

#### Theory - computation of the stresses

The calculated macroscopic stress in small deformations is given by Hooke's law:

$$\Sigma_{ij} = \frac{E}{(1 + \nu)(1 - 2\nu)} \{ (1 - 2\nu)\varepsilon_{ij} + \nu\varepsilon_{ll}\delta_{ij} \} , \quad (\text{C.6})$$

with<sup>4</sup>  $\varepsilon_{ij} = L_{ij} * t$ . Thus, in the first direction and in the case  $\varepsilon_{11} + \varepsilon_{22} + \varepsilon_{33} = 0$ ,

$$\Sigma_{11} = \frac{E}{(1 + \nu)(1 - 2\nu)} \{(1 - 2\nu)\varepsilon_{11} + \nu(\varepsilon_{11} + \varepsilon_{22} + \varepsilon_{33})\} = \frac{E}{(1 + \nu)} L_{11} * t . \quad (\text{C.7})$$

The calculated stress matrix is thus, for  $E = 100000$  MPa,  $\nu = 0.3$ ,  $t = 1$  sec and the macroscopic velocity gradient given above,

$$\Sigma = \begin{pmatrix} 46153.8 & 0 & 0 \\ 0 & -23076.9 & 0 \\ 0 & 0 & -23076.9 \end{pmatrix} \text{ MPa} . \quad (\text{C.8})$$

### Application

In Figure (C.3), the theoretical results are compared to the macroscopic numerical ones and the microscopic ones (in one element). As expected, the microscopic stress tensor is the same in each grain and the same as the macroscopic one. The results are equivalent to the theoretical ones.

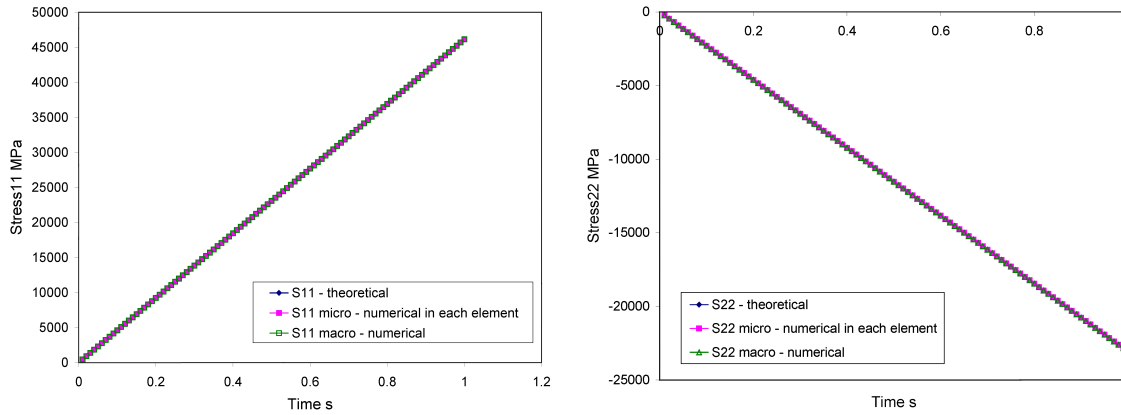


**Figure C.3:** Components of the stress during a tensile test in an elastic homogeneous sample: (left) component 11 and (right) component 22. Theoretical and numerical (microscopic and macroscopic) results are superimposed.

## C.3 Elastic-plastic homogeneous case

This second test is similar to the first one, except for plasticity onset. Now, the material is not purely elastic after a strain value of 0.02. Young's modulus is equal to 100000 MPa as in the first test and the plastic modulus is equal to 4000 MPa.

### C.3.1 Updated coordinates

The theoretical and the numerical coordinates of node 6 (using exact integration) are represented in Figure (C.4).

<sup>4</sup>In the general case where  $\mathbf{L}$  is not symmetric,  $\varepsilon = \frac{1}{2}(\mathbf{L} + \mathbf{L}^T) * \Delta t$  .

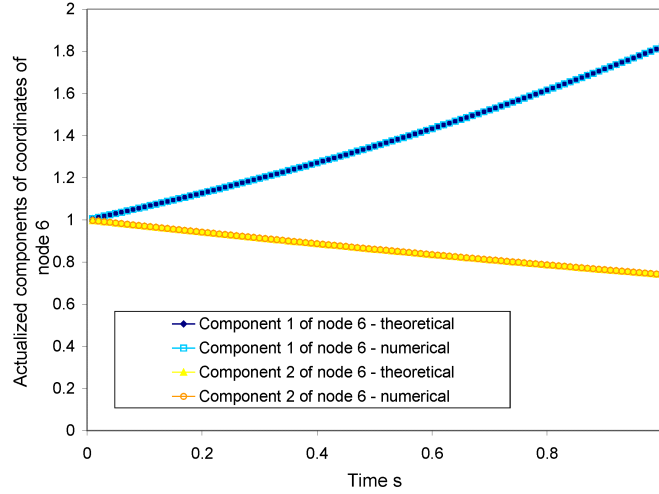


**Figure C.4:** Evolution of the first and second components of the coordinates of node 6 during the elastic-plastic test. Comparison of theoretical and numerical results.

### C.3.2 Evolution of the microscopic velocity gradient

As in the first case and as was expected due to the homogeneity of the sample, the microscopic velocity gradient is equal to the macroscopic one and does not evolve during the test. Furthermore, as was expected, the periodic velocity is equal to zero during the entire test.

### C.3.3 Macroscopic and microscopic stresses

The macroscopic stress in the first direction ( $\Sigma_{11}$ ) and the corresponding microscopic ( $\sigma_{11}$ ) one in the first element are superimposed during the test in Figure (C.5). The microscopic and macroscopic results are identical.

## C.4 Elastic heterogeneous case

In this test, the same loading as described in Section (C.2) is applied. The mesh is composed of two elastic materials. The distribution of these two materials in the sample is depicted in Figure (C.6). The first material has a Young's modulus  $E_1$  and the second, a Young's modulus  $E_2$  with

$$\begin{cases} E_1 = 100000 \text{ MPa} \\ E_2 = 71428.6 \text{ MPa} \end{cases} \quad (\text{C.9})$$

### C.4.1 Stress in each element

The stress along the first direction is saved during the simulation in each element (Figure (C.7)). It appears that, in this heterogeneous sample,  $\sigma_{11}$  is different from one element to

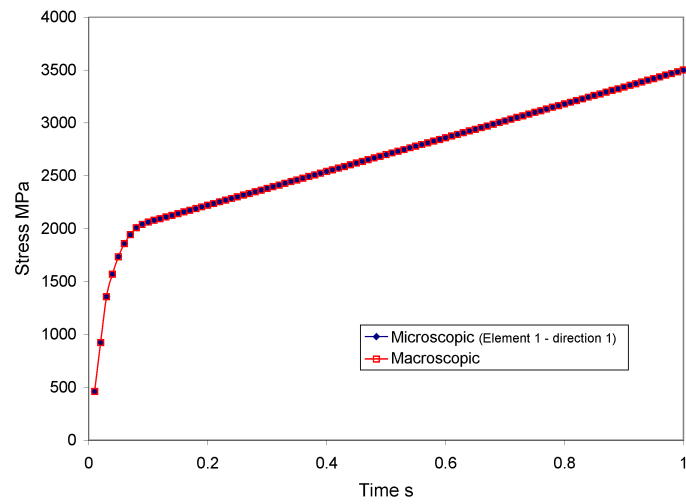


**Figure C.5:** Numerical stress versus time obtained for elastic-plastic homogeneous expansion test.

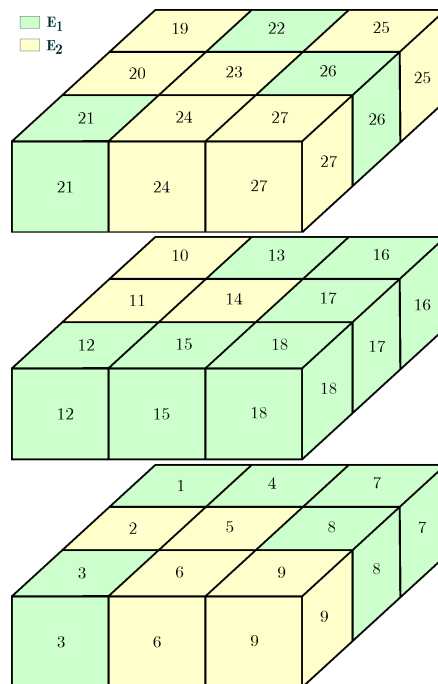


**Figure C.6:** The 3 layers of the FE sample composed of 27 elements. Elements 1, 3, 4, 7, 8, 12, 13, 15, 16, 17, 18, 21, 22 and 26 have Young's modulus  $E_1$ . Elements 2, 5, 6, 9, 10, 11, 14, 19, 20, 23, 24, 25 and 26 have Young's modulus  $E_2$ .

another. The macroscopic stress in the same direction, obtained from the macroscopic nodes, is superimposed onto these results. In the figure on the right, this first component of the macroscopic stress is compared to the average of the weighted microscopic stresses, leading to identical results.

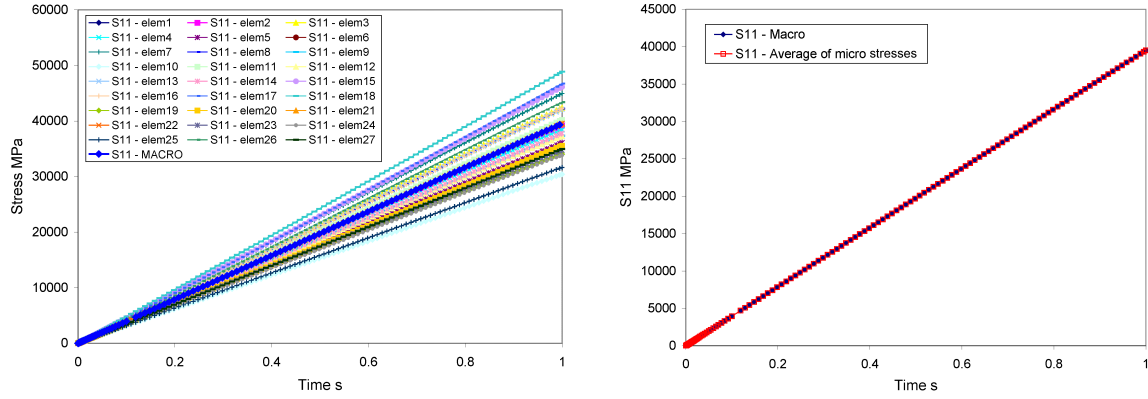


**Figure C.7:** Component 11 of the stress tensor in the heterogeneous elastic-plastic case. (Left) Component  $\sigma_{11}$  in each element of the mesh during the simulation. The macroscopic component is superimposed. (Right) The same macroscopic component is compared to the average one (obtained from those obtained in each element, taking into account the updated volume of each element).

### C.4.2 Periodic velocity

In this heterogeneous case, the periodic velocity of some nodes of the sample should be different from zero. However, due to the periodic conditions imposed, the periodic velocity of the corner nodes should be equal to zero. This condition was successfully proved.

Moreover, the periodic velocity of some nodes must be identical due to the periodic conditions. For example, nodes 2, 14, 50 and 62 should have the same periodic velocity. These are shown for these four nodes in Figure (C.8) during the simulation in the three directions. These nodes have the same periodic velocity in each direction, as was expected.

### C.4.3 Periodic displacement

Figure (C.9) shows the initial configuration (in black) and the periodic displacement of the sample at the end of the test (in red). The mesh at the end of the test at which only the periodic displacement is added to the initial configuration is shown in Figure (C.9, right).

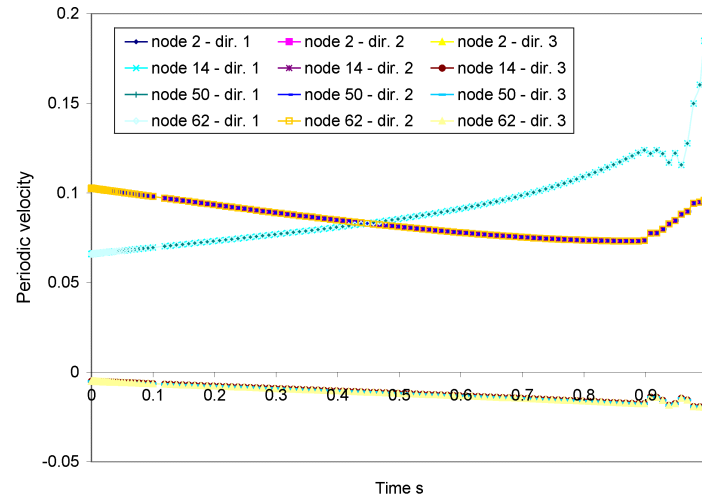


**Figure C.8:** Periodic velocity during the test for corresponding nodes: 2, 14, 50 and 62.

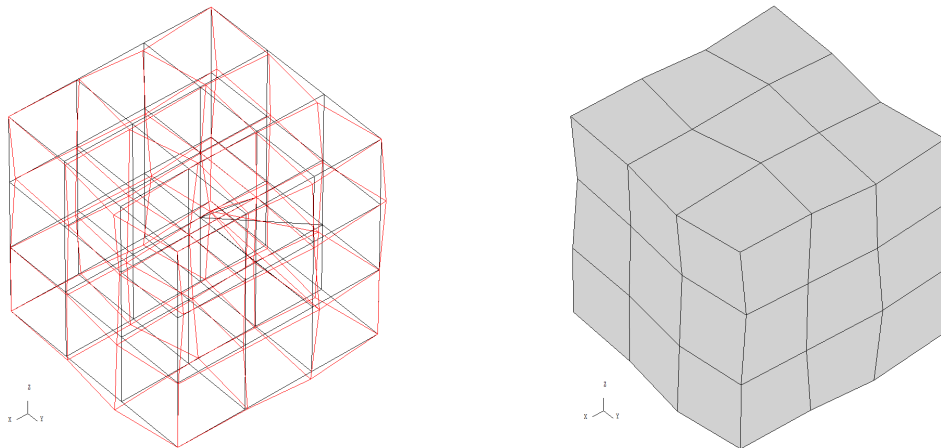


**Figure C.9:** Mesh in the initial configuration (in black) and with the periodic displacement of the sample at the end of the test (in red). On the right, periodic displacement of the mesh at the end of the test.



## C.5 Elastic-plastic heterogeneous case

### C.5.1 Elastic heterogeneities

In this test, the loading described in Section (C.2) is applied. Only Young's modulus is different from one element to another, the plastic modulus being the same for each element. The total sample is composed of elements for which Young's modulus is equal to  $E_1 = 100000$  MPa or  $E_2 = 70000$  MPa. The distribution of the two materials in the sample is the same as depicted in Figure (C.6).

The stress along the first direction is saved for each element during the numerical simulation and is shown in Figure (C.10). It appears that  $\sigma_{11}$  is different from one element to another in the elastic part and the slope is thus identical for each element in the plastic part. The macroscopic stress (obtained from macroscopic nodes) in the same direction is also superimposed onto these results. In the figure on the right, this first component of the macroscopic stress is compared to the average of the weighted microscopic corresponding components, leading to identical results.

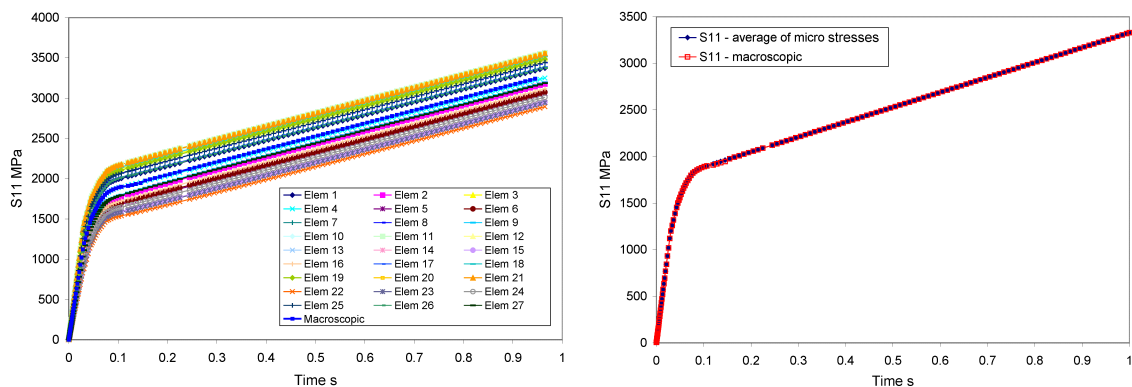


**Figure C.10:** Component 11 of the stress tensor in the heterogeneous elastic-plastic case. (Left) Component  $\sigma_{11}$  in each element of the mesh during the simulation and macroscopic corresponding component. (Right) The macroscopic component 11 is compared to the average one (obtained from the stress in each element, taking into account the updated volume of each element).

The periodic displacement is superimposed onto the initial configuration at the end of the test (Figure (C.11)). There is hardly any periodic displacement at this stage of the test. This result is not surprising. Indeed, only the elastic part is heterogeneous. Thus, at the beginning, the periodic displacement is not negligible. Later, when the homogeneous plastic part grows, the heterogeneous behavior reduces and becomes negligible. This result can also be observed looking at the periodic velocities (Figures (C.12) and (C.13)) in the three directions, for nodes 1 to 16 during the test.

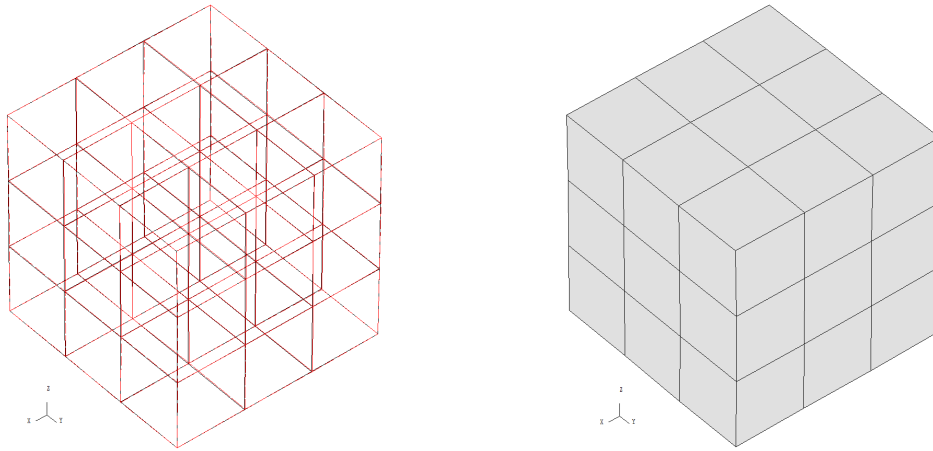


**Figure C.11:** Mesh in the initial configuration (in black) and with the periodic displacement of the sample at the end of the test (in red). On the right, periodic displacement at the end of the test.

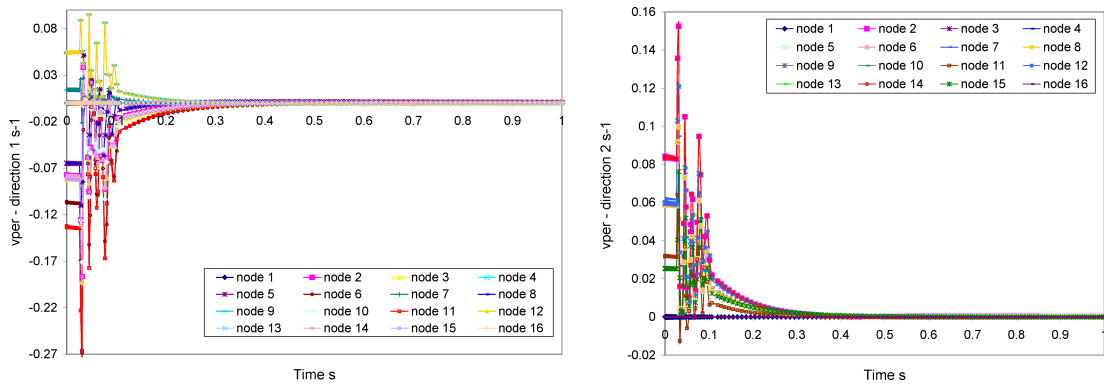


**Figure C.12:** Periodic velocities in directions  $x$  (left) and  $y$  (right) for nodes 1 to 16 during the test.

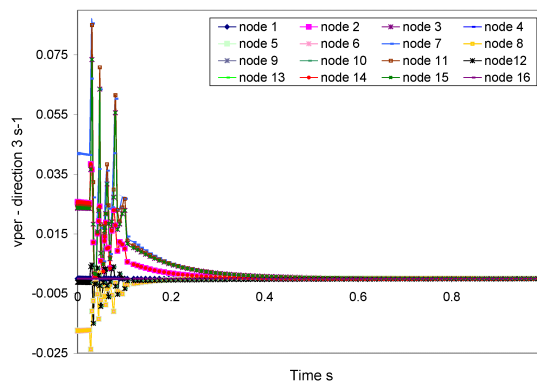


**Figure C.13:** Periodic velocities in direction  $z$  for nodes 1 to 16 during the test.

### C.5.2 Plastic heterogeneities

In this test, each element has an identical Young's modulus equal to  $E = 100000$  MPa. Elements of the first group in Figure (C.6) have a plastic modulus of  $E_{T_1} = 6000$  MPa and this parameter is equal to  $E_{T_2} = 2000$  MPa for the other elements.

The component 11 of the stress tensor of each element is superimposed in Figure (C.14). As expected, the homogeneous elastic part is the same for all elements and the heterogeneous plastic part is different from one element to another. The periodic displacement can be observed in Figure (C.15) at the end of the test.

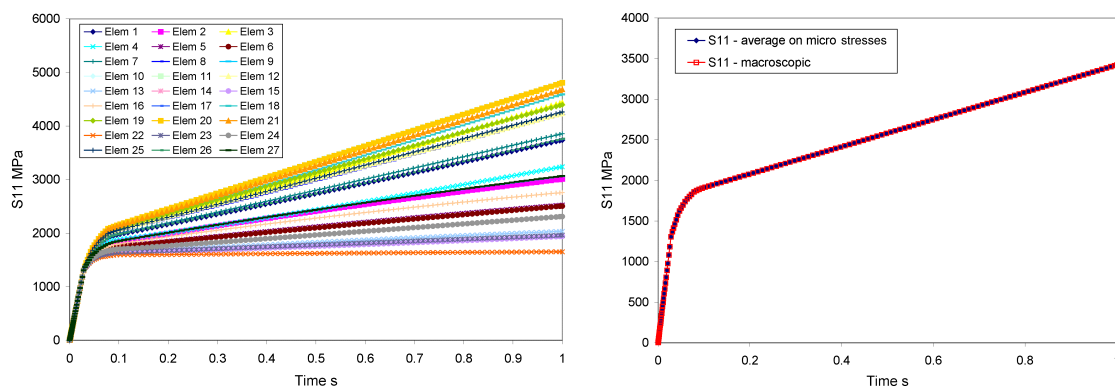


**Figure C.14:** Component 11 of the stress tensor in the heterogeneous elastic-plastic case. (Left)  $\sigma_{11}$  in each element of the mesh during the simulation and macroscopic component. (Right) The same macroscopic component is compared to the average one (obtained from each element, taking into account the updated volume of each element).

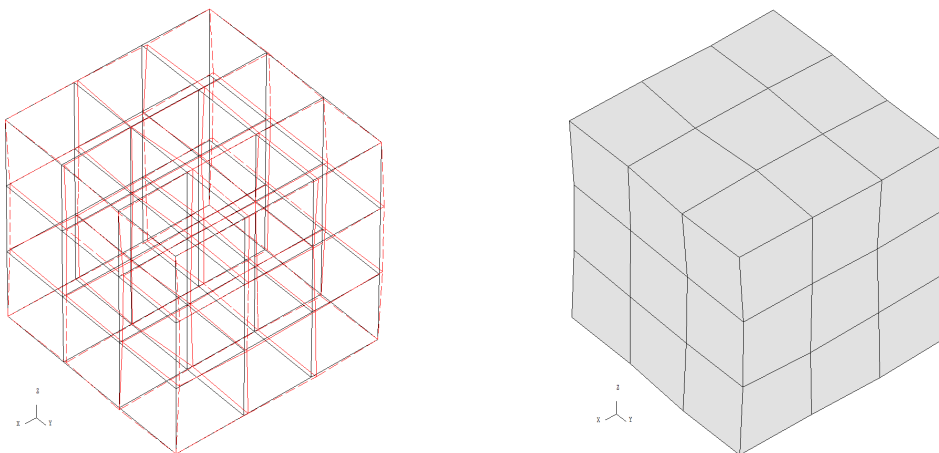


**Figure C.15:** Mesh in the initial configuration (in black) and with the periodic displacement of the sample at the end of the test (in red). On the right, periodic displacement of the mesh at the end of the test.

In Figure (C.16), the periodic velocities in the  $x$  direction of nodes 1 to 16 are represented during the test. In the elastic part (from  $t = 0$  until  $t = 0.0283$  seconds), the periodic velocities are equal to zero, due to the homogeneous behavior of the elastic part. Later, in the plastic part, the periodic velocities become non-negligible.

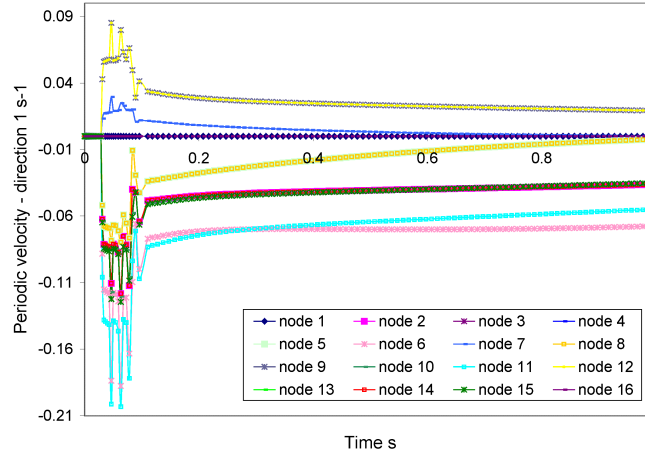


**Figure C.16:** Periodic velocities in the  $x$  direction for nodes 1 to 16 during the test (elastic homogeneous behavior and plastic heterogeneous behavior).

## C.6 Non-symmetrical loading matrix $\mathbf{L}$

Finally, a test was performed in the elastic domain ( $E = 100000$  MPa ;  $\nu = 0.3$ ) with an off-diagonal term in the  $\mathbf{L}$  matrix:

$$\mathbf{L} = \begin{pmatrix} 0.6 & 0.3 & 0 \\ 0 & -0.3 & 0 \\ 0 & 0 & -0.3 \end{pmatrix} . \quad (\text{C.10})$$

### C.6.1 Updated coordinates

In this case, the exact integration cannot be used due to the asymmetry in the  $\mathbf{L}$  matrix. A second-order approximation is chosen in this case. This consists in approaching the exponential function from its limited development:

$$e^x = \sum \frac{x^n}{n!} = 1 + x + \frac{x^2}{2} + \frac{x^3}{6} + \dots \quad (\text{C.11})$$

For a development limited to the second order (which [BB06] showed to be sufficient), the equation becomes

$$\mathbf{x}^{t+\Delta t} = (\mathbf{I} + \Delta t \mathbf{L} + \frac{(\Delta t \mathbf{L})^2}{2}) \mathbf{x}^t + \lambda^{-1} (\Delta t \mathbf{L} + \frac{(\Delta t \mathbf{L})^2}{2}) \mathbf{v}_{per}^t . \quad (\text{C.12})$$

Using this approximation, the updated coordinates of a node of initial coordinates  $(1, 1, 0)$  are given in Figure (C.17), during the simulation and as a function of the time step used to perform the simulation.

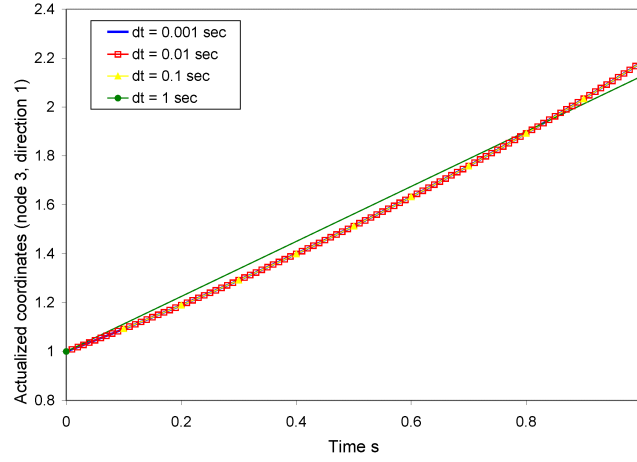


**Figure C.17:** Updated coordinates for node 6 of initial coordinates (1,1,0) during the test for the loading of Eqn.(C.10).

### C.6.2 Periodic velocity and microscopic velocity gradient $l$

The periodic velocities should be equal to zero for all nodes due to the homogeneous behavior of the sample. This was checked and the results matched expectations.

For the same reason, in all elements, the microscopic velocity gradient should be the same and equal to the macroscopic one, due to the homogeneous behavior. It is in fact the case, even during the whole simulation.

### C.6.3 Stresses

The microscopic stress is the same in each element, as predicted.

#### Theoretical values of the stress tensor

Here, the tensor  $\mathbf{L}$  (Eqn.(C.10)) is not symmetric. Thus, to avoid rotation and Jaumann's correction<sup>5</sup>, only small strains are imposed. The macroscopic loading is

$$\boldsymbol{\varepsilon} = \frac{1}{2}(\mathbf{L} + \mathbf{L}^T) = \begin{pmatrix} 0.6 & 0.15 & 0 \\ 0.15 & -0.3 & 0 \\ 0 & 0 & -0.3 \end{pmatrix} * t \quad (\text{C.13})$$

and from Hooke's law, for small strains,

$$\Sigma_{ij} = \frac{E}{(1 + \nu)(1 - 2\nu)} \{(1 - 2\nu)\varepsilon_{ij} + \nu\varepsilon_{ll}\delta_{ij}\} \quad (\text{C.14})$$

<sup>5</sup>Jaumann's rate is generally used to perform objective time derivatives for non-objective tensors. Jaumann's stress rate is defined [FRH05] as

$$\overset{\circ}{\boldsymbol{\sigma}} = \dot{\boldsymbol{\sigma}} + \boldsymbol{\sigma} \cdot \boldsymbol{\omega} - \boldsymbol{\omega} \cdot \boldsymbol{\sigma}$$

where  $\boldsymbol{\omega}$  is the antisymmetric part of the tensor  $\mathbf{L}$ :  $\boldsymbol{\omega} = \frac{1}{2}(\mathbf{L} - \mathbf{L}^T)$ .

Theoretically, the corresponding stress tensor becomes, after a time  $t = 0.05$  seconds (in MPa),

$$\Sigma = \begin{pmatrix} 2307.69 & 576.9 & 0 \\ 576.9 & -1153.8 & 0 \\ 0 & 0 & -1153.8 \end{pmatrix}. \quad (\text{C.15})$$

### Numerical values of the stress tensor

Numerically, the stress tensor obtained for each element, after the time step  $t = 0.05$  seconds, is nearly the same:

$$\sigma = \begin{pmatrix} 2311.9 & 563.9 & 7.18E - 12 \\ 563.9 & -1158.1 & -2.15E - 12 \\ 7.18E - 12 & -2.15E - 12 & -1153.8 \end{pmatrix}. \quad (\text{C.16})$$

The minor differences that appear (Figure (C.18), left) come from the approximation of the calculated coordinates but also from Jaumann's corrections due to the asymmetry of the  $\mathbf{L}$  matrix. For greater strains (Figure (C.18), right), Jaumann's correction and as a result the gap between both curves grows.

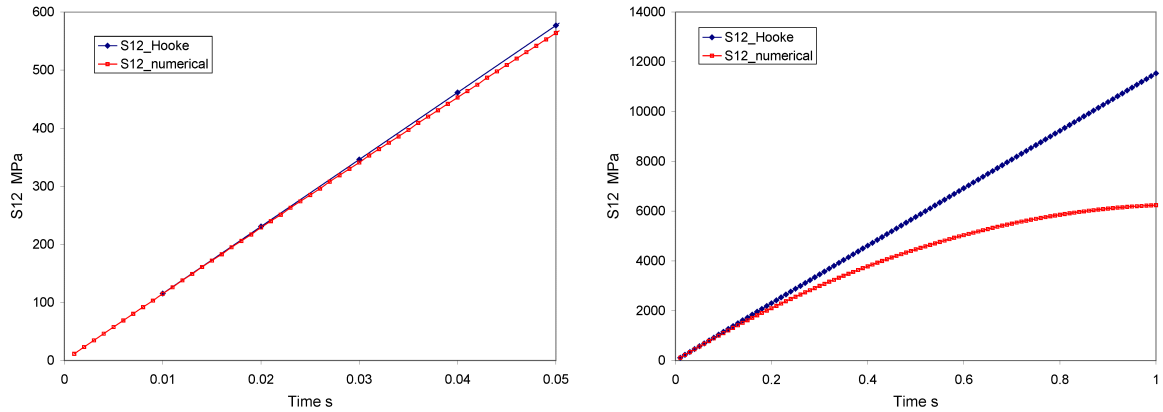


**Figure C.18:** Component 12 of the stress tensor. Calculated values from Hooke's law and the ones obtained numerically for the macroscopic loading of Eqn.(C.10) in an elastic and homogeneous environment. The figure on the left is a zoom of the right one for the beginning of the test.

## Appendix D

# Periodic homogenization: practical use in Lagamine and imposed macroscopic stress

### D.1 Practical use in Lagamine

To use the periodic homogenization method in the *Lagamine* finite element code, several pieces of information are necessary.

- In the data file (*\*.dat* file):
  1. the parameter IANA=6<sup>1</sup> in the case of periodic homogenization;
  2. 3 additive nodes must be added. The coordinates of these three nodes correspond to the macroscopic loading matrix  $\mathbf{L}$ ;
  3. to impose the periodic displacements, the IDMAT matrix must be filled, instead of giving fixed nodes. A corner node of the mesh (situated at point (0,0,0)) is fixed to avoid rigid-body motion (3 negative values in the IDMAT matrix). Due to periodicity, the other corner nodes have the same values as the first one in the IDMAT matrix. The three added nodes are also negative (i.e. fixed). For the other nodes, all free, similar values are imposed on the IDMAT matrix for corresponding nodes. The filling of the IDMAT matrix is explained in an internal report<sup>2</sup>. For the representative cell meshes used in Part (V), a tool<sup>3</sup> was developed to facilitate the filling of this matrix.
  
- In the imposed displacement file (*\*.dep* file): In this file, macroscopic loading (the 9 components of the three added nodes) is given at the beginning and at the end of the simulation.
  
- Visualization of the deformed configuration:

---

<sup>1</sup>IANA is the second parameter of the first parameter line in the *\*.dat* file.

<sup>2</sup>Report: the *Lagamine code preprocessor user's guide* (page 9).

<sup>3</sup>Tool called *IDMAT.F90* located in the department server in the following directory:  $Z : \backslash Lagateam \backslash Maillage \backslash Gerday \backslash maillages \backslash cellules \backslash representatives$ .

1. To visualize only the periodic displacements of the representative cell, the SELECT and DESFIN tools can be used as usual. The deformed configuration is just the initial configuration at which the periodic displacements are added.
2. To visualize the total deformed configuration, it is necessary to modify one parameter of the *\*.dat* file before the beginning of the numerical simulation: the IMDIS parameter<sup>4</sup>. IMDIS=6 for periodic homogenization when the total deformed configuration has to be drawn. Once the simulation has been achieved, the tool MESCONDPER<sup>5</sup> must be used before the SELECT tool. The former tool gives three new files: *\*\_CP.F01*, *\*\_CP.F03* and *\*\_CP.DON*. Using these files, the deformed configuration can be observed with DESFIN.

## D.2 Periodic homogenization: Imposed macroscopic stress

In this work, when the periodic homogenization technique was used, the imposed loading was always the macroscopic velocity gradient. However, with this theory, it should be also possible to impose the macroscopic stress tensor instead of the macroscopic velocity gradient tensor or a combination of these two tensors (using some components of the macroscopic stress tensor and some components of the microscopic tensor).

In the case of imposing a macroscopic stress tensor or a combination of both tensors, some modifications are needed in the data files and in the code. These modifications are not performed in the *Lagamine* code but some comments about them are given hereafter.

### D.2.1 In the data files

#### In the *\*.DAT* file

- Similar to the imposed macroscopic velocity gradient  $\mathbf{L}$ , three nodes will have to be added. The imposed components of the  $\mathbf{L}$  matrix and an approximate value of the other components will be given as the three coordinates of the three added nodes.
- In the *IDMAT* matrix, some changes are needed compared to the case where just  $\mathbf{L}$  components are imposed:
  - For imposed  $\mathbf{L}$  components, the corresponding components in the *IDMAT* matrix will have to be negative.
  - For imposed  $\mathbf{\Sigma}$  components, the corresponding components in the *IDMAT* matrix will have to be positive.

<sup>4</sup>IMDIS is the eighth of the second line containing parameters in the *\*.dat* file.

<sup>5</sup>This tool replaces the first column of CONEC by the true updated coordinates calculated at each step in the element subroutine BWD3DB. This tool can be found in the department server in the following directory: *Z : \TITAERO \ Donnees \ Mes outils Lagamine*.



### The loading file(s)

For the imposed macroscopic velocity gradient components, a *\*.DEP* file has to be filled in. Moreover, in the case of macroscopic imposed stress components, a *\*.LOA* file also has to be filled in.

#### D.2.2 In the code

In *Lagamine*, the unknown components of the  $\mathbf{L}$  matrix are first estimated and used as input for the constitutive law. Once the system is solved, the imposed stresses are used. Consequently, to ensure equilibrium, a possible correction of the unknown  $\mathbf{L}$  should be imposed for the next iteration.

In practical terms, to ensure that the code runs correctly using imposed macroscopic stress components, several modifications will be needed. Some of these are mentioned hereafter:

- The unknown components of the  $\mathbf{L}$  matrix are not constant for one step. An average value of these components on the step (using the components of the *CONEC* matrix where the coordinates of each node are saved at the beginning and at the end of each step) will have to be used to better approximate the macroscopic velocity gradient components before the computation of the corresponding microscopic ones.
- There may be some changes to perform in the subroutines that compute the norms to ensure that no problem of dimension in these norms occurs.



## Appendix E

# Finite element "BWD3D" and mechanical contact

### E.1 3D finite element BWD3D

The following description of the BWD3D element, written by C. Henrard [Hen09], is a simplified version of the description published by L. Duchêne in one of his papers [DEHH07].

The BWD3D element, shown in Figure (E.1), is a 3D 8-node brick element with a mixed formulation adapted to large strains and large displacements. This element can be coupled with any 3D mechanical law and its stress and strain tensors are expressed in global axes.

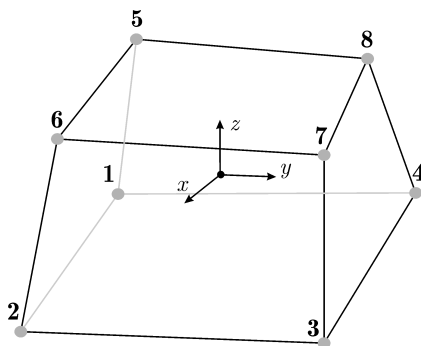


**Figure E.1:** *BWD3D* brick element and its local axes.

This element uses a reduced integration scheme (i.e. only one integration point in its center) and an hourglass control technique. It is based on the non-linear three-field<sup>1</sup> Hu-Washizu variational principle with the “assumed strain method” [SH86], [BB91].

One main feature of the BWD3D element is a new shear locking treatment based on Wang and Wagoner’s method [WW04]. This method identifies the hourglass modes responsible for shear locking and removes them. The two bending hourglass modes and the (non-physical) warp hourglass mode are eliminated. The volumetric locking treatment is also based on the

---

<sup>1</sup>The three fields are the stress, strain, and displacement field.

elimination of inconvenient hourglass modes.

A second feature of this element is the use of a corotational reference system. In order to be able to identify the hourglass modes, crucial to the method, the formulation of the element's kinematics must be expressed in a corotational reference system [BB91], closely linked to element coordinates. This reference system must have its origin at the center of the element and its reference axes are aligned (as much as possible, depending on the element shape) with element edges. A fortunate consequence of this corotational reference system is a simple and accurate treatment of hourglass stress objectivity, by using initial and final time step rotational matrices.

The shear locking and the volumetric locking methods proposed by Wang and Wagoner, together with the corotational reference system, have been successfully implemented in the BWD3D element. Wang and Wagoner's method, as opposed to other shear locking methods (see, for example, [LC97]), has deep physical roots, which makes it very efficient for various FE analyses. Further details about the hourglass and the locking treatments in the BWD3D element can be found in [DdMEH<sup>+</sup>05] and in [DdMH06]. Also, a more complete description of the rotation of the local axis can be found in [DLF<sup>+</sup>08].

## E.2 Modeling of the mechanical contact

This section gives a few basic details about the contact and the penalisation method used in the *Lagamine* finite element code. More specific details can be found in [Cha87].

### E.2.1 General aspects

The aim of the contact model used here is to determine the loading applied on the boundary of a solid by another body (or a foundation). Let's consider the local axes ( $\mathbf{e}_n$ ,  $\mathbf{e}_r$ ,  $\mathbf{e}_s$ ) at a point of the boundary between both solids (Figure (E.2)):  $\mathbf{e}_n$  is the outward normal to the surface, and  $\mathbf{e}_r$  and  $\mathbf{e}_s$  are tangential to the surface.

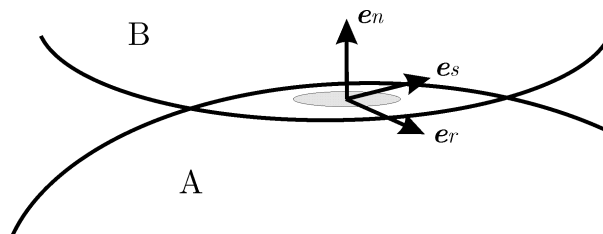


Figure E.2: Local axes at one point of contact.

The loading is composed of the contact pressure  $p$  which is normal to the contact surface, and the friction  $\boldsymbol{\tau}$ , tangential to the contact surface. So, a contact stress tensor  $\boldsymbol{\sigma}_A$  at a point A on the surface, can be written, in the local axes,

$$\boldsymbol{\sigma}_A = \begin{pmatrix} p \\ \tau_r \\ \tau_s \end{pmatrix} . \quad (\text{E.1})$$

The goal of constitutive contact laws is to evaluate of the relationship between friction  $\boldsymbol{\tau}$  and contact pressure  $p$ , taking different contact parameters, such as relative velocity, time, roughness of the surface, into account.

### E.2.2 Unilateral contact

Figure (E.3) shows two bodies in contact.  $\mathbf{v}_A$  and  $\mathbf{v}_B$  are the velocities at the contact points on the surface of A and B bodies respectively.

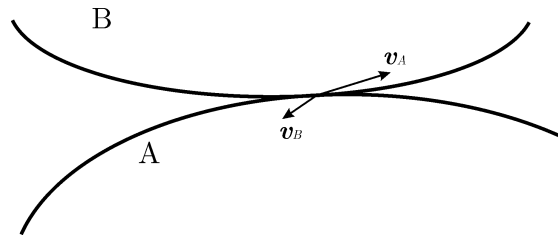


**Figure E.3:** Bodies A and B in contact and velocities at contact points.

The relative velocity of a contact point on body A with respect to the velocity of a contact point on body B,  $\Delta\mathbf{v}$  is given by:

$$\Delta\mathbf{v} = \mathbf{v}_A - \mathbf{v}_B .$$

Thus, the condition of non-penetration during contact is given by

$$\Delta\mathbf{v} \cdot \mathbf{e}_n \leq 0 \quad (\text{E.2})$$

where  $\mathbf{e}_n$  is the outward vector normal to the contact surface of body A. This condition is illustrated in Figure (E.4).

From this figure and from the condition of no penetration, if the dot product ( $\Delta\mathbf{v} \cdot \mathbf{e}_n$ ) is

- **equal to zero**, then there are two possibilities. The first corresponds to a relative velocity perpendicular to the normal vector and then, to a relative movement tangential and the bodies are sliding along each other. The second corresponds to a null vector of relative velocity. In this case, the velocity of the two bodies is the same and the bodies are sticking.
- **negative**, the loss of contact occurs.
- **positive**, the first body (A) is penetrating the second one (B).

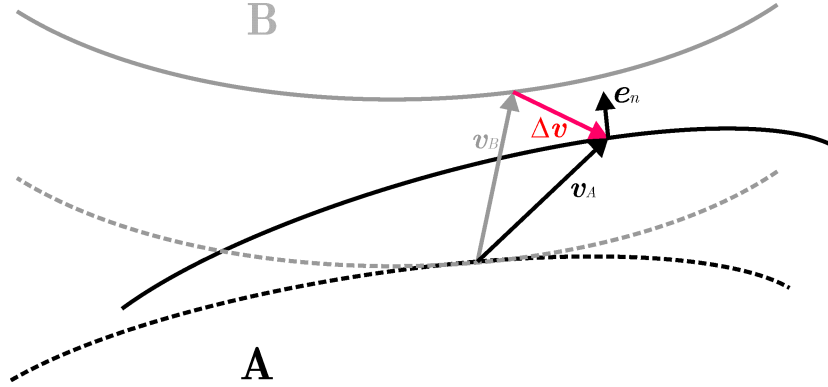


Figure E.4: Illustration of the non-penetration condition.

Considering the value of  $\sigma_n$  (or  $p$ ), the contact is characterized by

$$\sigma_n \geq 0 . \quad (\text{E.3})$$

The normal stress is positive when there is a mechanical interaction between the two bodies. It can be equal to zero when the two bodies are just touching each other, without loading.

Both kinetic and mechanical conditions presented above and known as Signorini's conditions of unilateral contact are summarized hereafter:

$$\left\{ \begin{array}{l} \sigma_n \geq 0 \\ \Delta \mathbf{v} \cdot \mathbf{e}_n = 0 \\ (\Delta \mathbf{v} \cdot \mathbf{e}_n) \cdot \sigma_n = 0 . \end{array} \right. \quad (\text{E.4})$$

The third condition implies that the contact stress is equal to zero when the contact is lost (corresponding to  $\Delta \mathbf{v} \cdot \mathbf{e}_n < 0$ ), and that the contact remains ( $\Delta \mathbf{v} \cdot \mathbf{e}_n = 0$ ) when the pressure is maintained ( $\sigma_n > 0$ ).

### E.2.3 Coulomb's model

The constitutive contact law used is Coulomb's, a well-known model. The absolute value of friction  $|\tau|$  is limited to a maximum (or critical) value  $\tau_c$  equal to

$$\tau_c = \mu p \quad (\text{E.5})$$

where  $\mu$  is the friction coefficient. This is illustrated in Figure (E.5).

The contact is sticking as long as the tangential loading is lower than the critical value  $\tau_c$ . This means that no relative displacement between the bodies in contact can be observed. Once the critical value  $\tau_c$  is reached, the bodies are sliding along each other and the friction is equal to  $\tau_c$ . Assuming isotropic friction, the critical value  $\tau_c$  does not depend on the sliding direction.

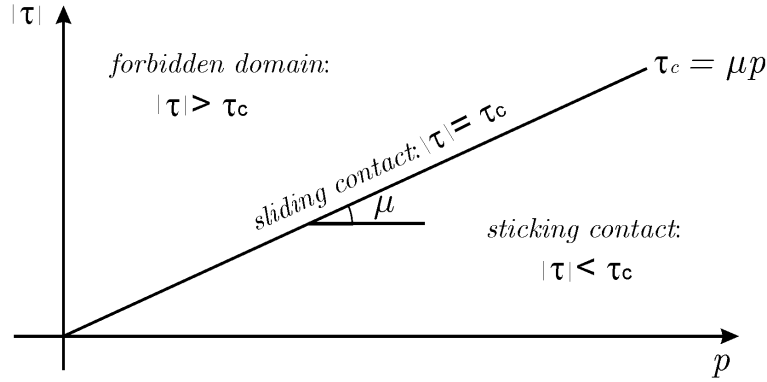


Figure E.5: Coulomb's friction model.

#### E.2.4 Penalty technique

According to the method of resolution used, mechanical or geometrical aspects of contact can be privileged. In a first approach, the exact geometry is given, regardless of contact conditions. Stresses are then deduced from imposed strains. This method is generally performed thanks to Lagrangian multipliers. Its advantage is that the exact geometry is respected, but it introduces multipliers and so new degrees of freedom, and it requires adapted algorithms [Pas03]. In a second approach, the right forces are applied to the solids and the geometry follows. To respect the non-penetration condition as much as possible, the parts of the solids that penetrate into one another are rejected. This is the *penalty technique*.

When two bodies come into contact, the distance,  $d$ , between them decrease to zero. Then, the contact pressure ( $\sigma_n$ ) increases suddenly. From a numerical point of view, this phenomenon is expressed by an infinite value in the stiffness matrix of the system:

$$\left\{ \begin{array}{l} \frac{\partial \sigma_n}{\partial d} = 0 \quad \text{until contact occurs} \\ \frac{\partial \sigma_n}{\partial d} \rightarrow \infty \quad \text{during contact} . \end{array} \right. \quad (\text{E.6})$$

To avoid numerical problems, it is convenient to admit a progressive interpenetration of the bodies. However, this is penalized to remain as slight as possible. This is illustrated in Figure (E.6). In the case of penetration, a repulsive stress,  $\sigma_p$ , proportional to the distance of penetration,  $d$ , takes place in order to reject the body entering:

$$\sigma_p = K_p d . \quad (\text{E.7})$$

Another infinite term appears. Considering  $e$ , the relative tangential displacement of two bodies in contact, if friction  $\tau$  is lower than the critical value  $\tau_c$ , no sliding  $e$  occurs. Thus, friction can increase up to this critical value before any displacement can be measured. The

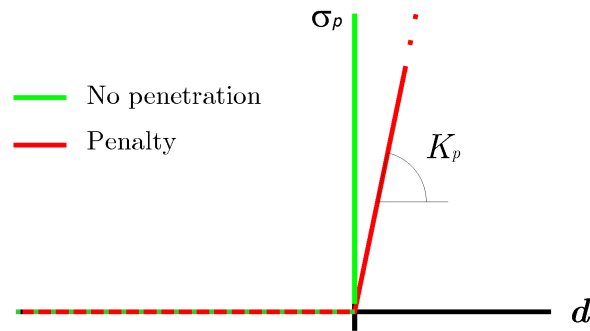


**Figure E.6:** Penalty of penetration.

derivative of  $\tau$  with respect to the displacement  $e$  is thus also positive in the case of sticking contact. On the contrary, once the friction reaches the critical value  $\tau_c$ , sliding occurs and the displacement continues without any increase in friction. This is shown in Figure (E.7).

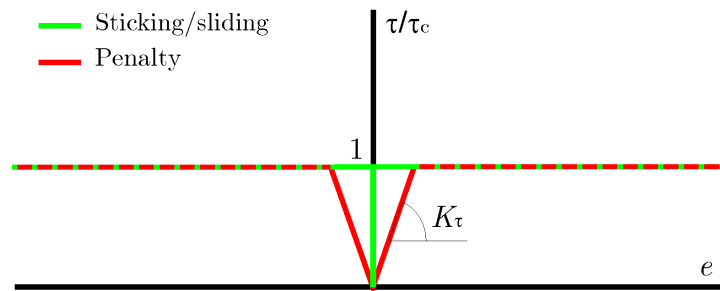


**Figure E.7:** Penalty of sticking contact.

$K_p$  and  $K_\tau$  are also called penalty coefficients. They have to be high compared to the rigidity of the solid in order to avoid the penetration of both surfaces in contact as much as possible.



## Appendix F

# Modifications in the FE code to allow for $h_s$ 's evolution

### F.1 Modifications in the preprocessor

Small modifications have to be made in the \*.dat data file in order to introduce an  $h_s$  evolution of the type:

$$h_s^{(\alpha)}(\dot{\varepsilon}) = A^{(\alpha)} \ln(\dot{\varepsilon}) + B^{(\alpha)} .$$

Instead of giving the value of the parameter  $h_s$  for each set of slip systems as done before, the values of parameters  $A$  and  $B$  have to be provided<sup>1</sup> (Figure F.1).

### F.2 Modifications in the constitutive law subroutine

In the crystalline plasticity-based constitutive law subroutine, these changes were performed to introduce the evolution of  $h_s$  with the strain rate.

1. Computation of the increment of equivalent (Von Mises') strain rate,  $\Delta\dot{\varepsilon}_{eq}^{VM}$ .

First, the increment of equivalent Von Mises' strain is obtained from the strain matrix:

$$\Delta\varepsilon_{eq}^{VM} = \sqrt{\frac{2}{3}\Delta\varepsilon_{ij} : \Delta\varepsilon_{ij}} .$$

Secondly, the increment of strain rate is computed from

$$\Delta\dot{\varepsilon} = \frac{\Delta\varepsilon_{eq}^{VM}}{\Delta t} .$$

Then, an average between this value of the strain rate obtained at the current step and the one obtained at the previous step is computed to avoid convergence problems. This value is then saved in the state variable vector.

---

<sup>1</sup>Note that the description of  $h_s$  with only one parameter ( $h_s = \text{constant}$ ) is still possible.

```

COLAW
1 803  UMATEVP
82000  0.0  0.0
0.31  0.0  0.0
0.0  0.0  0.0
0.0  0.0  0.0  0.0  0.0  0.0
0.0  0.0  0.0  0.0  0.0  0.0
2.0  0.0  0.0  1
1.0  1.0  1.0  0.0
1.0  1.0  0.0  0.0
1.0  1.0  1.0  0.0
2.0  1.0  1.0  0.0
0.0  0.0  0.0  0.0
0.0  0.0  0.0  0.0
1.0  0.0  0.0  1.0  0.0  0.0
0.0  1.0  0.0  0.0  1.0  0.0
50.0  0.001
50.0  0.001
0.0  0.0
7482.  304.0  300.0
7482.  304.0  300.0
0.0  0.0  0.0
hs1  6.6891  0.00091  0.000314  14.6  17.9
hs2  6.6891  0.00091  0.000314  14.6  17.9
0.0  0.0  0.0  0.0  0.0
0.0  0.0
0.0  0.0
0.5  1.0
1.0  50.0  0.0001
2 280  Tool contact
0
1.0D+06  1.0D+06  0.200  0.0  0.0  0.0  0.0
0.0  0.0  0.0

```

**Figure F.1:** Part of the data file where the values of the parameters are given. In the rectangle are defined some values of parameters of Bassani's hardening, for each slip system. The lines containing the parameters  $h_s^{(\alpha)}$ ,  $\gamma_{0\alpha}$ ,  $\gamma_{0\alpha\beta}$ ,  $f_{\alpha\alpha}$  and  $f_{\alpha\beta}$  are replaced by:  $A^{(\alpha)}$ ,  $B^{(\alpha)}$ ,  $\gamma_{0\alpha}$ ,  $\gamma_{0\alpha\beta}$ ,  $f_{\alpha\alpha}$  and  $f_{\alpha\beta}$ .

## 2. Determination of $h_s$ :

Thanks to the knowledge of parameters  $A$  and  $B$  (from the data file) and the computed value of the strain rate, the  $h_s$  evolution can be updated for each set of slip systems ( $\alpha$ ) using:

$$h_s^{(\alpha)}(\dot{\epsilon}) = A^{(\alpha)} \ln(\dot{\epsilon}) + B^{(\alpha)} \quad .$$

## Appendix G

# Orientations of the $\beta$ grains in numerical simulations of shear tests

The orientations of the 30 grains used to performed the numerical shear test on 100%  $\beta$  material using the 90 FE mesh and the crystalline plasticity-based constitutive law are given in Table (G.1), on the next page.

Grain	Coordinates of local axis 1	Coordinates of global axis 1	Coordinates of local axis 2	Coordinates of global axis 2
1	(1 0 0)	(1 0 0)	(0 1 0)	(0 1 0)
2	(1 0 0.1)	(1 0 0)	(0 1 0)	(0 1 0)
3	(1 0 0)	(1 0 0)	(0 1.2 -0.1)	(0 1 0)
4	(1.2 0 -0.2)	(1 0 0)	(0 1 0)	(0 1 0)
5	(1 0 0)	(1 0 0)	(0 1 0)	(0 1 0)
6	(1 0 0.2)	(1 0 0)	(0 1 0)	(0 1 0)
7	(1 0 0)	(1 0 0)	(0 0.9 0.1)	(0 1 0)
8	(1 0 0)	(1 0 0)	(0 1.2 -0.1)	(0 1 0)
9	(0.9 0 0)	(1 0 0)	(0 1 -0.1)	(0 1 0)
10	(1 0 0)	(1 0 0)	(0 1 0.1)	(0 1 0)
11	(1 0 0.2)	(1 0 0)	(0 1 0)	(0 1 0)
12	(1 0 0)	(1 0 0)	(0 0.8 0.2)	(0 1 0)
13	(1 0 0)	(1 0 0)	(0 1 0)	(0 1 0)
14	(1 0 -0.1)	(1 0 0)	(0 1 0)	(0 1 0)
15	(1 0 0)	(1 0 0)	(0 1.2 -0.2)	0 1 0)
16	(1 0 -0.1)	(1 0 0)	(0 1 0)	0 1 0)
17	(0.9 0 0)	(1 0 0)	(0 1 -0.2)	(0 1 0)
18	(1 0 0)	(1 0 0)	(0 1 0)	(0 1 0)
19	(1 0 0.1)	(1 0 0)	(0 1.1) 0	(0 1 0)
20	(1 0 0.1)	(1 0 0)	(0 0.9 0)	(0 1 0)
21	(1 0 0)	(1 0 0)	(0 1 0.2)	(0 1 0)
22	(1 0 0.2)	(1 0 0)	(0 0.8 0)	(0 1 0)
23	(1.1 0 0)	(1 0 0)	(0 1 0.1)	(0 1 0)
24	(1 0 0.1)	(1 0 0)	(0 1 0)	(0 1 0)
25	(1 0 0)	(1 0 0)	(0 0.9 -0.1)	(0 1 0)
26	(0.9 0 0.1)	(1 0 0)	(0 1 0)	(0 1 0)
27	(1 0 0)	(1 0 0)	(0 1 0)	(0 1 0)
28	(1 0 0)	(1 0 0)	(0 1 0.2)	(0 1 0)
29	(1 0 -0.1)	(1 0 0)	(0 1.1 0)	(0 1 0)
30	(1 0 0)	(1 0 0)	(0 0.9 0.1)	(0 1 0)

**Table G.1:** Orientations of the 30 grains used in numerical shear test.

## Appendix H

### Definition of the positions in nanoindentation simulations

The macroscopic axes in which all the parts of the problem are defined are called the global axes  $\mathbf{X}$  with  $\mathbf{X}_1=(100)$ ,  $\mathbf{X}_2=(010)$  and  $\mathbf{X}_3=(001)$ .

The position of the indenter in these axes is shown in Figure (H.1).

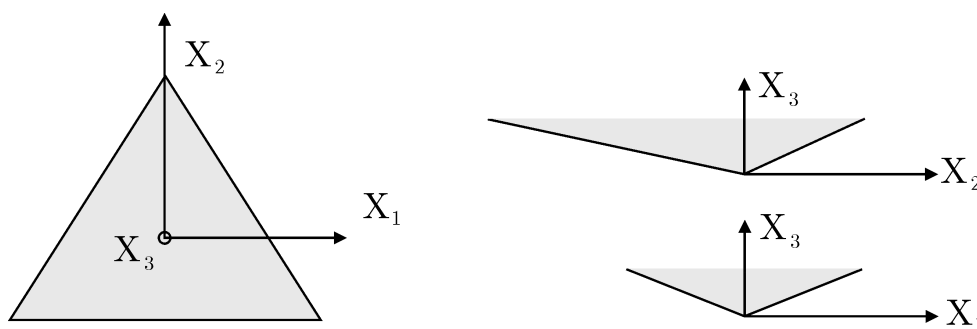


**Figure H.1:** Berkovich indenter in the global axes.

The orientation of the grains are generally given by their Euler angles. Thus, their local axes compared to the global ones are given by  $\mathbf{x} = [\mathbf{R}]\mathbf{X}$  with  $[\mathbf{R}]$  defined by [Duc03]

$$[\mathbf{R}] = \begin{pmatrix} \cos\varphi_1\cos\varphi_2 - \sin\varphi_1\sin\varphi_2\cos\phi & \sin\varphi_1\cos\varphi_2 + \cos\varphi_1\sin\varphi_2\cos\phi & \sin\varphi_2\sin\phi \\ -\cos\varphi_1\sin\varphi_2 - \sin\varphi_1\cos\varphi_2\cos\phi & -\sin\varphi_1\sin\varphi_2 + \cos\varphi_1\cos\varphi_2\cos\phi & \cos\varphi_2\sin\phi \\ \sin\varphi_1\sin\phi & -\cos\varphi_1\sin\phi & \cos\phi \end{pmatrix} .$$



## Appendix I

### Influence of the friction coefficient: complementary information

In this chapter, the minute influence of the friction coefficient on load versus displacement nanoindentation curves using a Berkovich indenter tip is explained.

Figure (I.1) provides a conical indenter with  $p$  as the contact pressure on the normal area,  $R_c$  the corresponding contact radius and  $\theta$  the included angle<sup>1</sup> (Figure I.1).

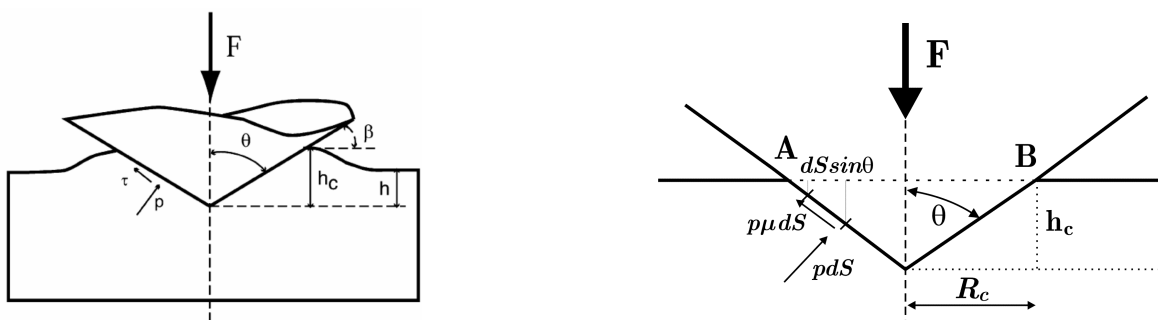


**Figure I.1:** (Left) Conical indenter in the material. Figure reproduced from [BSFM03]. (Right) Role of friction between a conical indenter and the deformed metal.

On each element of the surface of the conical indenter  $dS$ , the corresponding normal load is given by  $p dS$ . If  $\mu$  is the friction coefficient between the indenter and the material, the frictional force tangential to the element  $dS$  is  $\tau dS = \mu p dS$ . The components of these forces in the horizontal direction, when summed over the whole area of the cone, cancel out because of symmetry. Nevertheless, in the vertical direction, the components of the forces are  $p dS \sin(\theta)$  and  $\mu p dS \cos(\theta)$ . Consequently, when summed over the area of the cone,  $F$  becomes

$$F = \int dF = \int p dS \sin(\theta) + \mu p dS \cos(\theta)$$

$$\Leftrightarrow F = p \left( 1 + \frac{\mu}{\tan(\theta)} \right) \int \sin(\theta) dS .$$

<sup>1</sup>A conical indenter with  $\theta$  equal to  $70.3^\circ$  has the same area function as a pyramidal Berkovich tip [BSFM03].

However,  $dS \sin(\theta)$  is the projection of the area  $dS$  on the section AB. Hence,

$$\int dS \sin(\theta) = \pi R_c^2$$

and so

$$F = p \left( 1 + \frac{\mu}{\tan(\theta)} \right) \pi R_c^2 .$$

- For  $\mu = 0 \Rightarrow F = (\pi R_c^2)p$  .
- For  $\mu > 0$  and for a Berkovich tip ( $\theta = 70.3^\circ$ ):

$$\left\{ \begin{array}{l} \mu = 0.02 \rightarrow \frac{\mu}{\tan(70.3^\circ)} \sim 0.00716 \ll 1 \\ \mu = 0.2 \rightarrow \frac{\mu}{\tan(70.3^\circ)} \sim 0.0716 \ll 1 \end{array} \right.$$

$\Rightarrow$  *For a Berkovich indenter tip, the friction component is always less than 1. Thus, the variations in the load due to modifications of the friction coefficient are negligible.*



## Appendix J

# Modifying indenter tips to study the effect of the verticality defect on the results

The three tips used to perform numerical nanoindentation simulations are described below.

### J.1 Tip 1

The four nodes of the first tip (Figure (J.1)) are defined by the coordinates given in Table (J.1). This tip has its axis along the perfectly vertical  $z$  direction.

Node	Coord. $x$	Coord. $y$	Coord. $z$
1	0	0	0
2	50.3	-29.04	10
3	0	58.08	10
4	-50.3	-29.04	10

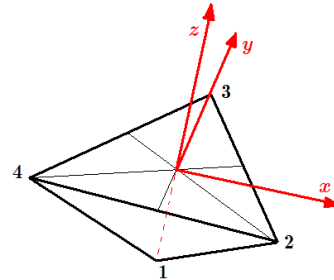


**Figure J.1:** Coordinates of the nodes defining the first tip. (Right) First indenter tip.

### J.2 Tip 2

For the second tip, it was assumed that the indenter is not perfectly vertical but rotated by  $5^\circ$  around the  $x$  axis (Figure J.2). The new tip is now the blue one in the figure with nodes  $1'$  to  $4'$ . The corresponding coordinates of the second indenter are given in the table in Figure (J.2).

### J.3 Tip 3

To complete the study, another tip rotation was done, around the axis in red (Figure (J.3)). The final coordinates of the nodes of this tip are given by

$$\mathbf{x}' = [\mathbf{R}_1]^T [\mathbf{R}_2] [\mathbf{R}_1] \mathbf{x} \quad (\text{J.1})$$

Node	Coord. $x$	Coord. $y$	Coord. $z$
1'	0	0	0
2'	50.3	-28.0579	12.493
3'	0	58.73	4.9
4'	-50.3	-28.0579	12.493

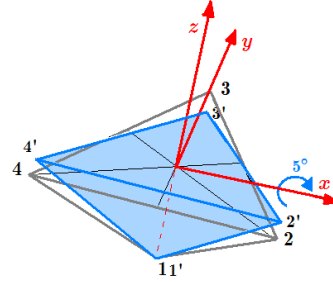


**Figure J.2:** Coordinates of the nodes defining the second tip. (Right) Second (in blue) indenter tip.

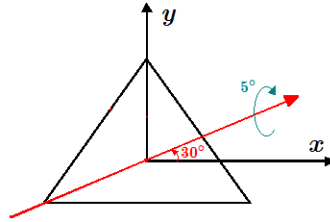


**Figure J.3:** Rotation to obtain the third indenter tip.

where  $[\mathbf{R}_1]$  rotates the  $x$  axis to the red one ( $\theta = 30^\circ$  around the  $z$  axis),

$$[\mathbf{R}_1] = \begin{pmatrix} \cos(\theta) & \sin(\theta) & 0 \\ -\sin(\theta) & \cos(\theta) & 0 \\ 0 & 0 & 1 \end{pmatrix} \quad (\text{J.2})$$

and  $[\mathbf{R}_2]$  is the rotation around the red axis ( $\varphi = 5^\circ$ ),

$$[\mathbf{R}_2] = \begin{pmatrix} 1 & 0 & 0 \\ 0 & \cos(\varphi) & \sin(\varphi) \\ 0 & -\sin(\varphi) & \cos(\varphi) \end{pmatrix}. \quad (\text{J.3})$$

The new coordinates of the tip's nodes are given in Table (J.1).

Node	Coord. $x$	Coord. $y$	Coord. $z$
1''	0	0	0
2''	49.7685	-28.1194	14.3458
3''	-0.340077	58.66903	5.57812
4''	-50.73577	-28.28521	9.96

**Table J.1:** Coordinates of the nodes defining the third tip.

## Appendix K

# Influence of the indenter's position on pile-up patterns

### K.1 Introduction

In the set of experimental nanoindentation tests performed<sup>1</sup> on the  $\beta$  phase, pile-up patterns around the indenter often have a similar asymmetric aspect, as shown in Figure (K.1).

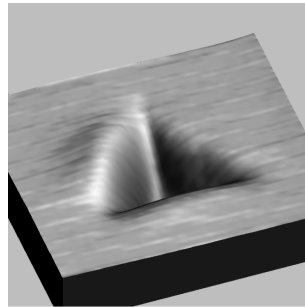


**Figure K.1:** Imprint in a  $\beta$  grain of Ti-5553 after an indentation test.

A non-negligible pile-up is observed on one side, a smaller one is observed on the second side and no pile-up appears on the third one. This qualitative result was perceived on several samples of different orientations. This is the reason why, in this chapter, the origin of these patterns is studied.

In the experimental setup, nothing is present to check the positioning of the indenter. Consequently, a defect of the tip's verticality might lead to results not linked to the material's behavior.

In this context, several numerical simulations were carried out in order to fully understand the real origin of pile-up patterns.

---

<sup>1</sup>Nanoindentation tests performed by N. Clement from UCL.

## K.2 Finite element simulations

The different tips used to perform the simulations were presented in Appendix (J). The microscopic constitutive law (with the PAN model for hardening) is used here, in order to take microscopic phenomena into account. Thus, the influence of the tip's orientation on the more or less rapid activation of slip systems will be taken into account. Moreover, the finer mesh (4544 elements) is chosen here, to increase the visualization of pile-up patterns around the indentation. The maximum penetration depth of the tip in the material is 103.5 nm.

The different cross sections were performed in the material after unloading are represented in Figure (K.2). They are in the vertical plane containing, each time, a node of the triangular indented tip and the center of the tip.

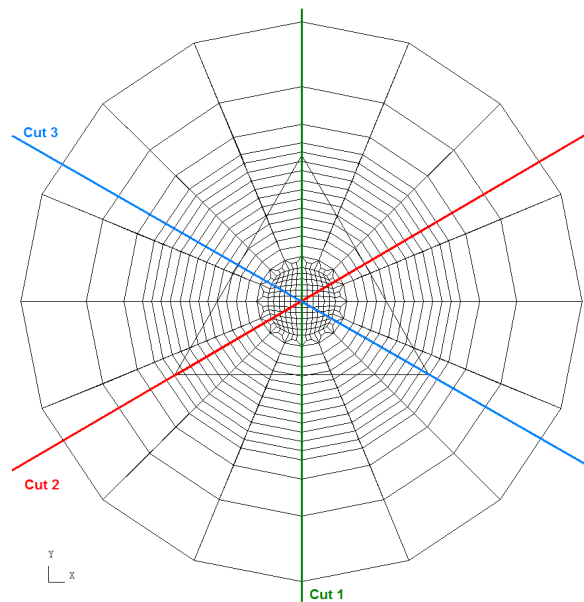


**Figure K.2:** Top view of the indented material's mesh and superimposed indenter tip. Orientation of the cross sections in the material along the three heights of the indenter.

At the end of the simulation, after tip removal, the imprints obtained with three tips are presented in Figure (K.3). The three tips are those presented in Appendix (J). The first one is perfectly vertical, the second is rotated by  $5^\circ$  around the  $x$  axis and the third one is rotated by  $5^\circ$  around an axis situated at  $30^\circ$  from the  $x$  axis, in the  $xy$  plane. This figure provides the variation of depth into the material. From these figures, it is not clear that a rotation of the indenter could lead to a change in the pile-up patterns.

Then, cross sections in Figure (K.2) were performed in the unloaded material. Results are presented for the three tips' positioning in Figure (K.4) for the first cross section, in Figure (K.5) for the second cross section and in Figure (K.6) for the third cross section.

Looking at these Figures, it is clear that there is no significant modification of pile-up heights due to a reasonable change in the verticality of the tip's positioning. To ensure that this

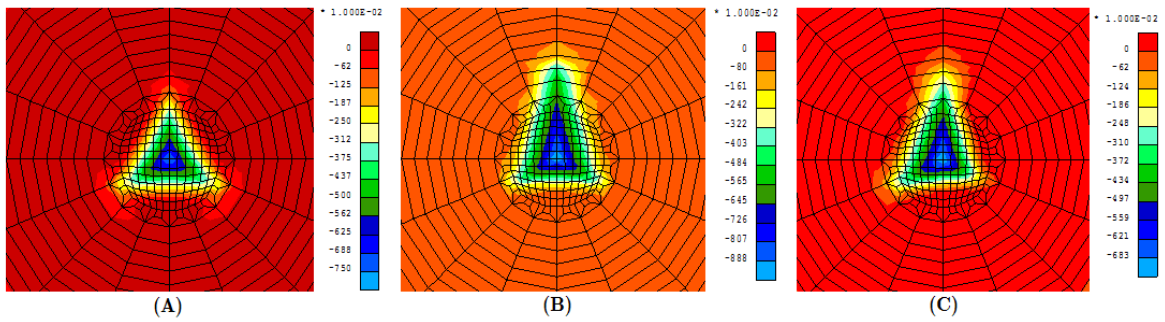


**Figure K.3:** Top view of the material indented after a penetration depth of 103.5 nm, and with (A) tip 1, (B) tip 2 and (C) tip 3 (cf. Appendix (J)). Variation depth in  $10^{-8}$  m.

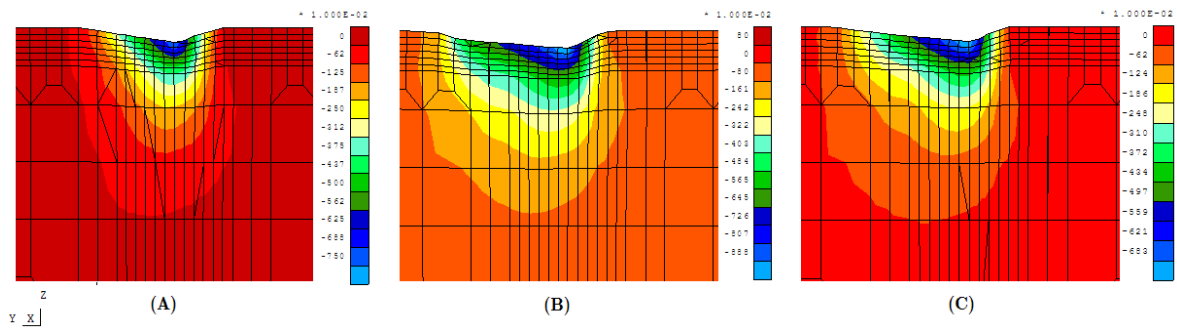


**Figure K.4:** Cross section 1 of Figure (K.2) in the material indented after a penetration depth of 103.5 nm, and with (A) tip 1, (B) tip 2 and (C) tip 3 (cf. Appendix (J)). Variation depth in  $10^{-8}$  m.

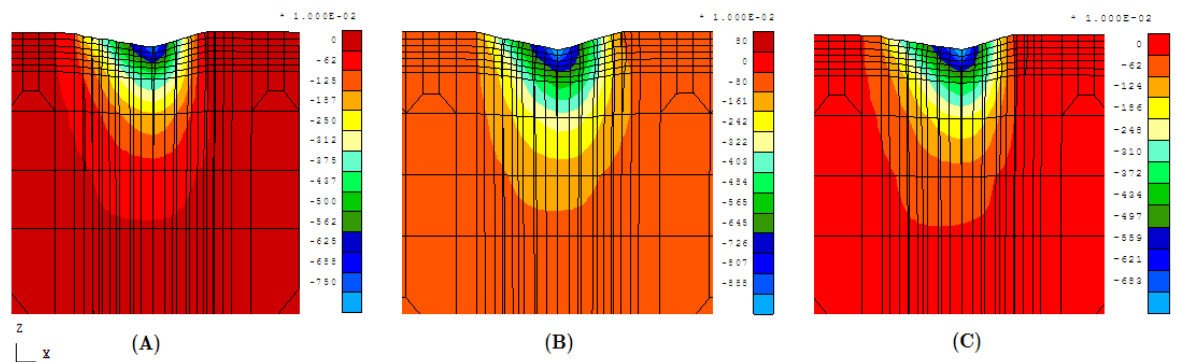


**Figure K.5:** Cross section 2 of Figure (K.2) in the material indented after a penetration depth of 103.5 nm, and with (A) tip 1, (B) tip 2 and (C) tip 3 (cf. Appendix (J)). Variation depth in  $10^{-8}$  m.

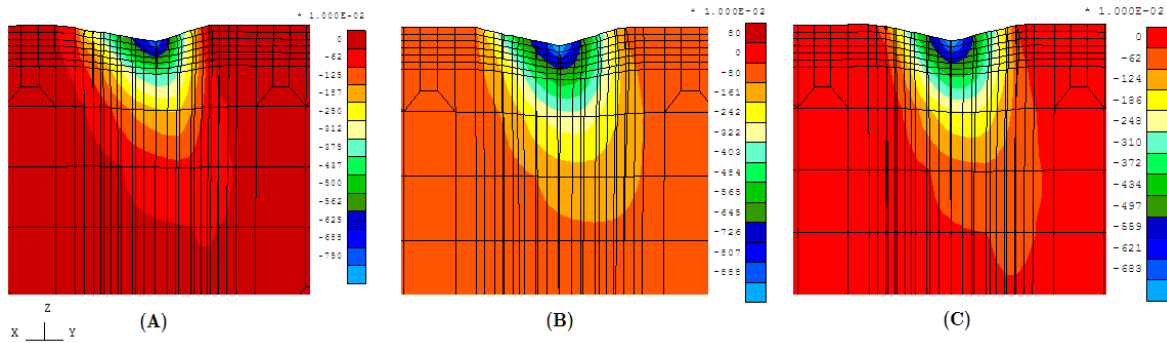


**Figure K.6:** Cross section 3 of Figure (K.2) in the material indented after a penetration depth of 103.5 nm, and with (A) tip 1, (B) tip 2 and (C) tip 3 (cf. Appendix (J)). Variation depth in  $10^{-8}$  m.

conclusion is not due to a poor visualization, another figure was performed in which only the positive contour lines of the vertical displacement (DZ) are drawn (Figure (K.7)). These ensure improved visualization of the appearance of possible pile-up patterns.

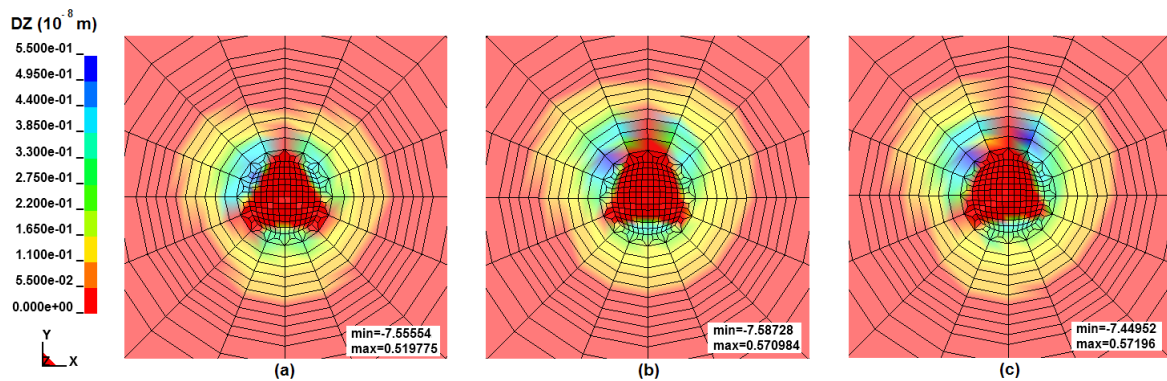


**Figure K.7:** Top view of the material unloaded after a penetration depth of 103.5 nm. The scale is limited to positive vertical displacements. The maximum and minimum values of the vertical displacement are recalled in the bottom of each figure. (A) tip 1, (B) tip 2 and (C) tip 3 (cf. Appendix (J)). Variation depth in  $10^{-8}$  m.

### K.3 Conclusions

With these simulations, the hardening law used and the position of the tips, it is not an easy matter to draw a clear conclusion from these profiles on the possible appearance of pile-up patterns due to the orientation of the indenter. As a result, in this case, the finite elements cannot provide an explanation for the appearance of experimental pile-up patterns.

## Appendix L

# Methods for analyzing mechanical properties using the load versus displacement nanoindentation curves

In this chapter, the method commonly used to determine elastic parameters like Young's modulus  $E$  and the hardness  $H$  of a material from load versus displacement curves is briefly explained. More details can be found in [LB02], [XL08], [SN02], [HPO<sup>+</sup>01] and [FM05].

A typical load versus displacement curve and the deformation pattern of an elastic-plastic sample during and after indentation are shown in Figure (L.1). In this figure,  $h_{max}$  represents the displacement at the peak load,  $P_{max}$ .  $h_c$  and  $h_f$  represent the contact depth (defined as the depth of the indenter that is in contact with the sample under load) and the final displacement, corresponding to complete unloading respectively.  $S$  represents the stiffness ( $S = \frac{dP}{dh}$ ) measured from the unloading nanoindentation curve at  $h_{max}$ , the maximum penetration depth, i.e. the slope of the initial portion of the unloading curve.

Nanoindentation hardness is defined by

$$H = \frac{P_{max}}{A} \quad (\text{L.1})$$

where  $A$  is the projected (real) contact area under the peak indentation load.

The elastic modulus is calculated, based on relationships developed by Sneddon for the indentation of an isotropic elastic half-space [XL08], by any punch that can be described as a solid of revolution of a smooth function

$$E_r = \frac{1}{\beta} \frac{\sqrt{\pi}}{2} \cdot \frac{S}{\sqrt{A}} \quad (\text{L.2})$$

where  $\beta$  is a correction factor (constant) that depends on the geometry of the indenter ( $\beta = 1.034$  for a Berkovich indenter and  $\beta = 1$  for a conical one). The reduced elastic modulus,  $E_r$ , takes the contribution of the substrate (subscript  $s$ ) and the indenter (subscript  $i$ ) moduli  $E_s$  and  $E_i$  into account:

$$\frac{1}{E_r} = \frac{1 - \nu_i^2}{E_i} + \frac{1 - \nu_s^2}{E_s} \quad (\text{L.3})$$

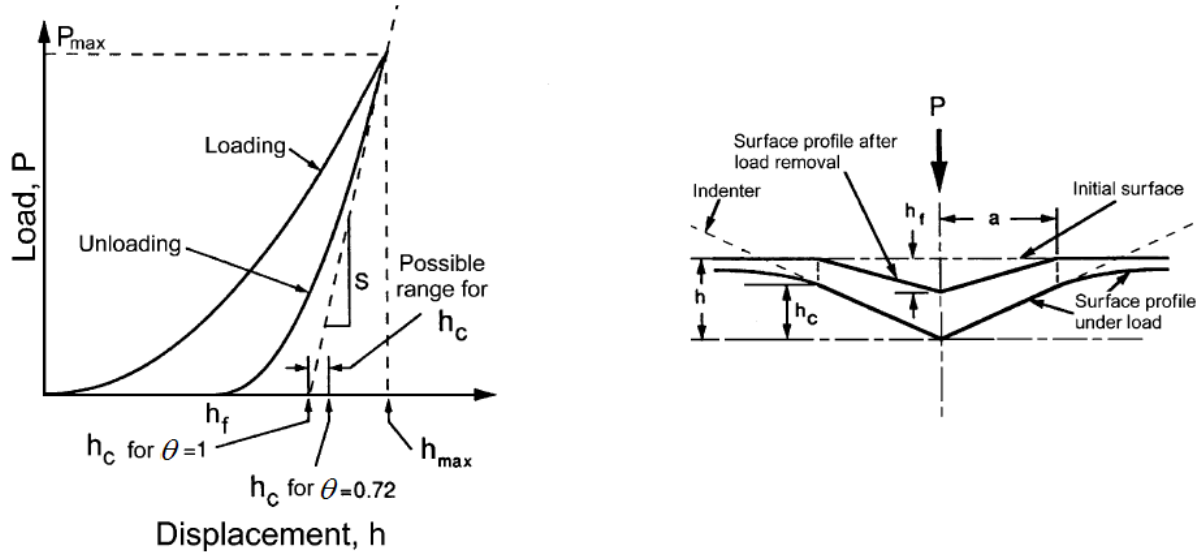


**Figure L.1:** (left) Typical load versus displacement nanoindentation curve. (right) Deformed pattern of an elastic-plastic sample during and after indentation. Figures from [LB02].

where  $\nu_i$  and  $\nu_s$  represent Poisson's ratio of the indenter<sup>1</sup> and of the specimen respectively.

The contact stiffness,  $S$ , and the projected contact area,  $A$ , must be determined to compute the elastic modulus from Eqn.(L.2) and (L.3). As mentioned by [FM05], the most common analytical techniques used to determine the contact area are those proposed by *Doerner and Nix* and by *Oliver and Pharr*:

- *Doerner and Nix* assume the initial unloading part of the curve to be linear. Thus, to estimate the contact area, they use a simple linear extrapolation of the initial linear part of the unloading curve. This is extrapolated to zero load (see Figure (L.1)) and the corresponding depth ( $h_c$ ) is used to determine the correct contact area to determine the elastic modulus and the hardness of a material.
- *Oliver and Pharr* suggest fitting the initial section of the unloading curve by a power law. Their developments estimate the area better and provide a more accurate evaluation of the elastic modulus and hardness.

The power law relationship of *Oliver and Pharr* used to describe the initial unloading curve is

$$P = B(h - h_f)^m \quad (\text{L.4})$$

where  $h_f$  is the final displacement after complete unloading (Figure (L.1)) and  $B$  and  $m$  are fitting parameters. From this equation, the unloading stiffness  $S$  is

$$S = \left( \frac{dP}{dh} \right)_{h=h_{max}} = Bm(h_{max} - h_f)^{m-1} . \quad (\text{L.5})$$

<sup>1</sup>For a diamond indenter,  $E_i = 1141$  GPa and  $\nu_i = 0.07$ .



---

For a perfect Berkovich indenter, the contact area function is given by

$$A(h_c) = 24.56 h_c^2 . \quad (\text{L.6})$$

Thus, to determine  $A(h_c)$  in order to compute Young's modulus, the contact depth must be determined. It can be estimated from the load versus displacement data:

$$h_c = h_{max} - \theta \frac{P_{max}}{S} , \quad (\text{L.7})$$

where  $\theta$  is a constant that depends on the indenter's geometry. For a Berkovich indenter,  $\theta$  is generally assumed to be 0.75.

Once  $h_c$  obtained by Eqn.(L.7), the contact area can be computed using Eqn.(L.6). The hardness  $H$  and the elastic modulus of the substrate can then be obtained using Eqn.(L.1), (L.2) and (L.3).



## Appendix M

# Indentation on FCC materials

### M.1 Introduction

The main objective of this chapter is to visualize the influence of the grain's orientation on numerical nanoindentation phenomena like pile-up patterns, using the microscopic constitutive law and the available meshes. The tests performed are based on the work of [WRKR04]. In this work, the authors study an FCC (face centered cubic) material (copper) and they observe that changing the orientation of the crystal to be indented modifies pile-up patterns. They found that pile-up patterns on the surfaces of (001)-, (011)- and (111)-oriented single crystals have four-, two-, and sixfold symmetry, respectively, in the experiments as well as in the numerical simulations. These results confirm the necessity to simulate the nanoindentation tests in three dimensions if the influence of the grain orientation and pile-up patterns are studied.

In the next section, the material and numerical data are discussed. Then, numerical results obtained for different crystal orientations are presented.

### M.2 Material, parameters and numerical aspects

To perform numerical nanoindentation simulations on FCC material, the single crystal plasticity law is used with the PAN model (Eqn.(4.18)). In FCC crystals, plastic deformation occurs along the  $\{111\}\langle 110\rangle$  family of slip systems, which means 12 potentially active slip systems [PHHL06].

The parameters of the material studied are those chosen by [Ler03] and are given in Table (M.1). The elastic parameters  $C_{11}$ ,  $C_{12}$  and  $C_{44}$  correspond to aluminum material, and plastic parameters used are those recommended by [Hua91].

The meshes used to perform simulations are composed of 1772 and 4544 eight-node brick elements, recalled in Figure (M.1).

The indenter tip is modelled as a rigid conical tool (Figure (M.2)). This tip is used instead of a Berkovich one to avoid symmetries other than those of the crystal structure.

Simulations were conducted on three crystallographic orientations: (001), (011), and (111). Each element of the mesh has the same orientation. Thus, it is assumed that the entire mesh

	Parameter	Value
Elastic parameters	$C_{11}$	107000 MPa
	$C_{12}$	61000 MPa
	$C_{44}$	14000 MPa
Plastic parameters	$h_0$	541.5 MPa
	$\tau_0$	60.8 MPa
	$\tau_s$	109.5 MPa
	$\dot{a}$	$0.001 \text{ s}^{-1}$
	$n$	10

**Table M.1:** Parameters of FCC material used in simulations [Ler03]. These parameters correspond to aluminum material.

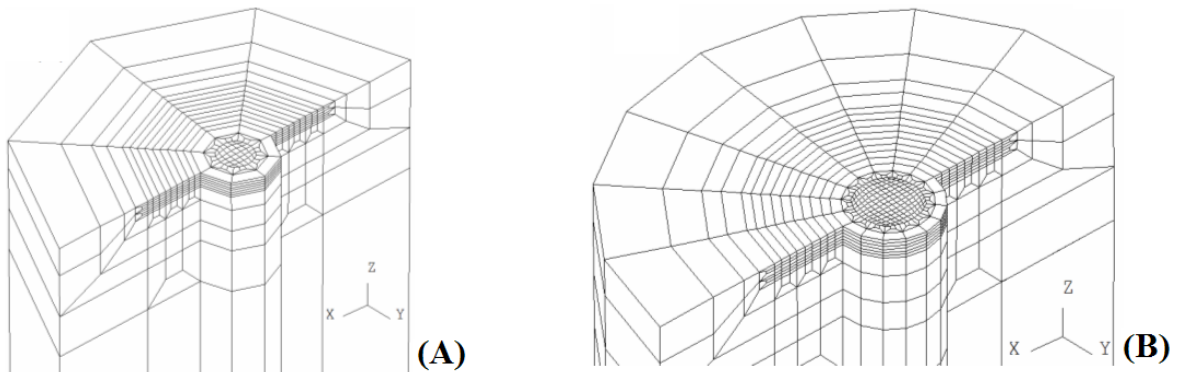


**Figure M.1:** Part of the meshes used for nanoindentation simulations: (A) mesh with 1772 elements and (B) mesh with 4544 elements.

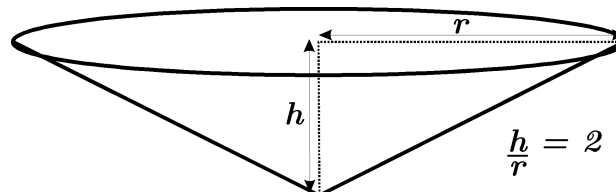


**Figure M.2:** Rigid conical indenter used for numerical simulations on FCC.

corresponds to one crystal.

### M.3 Numerical results

For these three different surface orientations, the finite element calculations show different surface profiles around the indents simulated. Figure (M.3) gives the three  $DZ$  profiles at the indented surface after an indentation of 162 nm. They were obtained with the finer mesh containing 4544 elements. Only the indented part of the mesh is shown. Figure (M.4) gives the corresponding equivalent Von Mises' stress. Results obtained with the 1772-element mesh are not shown here. With this mesh, the number of elements in the indented zone is too small to distinguish the difference in pile-up patterns correctly for small indentations.

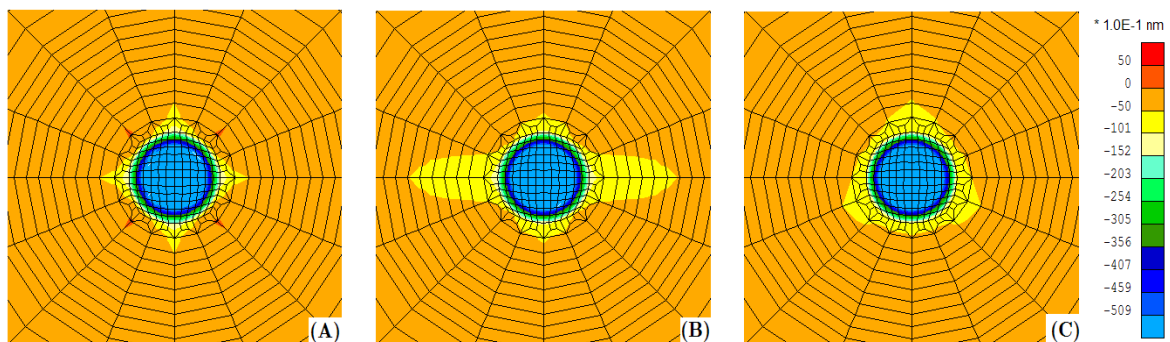


**Figure M.3:** Variation depth profile after an indentation of 162 nm of the indented surface of the material for 3 orientations of the crystal. In the global axes, the directions (100) and (001) become, (a) (100) and (001), (b) (100) and (011) and (c) (10-1) and (111), with indentation along the (001) direction in the global axes. Simulations performed with the 4662-element mesh.

In these three figures (M.3), looking at the center, the indenter seems to be spherical and imperfectly conical. This impression is simply due to the scale chosen to visualize the difference between the imprints.

Results obtained are qualitatively similar to those obtained by [WRKR04] on copper. From these figures, it is clear that the orientation of the indented crystal's surface influences the pile-up patterns around the indent.

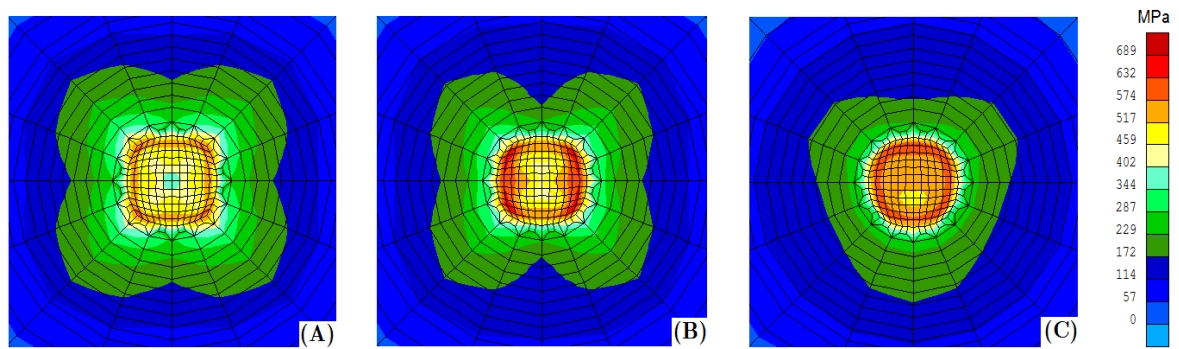


**Figure M.4:** Equivalent Von Mises' stress profile after an indentation of 162 nm of the indented surface of the material for 3 orientations of the crystal. In the global axes, the directions (100) and (001) become, (a) (100) and (001), (b) (100) and (011) and (c) (10-1) and (111), with indentation along the (001) direction in the global axes.

## Appendix N

# Identification of the $\alpha$ phase: shear strain on each slip system in several simulations

### N.1 Introduction

To contribute to the identification of the  $\alpha$  phase, several numerical simulations were performed using arbitrary sets of slip systems that can be activated. These numerical simulations were performed in different grain orientations.

In this chapter, the shear strain of each slip system that can be activated in several numerical simulations is provided during the indentation test. The results are given for three grain orientations, corresponding to grains 12, 43 and 58 from Figure (10.1). First, the basal, prismatic and pyramidal  $\langle a \rangle$  slip systems were chosen to be activated. Secondly, the slip systems that can be activated were the basal, the prismatic and the pyramidal  $\langle c+a \rangle$  ones. Finally, the basal, the pyramidal  $\langle a \rangle$  and the pyramidal  $\langle c+a \rangle$  slip systems were tested.

### N.2 Basal - prismatic - pyramidal $\langle a \rangle$ slip systems

First, three simulations were performed. Their setup was exactly the same except for the orientation of the indented grain. All slip systems that can be activated (here, the basal (3), prismatic (3) and pyramidal  $\langle a \rangle$  (6) ones) were given the same parameters ( $\tau_0$ ,  $\tau_s$ , ...).

During the loading of these nanoindentation simulations, the shear strain on each slip system was recorded. Results are shown in Figures (N.1), (N.2) and (N.3) for indentations 12, 43 and 58 respectively.

Observing these figures leads to several findings:

- The pyramidal  $\langle a \rangle$  slip systems are highly activated in the three grains. In indentations 43 and 58, this is clearly the most activated set of slip systems.
- The basal slip systems are also highly activated in the 12th indentation.
- Prismatic slip systems are slightly activated in indentation 43 and more so in indentation 58.

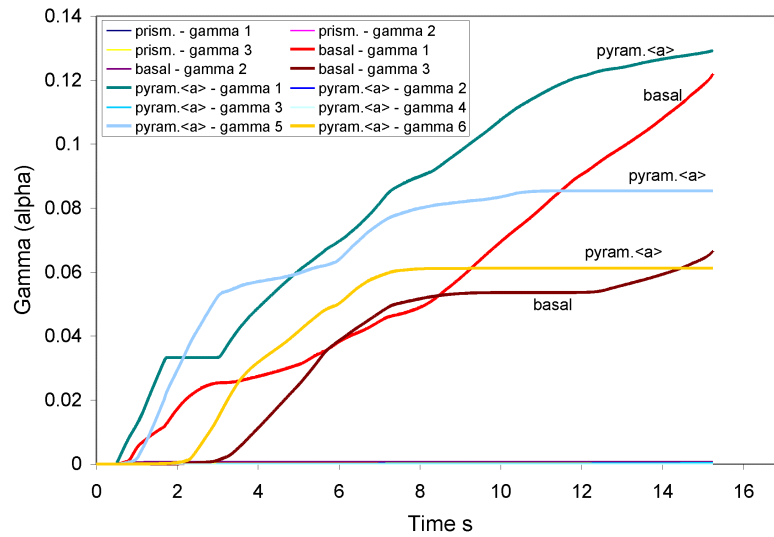


**Figure N.1:** Indentation 12. Shear strain on each slip system that can be activated during the loading phase of a nanoindentation test. The slip systems that can be activated are the 3 basal systems, the 3 prismatic systems and the 6 pyramidal  $\langle a \rangle$  systems.

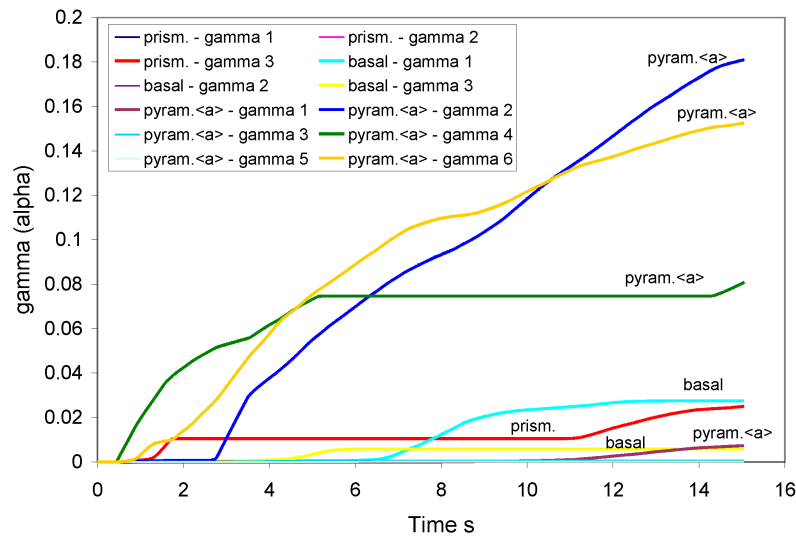


**Figure N.2:** Indentation 43. Shear strain on each slip system that can be activated during the loading phase of a nanoindentation test. The slip systems that can be activated are the 3 basal systems, the 3 prismatic systems and the 6 pyramidal  $\langle a \rangle$  systems.



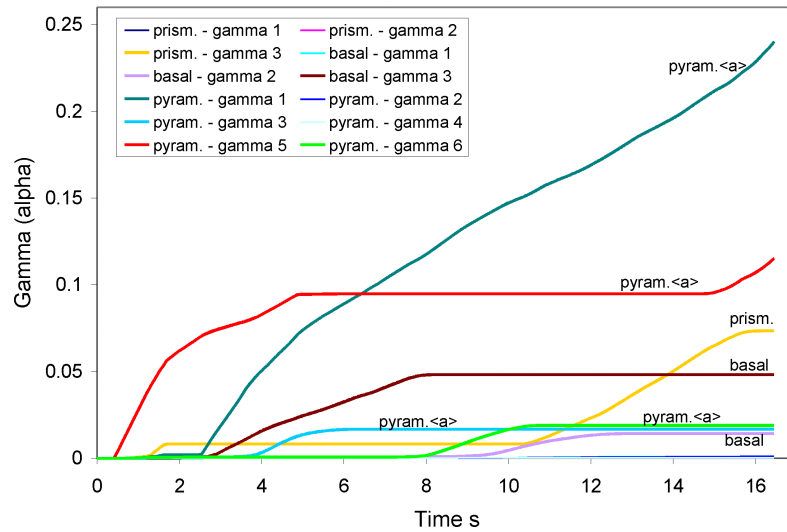


**Figure N.3:** Indentation 58. Shear strain on each slip system that can be activated during the loading phase of a nanoindentation test. The slip systems that can be activated are the 3 basal systems, the 3 prismatic systems and the 6 pyramidal  $\langle a \rangle$  systems.

### N.3 Basal - prismatic - pyramidal $\langle c+a \rangle$ slip systems

The same numerical simulations were performed with the basal (3), prismatic (3) and pyramidal  $\langle c+a \rangle$  (12) sets of slip systems.

Here as well, during the loading phase of these nanoindentation simulations, the shear strain on each slip system was recorded. Results are shown in Figures (N.4), (N.5) and (N.6) for indentations 12, 43 and 58 respectively.

Observation of these figures leads to some findings:

- In indentation 12, pyramidal  $\langle c+a \rangle$  slip systems are the most activated and then, to a lesser degree, the basal ones.
- For indentations 43 and 58, the basal slip systems are the most activated. The pyramidal  $\langle c+a \rangle$  ones are also activated but less so.

### N.4 Basal - pyramidal $\langle a \rangle$ - pyramidal $\langle c+a \rangle$ slip systems

The same simulations were performed with, for the slip systems that can be activated, the basal (3), pyramidal  $\langle a \rangle$  (6) and pyramidal  $\langle c+a \rangle$  (12) systems.

During the loading phase of these nanoindentation simulations, the shear strain on each slip system was recorded. Results are shown in Figures (N.7), (N.8) and (N.9) for indentations 12, 43 and 58 respectively.

Observation of these figures leads to some findings:

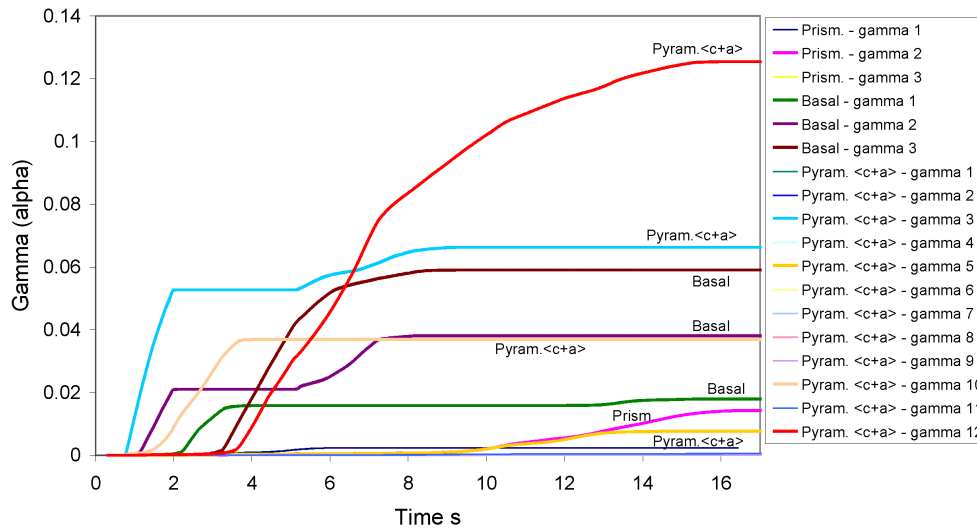


**Figure N.4:** Indentation 12. Shear strain on each slip system that can be activated during the loading phase of a nanoindentation test. The slip systems that can be activated are the 3 basal systems, the 3 prismatic systems and the 12 pyramidal  $\langle c+a \rangle$  systems.

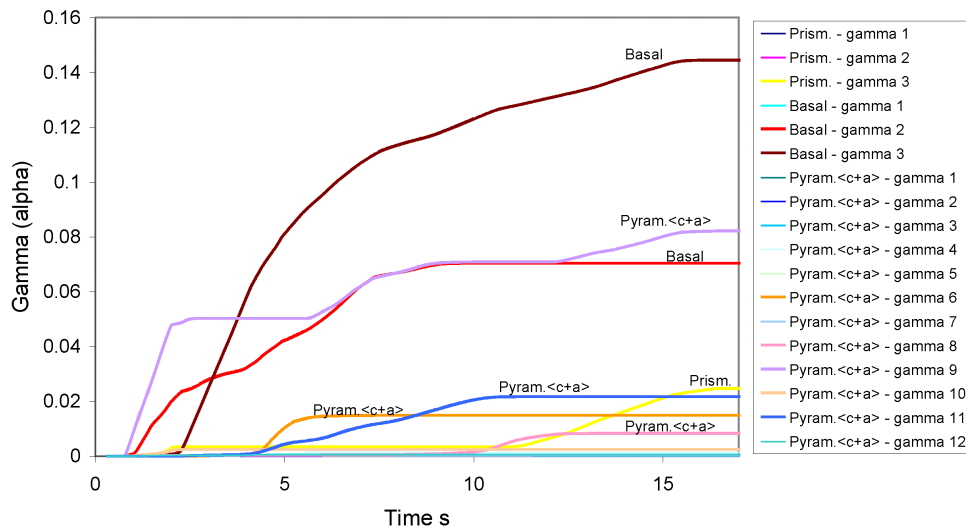


**Figure N.5:** Indentation 43. Shear strain on each slip system that can be activated during the loading phase of a nanoindentation test. The slip systems that can be activated are the 3 basal systems, the 3 prismatic systems and the 12 pyramidal  $\langle c+a \rangle$  systems.

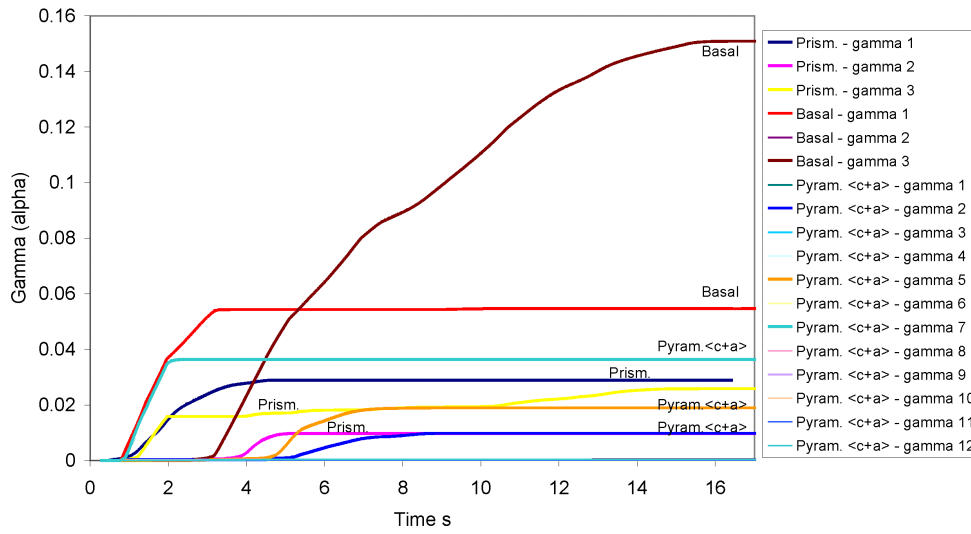


**Figure N.6:** Indentation 58. Shear strain on each slip system that can be activated during the loading phase of a nanoindentation test. The slip systems that can be activated are the 3 basal systems, the 3 prismatic systems and the 12 pyramidal <c+a> systems.

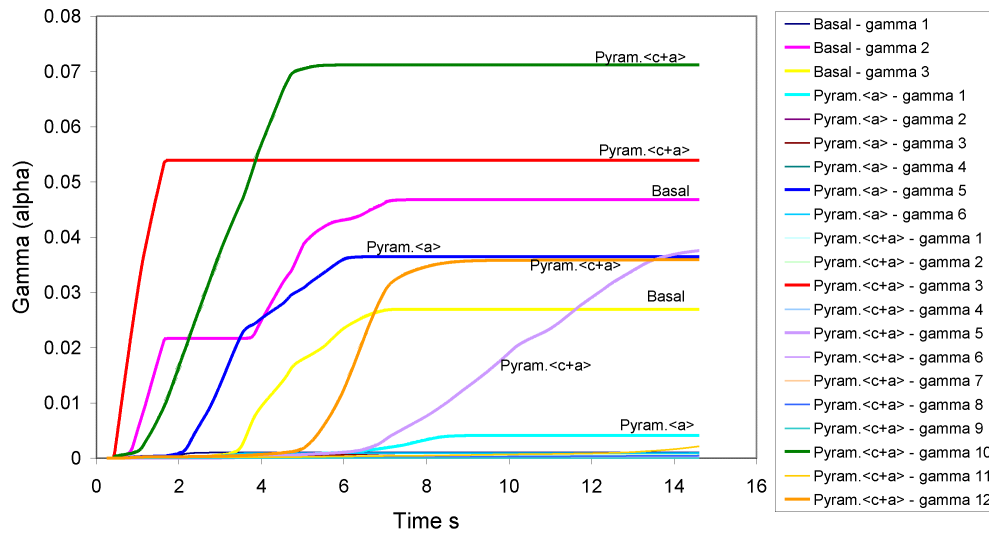


**Figure N.7:** Indentation 12. Shear strain on each slip system that can be activated during the loading phase of a nanoindentation test. The slip systems that can be activated are the 3 basal systems, the 6 pyramidal <a> systems and the 12 pyramidal <c+a> systems.

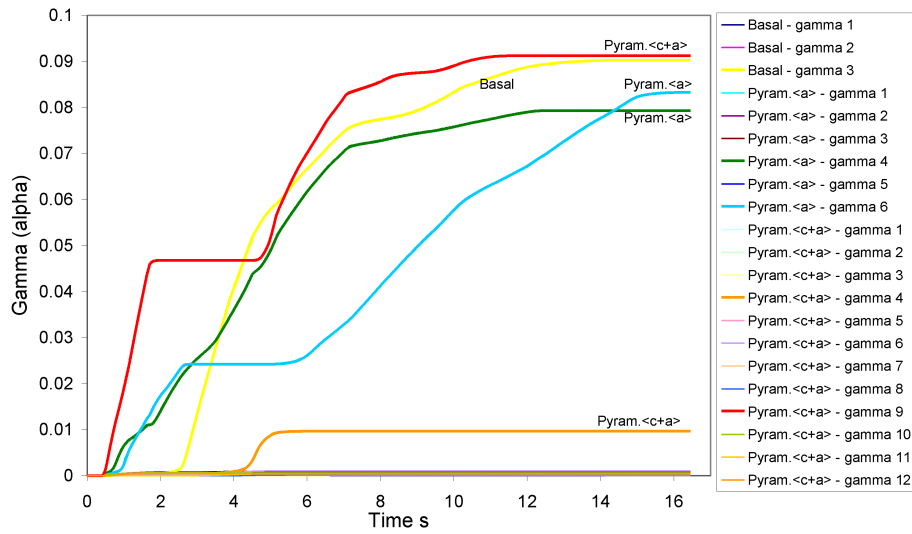


**Figure N.8:** Indentation 43. Shear strain on each slip system that can be activated during the loading phase of a nanoindentation test. The slip systems that can be activated are the 3 basal systems, the 6 pyramidal  $\langle a \rangle$  systems and the 12 pyramidal  $\langle c+a \rangle$  systems.

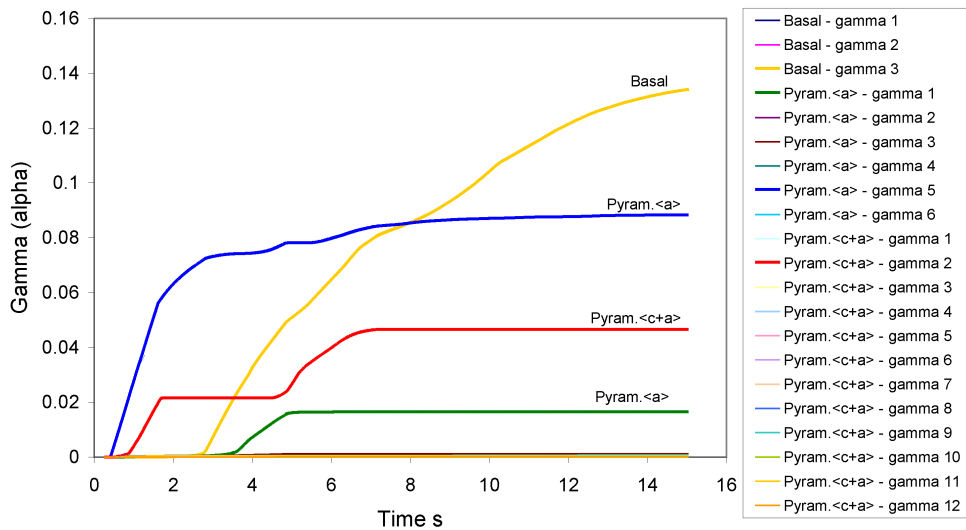


**Figure N.9:** Indentation 58. Shear strain on each slip system that can be activated during the loading phase of a nanoindentation test. The slip systems that can be activated are the 3 basal systems, the 6 pyramidal  $\langle a \rangle$  systems and the 12 pyramidal  $\langle c+a \rangle$  systems.

- 
- In indentation 12, the pyramidal  $\langle c+a \rangle$  slip systems are the most activated ones. Then follows the basal ones and, somewhat lower, the pyramidal  $\langle a \rangle$  ones.
  - For indentation 43, the three slip systems are similarly activated but with one more slip for the pyramidal  $\langle a \rangle$  ones at high values of  $\gamma^{(\alpha)}$ .
  - For indentation 58, the basal slip system is the greatest, followed by the pyramidal  $\langle a \rangle$  and, finally, the pyramidal  $\langle c+a \rangle$ .



## Appendix O

# Identification of the plastic parameters of the $\alpha$ phase using the basal, pyramidal $\langle a \rangle$ and pyramidal $\langle c+a \rangle$ slip systems

In this appendix, results obtained with different values of initial CRSS (Table (O.1)) and for different grain orientations are presented.

	$\tau_{0_{basal}}$	$\tau_{0_{pyram.\langle a \rangle}}$	$\tau_{0_{pyram.\langle c+a \rangle}}$
Param. 1	50	200	300
Param. 2	100	200	300
Param. 3	100	200	400

**Table O.1:** CRSS of the different sets of slip systems to identify the  $\alpha$  phase of Ti-5553.

Results are shown in Figures (O.1) and (O.2). Very slight differences appear between the different grain orientations, for identical sets of parameters.

All the simulations performed with the sets of parameters in Table (O.1) are superimposed on the right part of Figure (O.2). From this figure, it is clear that, even though there is very little distinction between the different grain orientations, using the same sets of parameters, there is also no significant difference when the sets of parameters change.

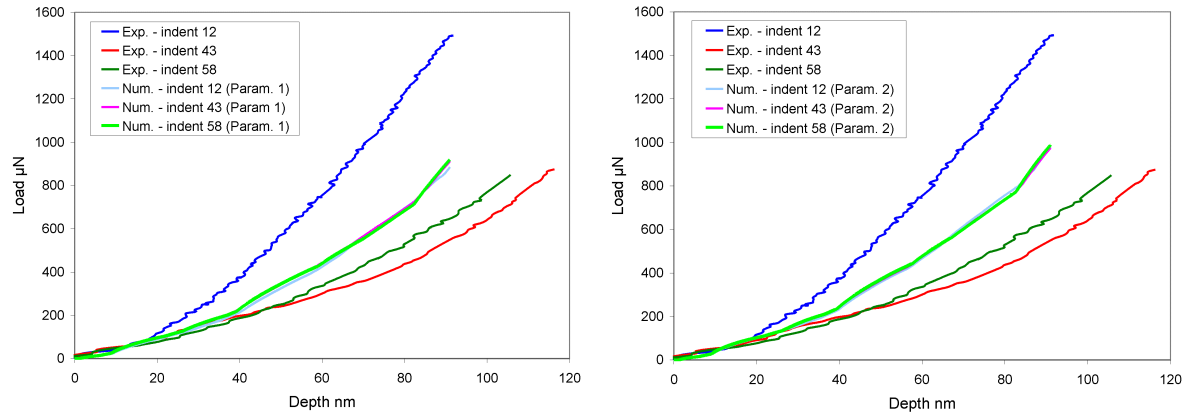


**Figure O.1:** Simulations of nanoindentations (loading phase only) 12, 43 and 58 and comparison with experiments. The CRSS of slip systems (basal, pyramidal  $\langle a \rangle$  and pyramidal  $\langle c+a \rangle$ ) are given in Table (O.1).

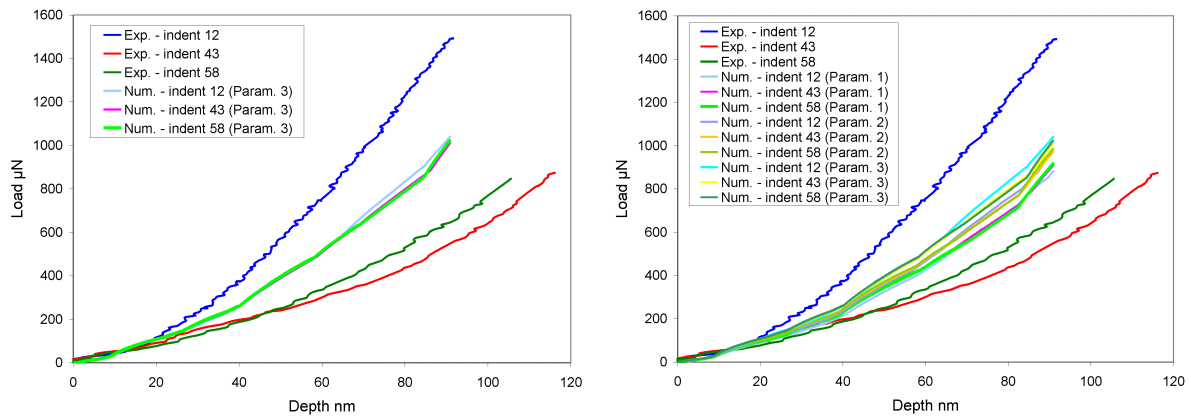


**Figure O.2:** Simulations of nanoindentations (loading phase only) 12, 43 and 58 and comparison with experiments. The CRSS of slip systems (basal, prismatic, pyramidal  $\langle a \rangle$  and pyramidal  $\langle c+a \rangle$ ) are given in Table (O.1). All the simulations performed with these sets of parameters and the initial CRSS in Table (O.1) are superimposed on the figure on the right.



## Appendix P

# Slip systems and CRSS tested to identify the material behavior of the $\alpha$ phase

Different sets of parameters were tested in order to identify the material behavior of the  $\alpha$  phase from nanoindentation tests accurately. For a great number of numerical simulations, the isotropic elastic parameters ( $E = 125000$  MPa and  $\nu = 0.33$ ) and the plastic parameters are those from Table (10.2), except for  $\tau_0$  and  $\tau_s$  of the chosen slip systems.

	Prismatic		Basal		Pyramidal <a>		Pyramidal <c+a>	
	$\tau_0$	$\tau_s$	$\tau_0$	$\tau_s$	$\tau_0$	$\tau_s$	$\tau_0$	$\tau_s$
1	200	204	200	204	50	51	/	/
2	250	255	250	255	45	45.9	/	/
3	200	204	200	204	200	204	/	/
4	200	204	200	204	/	/	200	204
5	/	/	200	204	200	204	200	204
6	50	51	200	204	100	102	/	/
7	45	45.9	300	306	50	51	/	/
8	45	45.9	300	306	150	153	/	/
9	/	/	50	51	200	204	300	306
10	/	/	100	102	200	204	300	306
11	/	/	100	102	200	204	400	408
12	300	306	50	50.5	70	70.7	/	/
13	20	20.4	400	400.8	100	100.2	/	/
14	10	10.2	500	500.8	120	122.4	/	/
15	10	10.2	1000	1016	120	122.4	/	/
16	10	10.1	500	526.3	120	122.4	/	/
17	10	10.1	500	625	120	122.4	/	/
18	50	50.5	200	202	100	101	/	/

**Table P.1:** Sets of slip systems and corresponding  $\tau_0$  and  $\tau_s$  values tested to identify the  $\alpha$  phase.

Additional numerical simulations were performed, changing other parameters. For example,

- parameter set 16 with  $h_0=10000$ ,
- parameter set 15 with an anisotropic  $C$  matrix,
- parameter set 17 with an anisotropic  $C_2$  matrix,
- parameter set 18 with an anisotropic  $C_1$  matrix,
- parameter set 18 with an anisotropic  $C_2$  matrix,

were tested with the components of the  $C$ ,  $C_1$  and  $C_2$  matrices given in Table (P.2).

	$C_{11}$	$C_{12}$	$C_{13}$	$C_{33}$	$C_{44}$
$C$	275000	99524	124405	265833	49107
$C_1$	210000	76000	95000	203000	37500
$C_2$	214200	77520	96900	207060	38250

**Table P.2:** Anisotropic elastic matrix components tested (MPa).

The most interesting results were presented in Part (IV). The other results were not conclusive for all grains' orientations and thus are not presented here.

# List of Figures

1.1	Examples of titanium applications: Fukuoka Dome <sup>1</sup> , watches <sup>2</sup> , golf club heads <sup>3</sup> , and bicycle frames <sup>4</sup> . . . . .	4
1.2	Flanges linking the synchronizing rings together. . . . .	5
1.3	Stress versus strain curves for Ti-6Al-4V and for Ti-5553 alloys. . . . .	6
2.1	Crystallography of pure titanium at different temperatures. Figure from [Pri00].	8
2.2	Unit cells of $\alpha$ and $\beta$ phases of titanium [Len07]. . . . .	9
2.3	Phases of Ti-LCB as a function of the ageing temperature after quenching (at room temperature) [Dep04]. . . . .	11
2.4	Ti-5553 compared to other usual titanium alloys. Classification based on their $[\text{Mo}]_{\text{eq}}$ and $[\text{Al}]_{\text{eq}}$ contents. . . . .	12
2.5	Orowan mechanism: the dislocations cannot go through the precipitate (because the deformation propagated by the dislocation is not compatible with the crystal structure of the precipitate). The dislocation bypasses the precipitate and leaves a dislocation loop around the precipitate [Oro]. . . . .	14
2.6	Shearing of the precipitate: the deformation propagated by the dislocation is compatible with the crystalline structure of the precipitate. Thus, the dislocation deforms the precipitate [Oro]. . . . .	14
4.1	Microscopic constitutive law subroutine. General principle of implementation in the <i>Lagamine</i> FE code. . . . .	24
4.2	Multiplicative decomposition of the total strain gradient tensor, $\mathbf{F} = \mathbf{F}^*\mathbf{F}^p$ . The rotation and stretching of the lattice are taken into account through the elastic deformation gradient $\mathbf{F}^*$ . Figure inspired from [BMO00]. . . . .	25
4.3	Schematic diagram for Bassani and Wu's form of hardening. Figure from [Bal95].	29
4.4	Integration scheme of the plastic law. . . . .	30
4.5	Axes in the hexagonal system ( $\mathbf{a}_{\text{hex}}$ ) and in the corresponding orthogonal one ( $\mathbf{a}_i$ ). . . . .	33
6.1	Homogenization principle. Heterogeneous and equivalent homogeneous environments. Definitions of the RVE and the microscopic and macroscopic scales. Figure inspired from [BB06]. . . . .	39
6.2	Illustration of the deformation of a cube-shaped microstructure $V$ for the constraints on the boundary $\partial V$ : (a) homogeneous displacement fluctuations $\mathbf{u}_{\text{per}} = 0$ and (b) periodic fluctuations $\mathbf{u}_{\text{per}+} = \mathbf{u}_{\text{per}-}$ , figure adapted from [MSL02]. . . . .	41

6.3	Hexagonal array. Different possible choices for the unit cell, adapted from [MMS99]. . . . .	43
6.4	Periodicity conditions: notations. . . . .	44
6.5	FE mesh of eight elements composed of eight nodes. . . . .	45
6.6	Resolution algorithm. . . . .	48
7.1	Experimental tensile tests performed on 100% $\beta$ Ti-5553 at different strain rates: $10^{-2}$ , $10^{-3}$ , $10^{-4}$ and $10^{-5}$ $s^{-1}$ (UCL, July 2006). . . . .	60
7.2	Example of true stress versus true strain for a tensile test using Norton-Hoff. Elastic, plastic and total models. . . . .	62
7.3	Comparison of the true stress versus true strain experimental tensile tests for different strain rates and the corresponding curves computed from Norton-Hoff and the parameters of Table (7.1). . . . .	63
7.4	Comparison of true stress versus true strain curves obtained from experimental tensile tests for different strain rates ( $10^{-5}$ and $10^{-4}$ $s^{-1}$ ) with the corresponding curves obtained with Norton-Hoff and the parameters from Table (7.2). . . . .	65
7.5	Comparison of true stress versus true strain curves obtained from experimental tensile tests for different strain rates ( $10^{-2}$ and $10^{-3}$ $s^{-1}$ ) with the corresponding curves obtained with Norton-Hoff and the parameters from Table (7.2). . . . .	65
7.6	Influence of parameters $\dot{a}$ (left) and $n$ (right). The other parameters used here are $h_0 = 15000$ ; $\tau_0 = 300$ and $\tau_s = 545$ . $\dot{a}$ is taken to 0.001 when $n$ changes and $n$ is equal to 50 when $\dot{a}$ varies. For both figures, the strain rate is approximately $10^{-4}$ $s^{-1}$ . . . . .	67
7.7	Experimental and numerical tensile tests for different strain rates on 100 % $\beta$ Ti-5553. The parameters used are those given in Table (7.3) and in Table (7.4). . . . .	69
7.8	Optimized parameters for tensile tests performed at $10^{-5}$ $s^{-1}$ . Experimental (10-5) and numerical (10-5-opt) tensile tests for a strain rate of $10^{-5}$ $s^{-1}$ on 100% $\beta$ material. . . . .	69
7.9	Experimental (10-4) and numerical (10-4-opt) tensile tests for a strain rate of $10^{-4}$ $s^{-1}$ on 100% $\beta$ material. For the numerical test, the parameters are those given in the table in Figure (7.8), except for $\tau_s$ : $\tau_s = 323.44$ MPa. . . . .	70
7.10	Optimized parameters for tensile tests performed at $10^{-3}$ $s^{-1}$ . Experimental (10-3) and numerical (10-3-opt) tensile tests for a strain rate of $10^{-3}$ $s^{-1}$ on 100% $\beta$ material. . . . .	70
7.11	Optimized parameters for tensile tests performed at $10^{-2}$ $s^{-1}$ . Experimental (10-2) and numerical (10-2-opt) tensile tests for a strain rate of $10^{-2}$ $s^{-1}$ on 100% $\beta$ material. . . . .	71
7.12	Experimental and numerical tensile tests with the crystalline plasticity constitutive law and Bassani and Wu's hardening for a strain rate of $10^{-2}$ $s^{-1}$ on 100% $\beta$ Ti-5553 and for different values of the parameter $\tau_0$ . . . . .	73
7.13	Experimental and numerical tensile tests with the crystalline plasticity constitutive law and Bassani and Wu's hardening for a strain rate of $10^{-2}$ $s^{-1}$ on 100% $\beta$ Ti-5553 and for different values of the parameter $\tau_0$ . Zoom on the yield point. . . . .	73
7.14	Experimental and numerical tensile tests with the crystalline plasticity constitutive law and Bassani and Wu's hardening for a strain rate of $10^{-2}$ $s^{-1}$ on 100% $\beta$ Ti-5553 and for different values of the parameter $\tau_s$ . . . . .	74

7.15	Experimental and numerical tensile tests with the crystalline plasticity constitutive law and Bassani and Wu's hardening for a strain rate of $10^{-2} \text{ s}^{-1}$ on 100% $\beta$ Ti-5553 and for different values of the parameter $h_0$ . . . . .	74
7.16	Experimental and numerical tensile tests with the crystalline plasticity constitutive law and Bassani and Wu's hardening for a strain rate of $10^{-2} \text{ s}^{-1}$ on 100% $\beta$ Ti-5553 and for different values of the parameter $h_s$ . . . . .	75
7.17	Experimental and numerical tensile tests with the crystalline plasticity constitutive law and Bassani and Wu's hardening for a strain rate of $10^{-2} \text{ s}^{-1}$ on 100% $\beta$ Ti-5553 and for different values of the parameter $\gamma_{0\alpha}$ . . . . .	75
7.18	Experimental and numerical tensile tests with the crystalline plasticity constitutive law and Bassani and Wu's hardening for a strain rate of $10^{-2} \text{ s}^{-1}$ on 100% $\beta$ Ti-5553 and for different values of the parameter $\gamma_{0\alpha\beta}$ . . . . .	76
7.19	Experimental and numerical tensile tests with the crystalline plasticity constitutive law and Bassani and Wu's hardening for a strain rate of $10^{-2} \text{ s}^{-1}$ on 100% $\beta$ Ti-5553 and for different values of the parameter $f_{\alpha\alpha}$ . . . . .	76
7.20	Experimental and numerical tensile tests with the crystalline plasticity constitutive law and Bassani and Wu's hardening for a strain rate of $10^{-2} \text{ s}^{-1}$ on 100% $\beta$ Ti-5553 and for different values of the parameter $f_{\alpha\beta}$ . . . . .	77
7.21	Experimental and numerical tensile tests with the crystalline plasticity constitutive law and Bassani and Wu's hardening for a strain rate of $10^{-2} \text{ s}^{-1}$ on 100% $\beta$ Ti-5553 and for optimized parameters. . . . .	77
7.22	Experimental and numerical tensile stress versus strain curves with the crystalline plasticity constitutive law and Bassani and Wu's hardening for all strain rates on 100% $\beta$ Ti-5553 and with the optimized parameters in Table (7.6). Except for $h_s$ , all other parameters have the same value for each strain rate. . . . .	79
7.23	Evolution of the parameter $h_s$ optimized for numerical tensile tests as a function of the strain rate of the test (logarithmic scale). . . . .	79
7.24	Identification of the parameters $A$ and $B$ from Eqn.(7.9) to simulate $h_s$ 's evolution. (Left) logarithmic scale and (right) linear scale for the strain rate evolution. Blue dots correspond to $h_s$ parameters determined for curves separately identified and the discontinuous black line corresponds to a fit of these linked blue dots by a logarithmic progression. . . . .	80
7.25	Tensile tests using the crystalline constitutive law with Bassani and Wu's hardening and $h_s$ evolution. (left) Strain rate evolution during the test and (right) the corresponding $h_s$ evolution. . . . .	81
7.26	Tensile tests (at different strain rates) using the crystalline constitutive law with Bassani and Wu's hardening and $h_s$ evolution. The experimental corresponding ones are superimposed. The parameters used are given in Table (7.7). . . . .	82
8.1	Bi-axial test machine used to perform simple shear tests. . . . .	84
8.2	Sample submitted to shear. The shearing zone is in red. For these tests, $h = 3 \text{ mm}$ , $e = 1.5 \text{ mm}$ and $l = 30 \text{ mm}$ . The shear strain $\gamma = \frac{d}{h} = \tan(\theta)$ . . . . .	84
8.3	Shear strain in the material at the end of the shear test. Image from Aramis measurement. . . . .	85
8.4	View of the shearing part of a specimen of $(\alpha + \beta)$ Ti-5553, at the end of the shear test. On the right, optical image of the shear strain is superimposed on the experimental sheared specimen. . . . .	86

8.5	View of the shearing part of a specimen of 100% $\beta$ Ti-5553, at the end of the shear test. On the right, optical image of the shear strain is superimposed on the experimental sheared specimen. . . . .	86
8.6	Shear strain in the material (100% $\beta$ ) at the end of the shear test (shear in one direction and then in the opposite direction). Image from Aramis measurement. The location of the saved results are shown in the figure. . . . .	87
8.7	Shear stress during a shear test performed in one direction and then in the opposite one. On the right, the absolute value of the shear stress (of the same test as the left figure) is drawn as a function of the cumulated gamma, the strain in the shearing direction. The number of the curves correspond to results saved at different parts of the sample (shown in Figure (8.6)). . . . .	87
8.8	Numerical simulation of shear test with Norton (1st set of parameters) - 90 FE - Distribution of $\sigma_{12}$ (MPa) in each element after a displacement of 2.6 mm. . . . .	89
8.9	Numerical simulation of shear test with Norton (1st set of parameters) - 90 FE - Smoothed distribution of $\sigma_{12}$ (MPa) in each element after a displacement of 2.6 mm. . . . .	89
8.10	Numerical simulation of shear test with Norton (1st set of parameters) - 707 FE - Distribution of $\sigma_{12}$ (MPa) in each element after a displacement of 2.1 mm. . . . .	89
8.11	Tensile tests on Ti-5553 100% $\beta$ - strain rate = $10^{-4}$ and $10^{-5} s^{-1}$ . . . . .	90
8.12	Numerical simulation of shear test with Norton (second set of parameters) - 90 FE - Distribution of $\sigma_{12}$ (MPa) in each element after a displacement of 2.6 mm. . . . .	91
8.13	Numerical simulation of shear test with Norton (second set of parameters) - 90 FE - Distribution of $\sigma_{12}$ (MPa) in each element after a displacement of 2.6 mm. . . . .	91
8.14	Numerical simulation of shear test with Norton (second set of parameters) - 707 FE - Distribution of $\sigma_{12}$ (MPa) in each element after a displacement of 2.6 mm. . . . .	92
8.15	View of the shearing part of a Ti-5553 specimen, at the end of the shear test. On the right, optical image of the shear strain in a ( $\alpha + \beta$ ) material is superimposed on the experimental specimen. . . . .	92
8.16	90 FE mesh. "Definition" of the shape of the grains. . . . .	93
8.17	Numerical simulation of shear test with the microscopic constitutive law - 90 FE - Smoothed distribution of $\sigma_{12}$ (MPa) in each element. . . . .	94
8.18	Numerical simulation of shear test with the microscopic constitutive law - 90 FE - Distribution of $\varepsilon_{12}$ in each element. . . . .	94
8.19	707 FE mesh. "Definition" of the shape of the grains. . . . .	94
8.20	Numerical simulation of shear test with the microscopic constitutive law (second set of parameters) - 707 FE - Distribution of $\sigma_{12}$ (MPa). . . . .	95
8.21	Experimental shear tests on the $\beta$ material. Shear stress versus strain curves. . . . .	96
8.22	Experimental shear tests on the ( $\alpha + \beta$ ) material. Shear stress versus shear strain curves. . . . .	97
8.23	Experimental shear tests on $\beta$ and ( $\alpha + \beta$ ) materials. Shear stress versus shear strain. . . . .	97
8.24	Experimental shear tests on $\beta$ and ( $\alpha + \beta$ ) materials. Load versus displacement curves. . . . .	98
8.25	Experimental tensile tests on the tempered (100% $\beta$ ) and the as-received ( $\alpha + \beta$ ) materials at different strain rates ranging from $\dot{\varepsilon} = 10^{-5} s^{-1}$ until $10^{-2} s^{-1}$ . True stress versus true strain curves. Each test was performed twice. . . . .	99

9.1	Schematic drawing of a conical indentation. $\tau$ and $p$ represent the tangential and normal stresses, respectively, at each contact point. . . . .	103
9.2	Nanoindentation principle. . . . .	104
9.3	Experimental load versus displacement nanoindentation curve. Example of a test performed in a $\beta$ grain. . . . .	105
9.4	Three-sided Berkovich indenter tip. Included angle. . . . .	105
9.5	Berkovich indenter. The right figure comes from [Gia06]. . . . .	106
9.6	Sample of indented 100% $\beta$ Ti-5553. The numbers of the grains are indicated and the corresponding orientations are given in Table (9.1). . . . .	106
9.7	Stress versus strain curve. Illustration of the parameters of the EP constitutive law. . . . .	108
9.8	Parts of meshes used for nanoindentation simulations: (A) 1044 elements, (B) 1772 elements. . . . .	108
9.9	Part of the third mesh used for nanoindentation simulations: 4544 elements. . .	109
9.10	Second mesh, composed of 1772 elements. . . . .	110
9.11	Second mesh with graduations in $10^{-8}$ m. (Left) Top view and (right) cross section in the plane $x = 0$ . The Berkovich indenter tip is also shown, in the middle. . . . .	110
9.12	Nanoindentation in a $\beta$ grain of Ti-5553. Comparison between experimental results and numerical ones obtained with the EP constitutive law for which parameters were optimized from tensile tests on 100 % $\beta$ material. . . . .	111
9.13	Numerical nanoindentation simulations with three different meshes. . . . .	112
9.14	Nanoindentation numerical load versus time curves obtained with meshes (B) and (C) and with the EP constitutive law. Red arrows show the pressure applied by the indenter at the integration points of the contact elements under the tip. . . . .	113
9.15	Numerical nanoindentation simulations: influence of the opening angle of the tip. . . . .	114
9.16	Influence of the curvature of the tip on load versus displacement curves. (A) Tip without curvature, (B) 3 more nodes and (C) 6 more nodes to better simulate the real curvature of the indenter. . . . .	115
9.17	Numerical nanoindentation simulations: influence of the positioning of the tip. . . . .	116
9.18	Imprint in a $\beta$ grain of Ti-5553 after an indentation test. . . . .	117
9.19	Influence of Young's modulus on numerical nanoindentation simulations. . . . .	118
9.20	Influence of Poisson's ratio on numerical nanoindentation curves. . . . .	118
9.21	Influence of the tangent modulus on nanoindentation load versus displacement curves. . . . .	119
9.22	Influence of the yield strength on nanoindentation load versus displacement curves. . . . .	120
9.23	Influence of the friction coefficient on nanoindentation load versus displacement curves. . . . .	121
9.24	Half apex angle of a rigid cone indenter. . . . .	122
9.25	Top view of the indented material and the Berkovich indenter. Cross sections of the material. . . . .	123
9.26	Contours of Z-displacement (in $10^{-8}$ m) in the material indented after a penetration depth of approximately 180 nm. (a) Top view and (b) 3D view of the top of the material indented. Just the positive displacements are shown in the legend to visualize the pile-up patterns. . . . .	126

9.27	Contours of Z-displacement (in $10^{-8}$ m) in the material indented after a penetration depth of approximately 180 nm. (a) Top view and (b) 3D view of the top of the material indented. . . . .	127
9.28	Influence of the orientation of the BCC $\beta$ grain (of a Ti-5553 alloy) indented on load versus displacement indentation curve. The orientation of the grains indented and their positions in the material are superimposed. . . . .	129
9.29	Experimental patterns obtained after indentation in three different grain orientations. . . . .	129
9.30	Variation depth profile after an indentation of 117 nm (and after tip removal) of the indented surface for 3 grain orientations corresponding to grains 6, 7 and 9. Simulations performed with the 1772 finite element mesh. . . . .	130
9.31	Stress profile after an indentation of 117 nm (and after tip removal) of the indented surface for 3 grain orientations corresponding to grains 6, 7 and 9. Simulations performed with the 1772 finite element mesh. . . . .	130
10.1	EBSD image of the indented material. Indentations were performed in $\alpha$ grains. Each number corresponds to one indentation. The white numbers correspond to the first set of indentations and the black ones to the second set. . . . .	137
10.2	Nanoindentation experiment in $\alpha$ grain: load versus displacement (number 12 of Figure (10.1)). . . . .	138
10.3	Nanoindentation in $\alpha$ grain (12th indentation of Figure (10.1)): load versus displacement curves. Comparison between numerical results with and without unloading. The corresponding experimental result is superimposed. . . . .	139
10.4	Nanoindentation: load versus displacement curves. Grain numbers of black set from Figure (10.1). . . . .	143
10.5	Nanoindentation: load versus displacement curves for different Young's moduli. Grain numbers of black set from Figure (10.1). Unloading slopes in $\mu N/nm$ . . . . .	144
10.6	Top view of a Berkovich indenter in the XYZ axes. . . . .	145
10.7	Different indenter geometries in the plane ( $X = 0$ ) used to perform simulations: on the right, zoom on the tip of the indenters shown in whole on the left figure. . . . .	145
10.8	Nanoindentation: load versus displacement curves for different tip geometries (Figures (10.7)) and for a Young's modulus equal to 115 GPa. Unloading slopes in $\mu N/nm$ . . . . .	145
10.9	Nanoindentation: load versus displacement curves for different tip geometries (Figures (10.7)) and a Young's modulus equal to 125 GPa. Comparison with the experimental curve. Unloading slopes in $\mu N/nm$ . . . . .	146
10.10	Nanoindentation: load versus displacement curves for Tip 4 (Figures (10.7)) and Young's modulus equal to 115 and 125 GPa. Comparison with the experimental curve. Unloading slopes in $\mu N/nm$ . . . . .	147
10.11	Nanoindentation: load versus displacement performed with Tip 4 (Figures (10.7)) and $E = 125$ GPa on different grain orientations. . . . .	147
10.12	Nanoindentation: Experimental load versus displacement curves performed in different grain orientations (Indentations 12, 43 and 58 of Figure (10.1)). . . . .	148
10.13	Nanoindentation: Load versus displacement curves obtained with the elastic anisotropic parameters from [Tri06], all multiplied by 1.31, and with the plastic parameters from Table (10.2). Indentations in 3 grains corresponding to indentation 12, 43 and 58. . . . .	149



10.14	Nanoindentation: load versus displacement curves performed with $\tau_0$ parameters from Luquiau (Table (10.5)), $\tau_0/\tau_s = 0.98$ for the 12th (for which only the loading part is shown), 43rd and 58th indentations. The isotropic elastic parameters are $E = 125$ GPa and $\nu = 0.33$ . Comparison with experimental results. . . . .	150
10.15	Nanoindentation: Numerical load versus displacement curves performed with $\tau_0$ parameters from Luquiau (Table (10.5)), $\tau_0/\tau_s = 0.98$ for the 12th (only the loading part), 43rd and 58th indentations. The elastic anisotropic parameters chosen are those from [Tri06], all multiplied by 1.31. Comparison with experimental results. . . . .	150
10.16	Basal $\langle \mathbf{a} \rangle$ , prismatic $\langle \mathbf{a} \rangle$ , pyramidal $\langle \mathbf{a} \rangle$ slip systems, and first- and second-order pyramidal $\langle \mathbf{c} + \mathbf{a} \rangle$ slip systems in HCP materials. Figure collected from [BA02]. . . . .	152
10.17	Load versus displacement nanoindentation curves performed with $\tau_0$ parameters from literature (Table (10.7)) and comparison with experimental results of indentation 12. . . . .	154
10.18	Load versus displacement nanoindentation curves performed with Luquiau's $\tau_0$ parameters (Table (10.7)) and $\tau_0/\tau_s = 0.98$ . Comparison with experimental curve 12. . . . .	155
10.19	Load versus displacement nanoindentation curves performed with Luquiau's $\tau_0$ parameters (Table (10.7)) and $\tau_0/\tau_s = 0.98$ for 12th, 58th and 43rd indentations. The elastic parameters are $E = 125$ GPa and $\nu = 0.33$ . Comparison with experimental results. . . . .	156
10.20	Indentation 12. Shear strain on each slip system that can be activated during the loading of a nanoindentation test. The slip systems that can be activated are the 3 basal systems, the 3 prismatic systems and the 6 pyramidal $\langle \mathbf{a} \rangle$ systems. . . . .	157
10.21	Load versus displacement nanoindentation curves (loading only) in three different grain orientations and with different slip systems that could be activated (all with the same initial and saturation shear stresses). . . . .	159
10.22	Simulation of nanoindentations (loading phase only) 12, 43 and 58 and comparison with experiments. The CRSS of slip systems (basal, prismatic and pyramidal $\langle \mathbf{a} \rangle$ ) are provided in Table (10.10). . . . .	160
10.23	Simulation of nanoindentations (loading phase only) 12, 43 and 58 and comparison with experiments. The CRSS of slip systems (basal, prismatic and pyramidal $\langle \mathbf{a} \rangle$ ) are provided in Table (10.10). . . . .	160
10.24	Simulation of nanoindentations (loading phase only) 12, 43 and 58 and comparison with experiments. The CRSS of slip systems (basal, prismatic and pyramidal $\langle \mathbf{a} \rangle$ ) are provided in Table (10.10). . . . .	161
10.25	Simulation of nanoindentations (loading phase only) 12, 43 and 58 and comparison with experiments. The CRSS of slip systems (basal, prismatic and pyramidal $\langle \mathbf{a} \rangle$ ) are provided in Table (10.10). . . . .	161
10.26	Experimental and numerical nanoindentation load versus displacement curves in four different grain orientations (numbers 12, 31, 43 and 58 of Table (10.1)). Numerical tests were performed with the parameters from Table (10.11). . . . .	163
11.1	Thermal treatment ( $n^\circ 1$ ) used to obtain the first microstructure. . . . .	168

11.2	First microstructure, obtained with the thermal treatment of Figure (11.1). . .	169
11.3	Mesh of the representative cell of the first microstructure: one globular $\alpha$ grain in a $\beta$ matrix. . . . .	169
11.4	Representative cell of the first microstructure: one globular $\alpha$ grain inside a $\beta$ matrix. (a) Cross section along a ( $z = \text{constant}$ ) plane that shows the mesh inside the cell. (b),(c) Parts of the mesh: the $\alpha$ phase in the (blue) globular part, in the middle, and the surrounding $\beta$ phase (in orange). . . . .	169
11.5	Thermal treatment ( $n^{\circ}2$ ) used to obtain the second microstructure. . . . .	170
11.6	Second microstructure, obtained with the thermal treatment described in Figure (11.5). . . . .	170
11.7	Representative cell of the second microstructure: an elongated $\alpha$ phase inside a $\beta$ matrix. (a) Cross section along a $x$ plane that shows the mesh inside the cell. (b),(c) Parts of the mesh: the $\alpha$ phase in the (blue) part, in the middle, and the surrounding $\beta$ phase (in orange). . . . .	171
11.8	Cross sections in the representative cells of the two microstructures. (a) Globular $\alpha$ and (b) coarse plate $\alpha$ . . . . .	172
11.9	Orientation of the $\alpha$ phase ( $\alpha(1)$ and $\alpha(2)$ ) in the global ( $XYZ$ ) axes. . . . .	173
11.10	Von Mises' strain in the deformed configuration and the first loading. (Left) 100% $\beta$ sample, (right) globular $\alpha$ inside the $\beta$ matrix. . . . .	174
11.11	Von Mises' stress (MPa) in the deformed configuration and the first loading. (Left) 100% $\beta$ sample, (right) globular $\alpha$ inside the $\beta$ matrix. . . . .	174
11.12	Von Mises' macroscopic stress versus strain for the 100% $\beta$ and ( $\alpha + \beta$ ) samples. . . . .	175
11.13	Experimental tensile tests on the tempered (100% $\beta$ ) and the as-received ( $\alpha + \beta$ ) materials at different strain rates ranging from $\dot{\epsilon} = 10^{-5} \text{ s}^{-1}$ up to $10^{-2} \text{ s}^{-1}$ . True stress versus true strain curves. Each test was performed twice. . . . .	176
11.14	Numerical tensile test performed with one element, with the orientation $\alpha(1)$ and with the parameters of the $\alpha$ phase (Table (10.11) in Part (IV)). Strain rate $\dot{\epsilon} = 0.6 \text{ s}^{-1}$ . . . . .	176
11.15	Von Mises' strain in the two microstructures in the deformed configuration and submitted to the first loading phase. (Left) first microstructure, (right) second microstructure. . . . .	177
11.16	Von Mises' stress (MPa) in the two microstructures in the deformed configuration and submitted to the first loading phase. (Left) first microstructure, (right) second microstructure. . . . .	177
11.17	Von Mises' stress versus strain for the two microstructures. . . . .	178
11.18	Plot of the final periodic displacement in the initial configuration. . . . .	179
11.19	First microstructure in the deformed configuration. (Left) first loading phase, (right) second loading phase. . . . .	179
11.20	Periodic displacement during the test for two corresponding nodes: nodes 326 and 382 (shown in Figure (11.18)). . . . .	179
11.21	Von Mises' strain of the first microstructure in the deformed configuration. (Left) first loading phase, (right) second loading phase. . . . .	180
11.22	Von Mises' strain of the first microstructure in a part of the deformed configuration. (Left) first loading phase, (right) second loading phase. . . . .	180
11.23	Von Mises' strain of the first microstructure in a part of the deformed configuration. (Left) first loading phase, (right) second loading phase. . . . .	181

11.24	Von Mises' stress (MPa) of the first microstructure in a part of the deformed configuration. (Left) first loading phase, (right) second loading phase. . . . .	181
11.25	Von Mises' stress (MPa) of the first microstructure in a part of the deformed configuration. (Left) first loading phase, (right) second loading phase. . . . .	181
11.26	Von Mises' stress versus strain for the two loading phases on the first microstructure. . . . .	182
11.27	Von Mises' strain of the second microstructure in the deformed configuration. (Left) first loading phase, (right) second loading phase. . . . .	182
11.28	Von Mises' strain of the second microstructure in a part of the deformed configuration. (Left) first loading phase, (right) second loading phase. . . . .	183
11.29	Von Mises' strain of the second microstructure in a part of the deformed configuration. (Left) first loading phase, (right) second loading phase. . . . .	183
11.30	Von Mises' stress (MPa) of the second microstructure in a part of the deformed configuration. (Left) first loading phase, (right) second loading phase. . . . .	183
11.31	Von Mises' stress (MPa) of the second microstructure in a part of the deformed configuration. (Left) first loading phase, (right) second loading phase. . . . .	184
11.32	Von Mises' stress versus strain curves for the two loading phases on the second microstructure. . . . .	184
11.33	Von Mises' strain (MPa) of the first microstructure, submitted to the first loading phase and with (left) the first $\alpha$ orientation and, (right) the second $\alpha$ orientation in a part of the deformed configuration. . . . .	185
11.34	Von Mises' strain (MPa) of the first microstructure, submitted to the first loading phase and with (left) the first $\alpha$ orientation and, (right) the second $\alpha$ orientation in a part of the deformed configuration. . . . .	185
11.35	Von Mises' stress (MPa) of the first microstructure, submitted to the first loading phase and with (left) the first $\alpha$ orientation and, (right) the second $\alpha$ orientation in a part of the deformed configuration. . . . .	185
11.36	Von Mises' stress (MPa) of the first microstructure, submitted to the first loading phase and with (left) the first $\alpha$ orientation and, (right) the second $\alpha$ orientation in a part of the deformed configuration. . . . .	186
11.37	Von Mises' stress versus strain curves for the first microstructure submitted to the first loading phase and for the two $\alpha$ grain orientations. . . . .	186
11.38	Schematic representation of the allotropic transformation $\beta$ (BCC) $\rightarrow$ $\alpha$ (HCP). 187	
11.39	Von Mises' stress versus strain curves for the first representative cell submitted to the first loading phase and for three $\alpha$ grain orientations. . . . .	188
11.40	Von Mises stress versus strain for all the microstructures, loadings and orientations studied. . . . .	190
A.1	Geometry of a general unit cell. . . . .	199
B.1	Geometry of a general unit cell. . . . .	201
B.2	Fundamental vectors of a lattice. . . . .	204
B.3	Lattice planes - Miller indices. . . . .	204
B.4	Lattice planes - Miller indices. . . . .	205
B.5	Lattice directions - Cubic system. . . . .	205
B.6	Hexagonal system. . . . .	206
B.7	Body-centered cubic structure. . . . .	206

B.8	Face-centered cubic structure. . . . .	207
B.9	Hexagonal close packed structure. . . . .	207
B.10	(a) Stacking sequence of some parallel atomic (111) planes in an FCC structure. Only one atom of the parallel C plane is shown. (b) Stacking sequence of parallel atomic (111) planes in the FCC structure. The positions of the A, B and C layers are all different and repeat periodically. (c) Stacking sequence of the atomic planes in an HCP structure. (d) HCP structure, A and B planes alternate. Figures reproduced from [FA08]. . . . .	208
B.11	Sliding of one plane of atoms past an adjacent one. This high-stress process is necessary to plastically (permanently) deform a perfect crystal. Figure inspired from [Sha96]. . . . .	209
B.12	A low-stress alternative for plastically deforming a crystal involves the motion of a dislocation along a slip plane. Figure inspired from [Sha96]. . . . .	210
B.13	Slip systems in BCC materials. Information from [LW07]. . . . .	211
B.14	Basal $\langle \mathbf{a} \rangle$ , prismatic $\langle \mathbf{a} \rangle$ , pyramidal $\langle \mathbf{a} \rangle$ slip systems, and first- and second-order pyramidal $\langle \mathbf{c} + \mathbf{a} \rangle$ slip systems in HCP materials. Figure collected from [BA02]. . . . .	211
C.1	FE mesh of 27 elements composed of eight nodes. The nodes are numbered. . . . .	213
C.2	Evolution of the microscopic velocity gradient (in the three directions) in one element of the mesh. . . . .	215
C.3	Components of the stress during a tensile test in an elastic homogeneous sample: (left) component 11 and (right) component 22. Theoretical and numerical (microscopic and macroscopic) results are superimposed. . . . .	216
C.4	Evolution of the first and second components of the coordinates of node 6 during the elastic-plastic test. Comparison of theoretical and numerical results. . . . .	217
C.5	Numerical stress versus time obtained for elastic-plastic homogeneous expansion test. . . . .	218
C.6	The 3 layers of the FE sample composed of 27 elements. Elements 1, 3, 4, 7, 8, 12, 13, 15, 16, 17, 18, 21, 22 and 26 have Young's modulus $E_1$ . Elements 2, 5, 6, 9, 10, 11, 14, 19, 20, 23, 24, 25 and 26 have Young's modulus $E_2$ . . . . .	218
C.7	Component 11 of the stress tensor in the heterogeneous elastic-plastic case. (Left) Component $\sigma_{11}$ in each element of the mesh during the simulation. The macroscopic component is superimposed. (Right) The same macroscopic component is compared to the average one (obtained from those obtained in each element, taking into account the updated volume of each element). . . . .	219
C.8	Periodic velocity during the test for corresponding nodes: 2, 14, 50 and 62. . . . .	220
C.9	Mesh in the initial configuration (in black) and with the periodic displacement of the sample at the end of the test (in red). On the right, periodic displacement of the mesh at the end of the test. . . . .	220
C.10	Component 11 of the stress tensor in the heterogeneous elastic-plastic case. (Left) Component $\sigma_{11}$ in each element of the mesh during the simulation and macroscopic corresponding component. (Right) The macroscopic component 11 is compared to the average one (obtained from the stress in each element, taking into account the updated volume of each element). . . . .	221

C.11	Mesh in the initial configuration (in black) and with the periodic displacement of the sample at the end of the test (in red). On the right, periodic displacement at the end of the test. . . . .	222
C.12	Periodic velocities in directions $x$ (left) and $y$ (right) for nodes 1 to 16 during the test. . . . .	222
C.13	Periodic velocities in direction $z$ for nodes 1 to 16 during the test. . . . .	222
C.14	Component 11 of the stress tensor in the heterogeneous elastic-plastic case. (Left) $\sigma_{11}$ in each element of the mesh during the simulation and macroscopic component. (Right) The same macroscopic component is compared to the average one (obtained from each element, taking into account the updated volume of each element). . . . .	223
C.15	Mesh in the initial configuration (in black) and with the periodic displacement of the sample at the end of the test (in red). On the right, periodic displacement of the mesh at the end of the test. . . . .	223
C.16	Periodic velocities in the $x$ direction for nodes 1 to 16 during the test (elastic homogeneous behavior and plastic heterogeneous behavior). . . . .	224
C.17	Updated coordinates for node 6 of initial coordinates (1, 1, 0) during the test for the loading of Eqn.(C.10). . . . .	225
C.18	Component 12 of the stress tensor. Calculated values from Hooke's law and the ones obtained numerically for the macroscopic loading of Eqn.(C.10) in an elastic and homogeneous environment. The figure on the left is a zoom of the right one for the beginning of the test. . . . .	226
E.1	$BWD3D$ brick element and its local axes. . . . .	231
E.2	Local axes at one point of contact. . . . .	232
E.3	Bodies A and B in contact and velocities at contact points. . . . .	233
E.4	Illustration of the non-penetration condition. . . . .	234
E.5	Coulomb's friction model. . . . .	235
E.6	Penalty of penetration. . . . .	236
E.7	Penalty of sticking contact. . . . .	236
F.1	Part of the data file where the values of the parameters are given. In the rectangle are defined some values of parameters of Bassani's hardening, for each slip system. The lines containing the parameters $h_s^{(\alpha)}$ , $\gamma_{0\alpha}$ , $\gamma_{0\alpha\beta}$ , $f_{\alpha\alpha}$ and $f_{\alpha\beta}$ are replaced by: $A^{(\alpha)}$ , $B^{(\alpha)}$ , $\gamma_{0\alpha}$ , $\gamma_{0\alpha\beta}$ , $f_{\alpha\alpha}$ and $f_{\alpha\beta}$ . . . . .	238
H.1	Berkovich indenter in the global axes. . . . .	241
I.1	(Left) Conical indenter in the material. Figure reproduced from [BSFM03]. (Right) Role of friction between a conical indenter and the deformed metal. . . . .	243
J.1	Coordinates of the nodes defining the first tip. (Right) First indenter tip. . . . .	245
J.2	Coordinates of the nodes defining the second tip. (Right) Second (in blue) indenter tip. . . . .	246
J.3	Rotation to obtain the third indenter tip. . . . .	246
K.1	Imprint in a $\beta$ grain of Ti-5553 after an indentation test. . . . .	247

K.2	Top view of the indented material's mesh and superimposed indenter tip. Orientation of the cross sections in the material along the three heights of the indenter. . . . .	248
K.3	Top view of the material indented after a penetration depth of 103.5 nm, and with (A) tip 1, (B) tip 2 and (C) tip 3 (cf. Appendix (J)). Variation depth in $10^{-8}$ m. . . . .	249
K.4	Cross section 1 of Figure (K.2) in the material indented after a penetration depth of 103.5 nm, and with (A) tip 1, (B) tip 2 and (C) tip 3 (cf. Appendix (J)). Variation depth in $10^{-8}$ m. . . . .	249
K.5	Cross section 2 of Figure (K.2) in the material indented after a penetration depth of 103.5 nm, and with (A) tip 1, (B) tip 2 and (C) tip 3 (cf. Appendix (J)). Variation depth in $10^{-8}$ m. . . . .	249
K.6	Cross section 3 of Figure (K.2) in the material indented after a penetration depth of 103.5 nm, and with (A) tip 1, (B) tip 2 and (C) tip 3 (cf. Appendix (J)). Variation depth in $10^{-8}$ m. . . . .	250
K.7	Top view of the material unloaded after a penetration depth of 103.5 nm. The scale is limited to positive vertical displacements. The maximum and minimum values of the vertical displacement are recalled in the bottom of each figure. (A) tip 1, (B) tip 2 and (C) tip 3 (cf. Appendix (J)). Variation depth in $10^{-8}$ m. . . . .	250
L.1	(left) Typical load versus displacement nanoindentation curve. (right) Deformed pattern of an elastic-plastic sample during and after indentation. Figures from [LB02]. . . . .	252
M.1	Part of the meshes used for nanoindentation simulations: (A) mesh with 1772 elements and (B) mesh with 4544 elements. . . . .	256
M.2	Rigid conical indenter used for numerical simulations on FCC. . . . .	256
M.3	Variation depth profile after an indentation of 162 nm of the indented surface of the material for 3 orientations of the crystal. In the global axes, the directions (100) and (001) become, (a) (100) and (001), (b) (100) and (011) and (c) (10-1) and (111), with indentation along the (001) direction in the global axes. Simulations performed with the 4662-element mesh. . . . .	257
M.4	Equivalent Von Mises' stress profile after an indentation of 162 nm of the indented surface of the material for 3 orientations of the crystal. In the global axes, the directions (100) and (001) become, (a) (100) and (001), (b) (100) and (011) and (c) (10-1) and (111), with indentation along the (001) direction in the global axes. . . . .	258
N.1	Indentation 12. Shear strain on each slip system that can be activated during the loading phase of a nanoindentation test. The slip systems that can be activated are the 3 basal systems, the 3 prismatic systems and the 6 pyramidal $\langle a \rangle$ systems. . . . .	260
N.2	Indentation 43. Shear strain on each slip system that can be activated during the loading phase of a nanoindentation test. The slip systems that can be activated are the 3 basal systems, the 3 prismatic systems and the 6 pyramidal $\langle a \rangle$ systems. . . . .	260

N.3	Indentation 58. Shear strain on each slip system that can be activated during the loading phase of a nanoindentation test. The slip systems that can be activated are the 3 basal systems, the 3 prismatic systems and the 6 pyramidal $\langle a \rangle$ systems. . . . .	261
N.4	Indentation 12. Shear strain on each slip system that can be activated during the loading phase of a nanoindentation test. The slip systems that can be activated are the 3 basal systems, the 3 prismatic systems and the 12 pyramidal $\langle c+a \rangle$ systems. . . . .	262
N.5	Indentation 43. Shear strain on each slip system that can be activated during the loading phase of a nanoindentation test. The slip systems that can be activated are the 3 basal systems, the 3 prismatic systems and the 12 pyramidal $\langle c+a \rangle$ systems. . . . .	262
N.6	Indentation 58. Shear strain on each slip system that can be activated during the loading phase of a nanoindentation test. The slip systems that can be activated are the 3 basal systems, the 3 prismatic systems and the 12 pyramidal $\langle c+a \rangle$ systems. . . . .	263
N.7	Indentation 12. Shear strain on each slip system that can be activated during the loading phase of a nanoindentation test. The slip systems that can be activated are the 3 basal systems, the 6 pyramidal $\langle a \rangle$ systems and the 12 pyramidal $\langle c+a \rangle$ systems. . . . .	263
N.8	Indentation 43. Shear strain on each slip system that can be activated during the loading phase of a nanoindentation test. The slip systems that can be activated are the 3 basal systems, the 6 pyramidal $\langle a \rangle$ systems and the 12 pyramidal $\langle c+a \rangle$ systems. . . . .	264
N.9	Indentation 58. Shear strain on each slip system that can be activated during the loading phase of a nanoindentation test. The slip systems that can be activated are the 3 basal systems, the 6 pyramidal $\langle a \rangle$ systems and the 12 pyramidal $\langle c+a \rangle$ systems. . . . .	264
O.1	Simulations of nanoindentations (loading phase only) 12, 43 and 58 and comparison with experiments. The CRSS of slip systems (basal, pyramidal $\langle a \rangle$ and pyramidal $\langle c+a \rangle$ ) are given in Table (O.1). . . . .	268
O.2	Simulations of nanoindentations (loading phase only) 12, 43 and 58 and comparison with experiments. The CRSS of slip systems (basal, prismatic, pyramidal $\langle a \rangle$ and pyramidal $\langle c+a \rangle$ ) are given in Table (O.1). All the simulations performed with these sets of parameters and the initial CRSS in Table (O.1) are superimposed on the figure on the right. . . . .	268





# List of Tables

2.1	Characteristics of titanium and titanium alloys and comparison with other metals based on Fe, Ni, and Al [LW07]. . . . .	7
2.2	Parameters of Ti-LCB (indicative values): Young's modulus $E$ of the $\beta$ and the $\alpha$ phases, Poisson's ratio $\nu$ and $T_\beta$ . . . . .	10
2.3	Parameters of Ti-5553 (indicative values): Young's modulus of $\beta$ and $\alpha$ phases, Poisson's ratio and $T_\beta$ temperature of the transformation $\alpha \leftrightarrow \beta$ . . . . .	13
7.1	A set of Norton-Hoff's parameters optimized for 100% $\beta$ Ti-5553 at different strain rates ( $\dot{\epsilon} \simeq 10^{-2}$ to $10^{-5} \text{ s}^{-1}$ ). . . . .	63
7.2	Sets of Norton-Hoff's parameters optimized for 100% $\beta$ Ti-5553 and for two strain rate ranges. . . . .	64
7.3	Optimized parameters of the microscopic plasticity law using Asaro and Pierce's hardening for tensile tests performed at $10^{-3}$ , $10^{-4}$ and $10^{-5} \text{ s}^{-1}$ . . . . .	68
7.4	Optimized parameter $h_0$ for tensile tests performed at all strain rates. . . . .	68
7.5	Initial parameters for Bassani and Wu's hardening. . . . .	72
7.6	Optimized parameters for tensile tests performed at all strain rates. . . . .	78
7.7	Optimized parameters for tensile tests performed at all strain rates. . . . .	81
8.1	First set of Norton-Hoff's parameters. . . . .	88
8.2	Second set of Norton-Hoff's parameters. . . . .	90
8.3	Parameters of the microscopic constitutive law for $\beta$ Ti-5553. . . . .	93
9.1	Orientation of the indented $\beta$ grains illustrated in Figure (9.6). . . . .	107
9.2	Parameters optimized for the $\beta$ phase of Ti-5553: Elastic modulus $E$ , Poisson's ratio $\nu$ , plastic strength $\sigma_y$ , tangent modulus $E_T$ and friction coefficient $\mu$ . . . . .	109
9.3	Parameters of Pierce, Needleman and Asaro's hardening model, for the $\beta$ phase of Ti-5553. . . . .	111
9.4	Parameters of Bassani and Wu's hardening model for the $\beta$ phase of Ti-5553. . . . .	111
9.5	Comparison of the computation time of two numerical simulations. These simulations are exactly the same except for friction coefficient. . . . .	120
9.6	Numerical nanoindentation simulations. Cross sections in the unloaded material ( $\sigma_y = 6000 \text{ MPa}$ ). Cross sections along the planes ( $x = 0$ ) and ( $y = 0$ ). The scale (in $10^{-10} \text{ m}$ ) represents the Z-displacement of the material indented. . . . .	124
9.7	Numerical nanoindentation simulations. Results are shown after a penetration depth of 200 nm. Cross sections in the material indented ( $\sigma_y = 354 \text{ MPa}$ ) before tip removal. Cross sections along the planes ( $x = 0$ ) and ( $y = 0$ ). The scale (in $10^{-10} \text{ m}$ ) represents the Z-displacement of the material indented. . . . .	124

9.8	Parameters $\tau_0$ and $\tau_s$ of the PAN model for the two numerical simulations performed with the microscopic constitutive law. . . . .	125
9.9	Sensitivity analysis about nanoindentation in the $\beta$ phase of Ti-5553. Concluding results. . . . .	131
10.1	Euler angles of indentations chosen (indentation number of the black set from Figure (10.1)). . . . .	138
10.2	Plastic parameters used in this section for the identification of the elastic parameters. . . . .	140
10.3	Corresponding indices between notations of $C_{ijkl}$ . . . . .	141
10.4	Values of elastic parameters (in GPa) for the $\alpha$ phase of titanium from the literature. The last column gives an idea of the corresponding Young's modulus (computed from an average of the anisotropic coefficients). . . . .	142
10.5	Plastic parameters used in this section where only elastic parameters are identified. . . . .	149
10.6	Slip systems in HCP materials. . . . .	152
10.7	Initial CRSS (in MPa or relative values) of HCP materials collected in the literature. In the last column, values labelled "1°" correspond to initial CRSS of 1st order pyramidal $\langle c+a \rangle$ slip systems and values labelled "2°" correspond to initial CRSS of 2nd order pyramidal $\langle c+a \rangle$ slip systems. These slip systems are illustrated in Figure (10.16). . . . .	153
10.8	Set of slip systems that could be activated in simulations 1, 2 and 3. . . . .	156
10.9	Summary of the number of slip systems activated for the three simulations in three orientations. Red color means that the corresponding number of slip systems in one set are highly activated, pink is associated with corresponding slowly activated slip systems and white is for slip systems that were not activated. . . . .	158
10.10	Ratio of the CRSS between the different sets of slip systems to identify the $\alpha$ phase of Ti-5553. . . . .	159
10.11	Elastic and plastic parameters optimized to characterize the $\alpha$ phase of Ti-5553. The three sets of slip systems that can be activated are the basal, the prismatic and the pyramidal $\langle a \rangle$ ones. . . . .	162
11.1	Ratios between the greatest length ( $L$ ) of the inclusion and the smallest one ( $l$ ) for the two meshes in Figure (11.8). . . . .	171
11.2	Orientations of the phases in the representative cell: the $\beta$ matrix and two orientations for the $\alpha$ phase. Two local and corresponding global (macroscopic) axes are given. . . . .	173
11.3	Summary of the tests performed in this chapter. . . . .	189
B.1	The seven crystal systems. Figure inspired from [Sha96] and from [FA08]. . . . .	202
B.2	The fourteen crystal Bravais lattices. Figure inspired from [Sha96]. . . . .	203
B.3	Major slip systems in BCC and HCP metal structures. . . . .	209
G.1	Orientations of the 30 grains used in numerical shear test. . . . .	240
J.1	Coordinates of the nodes defining the third tip. . . . .	246
M.1	Parameters of FCC material used in simulations [Ler03]. These parameters correspond to aluminum material. . . . .	256

O.1 CRSS of the different sets of slip systems to identify the  $\alpha$  phase of Ti-5553. . . 267

P.1 Sets of slip systems and corresponding  $\tau_0$  and  $\tau_s$  values tested to identify the  $\alpha$  phase. . . . . 269

P.2 Anisotropic elastic matrix components tested (MPa). . . . . 270



# Bibliography

- [Aba03] Abaqus. *User's Manual. Version 6.4*. Habbitt, Karlson and Sorensen, Inc., 2003.
- [ABB<sup>+</sup>07] A.M.L. Adib, C.A.R.P. Baptista, M.J.R. Barboza, C. Haga, and C.C.F. Marques. Aircraft engine bleed system tubes: Material and failure mode analysis. *Engineering Failure Analysis*, Volume 14, Issue 8:1605–1617, 2007.
- [ACO08] J. Alcala, O. Casals, and J. Ocenasek. Micromechanics of pyramidal indentation in fcc metals: Single crystal plasticity finite element analysis. *Journal of Mechanics and Physics of Solids*, Volume 56, Issue 11:3277–3303, 2008.
- [BA02] S. Balasubramanian and L. Anand. Plasticity of initially textured hexagonal polycrystals at high homologous temperatures: application to titanium. *Acta Materialia*, Volume 50, Issue 1:133–148, 2002.
- [Bal95] S. Balasubramanian. *Polycrystalline Plasticity and its Applications to Deformation Processing*. PhD thesis, Massachusetts Institute of Technology, 1995.
- [BB91] T. Belytschko and L. P. Bindeman. Assumed Strain Stabilization of the 4-Node Quadrilateral With 1-Point Quadrature for Nonlinear Problems. *Computer Methods in Applied Mechanics and Engineering*, Volume 88, Issue 3:311–340, 1991.
- [BB06] M. Ben Bettaieb. *Modélisation du comportement des matériaux polycristallins par homogénéisation périodique*. PhD thesis, University of Aix-Marseille II, 2006.
- [BBM05] M. Bocciarelli, G. Bolzon, and G. Maier. Parameter identification in anisotropic elastoplasticity by indentation and imprint mapping. *Mechanics of Materials*, Volume 37, Issue 8:855–868, 2005.
- [BD05] M.A. Baranov and E.A. Dubov. Definition of elastic modules of ordered hexagonal crystals. *EPhTJ*, 1:28–33, 2005.
- [BMO00] E.P. Busso, F.T. Meissonnier, and N.P. O'Dowd. Gradient-dependent deformation of two-phase single crystals. *Journal of the Mechanics and Physics of Solids*, Volume 48, Issue 11:2333–2361, 2000.
- [Bou97] S. Bourgeois. *Modélisations de panneaux structuraux légers*. PhD thesis, University of Aix-Marseille II, 1997.

- [BSFM03] J.L. Bucaille, S. Strauss, E. Felder, and J. Michler. Determination of plastic properties of metals by instrumented indentation using different sharp indenters. *Acta Materialia*, Volume 51, Issue 6:1663–1678, 2003.
- [BSM08] F. Bédoui, F. Sansoz, and N.S. Murthy. Incidence of nanoscale heterogeneity on the nanoindentation of a semicrystalline polymer: Experiments and modeling. *Acta Materialia*, Volume 56, Issue 10:2296–2306, 2008.
- [BTW<sup>+</sup>07] M. Büscher, G. Terlinde, G. Wegmann, C. Thoben, Y. Millet, G. Lütjering, and J. Albrecht. Forgings from Ti-5Al-5V-5Mo-3Cr with optimized fracture toughness. In M. Ikeda M. Hagiwara M.Niinomi, S. Akiyama and K. Maruyama, editors, *Proceedings of Ti-2007 Science and Technology*, The Japan Institute of Metals, 2007.
- [BW91] J.L. Bassani and T. Wu. Latent hardening in single crystals 2, analytical characterization and predictions. *Proceedings of the Royal Society of London, Series A*, Volume 435, Issue 1893:21–41, 1991.
- [CBB<sup>+</sup>07] J.D. Cotton, R.R. Boyer, R.D. Briggs, R.G. Baggerly, C.A. Meyer, M.D. Carter, W. Wood, G. Tewksbury, Victor Li, and X. Yao. Phase transformations in Ti-5Al-5Mo-5V-3Cr-0.5Fe. In M. Ikeda M. Hagiwara M.Niinomi, S. Akiyama and K. Maruyama, editors, *Proceedings of Ti-2007 Science and Technology*, The Japan Institute of Metals, 2007.
- [Cen] <http://www.cenaero.be>. Page last visited on August 12, 2008.
- [Cha87] R. Charlier. *Approche unifiée de quelques problèmes non linéaires de mécanique des milieux continus par la méthode des éléments finis (grandes déformations des métaux et des sols, contact unilatéral des solides, conduction thermique et écoulements en milieux poreux)*. PhD thesis, University of Liège, 1987.
- [Cha04] Kwai S. Chan. A micromechanical analysis of the yielding behavior of individual widmanstätten colonies of an  $\alpha + \beta$  titanium alloy. *Metallurgical and Materials Transactions A*, Volume 35, Issue 11:3409–3422, 2004.
- [CLJ07] N. Clement, A. Lenain, and P.J. Jacques. Mechanical property optimization via microstructural control of new metastable beta titanium alloys. *JOM*, pages 50–53, January 2007.
- [CLZ<sup>+</sup>07] W. Chen, M. Li, T. Zhang, Y.T. Cheng, and C.M. Cheng. Influence of indenter tip roundness on hardness behavior in nanoindentation. *Materials Science and Engineering A*, Volumes 445-446:323–327, 2007.
- [CV01] X. Chen and J.J. Vlassak. A numerical study on the measurement of thin film mechanical properties by means of nanoindentation. *Journal of Materials Research*, Volume 16, Issue 10:2979–2982, 2001.
- [DdMEH<sup>+</sup>05] L. Duchêne, P. de Montleau, F. El Houdaigui, S. Bouvier, and A. M. Habraken. Analysis of Texture Evolution and Hardening Behavior During Deep Drawing With an Improved Mixed Type FEM Element. In Lorenzo M. Smith, Farhang Pourboghrat, Jeong-Whan Yoon, and Thomas B. Stoughton, editors, *Proceedings of the 6th Numisheet Conference*, pages 409–414, Detroit, MI, USA, 2005.

- [DdMH06] L. Duchêne, P. de Montleau, and A. M. Habraken. Development and Performance Assessment of an Improved 8-Node Mixed Type FEM Element. In *Proceedings of the 9th Esaform conference*, pages 135–138, Glasgow, UK, April 2006.
- [DEHH07] L. Duchêne, F. El Houdaigui, and A. M. Habraken. Length Changes and Texture Prediction During Free End Torsion Test of Copper Bars With FEM and Remeshing Techniques. *International Journal of Plasticity*, Volume 23, Issue 8:1417–1438, 2007.
- [Del05] J. Delfosse. *Forgeage  $\beta$  du Ti17. Propriétés en fatigue*. PhD thesis, Ecole Centrale de Paris, 2005.
- [Dep04] V. Depauw. *Transformations de phase et microstructure d'un alliage  $\alpha/\beta$  à grains fins pour applications aéronautiques*. Graduation work, Université Catholique de Louvain, 2004.
- [DHC92] M. Dyduch, A.M. Habraken, and S. Cescotto. Automatic adaptive remeshing for numerical simulations of metal forming. *Computer Methods in Applied mechanics and Engineering*, Volume 101, Issues 1-3:283–298, 1992.
- [Dic06] T. Dick. *Modélisation multiéchelle du phénomène de fretting dans le contact aube-disque*. PhD thesis, Ecole des Mines de Paris, 2006.
- [DL99] E. Dominicy-Lenoble. *Plasticité de coques périodiques en grandes transformations*. PhD thesis, University of Aix-Marseille II, 1999.
- [DLF<sup>+</sup>08] L. Duchêne, T. Lelotte, P. Flores, S. Bouvier, and A. M. Habraken. Rotation of Axes for Anisotropic Metal in FEM Simulations. *International Journal of Plasticity*, Volume 24, Issue 3:397–427, 2008.
- [DLM<sup>+</sup>06] O. Débordes, C. Licht, J.J. Marigo, P. Mialon, and J.C. Michel. Calcul des charges limites de structures fortement hétérogènes. *Acts of the third colloque*, 2006.
- [DN86] M.F. Doerner and W.D. Nix. A method for interpreting the data from depth-sensing indentation instruments. *Journal of Material Research*, Volume 1, Issue 4:601–609., 1986.
- [Duc03] L. Duchêne. *FEM Study of Metal Sheets with a Texture based, Local Description of the Yield Locus*. PhD thesis, University of Liège, 2003.
- [DW96] W.J. Drugan and J.R. Willis. A micromechanics-based nonlocal constitutive equation and estimates of representative volume element size for elastic composites. *Journal of the Mechanics and Physics of Solids*, Volume 44, Issue 4:497–524, 1996.
- [FA08] H. Fredriksson and U. Akerlind. *Physics of Functional Materials*. John Wiley and Sons, Ltd, England, 2008.
- [Fey99] F. Feyel. Multiscale FE<sup>2</sup> elastoviscoplastic analysis of composite structures. *Computational Materials Sciences*, Volume 16, Issues 1-4:344–354, 1999.

- [Flo06] P. Flores. *Development of Experimental Equipment and Identification Procedures for Sheet Metal Constitutive Laws*. PhD thesis, University of Liège, 2006.
- [FM05] L.M. Farrissey and P.E. McHugh. Determination of elastic and plastic material properties using indentation: Development of method and application to a thin surface coating. *Materials Science and Engineering A*, Volume 399, Issues 1-2:254–266, 2005.
- [FNPM07] J.C. Fanning, S.L. Nyakana, K.M. Patterson, and R.C. McDaniel. Heat treatment, microstructure, and properties of TIMETAL 555. In M. Ikeda M. Hagiwara M.Niinomi, S. Akiyama and K. Maruyama, editors, *Proceedings of Ti-2007 Science and Technology*, The Japan Institute of Metals, 2007.
- [FPC97] X. Feaugas, Ph. Pilvin, and M. Clavel. Cyclic deformation behaviour of an  $\alpha/\beta$  titanium alloy - II. internal stresses and micromechanic modelling. *Acta Materialia*, Volume 45, Issue 7:2703–2714, 1997.
- [FPWE97] J.J. Fundenberger, M.J. Philippe, F. Wagner, and C. Esling. Modelling and prediction of mechanical properties for materials with hexagonal symmetry (zinc, titanium and zirconium alloys). *Acta Materialia*, Volume 45, Issue 10:4041–4055, 1997.
- [FRH05] P. Flores, E. Rondia, and A.M. Habraken. Development of an experimental equipment for the identification of constitutive laws. *International Journal of Forming Processes*, Volume 8:117–137, 2005.
- [FZNH07] J. Fanning, L. Zeng, S. Nyakana, and L. Haylock. Properties and microstructures of Ti-555 (Ti-5Al-5Mo-5V-3Cr-0.6Fe) for fasteners. In M. Ikeda M. Hagiwara M.Niinomi, S. Akiyama and K. Maruyama, editors, *Proceedings of Ti-2007 Science and Technology*, The Japan Institute of Metals, 2007.
- [GCD<sup>+</sup>07] A. Gouldstone, N. Chollacoop, M. Dao, J. Li, A.M. Minor, and Y.-L. Shen. Indentation across size scales and disciplines: Recent developments in experimentation and modeling. *Acta Materialia*, Volume 55, Issue 12:4015–4039, 2007.
- [GCJ<sup>+</sup>06] A.F. Gerday, N. Clement, P.J. Jacques, T. Pardoën, and Habraken A.M. Fe simulations of nanoindentation in beta metastable ti. In N. Juster and A. Rosochowski, editors, *Proceedings of ESAFORM 2006*, Poland, 2006.
- [GCJ<sup>+</sup>07] A.F. Gerday, N. Clement, P.J. Jacques, T. Pardoën, and A.M. Habraken. Inverse modeling of nanoindentation tests to identify ti-555 behavior. In M. Ikeda M. Hagiwara M.Niinomi, S. Akiyama and K. Maruyama, editors, *Proceedings of Ti-2007 Science and Technology*, The Japan Institute of Metals, 2007.
- [Ger06] A.F. Gerday. *Développement d'outils numériques en vue de la modélisation du comportement des alliages de titane*. DEA graduation work, University of Liège, 2006.
- [Gia06] A.E. Giannakopoulos. Elastic and viscoelastic indentation of flat surfaces by pyramid indentors. *Journal of the Mechanics and Physics of Solids*, Volume 54, Issue 7:1305–1332, 2006.



- [HC98] A.M. Habraken and S. Cescotto. Contact between deformable solids, the fully coupled approach. *Mathematical and Computer Modelling*, Volume 28, Issues 4-8:153–169, 1998.
- [Hen09] C. Henrard. *Numerical Simulations of the Single Point Incremental Forming Process*. PhD thesis, University of Liège, 2009.
- [HP07] X. Huang and A.A. Pelegri. Finite element analysis on nanoindentation with friction contact at the film/substrate interface. *Composites Science and Technology*, Volume 67, Issue 7-8:1311–1319, 2007.
- [HPO<sup>+</sup>01] E.G. Herbert, G.M. Pharr, W.C. Oliver, B.N. Lucas, and J.L. Hay. On the measurement of stress-strain curves by spherical indentation. *Thin Solid Films*, Volumes 398-399:331–335, 2001.
- [HR72] R. Hill and J.R. Rice. Constitutive analysis of elastic-plastic crystals at arbitrary strain. *Journal of the Mechanics and Physics of Solids*, Volume 20:401–413, 1972.
- [HR93] W.F. Hosford and Caddell R.M. *Metal forming*. PTR Prentice Hall, USA, 2nd edition edition, 1993.
- [Hua91] Y. Huang. A user-material subroutine incorporating single crystal plasticity in the abaqus finite element program, internal report. *internal report, Harvard University, Cambridge*, 1991.
- [Hut76] J.W. Hutchinson. Bounds and self-consistent estimates for creep of polycrystalline materials. *Proceedings of the Royal Society of London, Series A*, Volume 348:101–127, 1976.
- [IMA] <http://www.imap.ucl.ac.be>. Page last visited on August 12, 2008.
- [JDDJ08] N.G. Jones, R.J. Dashwood, D. Dye, and M. Jackson. Thermomechanical processing of Ti-5AL-5MO-5V-3CR. *Materials Science and Engineering A*, Volume 490, Issues 1-2:369–377, 2008.
- [JJDD07] N. Jones, M. Jackson, D. Dye, and R. Dashwood. Comparing the hot working behaviour of high strength beta alloys Ti-5AL-5MO-5V-3CR with that of Ti-10V-2FE-3AL. In M. Ikeda M. Hagiwara M.Niinomi, S. Akiyama and K. Maruyama, editors, *Proceedings of Ti-2007 Science and Technology*, The Japan Institute of Metals, 2007.
- [Kan03] T. Kanit. *Notion de volume élémentaire représentatif pour les matériaux hétérogènes: approche statistique et numérique*. PhD thesis, Ecole des Mines de Paris, 2003.
- [KFG<sup>+</sup>03] T. Kanit, S. Forest, I. Galliet, V. Mounoury, and D. Jeulin. Determination of the size of the representative volume element for random composites: statistical and numerical approach. *International Journal of Solids and Structures*, Volume 40, Issues 13-14:3647–3679, 2003.

- [KM08] M. Kopernik and A. Milenin. Sensitivity analysis of nanoindentation test for specimen composed of TiAlN and TiN using mathematical model. In Maciej Pietrzyk et al., editor, *Proceedings of the 12th international conference on Metal Forming*, pages 555–562, Krakow, Poland, 2008.
- [KSK09] Jalaaj Kumar, B. Srivathsa, and Vikas Kumar. Stress triaxiality effect on fracture behavior of IMI-834 titanium alloy: A micromechanics approach. *Materials and Design*, Volume 30, Issue 4:1118–1123, 2009.
- [KSM<sup>+</sup>07] Y. Kojima, M. Shima, T. Motoda, T. Jibiki, and Sugawara T. An estimation of friction from the indentation of metals by acute-angled conical indenters. *Tribology International*, Volume 40, Issues 10-12:1479–1483, 2007.
- [Kys01] J.W. Kysar. Continuum simulations of directional dependence of crack growth along copper/sapphire bicrystal interface. part I: experiments and crystal plasticity background. *Journal of the Mechanics and Physics of Solids*, Volume 49, Issue 5:1099–1128, 2001.
- [LB02] X. Li and B. Bhushan. A review of nanoindentation continuous stiffness measurement technique and its applications. *Materials Characterization*, Volume 48, Issue 1:11–36, 2002.
- [LC97] K. Li and S. Cescotto. An 8-Node Brick Element With Mixed Formulation for Large Deformation Analyses. *Computer Methods in Applied Mechanics and Engineering*, Volume 141, Issues 1-2:157–204, 1997.
- [LCD04] X. Liu, P.K. Chu, and C. Ding. Surface modification of titanium, titanium alloys, and related materials for biomedical applications. *Materials Science and Engineering, R: Reports*, Volume 47, Issues 3-4:49–121, 2004.
- [LDJ04] A. Lenain, V. Depauw, and P.J. Jacques. *Characterisation of the crack initiation under cyclic loading of Titanium alloys*. Presentation, Université Catholique de Louvain, 2004.
- [Len07] A. Lenain. *Relationships between Thermomechanical Processing, Microstructure and Mechanical Properties of the  $\beta$ -metastable Ti-LCB alloy*. PhD thesis, Université Catholique de Louvain, 2007.
- [Ler03] C. Leroy. *Micro-mécanique de matériaux polycristallins mono- ou biphasés en plasticité: simulations numériques*. Graduation work, University Catholique de Louvain, 2003.
- [Lev44] K. Levenberg. A method for the solution of certain non-linear problems in least squares. *The Quarterly of Applied Mathematics*, Volume 2:164–168, 1944.
- [LGS<sup>+</sup>96] P.L. Larsson, A.E. Giannakopoulos, E. Söderlund, D.J. Rowcliffe, and Vestergaard R. Analysis of Berkovich indentation. *International Journal of Solids and Structures*, Volume 33, Issue 2:221–248, 1996.
- [Lin96] Y. Ling. Uniaxial true stress-strain after necking. *AMP Journal of Technology*, Volume 5:37–48, June 1996.

- [LN06] E.T. Lilleodden and W.D. Nix. Microstructural length-scale effects in the nanoindentation behavior of thin gold films. *Acta Materialia*, Volume 54, Issue 6:1583–1593, 2006.
- [LVM<sup>+</sup>08] Y. Liu, S. Varghese, J. Ma, M. Yoshino, H. Lu, and R. Komanduri. Orientation effects in nanoindentation of single crystal copper. *International Journal of Plasticity*, Volume 24, Issue 11:1990–2015, 2008.
- [LW07] G. Lütjering and J.C. Williams. *Titanium*. Springer-Verlag, Berlin, second edition, 2007.
- [LWY<sup>+</sup>05] Y. Liu, B. Wang, M. Yoshino, S. Roy, H. Lu, and R. Komanduri. Combined numerical simulation and nanoindentation for determining mechanical properties of single crystal copper at mesoscale. *Journal of the Mechanics and Physics of Solids*, Volume 53, Issue 12:2718–2741, 2005.
- [Mag03] H. Magoaric. *Adaptation élastoplastique et homogénéisation périodique*. PhD thesis, University of Aix-Marseille II, 2003.
- [Mar63] D.W. Marquardt. An algorithm for least-squares estimation of nonlinear parameters. *SIAM Journal of Applied Mathematics*, Volume 11, Issue 2:431–440, 1963.
- [Mat] <http://sun.uni-regensburg.de/matlab-5.3.1/help/helpdesk.html>.
- [MMS] <http://www.metax.uclg.ac.be>. Page last visited on August 12, 2008.
- [MMS99] J.C. Michel, H. Moulinec, and P. Suquet. Effective properties of composite materials with periodic microstructure: a computational approach. *Computer Methods in Applied Mechanics and Engineering*, Volume 172, Issues 1-4:109–143, 1999.
- [MP06] R.A. Mirshams and R.M. Pothapragada. Correlation of nanoindentation measurements of nickel made using geometrically different indenter tips. *Acta Materialia*, Volume 54, Issue 4:1123–1134, 2006.
- [MSL02] C. Miehe, J. Schotte, and M. Lambrecht. Homogenization of inelastic solid materials at finite strains based on incremental minimization principles. Application to the texture analysis of polycrystals. *Journal of the Mechanics and Physics of Solids*, Volume 50, Issue 10:2123–2167, 2002.
- [NFB05] S.L. Nyakana, J.C. Fanning, and R.R. Boyer. Quick reference guide for beta titanium alloys in the 00s. *Journal of Materials Engineering and Performance*, Volume 14:799–811, 2005.
- [Nye61] J. Nye. *Propriétés Physiques des Cristaux*. Dunod editions, Paris, 1961.
- [OP92] W.C. Oliver and G.M. Pharr. An improved technique for determining hardness and elastic modulus using load and displacement sensing indentation experiments. *Journal of Material Research*, Volume 7, Issue 6:1564–1583, 1992.

- [Oro] <http://www.chez.com/deuns/sciences/matiere/disloc34.html>. Page last visited on July 3, 2006.
- [Osi07] N. Osipov. *Génération et calcul de microstructures bainitiques, approche locale intragranulaire de la rupture*. PhD thesis, Ecoles des mines de Paris, 2007.
- [Pas00] F. Pascon. *Finite element modelling of contact between the strand and the mould in continuous casting*. DEA graduation work, University of Liège, 2000.
- [Pas03] F. Pascon. *2D1/2 Thermal-mechanical model of continuous casting of steel using finite element method*. PhD thesis, University of Liège, 2003.
- [Pel05] H. Pelletier. Predictive model to estimate the stress-strain curves of bulk metals using nanoindentation. *Tribology International*, Volume 39, Issue 7:593–606, 2005.
- [PH07] F. Pascon and A.M. Habraken. Finite element study of the effect of some local defects on the risk of transverse cracking in continuous casting of steel slabs. *Computer Methods in Applied Mechanics and Engineering*, Volume 196, Issues 21-24:2285–2299, 2007.
- [PHHL06] G.P. Potirniche, J.L. Hearndon, M.F. Horstemeyer, and X.W. Ling. Lattice orientation effects on void growth and coalescence in fcc single crystals. *International Journal of Plasticity*, Volume 22, Issue 5:921–942, 2006.
- [PKCM00] H. Pelletier, J. Krier, A. Cornet, and P. Mille. Limits of using bilinear stress-strain curve for finite element modeling of nanoindentation response on bulk materials. *Thin Solid Films*, Volume 379, Issues 1-2:147–155, 2000.
- [Pri00] F. Prima. *Etude métallurgique d'un nouvel alliage de titane  $\beta$ -métastable*. PhD thesis, INSA of Rennes, 2000.
- [PS95] J.A. Medina Perilla and J.Gil Sevillano. Two-dimensional sections of the yield locus of a Ti-6Al-4V alloy with a strong transverse-type crystallographic alpha-texture. *Materials Science and Engineering A*, Volume 201, Issue 1-2:103–110, 1995.
- [Reg] <http://www.wallonie.be>. Page last visited on August 12, 2008.
- [Rob07] Y. Robert. *Simulation numérique du soudage du TA6V par laser Yag impulsif: caractérisation expérimentale et modélisation des aspects thermomécaniques associés à ce procédé*. PhD thesis, Ecole des Mines de Paris, 2007.
- [RQ06] H.J. Rack and J.I. Qazi. Titanium alloys for biomedical applications. *Materials Science and Engineering C*, Volume 26, Issue 8:1269–1277, 2006.
- [Saf] <http://www.safran-group.com>. Page last visited on August 12, 2008.
- [SH86] J.C. Simo and T.J.R. Hughes. On the variational foundations of assumed strain methods. *Journal of Applied Mechanics*, Volume 53, Issue 1:51–54, 1986.
- [Sha96] J.F. Shackelford. *Introduction to materials science and engineers*. Prentice Hall, fourth edition, 1996.

- [SN02] R. Saha and W.D. Nix. Effects of the substrate on the determination of thin film mechanical properties by nanoindentation. *Acta Materialia*, Volume 50, Issue 1:23–38, 2002.
- [SPCB01] P. Sanchez, A. Pochettino, T. Chauveau, and B. Bacroix. Torsion texture development of zirconium alloys. *Journal of Nuclear Materials*, Volume 298, Issue 3:329–339, 2001.
- [SSH07] A. Siddiq, S. Schmauder, and Y. Huang. Fracture of bicrystal metal/ceramic interfaces: A study via the mechanism-based strain gradient crystal plasticity theory. *International Journal of Plasticity*, Volume 23, Issue 4:665–689, 2007.
- [SYFT04] T. Sasaki, M. Yang, S. Fukushima, and R. Tsukano. Development of the CAE-assisted nano-indentation method for the evaluation of the anisotropic mechanical-properties of thin films. *Journal of Materials Processing Technology*, Volume 151, Issues 1-3:263–267, 2004.
- [TAAG<sup>+</sup>07] J.D.C. Teixeira, B. Appolaire, E. Aeby-Gautier, S. Denis, G. Cailletaud, and Späth N. Transformation kinetics and microstructures of Ti17 titanium alloy during continuous cooling. *Materials Science and Engineering A*, Volume 448, Issues 1-2:135–145, 2007.
- [Tab51] D. Tabor. *The hardness of metals*. Clarendon press, Oxford, 1951.
- [Tec] <http://www.techspace-aero.be>. Page last visited on August 12, 2008.
- [Tri06] V. Trinité. *Etude théorique des phases du titane*. PhD thesis, Ecole polytechnique, France, 2006.
- [VKF07] V. Venkatesh, M. Kamal, and J. Fanning. Thermomechanical processing of TIMETAL 555. In M. Ikeda M. Hagiwara M.Niinomi, S. Akiyama and K. Maruyama, editors, *Proceedings of Ti-2007 Science and Technology*, The Japan Institute of Metals., 2007.
- [WBL91] T. Wu, J.L. Bassani, and C. Laird. Latent hardening in single crystal I. Theory and experiments. *Proceedings of the Royal Society of London, Series A*, 435, Issue 1893:1–19, 1991.
- [WRKR04] Y. Wang, D. Raabe, C. Klüber, and F. Roters. Orientation dependence of nanoindentation pile-up patterns and of nanoindentation microtextures in copper single crystals. *Acta Materialia*, Volume 52, Issue 8:2229–2238, 2004.
- [WSD07] F. Warchomicka, M. Stockinger, and H.P. Degischer. Flow behaviour and microstructure during hot deformation of Ti-5Al-5Mo-5V-3Cr-1Zr. In M. Ikeda M. Hagiwara M.Niinomi, S. Akiyama and K. Maruyama, editors, *Proceedings of Ti-2007 Science and Technology*, The Japan Institute of Metals., 2007.
- [WW04] Jue Wang and R. H. Wagoner. A New Hexahedral Solid Element for 3D FEM Simulation of Sheet Metal Forming. In S. Ghosh, J. C. Castro, and J. K. Lee, editors, *Proceedings of the 8th Numiform conference*, Columbus, OH, USA., 2004.

- [WWJ<sup>+</sup>08] W. Wang, M. Wang, Z. Jie, F. Sun, and D. Huang. Research on the microstructure and wear resistance of titanium alloy structural members repaired by laser cladding. *Optics and Lasers in Engineering*, Volume 46, Issue 11:810–816, 2008.
- [XL08] Z.H. Xu and X. Li. Effects of indenter geometry and material properties on the correction factor of Sneddon’s relationship for nanoindentation of elastic and elastic-plastic materials. *Acta Materialia*, Volume 56, Issue 6:1399–1405, 2008.
- [YKC07] J. Yan, A.M. Karlsson, and X. Chen. Determining plastic properties of a material with residual stress by using conical indentation. *International Journal of Solids and Structures*, Volume 44, Issues 11-12:3720–3737, 2007.
- [Zen] <http://asm.confex.com/asm/aero06/techprogram.htm> (paper 14136). Page last visited on July 3, 2006.
- [ZRS<sup>+</sup>06] N. Zaafarani, D. Raabe, R.N. Singh, F. Roters, and S. Zaefferer. Three-dimensional investigation of the texture and microstructure below a nanoindent in a Cu single crystal using 3D EBSD and crystal plasticity finite element simulations. *Acta Materialia*, Volume 54, Issue 7:1863–1876, 2006.